

UCGE Reports
Number 20308

Department of Geomatics Engineering

Coherent Array Processing of GPS Sonobuoys
(URL: <http://www.geomatics.ucalgary.ca/graduatetheses>)

by

Abdalla Osman

April 2010



UNIVERSITY OF CALGARY

Coherent Array Processing of GPS Sonobuoys

By

Abdalla Mostafa Osman

A THESIS

SUBMITTED TO THE FACULTY OF GRADUATE STUDIES
IN PARTIAL FULFILMENT OF THE REQUIREMENTS FOR THE
DEGREE OF DOCTOR OF PHILOSOPHY

DEPARTMENT OF GEOMATICS ENGINEERING

CALGARY, ALBERTA

MARCH, 2010

© Abdalla Mostafa Osman 2010

Abstract

Underwater target tracking in ocean environment has attracted considerable interest in both military and civilian applications. Towards this purpose, sonobuoys are among the most capable sonar systems used in underwater environments. Sonobuoys are used to detect and track underwater objects emitting sounds. Recently GPS receivers have been integrated to sonobuoy systems to provide accurate information about sonobuoys positions. An accurate knowledge of geographic positions of deployed sonobuoys is critical for the conduct of antisubmarine warfare (ASW) operations and detected target localization. It enables processing array of GPS sonobuoys thus improving the target tracking accuracy. Considering that sonobuoy positions are accurately known, the main factors influencing the operation of sonobuoys would be the interference sources and background noise.

The background noise, the low sound pressure levels of some underwater targets, the sonobuoys drift, the attenuation of the sound pressure level, the sonobuoys deployment strategy and the self noise of hydrophones are among the main factors deteriorating the system accuracy and jeopardizing the overall performance. The present trend of decreasing signal of interest levels while increasing noise due to the growing ocean traffic has served to continually complicate ASW operations. Coherently processing an array of GPS sonobuoys can lead to noise reduction and hence higher signal to noise ratio (SNR). Some research activities targeted the utilization of an array of sonobuoys to utilize beamforming technology to reject unwanted noise and enhance the reception of desired signals. However, the limitation on the inter-element spacing was always considered the main factor affecting the system performance.

This research aims at: (1) Developing a high resolution spectral estimation algorithm to improve target detection and enhance the accuracy of bearing estimation; (2) Exploring the theoretical requirements for sonobuoy positioning in order to feasibly and coherently process a field of sonobuoys; (3) Designing a method for coherently processing uniform and arbitrary arrays of GPS sonobuoys; (4) Integrating frequency domain adaptive beamforming with artificial neural network (ANN) to resolve the ambiguity existing in bearing estimation when processing widely spaced array omnidirectional sonobuoys; (5) Developing a virtual array search method to enhance the bearing estimation when processing sparse array of directional sonobuoys.

The proposed methods are examined and their performances are verified using acoustic level simulated data development for different underwater environmental conditions. Comparisons to the conventional processing techniques are conducted to assess the benefits of the proposed methods. The results show the proposed methods are capable of enhancing the accuracy of target bearing estimation especially in cases of relatively low SNR. The merits and limitations of the proposed methodologies are discussed and analyzed in this thesis.

Acknowledgements

I would like to express my gratitude to my supervisor, Dr. Naser El-Sheimy, for his professional supervision, critical discussions and immeasurable contributions. I would like also to thank Dr. Aboelmagd Noureldin, my research co-supervisor, for his continuous support, encouragement and guidance throughout my studies. To him also belongs the credit for proposing the research project and attracting several sources of funding.

This research was supported in part by Aerospace Engineering Research Advisory Committee (AERAC) and Defence Research and Development Canada (DRDC) Atlantic. The technical support and guidance provided by Mr. Scott Campbell (DND), Mr. Jim Theriault and Dr. Garfield Mellema (DRDC – Atlantic) throughout the course of my PhD are highly appreciated. The scholarship and the research allowance provided by the University of Calgary are gratefully acknowledged.

Finally, I would like to thank my parents, Mostafa Osman and Aida El-Khosht, for their continuous and unlimited moral support. They have been a constant source of love, encouragement and inspiration. Also Thanks to my brother Ahmed. And special thanks to my soul guide Dr. Mahmoud Sobieh for his continuous support. I am also deeply grateful to my wife Nissrine and my daughter Yasmina for their patience, support and continuous encouragement.

Dedication

*To the soul of my father, to my mother and to my wife for their unlimited moral support and continuous encouragement.
“Words will never say how grateful I am to you.”*

Table of Contents

Abstract.....	ii
Acknowledgements.....	iv
Dedication.....	v
Table of Contents.....	vi
List of Tables.....	ix
List of Figures and Illustrations.....	x
List of Symbols, Abbreviations and Nomenclature.....	xviii
CHAPTER ONE: INTRODUCTION.....	1
1.1 Background.....	1
1.1.1 Underwater Acoustics.....	1
1.1.2 Anti Submarine Warfare.....	2
1.1.3 Underwater Acoustic sensors.....	3
1.1.3.1 Towed Arrays.....	4
1.1.3.2 Dipping (Dunking) Sonar Systems.....	6
1.1.3.3 Side can Sonar Systems.....	7
1.1.3.4 Synthetic Aperture Sonar systems (SAS):.....	8
1.1.3.5 Bottom Mounted Sensors.....	9
1.1.3.6 Sonobuoy Devices.....	10
1.1.4 DIFAR Sonobuoy.....	14
1.2 Problem Statement.....	15
1.3 Objectives and scope of research.....	17
1.4 Thesis Structure.....	19
CHAPTER TWO: UNDERWATER TARGET TRACKING.....	22
2.1 Fundamentals of Sonar Systems.....	22
2.1.1 Transmission Loss.....	23
2.1.1.1 Sound Velocity Profile (SVP).....	24
2.1.1.2 Sound Propagation Paths.....	25
2.2 Acoustic sources of ASW targets.....	32
2.3 Sonobuoys Devices.....	34
2.4 Passive Sonobuoys.....	35
2.5 DIFAR Sonobuoy.....	37
2.5.1.1 System Operation.....	37
2.5.1.2 Signal Processing Techniques and their Limitations.....	39
Spectrum analysis.....	40
2.6 Research progress and Current state of the art.....	48
2.6.1 Target detection.....	49
2.6.2 Bearing Estimation.....	50
2.6.3 TMA.....	52
2.7 Conclusion.....	53
CHAPTER THREE: IMPROVED TARGET DETECTION AND BEARING ESTIMATION UTILIZING FAST ORTHOGONAL SEARCH FOR REAL- TIME SPECTRAL ANALYSIS.....	54

3.1 Fast Orthogonal Search (FOS).....	56
3.2 Application of FOS to the problem of underwater target detection and localization.....	60
FOS accuracy enhancement parameters.....	62
3.3 Simulation WORK.....	64
3.4 Results and Discussion.....	70
3.4.1 First Scenario (Single source).....	70
3.4.2 Second Scenario (Target and two interference sources).....	78
3.5 Conclusions.....	84
CHAPTER FOUR: DIRECTION OF ARRIVAL ESTIMATION USING AN ARRAY OF GPS SONOBUOYS.....	85
4.1 Underwater Tracking Using Single DIFAR Sonobuoy.....	86
4.2 Underwater Tracking Using Uniform Linear Array (ULA) of DIFAR Sonobuoys.....	88
4.2.1 Radiation Pattern for a Linear Array of Omni-directional sensors.....	88
4.2.2 Radiation Pattern for a Linear Array of DIFAR sonobuoys.....	89
4.2.2.1 Modified Steering vector.....	90
4.2.2.2 Obtaining Radiation Pattern for a Linear Array of DIFAR sonobuoys.....	91
4.2.3 Simulation work:.....	98
4.2.4 Results and Discussion.....	100
4.2.4.1 ULA of DIFAR Sonobuoys spaced 10 m apart.....	100
4.2.4.2 ULA of DIFAR Sonobuoys spaced 50 meters apart.....	105
4.2.4.3 ULA of DIFAR Sonobuoys spaced 300m Apart.....	109
4.3 Processing arbitrary array of DIFAR sonobuoys:.....	112
4.3.1 Simulation work.....	113
4.3.2 Results and discussion.....	116
4.4 Conclusion.....	120
CHAPTER FIVE: A NEW DOA ESTIMATION APPROACH FOR WIDELY SPACED ARRAYS USING FREQUENCY BEAMFORMING AND ANN.....	122
5.1 Frequency domain adaptive beamforming for planar arrays.....	125
5.2 Methodology.....	129
5.2.1 FB for spatially aliased arrays.....	129
5.2.2 Design of an ANN module for phase ambiguity resolution.....	132
5.2.3 FB-NN DOA estimation module.....	136
5.3 Results and Discussion.....	137
5.3.1 Simulation Scenario.....	137
5.3.2 Results.....	138
5.4 Conclusion.....	145
CHAPTER SIX: DIRECTION OF ARRIVAL ESTIMATION USING VIRTUAL ARRAY SEARCH (VAS).....	147
6.1 Virtual Array Search (VAS).....	149
6.2 Array Mapping.....	151
6.2.1 Virtual array design parameters.....	158

6.3 Simulation work.....	159
6.3.1 Transformation Matrix design.....	162
6.3.2 Bearing estimation using VAS.....	164
6.4 Results and Discussion.....	165
6.4.1 DIFAR ULA array and Virtual array with 60m and 6m Inter-element spacing respectively.....	165
6.4.2 Arbitrary array of DIFAR sonobuoys.....	170
6.5 Performance analysis and limitations of VAS.....	176
6.6 Conclusion.....	178
CHAPTER SEVEN: CONCLUSION AND RECOMMENDATIONS FOR FUTURE RESEARCH.....	180
7.1 Summary.....	180
7.2 Conclusions.....	181
7.2.1 Qualitative study for the applicability of FOS in underwater Target Detection and Bearing Estimation.....	182
7.2.2 DOA Estimation using an Array of GPS Sonobuoys.....	182
7.2.3 DOA Estimation using Frequency Beamforming and ANN.....	183
7.2.4 Direction of Arrival Estimation using VAS.....	184
7.3 Thesis contributions.....	185
7.4 Recommendations for future research.....	186
7.4.1 Improving the parameters of TMA.....	186
7.4.2 Exploring the application of VAS with other bearing estimation methods...187	
7.4.3 Exploring the Benefits of FOS for ambiguity resolution of direction cosines in the frequency beamforming method.....	187
REFERENCES.....	188
APPENDIX A: VIRTUAL ARRAY TRANSFORMATION MATRIX DESIGN.....	204
A.1. Transformation matrix parameters.....	206
A.2. Least mean square solution for Transformation matrix minimization criterion..208	

List of Tables

Table 3.1. Bearing estimation results for first scenario	77
Table 3.2 Bearing estimation results for second scenario.....	83

List of Figures and Illustrations

Figure 1.1 Deployment of surface ship towed array	5
Figure 1.2 Submarine towed array	6
Figure 1.3 Dipping Sonar System	7
Figure 1.4 Sidescan Sonar	8
Figure 1.5 SAS Sonar systems	9
Figure 1.6 Bottom Mounted Sonar systems	10
Figure 1.7 Sonobuoy loaded on aircraft (Source: http://www.navy.mil)	12
Figure 1.8 Aircraft launched sonobuoy (Source: www.naval.com.br)	13
Figure 1.9 GPS Sonobuoys Concept (Source : Gregory01)	14
Figure 2.1 Typical Deep Ocean Sound Velocity Profile	24
Figure 2.2 Sound Propagation in Direct Path	25
Figure 2.3 Sound Propagation in Surface Duct	26
Figure 2.4 Deep and Shallow Water Channels	27
Figure 2.5 Sound Propagation in Half Channel	28
Figure 2.6 Bottom Bounce	28
Figure 2.7: Convergence Zone[Ultra06]	29
Figure 2.8 Sound Propagation in shallow Water	30
Figure 2.9 An Example of Propagation Loss Profile	32
Figure 2.10 Sound Pressure Levels of Broadband and Narrowband Sources	34
Figure 2.11 Illustration of Acoustic Dipole Response of DIFAR Sensor	39
Figure 2.12 DFT for Signal Received from Four sources at SNR -10 dB	41
Figure 2.13 DFT for Signal Received from Four sources at SNR -30 dB	42
Figure 2.14 Sample LOFARgram 10-150 Hz [Boh05]	47
Figure 2.15 Sample B-scan plot corresponding to Figure 2.17 [Boh05]	47

Figure 3.1. Application of FOS to the problem of underwater target detection and localization	61
Figure 3.2 Trajectory of simulated sources relative to sonobuoy location	66
Figure 3.3 Transmission Loss vs. depth and range for 100Hz source lying at a depth of 100 m	67
Figure 3.4 Transmission Loss vs. range for 100Hz source; source and receiver at a depth of 100 m	67
Figure 3.5 Transmission Loss vs range for 60Hz source; source and receiver at a depth of 100 m	68
Figure 3.6 Transmission Loss vs range for 160Hz source; source and receiver at a depth of 100 m	68
Figure 3.7a. PSD using FOS for SNR=-25 dB using 5s data window	71
Figure 3.7b. PSD using FFT for SNR=-25 dB using 5s data window	71
Figure 3.8a. PSD using FOS for SNR=-25 dB using 60s data window	71
Figure 3.8b. PSD using FFT for SNR=-25 dB using 60s data window	71
Figure 3.9a. PSD using FOS for SNR=-30 dB using 5s data window	72
Figure 3.9b. PSD using FFT for SNR=-30 dB using 5s data window	72
Figure 3.10a. PSD using FOS for SNR=-30 dB using 60s data window	73
Figure 3.10b. PSD using FFT for SNR=-30 dB using 60s data window	73
Figure 3.11a. PSD using FOS for SNR=-35 dB using 5s data window	73
Figure 3.11b. PSD using FFT for SNR=-35 dB using 5s data window	73
Figure 3.12a. PSD using FOS for SNR=-35 dB using 60s data window	74
Figure 3.12b. PSD using FFT for SNR=-35 dB using 60s data window	74
Figure 3.13a. PSD using FOS for SNR=-25 dB using 5s data window	78
Figure 3.13b. PSD using FFT for SNR=-25 dB using 5s data window	78
Figure 3.14a. PSD using FOS for SNR=-25 dB using 10s data window	79
Figure 3.14b. PSD using FFT for SNR=-25 dB using 10s data window	79

Figure 3.15a. PSD using FOS for SNR=-25 dB using 20s data window	79
Figure 3.15b. PSD using FFT for SNR=-25 dB using 20s data window.....	79
Figure 3.16a. PSD using FOS for SNR=-25 dB using 60s data window	80
Figure 3.16b. PSD using FFT for SNR=-25 dB using 60s data window.....	80
Figure 4.1 Acoustic dipole response of DIFAR sonobuoy	87
Figure 4.2. Radiation Pattern for DIFAR Sonobuoy (DOA=160°)	95
Figure 4.3a. Radiation Pattern for Linear array of 4 Omni-directional sensors (DOA=160° d=10 m)	96
Figure 4.3b. Radiation Pattern for Linear array of 4 DIFAR sonobuoys (DOA=160° d=10 m).....	96
Figure 4.3c. Radiation Pattern for Linear array of 4 Omni-directional sensors	97
Figure 4.3d. Radiation Pattern for Linear array of 4 DIFAR sonobuoys (DOA=160°.....	97
Figure 4.4 Linear Array of DIFAR Sonobuoys	100
Figure 4.5a. A sample of Bartlett Beamforming output ((DOA=160°, d=10m, SNR=- 25dB) for single DIFAR sonobuoy (top panel) and ULA of DIFAR sonobuoys (bottom panel).....	102
Figure 4.5b. Output of Monte Carlo simulations for single DIFAR sonobuoy ((DOA=160°, SNR=-25dB)	102
Figure 4.5c. Output of Monte Carlo simulations for ULA of DIFAR sonobuoys ((DOA=160°, d=10m, SNR=-25dB).....	102
Figure 4.6a. A sample of Bartlett Beamforming output ((DOA=160°, d=10m, SNR=- 35dB) for single DIFAR sonobuoy (top panel) and ULA of DIFAR sonobuoys (bottom panel).....	103
Figure 4.6b. Output of Monte Carlo simulations for single DIFAR sonobuoy ((DOA=160°, SNR=-35dB)	103
Figure 4.6c. Output of Monte Carlo simulations for ULA of DIFAR sonobuoys ((DOA=160°, d=10m, SNR=-35dB).....	103
Figure 4.7a. A sample of Bartlett Beamforming output ((DOA=160°, d=10m, SNR=- 40dB) for single DIFAR sonobuoy (top panel) and ULA of DIFAR sonobuoys (bottom panel).....	104

Figure 4.7b. Output of Monte Carlo simulations for single DIFAR sonobuoy ((DOA=160°, SNR=-40dB)	104
Figure 4.7c. Output of Monte Carlo simulations for ULA of DIFAR sonobuoys ((DOA=160°, d=10m, SNR=-40dB).....	104
Figure 4.8a. A sample of Bartlett Beamforming output ((DOA=160°, d=50m, SNR=- 35dB) for single DIFAR sonobuoy (top panel) and ULA of DIFAR sonobuoys (bottom panel).....	106
Figure 4.8b. Output of Monte Carlo simulations for ULA of DIFAR sonobuoys ((DOA=160°, d=50m, SNR=-25dB).....	106
Figure 4.9a. A sample of Bartlett Beamforming output ((DOA=160°, d=50m, SNR=- 35dB) for single DIFAR sonobuoy (top panel) and ULA of DIFAR sonobuoys (bottom panel).....	107
Figure 4.9b. Output of Monte Carlo simulations for ULA of DIFAR sonobuoys ((DOA=160°, d=50m, SNR=-35dB).....	108
Figure 4.10a. A sample of Bartlett Beamforming output (d=50m, SNR=-40dB) for single DIFAR sonobuoy (top panel) and ULA of DIFAR sonobuoys (bottom panel).....	108
Figure 4.10b. Output of Monte Carlo simulations for ULA of DIFAR sonobuoys ((DOA=160°, d=50m, SNR=-40dB).....	109
Figure 4.11a. A sample of Bartlett Beamforming output ((DOA=160°, d=300m, SNR=-25dB) for single DIFAR sonobuoy (top panel) and ULA of DIFAR sonobuoys (bottom panel).....	110
Figure 4.11b. Output of Monte Carlo simulations for ULA of DIFAR sonobuoys ((DOA=160°, d=300m, SNR=-25dB).....	111
Figure 4.12. Output of Monte Carlo simulations for ULA of DIFAR sonobuoys ((DOA=160°, d=300m, SNR=-35dB).....	111
Figure 4.13. Output of Monte Carlo simulations for ULA of DIFAR sonobuoys ((DOA=160°, d=300m, SNR=-40dB).....	112
Figure 4.14 (a) Irregular array of DIFAR sonobuoys , (b) Radiation pattern for a source with a bearing of 160o impinging an irregular array of 4 DIFAR sonobuoys with d1=50 m, d2=40m, d3=55 m, d4=70, d5=58 and d6= 100m.....	115
Figure 4.15 (a) Irregular array of DIFAR sonobuoys , (b) Radiation pattern for a source with a bearing of 160o impinging an irregular array of 4 DIFAR sonobuoys with d1=50 m, d2=70m, d3=55 m, d4=40, d5=58 and d6= 100m.....	116

Figure 4.16a. A sample of Bartlett Beamforming output (DOA=160° SNR=-35dB) for single DIFAR sonobuoy (top panel) and Arbitrary of DIFAR sonobuoys shown in Figure 4.14 (bottom panel)	118
Figure 4.16b. Output of Monte Carlo simulations for the Arbitrary array of DIFAR sonobuoys shown in Figure 4.14 (DOA=160° SNR=-35 dB).....	119
Figure 4.17a. A sample of Bartlett Beamforming output (DOA=160° SNR=-35dB) for single DIFAR sonobuoy (top panel) and Arbitrary of DIFAR sonobuoys shown in Figure 4.15 (bottom panel)	119
Figure 4.17b. Output of Monte Carlo simulations for the Arbitrary array of DIFAR sonobuoys shown in Figure 4.15 (DOA=160° SNR=-35 dB).....	120
Figure 5.1. Training procedure of ANN module.	133
Figure 5. 2. ANN operation for estimating the unwrapping parameters (r_x and r_y)	134
Figure 5. 3. Architecture of one hidden layer MLP network for phase ambiguity resolution.....	135
Figure 5.4. FB-NN DOA estimation module.....	137
Figure 5. 5. 3 X 3 planar array with d inter-element spacing and non moving source... ..	138
Figure 5.6. Error variation with the number of hidden nodes for Case I (10m dinter-element spacing)	140
Figure 5.7. Error variation with the number of hidden nodes for Case II (19m inter-element spacing)	141
Figure 5.8. Error variation with the number of hidden nodes for Case III (101m)	141
Figure 5.9. Variation of estimated unit vector in x axis against different source bearings	143
Figure 5. 10. Variation of estimated unit vector in y axis against different source bearings	143
Figure 5. 11. Error variation with SNR for 256 hidden layers	145
Figure 6.1. VAS approach	151
Figure 6.2 ULA of 2 DIFAR Sonobuoys.....	153
Figure 6.3 Virtual Array of DIFAR sonobuoys	153

Figure 6.4 (a) ULA of 3 DIFAR sonobuoys , (b) Radiation pattern for a source with a bearing of 160° impinging ULA of 3 DIFAR sonobuoys with $d=60$ m	161
Figure 6.5 (a) Arbitrary array of DIFAR sonobuoys , (b) Radiation pattern for a source with a bearing of 160° impinging an arbitrary array of 3 DIFAR sonobuoys with $d_1=60$ m, $d_2=80$ m, $d_3=70$ and $d_4= 40$ m	161
Figure 6.6 Bias error in bearing estimation for different sector width and fixed virtual inter-element spacing of $d_v=10$ m	163
Figure 6.7. Bias error in bearing estimation for different virtual inter-element spacing (d_v) and fixed sector width of 2 degree	163
Figure 6.8. Bias error in bearing estimation for different virtual inter-element spacing (d_v) and fixed sector width of 1 degree	164
Figure 6.9 A sample of Bartlett Beamforming output ($d=60$ m, $SNR=-30$ dB) for ULA of 3 DIFAR sonobuoy (top panel) and virtual array of 23 DIFAR sonobuoys (bottom panel).....	166
Figure 6.10a Output of Monte Carlo simulations for ULA of 3 DIFAR sonobuoys ($d=60$ m, $SNR=-30$ dB).....	167
Figure 6.10b Output of Monte Carlo simulations for VA of 23 DIFAR sonobuoys ($d=6$ m, $SNR=-30$ dB).....	167
Figure 6.11 A sample of Bartlett Beamforming output ($d=60$ m, $SNR=-40$ dB) for ULA of 3 DIFAR sonobuoy (top panel) and virtual array of 23 DIFAR sonobuoys (bottom panel).....	167
Figure 6.12a Output of Monte Carlo simulations for ULA of 3 DIFAR sonobuoys ($d=60$ m, $SNR=-40$ dB).....	168
Figure 6.12b Output of Monte Carlo simulations for VA of 23 DIFAR sonobuoys ($d=6$ m, $SNR=-40$ dB).....	168
Figure 6.13 A sample of Bartlett Beamforming output ($d=60$ m, $SNR=-30$ dB) for ULA of 3 DIFAR sonobuoy (top panel) and virtual array of 23 DIFAR sonobuoys (bottom panel).....	168
Figure 6.14a Output of Monte Carlo simulations for ULA of 3 DIFAR sonobuoys ($d=60$ m, $SNR=-30$ dB).....	169
Figure 6.14b Output of Monte Carlo simulations for VA of 23 DIFAR sonobuoys ($d=6$ m, $SNR=-30$ dB).....	169

Figure 6.15 A sample of Bartlett Beamforming output ($d=60\text{m}$, $\text{SNR}=-40\text{dB}$) for ULA of 3 DIFAR sonobuoy (top panel) and virtual array of 23 DIFAR sonobuoys (bottom panel).....	169
Figure 6.16a Output of Monte Carlo simulations for ULA of 3 DIFAR sonobuoys ($d=60\text{m}$, $\text{SNR}=-40\text{dB}$).....	170
Figure 6.16b Output of Monte Carlo simulations for VA of 23 DIFAR sonobuoys ($d=6\text{m}$, $\text{SNR}=-40\text{dB}$).....	170
Figure 6.17 A sample of Bartlett Beamforming output for arbitrary array shown in Figure 6.5 (top panel) and virtual array of 26 DIFAR sonobuoys (bottom panel) with $\text{SNR} -30 \text{ dB}$	172
Figure 6.18a The output of Monte Carlo simulations for ULA of 3 DIFAR sonobuoy with $d=60\text{m}$ and $\text{SNR}=-30 \text{ dB}$	172
Figure 6.18b The output of Monte Carlo simulations for Vitual ULA of DIFAR sonobuoys with $d=6\text{m}$ and $\text{SNR}=-30 \text{ dB}$	172
Figure 6.19 A sample of Bartlett Beamforming output for arbitrary array shown in Figure 6.2 (top panel) and virtual array of 26 DIFAR sonobuoys (bottom panel) with $\text{SNR} -40 \text{ dB}$	173
Figure 6.20a The output of Monte Carlo simulations for ULA of 3 DIFAR sonobuoy with $d=60\text{m}$ and $\text{SNR}=-40 \text{ dB}$	173
Figure 6.20b The output of Monte Carlo simulations for Vitual ULA of DIFAR sonobuoys with $d=6\text{m}$ and $\text{SNR}=-40 \text{ dB}$	173
Figure 6.21 A sample of Bartlett Beamforming output for arbitrary array shown in Figure 6.2 (top panel) and virtual array of 26 DIFAR sonobuoys (bottom panel) with $\text{SNR} -30 \text{ dB}$	174
Figure 6.22a The output of Monte Carlo simulations for ULA of 3 DIFAR sonobuoy with $d=60\text{m}$ and $\text{SNR}=-30 \text{ dB}$	174
Figure 6.22b The output of Monte Carlo simulations for Vitual ULA of DIFAR sonobuoys with $d=6\text{m}$ and $\text{SNR}=-30 \text{ dB}$	174
Figure 6.23 A sample of Bartlett Beamforming output for arbitrary array shown in Figure 6.2 (top panel) and virtual array of 26 DIFAR sonobuoys (bottom panel) with $\text{SNR} -40 \text{ dB}$	175
Figure 6.24a The output of Monte Carlo simulations for ULA of 3 DIFAR sonobuoy with $d=60\text{m}$ and $\text{SNR}=-40 \text{ dB}$	175

Figure 6.24b The output of Monte Carlo simulations for Virtual ULA of DIFAR sonobuoys with $d=6\text{m}$ and $\text{SNR}=-40\text{ dB}$	175
Figure 6.25 Performance of VAS versus Basic Processing of ULA at different inter-element distances for $\text{SNR} -30\text{ dB}$	176
Figure 6.26 Performance of VAS versus Basic Processing of ULA at different inter-element distances for $\text{SNR} -40\text{ dB}$	177

List of Symbols, Abbreviations and Nomenclature

Symbol	Definition
<i>SE</i>	Signal excess
<i>SL</i>	Source pressure level
<i>TL</i>	Transmission loss
<i>NL</i>	Noise pressure level
x_{ok}	Omni-directional Channel
x_{sk}	Sine (East-West) Channel
x_{ck}	Cosine (North-South) Channel
$x(n)$	The time series at time n
$X(k)$	Discrete Fourier Transform at frequency k
$\Phi(k)$	Power spectral density
Φ_{os}	Omni-sine cross-spectrum
Φ_{oc}	Omni-cosine cross-spectrum
$\hat{\theta}$	Sound direction of arrival
\hat{Q}	Cross Spectral Matrix
$\hat{E}_{CB}(\theta)$	Conventional beam power estimate at any arbitrary direction
$a(\theta)$	Array steering vector
$p_m(n)$	Arbitrary set of non-orthogonal candidate functions
a_m	Set of weights of the functional expansion for fast orthogonal search
$w_m(n)$	Set of orthogonal functions
g_m	Set of orthogonal weights of functional expansion of fast orthogonal search
$e(n)$	Error term of orthogonal functional expansion of fast orthogonal search
α_{mr}	Gram-Schmidt coefficients
$\frac{\varepsilon^2(n)}{Q_m}$	The mean square error of the orthogonal function expansion
Q_m	The mean square error reduction by the m^{th} candidate function for fast orthogonal search
ω_m	Digital frequency of the candidate m
C	The number of candidates
M_t	The number of terms in the final model of fast orthogonal search
N	The number of samples
f_s	The sampling frequency
v_{sr}	The relative velocity between source and receiver
v_o	The underwater sound propagation velocity
f_o	Source frequency
Δf	The Doppler shift
$ E(\theta, \theta_0) $	The magnitude of the radiation pattern

λ	The wavelength of the received signal
θ_0	Direction of arrival of the received signal
d	Inter-element spacing of array elements
Δt_n	The relative delay between array elements
$\Phi_{Single\ DIFAR}$	The normalized Fourier Transform of input sinusoidal signal arriving from direction θ_0 and received by the DIFAR sonobuoy three-sensors
R	The complex frequency domain samples at array elements
d_x	Inter-element spacing between array elements in X direction
d_y	Inter-element spacing between array elements in Y direction
u_o	Dimensionless direction cosines with respect to X axis.
v_o	Dimensionless direction cosines with respect to Y axis.
ψ_o	The depression angle
q	Index of frequency harmonics
c	Propagation velocity of underwater sound
$s(t)$	Received signal at a reference point at time t
$n(t)$	Noise vector at time t
$a_v(\theta)$	Steering vector of virtual array
N_{cal}	Number of calibration points
$\theta^{(c)}$	Collection of adjacent N_{cal} calibration directions
$A(\theta^{(c)})$	The matrix comprising the steering vectors obtained at N_{cal} calibration directions for real array
$A_v(\theta^{(c)})$	The matrix comprising the steering vectors obtained at N_{cal} calibration directions for virtual array
T	Transformation matrix for virtual array
T_{LS}	Least square solution for transformation matrix of virtual array
$\ \cdot\ _F$	Frobenius norm
$V(\theta_0, e_v)$	Criterion function associated with the MUSIC algorithm
e_v	Signal eigenvector of the virtual array from a single emitter
e_s	Signal eigenvector of the real array from a single emitter
g_v	The complex gradient of $V(\theta_0, e_v)$ with respect to e_v
$e_s^{(i)}$	The signal eigenvector of the real array from a single emitter in the i th calibration direction
$e_v^{(i)}$	The signal eigenvector of the virtual array from a single emitter in the i th calibration direction
$\Delta e_v^{(i)}$	The virtual signal eigenvector mapping error in the i th calibration direction
$\bar{a}(\theta)$	Normalized real array response vector
$\bar{a}_v(\theta)$	Normalized virtual array response vector
\otimes	Kronecker product
vec	Operator that transforms a matrix into a vector

t^{vec}	The vectorized version of virtual array transformation matrix
M^+	Moore-Penrose Pseudoinverse of M
$\Delta\theta$	Deterministic DOA perturbation
μ	Weighting factor
$\Pi_{\hat{e}_v}^\perp$	Orthogonal projector onto the estimated noise subspace
$\Pi_{a_v(\theta)}^\perp$	Orthogonal projector onto the array manifold complement
\bar{d}_v	Derivative of the normalized response vector $\bar{a}_v(\theta)$ of the virtual array with respect to θ
<i>dB re μ Pascal</i>	Decibel relative micro Pascal

ANN	Artificial Neural Network
AoA	Angle of arrival
AR	Autoregressive
ARMA	Auto-regressive moving average
ASW	Antisubmarine warfare
BOT	Bearings-only tracking
BO-TMA	Bearin-only target motion analysis
CSM	Cross Spectral Matrix
CZ	Convergence zone
DFT	Discrete Fourier transform
DIFAR	Directional Frequency Analysis and Recording
DOA	Direction of arrival
DSC	Deep Sound Channel
FFBP	Feed forward back propagation
FFT	Fast Fourier Transform
FOS	Fast orthogonal search
GPS	Global Positioning Systems
GS	Gram-Schmidt
LMS	Least-mean-square
LOFAR	Low-frequency analysis and recording
LOFARgram	Low-frequency analysis and recording spectrogram
LP	Linear prediction
MaxTTA	Maximum terms to add
MESA	Maximum entropy spectral analysis
MFT	Matched field tracking
MLM	Maximum-likelihood method
MLP	Multi-layer perceptron
MSE	Mean squared error
MUSIC	Multiple signal classification
PECan	Canadian Parabolic equation
PSD	Power spectral density

SAS	Synthetic Aperture Sonar systems
SNR	signal to noise ration
SVP	Sound Velocity Profile
TMA	Target Motion Analysis
TOI	Target of interest
ULA	Uniform Linear Array
VA	Virtual array
VAS	Virtual array search
WGN	White Gaussian noise
WSF	Weighted subspace fitting

Chapter One: Introduction

1.1 Background

1.1.1 Underwater Acoustics

Sound is considered the best form of radiation that travels through the sea. This is because sound is the most robust form of radiation against attenuation by underwater conditions especially when compared to other sources of radiations such as electromagnetic waves. Because of its relative ease of propagation, people have applied underwater sound to a variety of purposes in their use and exploration of seas. The technique that uses sound propagation under water to navigate, communicate or to detect objects underwater is called SONAR which is an acronym for sound navigation and ranging [Urick96].

Applications of Underwater sound can be classified into civilian and military applications [Urick96]. Civilian applications of underwater sound include acoustic devices for navigation and localization, remote control and monitoring of underwater equipments, location and identification of underwater mammals and emergency communications. These devices are being used in scientific, commercial and recreational exploitation of the oceans [Wenz72, McDonald04]. Military applications of underwater sound include acoustic mines (mines that explode when the acoustic level in their passband reaches a certain value) and detection of underwater objects (ships and submarines) [Urick96]. This research focuses on the application of underwater target tracking in ASW.

The detailed characteristics of underwater environment and its boundaries that affect sound transmission are multifaceted [Urick96 and Burdick84]. Sound speed is a function of temperature, depth and salinity. Temperature is a function of depth, time, location and weather conditions. The ocean surface varies from a glossy smooth reflector to very rough and turbulent surface that scatters sound in random fashion. The ocean bottom has a wide variety of compositions, slope and roughness, all of which influence sound transmission. The effects of sound speed profile, the sound propagation channel and depth of the medium interact to produce the final acoustic transmission characteristics [Burdick84].

1.1.2 Anti Submarine Warfare

The development of sonar systems is closely coupled to the evolution of the submarine. Early attempts for developing of sonar system started at the beginning of the twentieth century. This was followed by several attempts which were highly encouraged by the World wars. British and American developments tended to be based on active (asdic) sonar systems whilst the Germans tended to concentrate on passive sonar systems [Atkins94].

In 1940, the research in the area of ASW and the need to find sonar system that can detect German submarines led to the introduction of Omni-directional and directional sonar system called “sonobuoys” [Atkins94]. The main idea behind the development of sonobuoys was to have an expendable sonar system to be deployed from ships behind convoys and detect German submarines. In 1942 sonobuoys were redesigned to be

dropped from airplanes and by 1943 these devices were available for deployment in large quantities [Atkins94].

Enhancement of sonar systems and introduction of new systems continued during the next decades. This was emphasized by the applications of sonar systems in both civilian and military applications [Atkins94].

1.1.3 Underwater Acoustic sensors

Different types of acoustic sensors had been introduced since the early attempts for underwater target localization. These attempts [Atkins94] started at the beginning of the twentieth century using sound tubes coupled to the human ear. Later research work carried on this area aimed to improve underwater target detection and localization which finally led to the introduction of sonobuoy in 1940 by the Americans who started the development of omni-directional and directional sonobuoys. Since then sonobuoys have attracted much attention. Many research efforts have been invested in this area to further improve its operation [Holler06].

Sonar systems can be active or passive. Sonar systems, equipments, and devices are said to be active when sound is purposely generated by one of the system components called the projector. Active sonar systems are said to echo-range on their targets. Passive or listening sonar systems use sound radiated (usually unwittingly) by the target. In this case only one-way transmission through the sea is involved, and the system centers around the hydrophone used to listen to the target sounds. Communication, telemetry,

and control applications employ a hybrid form of sonar system using a projector and hydrophone at both ends of the acoustic communication path [Urick96].

Many of techniques that are used in current sonar systems were developed in the early part of the twentieth century [Atkins94].

Hull mounted sonars predominated at first [Atkins94 and Uick96] and, as these became larger, gyro stabilization and then electronic stabilization were required to counteract the movement of the vessel. Hull mounted sonars also had the advantage that the heading reference could be derived from the main heading compass [Atkins94] , whether magnetic or gyro, and that the transducer axes were fixed with respect to the axes of the vessel. The problems introduced by the self noise of the vessel could only be reduced by mounting the transducers away from the vessel. The first attempts involved towing the transducer array behind the host vessel [Atkins94 and Urick96]. Later developments included bottom mounted sensors, air launched sensors, dunking sonars, variable depth sonars, diver-held and side-scan sonars [Atkins94 and Urick96].

1.1.3.1 Towed Arrays

These are sonar arrays towed behind submarines or surface ships [Atkins94]. It is basically a long cable, up to 5000 m, with hydrophones that is trailed behind the ship when deployed. The hydrophones are placed at specific distances along the cable. Usually no hydrophones are placed at the first few hundred meters of the cable. This is because their effectiveness is significantly reduced by the self noise of the vessel generated by on-board machinery and propeller noise. Figure 1.1 shows a surface ship

towed array before deployment in water. An illustration of towed array shape underwater is shown in Figure 1.2 where the towed array is attached to submarine.



Figure 1.1 Deployment of surface ship towed array

(Source: www.nurc.nato.int/)

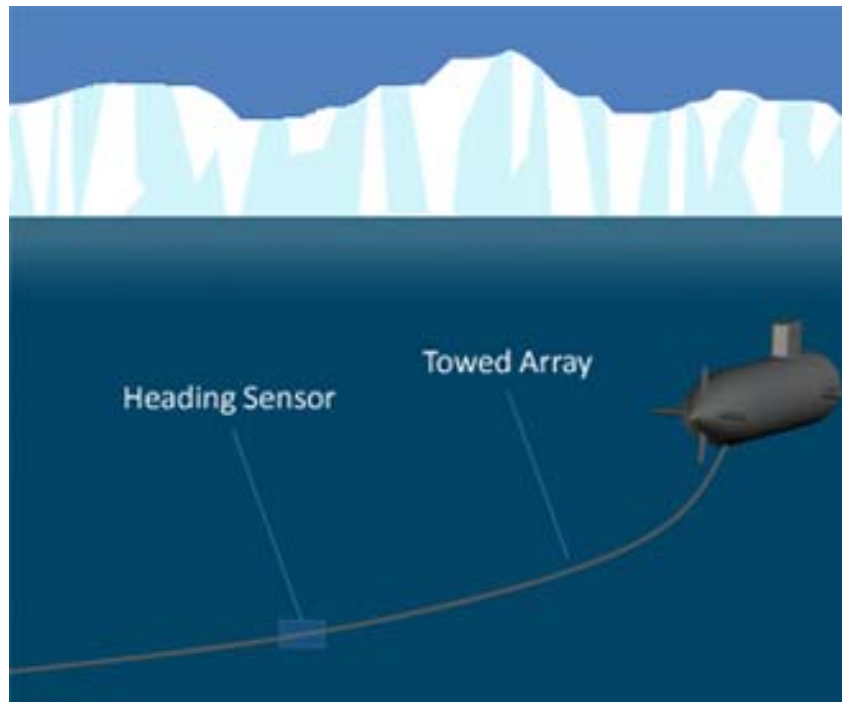


Figure 1.2 Submarine towed array (Source: www.sensingways.com)

1.1.3.2 Dipping (Dunking) Sonar Systems

These are sonar transducers that are lowered into the water from helicopters or sea launched from a vessel and then recovered after the search is complete. Figure 1.3 shows a Dipping sonar system lowered from a helicopter [Atkins94].



Figure 1.3 Dipping Sonar System (Source: www.dutchsubmarines.com)

1.1.3.3 Side can Sonar Systems

These systems are mainly used to efficiently create an image of large areas of the sea floor. This tool is used for mapping the seabed for a wide variety of purposes, including creation of nautical charts and detection and identification of underwater objects and Side scan uses a sonar device that emits fan-shaped pulses down toward the seafloor across a wide angle perpendicular to the path of the sensor through the water, which may be towed from a surface vessel or submarine, or mounted on the ship's hull. The intensity of the acoustic reflections from the seafloor of this fan-shaped beam is recorded in a series of cross-track slices. When stitched together along the direction of

motion, these slices form an image of the sea bottom within the swath (coverage width) of the beam. The sound frequencies used in side-scan sonar usually range from 100 to 500 kHz; higher frequencies yield better resolution but less range [Atkins94]. Figure 1.4 shows an example of sidescan sonar system attached to a surface ship.

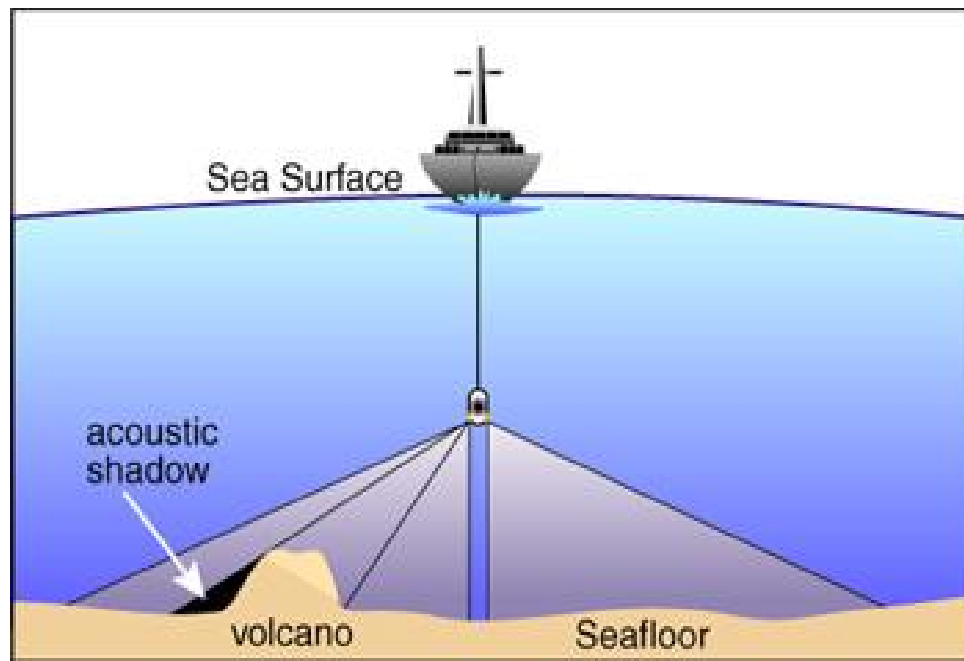


Figure 1.4 Sidescan Sonar (Source: www.punaridge.org)

1.1.3.4 Synthetic Aperture Sonar systems (SAS):

These systems use a combination of acoustic pings to form an image with much higher resolution than conventional sonars. SAS mainly produces a synthetic array equal to the distance traveled. Later on a synthetic aperture image is produced by reorganization of the data from all the pings. Figure 1.5 illustrates the operation of synthetic aperture sonar systems [Atkins94].

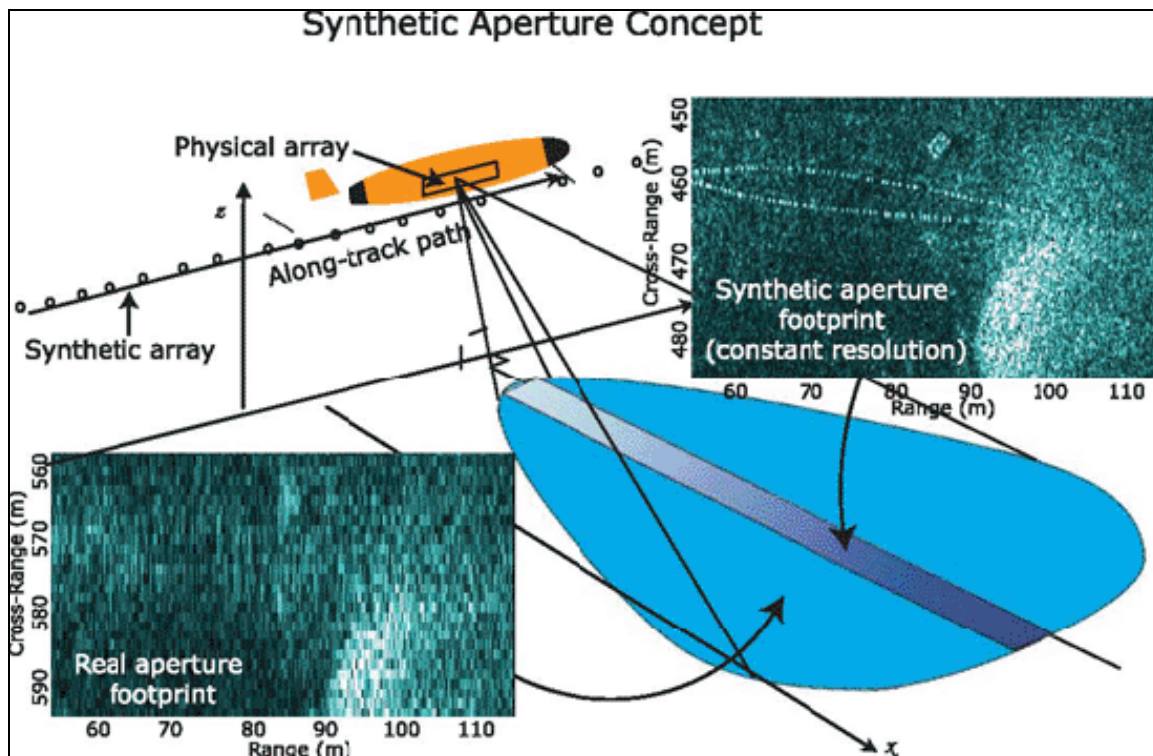


Figure 1.5 SAS Sonar systems (Source: www.appsig.com)

1.1.3.5 Bottom Mounted Sensors

Bottom mounted sensors for military applications are permanent installations which can be placed at well surveyed locations and subsequently calibrated using acoustic techniques [Atkins94]. They are normally buoyant devices but attached to concrete blocks via a release mechanism in order to recover them at a later date. Standard practice is to deploy them at positions determined by differential GPS and then to perform acoustic ranging calibrations. A bottom mounted sensor is shown in Figure 1.6



Figure 1.6 Bottom Mounted Sonar systems (Source: oceanexplorer.noaa.gov)

1.1.3.6 Sonobuoy Devices

Sonobuoy [Urick96, Boh05 and Des99] is mainly a microphone that is deployed from a platform to become submerged in the water and provides information about the local sound amplitude, as a function of frequency and time. Figure 1.7 shows loading of an aircraft with sonobuoys for future deployment in water.

Sonobuoys are used to estimate and track the position of underwater objects that emit sounds [Urick96]. The platforms that deploy sonobuoys are usually helicopters or

airplanes (as shown in Figure 1.8) [Urick96], but they can also be surface ships. In order to determine the position of a submarine, it should be within the detection range of at least three sonobuoys (preferably four to achieve better accuracy) [Johansson97, Boh05 and Des99]. However, the bearing of the submarine can be detected if the submarine lies in the detection range of one sonobuoy if equipped with a compass [Boh05 and Des99]. The advantages of sonobuoys [Johansson97] over other acoustic measuring systems include its relative low cost, ease of deployment and the fact that they are not disturbed by the noise from the deploying platform. An advantage of *passive* sonobuoys compared to *active* sonobuoys, which emit a sound signal, is that they do not reveal their presence [Johansson97]. The main factors that affect the operation of sonobuoys are interference from surrounding sources and background noise.

In order to use the data received from the sonobuoys to provide a target position, the location of the buoy must be known in the aircraft [Atkins94]. Present buoy geolocation schemes involve a variety of radio direction finding schemes to home on the RF transmission of the sonobuoy. These methods require the ASW aircraft to maneuver to obtain a sonobuoy position, and also in most cases require the use of some form of directional antenna. These methods also mean the aircraft cannot stand-off at any distance from the buoy pattern without degrading localization accuracy.



Figure 1.7 Sonobuoy loaded on aircraft (Source: <http://www.navy.mil>)



Figure 1.8 Aircraft launched sonobuoy (Source:www.naval.com.br)

Recently global positioning systems (GPS) were introduced to sonobuoys for accurate knowledge of their geographic locations. The sonobuoys system employing GPS for positioning of deployed sonobuoys is known as “GPS Sonobuoys” [White04]. Figure 1.9 shows a GPS sonobuoys system [Gregory01]. The floating part of the sonobuoy carries a GPS receiver which is used with another GPS receiver mounted on the platform (ship in this case) to apply differential GPS for the sonobuoy position. This will lead to highly accurate position of the sonobuoy and hence the detected source can be accurately localized.

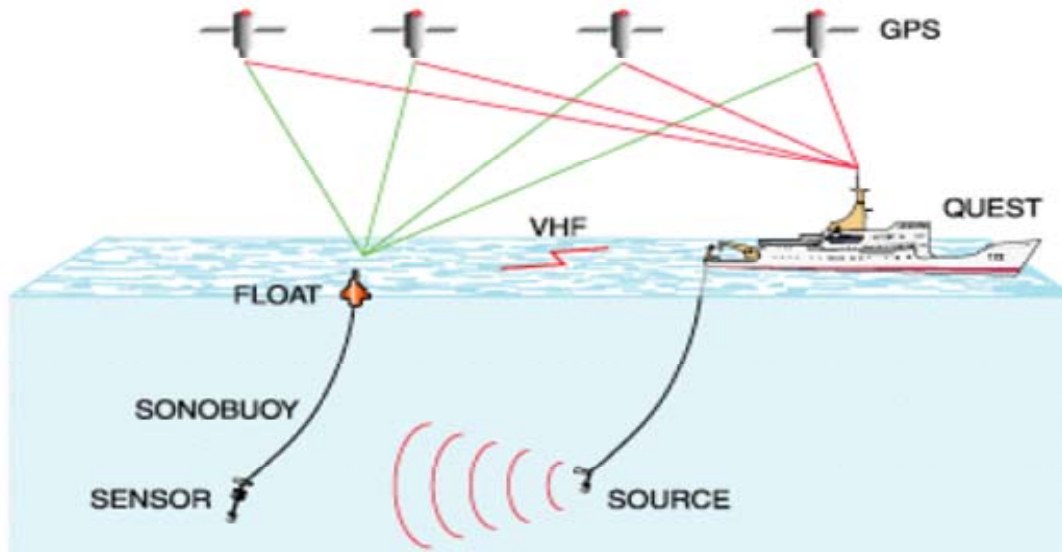


Figure 1.9 GPS Sonobuoys Concept (Source : Gregory01)

1.1.4 DIFAR Sonobuoy

A DIFAR is an acronym for directional frequency analysis and recording. A DIFAR sonobuoy is an expendable unit for the reception of acoustic energy in the ocean which is transmitted via UHF link to another platform for analysis. It is composed of a 3-element hydrophone array co-located in a submerged unit, attached to a floating electronics package at the surface [Boh05]. DIFAR sonobuoy is constituted from a small array of 3 acoustic sensors located in a single unit to provide both omni-directional amplitude and directional information. The acoustic sensors are suspended below a floating electronics assembly which contains processing and transmitter hardware.

The basic technique allows processing of the discrete Fourier transform (DFT) of each channel to generate a bearing estimate through a simple arctangent calculation. A

display of bearing versus frequency, known as a B-scan display, allows targets to be localized and discerned based on the estimated bearing presented to an operator. .

1.2 Problem Statement

In present ASW a group of passive sonobuoys are deployed according to some strategies in the water, each of which is equipped with a GPS. The sonobuoys simultaneously detect a single or multiple underwater targets (either static or mobile). In passive sonar detection and tracking, the sonar sensor receives a signal generated by the target. The detection process involves the recognition of target signals in the presence of background noise. Individual sonobuoys communicate with a central station (can be an airplane or a surface ship) directly and independently. Based on the information produced by the sonobuoys, we attempt to determine accurate target bearing.

The input conditions of the problem are influenced by:

1. Received signal to noise ratio:

This factor is mainly based on the surrounding underwater noise which is basically the undesired sound [Urick9 and Boh05]. Three basic kinds of underwater noise emerge in the sonar process [Wenz71]; these are radiated noise, self-noise, and ambient noise. *Radiated* noise is the acoustic output of marine vehicles (such as ships, submarines and torpedoes), which are usually received at some distance by sensors that are not associated with the systems of the noise-generating vehicle. *Self-noise* is that noise generated by the total system, including the vehicle or platform, which

appears at the receiver output of the sonar. Self-noise includes the acoustic output of the sonar-carrying vehicle which is received by its own acoustic sensors. *Ambient noise* is the all encompassing noise associated with the given environment and is the limiting noise if and when the other components are sufficiently reduced or eliminated. Another source of noise is the *Reverberation noise* which is defined as the sound from the active-sonar source that is scattered back in the direction of the receiver and persists to interfere with the reception of the desired echo. This source of noise is neglected in this study since it is associated with active sonar systems. Potential targets have recently become significantly quieter. As a result, there is a significant decrease in the current sonobuoys detection ranges.

Another factor that affects the SNR of the received acoustic signal is the environmental conditions of the propagation medium. These environmental conditions include [Urick96]: i) Ocean temperature; ii) The height and directional distribution of ocean swell; iii) wind speed and direction; iv) Atmospheric water content and rain rate; v) The changes in sea surface height associated with ocean tides, vi) Currents and planetary waves; vii) Concentrations of phytoplankton, sediments and suspended and dissolved material; x) The sound propagation path and the aerial extent and types of polar sea ice.

The above mentioned factors add to the weak signal of submarines and contribute to the degradation of overall system performance.

2. Sonobuoys Drift:

In ASW the sonobuoys are usually deployed from aircrafts. This strategy can affect the accuracy of deployment positions [McIntyre99] and hence the field of

sonobuoys cannot be accurately designed according to a regular arrangement. Further, after deployment, the sonobuoys drift from their initial positions due to the effects of wind and currents [McIntyre99]. This factor has a direct influence on the processing of the acoustic signal detected by the sonobuoys. Accordingly some sonobuoys might drift away such that the target is out of its detection range. Moreover, the sonobuoys drifting can prohibit proper simultaneous processing of the acoustic signal recorded by the sonobuoys field.

1.3 Objectives and scope of research

The Ultimate objective of this research is to develop a coherent array processing module of GPS sonobuoys field in order to enhance the target detection and bearing estimation accuracy. Towards achieving this goal, this thesis will focus on:

1- Developing a high resolution spectral estimation algorithm to improve target detection and enhance the accuracy of bearing estimation

Fast orthogonal search (FOS) algorithm with its high resolution spectral analysis capability is employed in this research for enhanced spectral estimation in low SNR environments. FOS enables target detection in case of low SNR and thus improves the bearing estimation accuracy. Moreover, the high resolution capability of FOS facilitates the detection of multiple targets that may be detected at very close frequencies.

2- Investigating the theoretical requirements for sensor positioning in order to feasibly and coherently process a field of sonobuoys.

This thesis will investigate the limitations imposed by the theoretical requirements for coherent processing of GPS sonobuoy field. This is considered an essential step through which the proposed research will introduce solutions to limitations preventing the application of coherent array processing of GPS sonobuoys field.

3- Designing an algorithm for coherently processing uniform and arbitrary arrays of GPS sonobuoys.

In target tracking applications (e.g. ASW), processing the signals received by an array of GPS sonobuoys can significantly improve the bearing estimation and target localization. This research introduces a new approach to jointly process the data recorded from sparse array of GPS sonobuoys. The approach is examined for its contribution in bearing estimation enhancement when applied to uniform and arbitrary arrays of GPS sonobuoys.

4- Developing beamforming algorithm to enhance target bearing estimation using widely spaced array of GPS sonobuoys.

This research targets the development of a beamforming algorithm for coherent array processing of widely spaced uniform array of omni-directional GPS sonobuoys at relatively low SNR, which is usually the case in ASW. This research aims at extending the application of frequency domain adaptive beamforming using artificial neural network (ANN), which is employed to resolve the ambiguity existing in bearing estimation that resulted from the widely spaced array elements.

5- *Designing a new bearing estimation technique for sparse array of DIFAR Sonobuoys based on searching virtual array transformation matrices*

Further enhancement of bearing estimation using an array of GPS DIFAR sonobuoys is targeted utilizing virtual array processing to design a set of transformation matrices. An advanced array mapping technique is employed to provide accurate transformation matrices of the DIFAR sonobuoys array elements. These transformation matrices are used by the proposed new technique to enhance bearing estimation for a group of widely spaced DIFAR sonobuoys at very low SNR.

6- *Examining the performance of the proposed methods using simulated data.*

In order to achieve the above objectives, acoustic level simulation of underwater sound received by sonobuoys is developed as part of this thesis research to enable examining the performance of the methods proposed above. This simulation provides an accurate knowledge of sound propagation from source to receiver and introduces the effect of different environmental conditions on sound propagation. The simulated environment is developed to be as close as possible to the real environment so that all the factors affecting sound propagation are considered.

1.4 Thesis Structure

The thesis is structured in seven chapters and includes a general conclusion and a list of references. The background of underwater acoustics, the recently developed

methods and the ongoing research work for underwater target tracking for both Omni and DIFAR sonobuoys are documented in Chapter 2. This chapter reviews the principles of both Omni and DIFAR systems, discusses the error sources associated with the present techniques, and outlines the limitations and shortcomings of the current processing methods. In addition, this chapter provides an overview of the recent developments in this technology and the research work related to the problem of underwater target tracking.

The FOS algorithm is introduced in Chapter 3 as a replacement for FFT to enable high resolution spectral analysis of GPS sonobuoys data. This chapter discusses the parameters of FOS algorithm and their effect on the target detection accuracy. The limitations imposed by the application of FOS are discussed as well showing a qualitative analysis of achieved accuracies in target detection and bearing estimation. This analysis is based on comparing the system performance using FOS to the current system performance using FFT for target detection and bearing estimation accuracies.

In Chapter 4 the processing of a group of DIFAR sonobuoys with omni, sine and cosine sensors is introduced as a new approach for enhancing bearing estimation. This chapter introduces derivations of the necessary changes required for array processing for different sonobuoys arrangements and provides a complete analysis of bearing estimation using a group of DIFAR sonobuoys. The presented analysis is based on examining the radiation pattern of the proposed array processing approach and the system performance at very low SNRs. Moreover, this chapter introduces an analysis of the effects of the operation environment on the overall system accuracy.

In Chapter 5 an array processing algorithm for a group of widely spaced DIFAR sonobuoys is introduced for Omni sonobuoys. The technique introduced in this chapter adopts the sole processing of data recorded by the Omni-directional sensors of DIFAR sonobuoys. This technique employs frequency domain beamforming algorithm which provides target bearing estimation using complex least mean square adaptive bearing estimation approach. This algorithm is aided by ANN to enable system operation for a widely spaced array of sonobuoys. Chapter 5 gives a complete analysis of the proposed system design parameters and discusses the enhancements introduced to the bearing estimation accuracy as well as the limitations of the proposed technique.

In Chapter 6 a new method based on virtual array processing is introduced for processing a sparse array of DIFAR sonobuoys. This chapter will demonstrate the benefits of searching a set of virtual array transformation matrices in order to enhance bearing estimation using both uniform linear and arbitrary array of DIFAR sonobuoys. The merits and limitations of the proposed method are discussed in this chapter.

Finally, Chapter 7 concludes the research work and provides recommendations for future development of the suggested techniques.

Chapter Two: Underwater Target Tracking

2.1 Fundamentals of Sonar Systems

Sonar systems are either active or passive. Sonar systems, equipments, and devices are said to be active when sound is purposely generated by one of the system components called the projector. Active sonar systems are said to echo-range on their targets. Passive or listening sonar systems use sound radiated (usually unwittingly) by the target. In this case only one-way transmission through the sea is involved, and the system centers around the hydrophone used to listen to the target sounds. Communication, telemetry, and control applications employ a hybrid form of sonar system using a projector and hydrophone at both ends of the acoustic communication path [Urick96].

The basic passive form of the sonar equation may be written as follows [Tiel76, Urick96]:

$$SE = SL - TL - NL \quad 2.1$$

Where SE is the signal excess, SL is source pressure level, TL is the transmission loss and NL is noise pressure level. These parameters can be defined as follows:

1. *Signal excess* is the received signal level (in dB) available for detection. When $SE > 0$ we are more likely to detect the target. When $SE < 0$ we are less likely to detect the target. When $SE = 0$ we are just as likely to detect the target as to not detect the target. In the last situation the probability of detecting the target is 50%.

2. *Source level* is the level of target radiated signal (in dB) at a distance of 1 yard from the source. Target source level is dependent upon the type of target and its mode of operation. It is a function of frequency, speed, depth, and ocean environment aspects. Target source levels may be obtained from various tactical intelligence publications.
3. *Transmission loss* is the decrease in signal intensity (in dB) as it travels through the ocean medium from the sound source to the receiving sensor. Propagation loss is a complex function of the environmental conditions.
4. *Ambient noise* is the steady-state level (in dB) of the total noise background existing at the receiving sensor, as measured by a non-directional hydrophone. It is noise unrelated to the target signal of interest and consists of all the steady-state background noise of the sea and self-noise which tend to mask the desired signal.

Apparently, the main factors that can influence the transmitted acoustic signal are the transmission loss and background noise.

2.1.1 Transmission Loss

As sound travels through the ocean, the absolute sound pressure level of sound source diminishes. This is referred to as transmission loss [Ultra06]. The two major phenomena contributing to propagation loss are: (1) Divergence (Spreading) which is a geometrical effect representing the regular weakening of a sound signal as it spreads outward from the source ; (2)Attenuation, and this mainly caused by different factors

including diffraction loss, absorption and scattering. These phenomena are mainly influenced by following factors:

2.1.1.1 Sound Velocity Profile (SVP)

The average speed of sound propagation in water is 1,500 m/sec (4,920 ft/sec). However, the speed of sound in the ocean depends upon temperature, salinity and depth. Figure 2.1 shows an example of sound speed profile and shows the variation in sound speed with the depth of the water medium [Urick96]. It should be noted that this profile differs from one underwater environment to another.

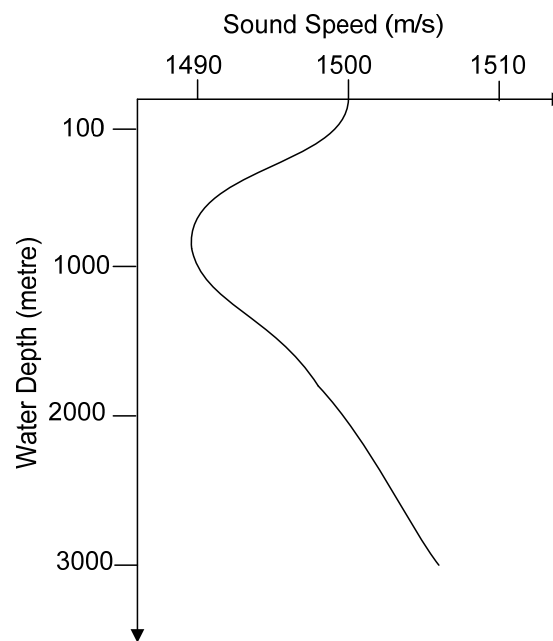


Figure 2.1 Typical Deep Ocean Sound Velocity Profile

2.1.1.2 Sound Propagation Paths

Sound propagation paths can be placed in one of the following categories [Ultra06 and Burdick84]:

1) Direct path

This occurs at short ranges where there is a near straight-line path between the sound source and the receiver (See Figure 2.2), with no reflection and only one change in direction due to refraction. Transmission loss equals spherical spreading loss plus attenuation loss [Urick96].

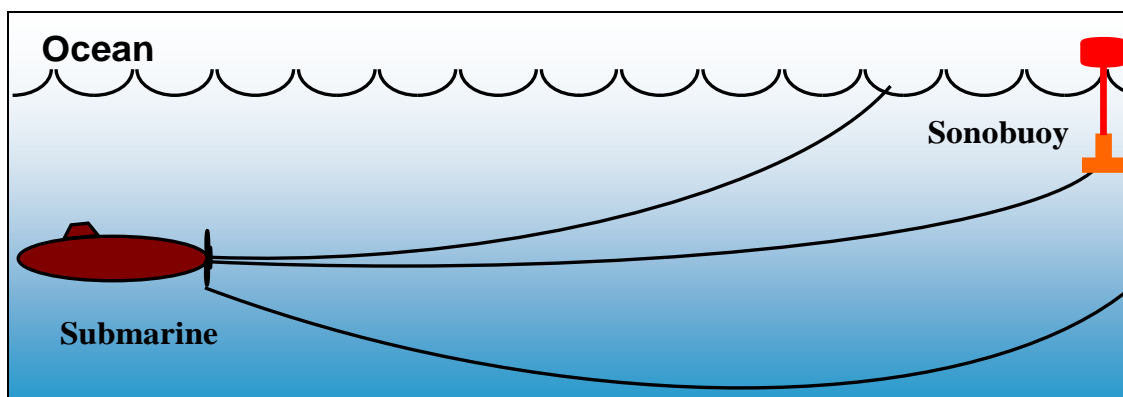


Figure 2.2 Sound Propagation in Direct Path

2) Surface duct

This is caused by [Urick96 and Burdick84] wind-induced stirring and surface cooling which cause the temperature of the upper layer of the ocean to be mixed. The increase of pressure with respect to depth in a thermally mixed layer forms a positive sound-speed gradient. Sound rays emitted from a source within the layer will be refracted upward away from the depth of maximum sound speed and

subsequently surface-reflected. Figure 2.3 shows surface duct effect on the transmitted signal between the source and the sonobuoy.

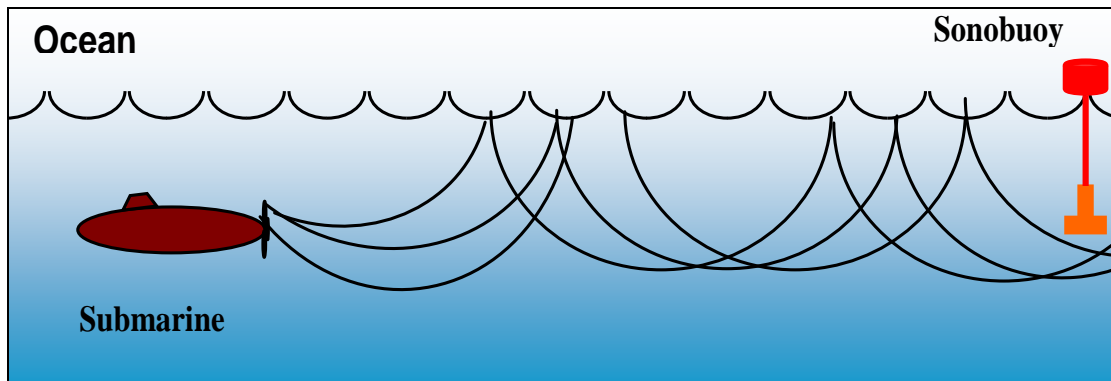


Figure 2.3 Sound Propagation in Surface Duct

3) Deep and shallow Sound channels

The Deep Sound Channel [Urick96 and Burdick84] (DSC) (Figure 2.4) is result of the deep sea being warm on top and cold below. The surface-warming effect is not sufficient to extend all the way to the ocean bottom and is limited to shallow depths, where it forms the main thermocline (area where temperature decreases continuously with depth). Below the DSC, the water is nearly isothermal, which produces a positive sound-speed gradient. Accordingly a depth of minimum velocity exists, called the axis, toward which the sound rays are continuously refracted. Those rays which start at angles above the axis are bent downward by refraction. Those rays that start at angles below the axis are refracted upward. Sounds traveling in this manner are often received at distances as great as 10,000 nautical miles from the source.

Shallow sound channels (Figure 2.4) trap sound sources [Urick96 and Burdick84] producing extended ducted ranges for high frequency sources and relatively shorter ducted ranges for low frequency sources.

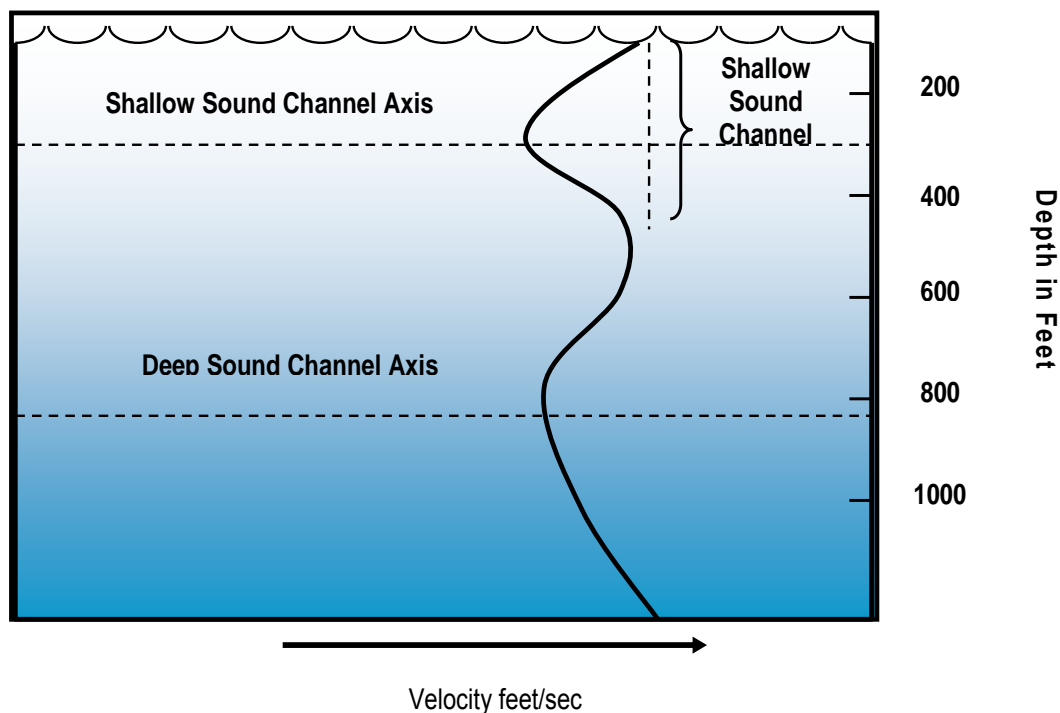


Figure 2.4 Deep and Shallow Water Channels

4) Half channel

This occurs in Polar Regions and the Mediterranean Sea [Urick96 and Burdick84]. This phenomenon occurs due to increase of sound-speed with depth from surface to bottom. Under these conditions, the greatest sound speed is at the bottom of the ocean, and sound rays will be refracted upward, then reflected downward at the surface, then refracted upward again [Urick96] (See Figure 2.5).

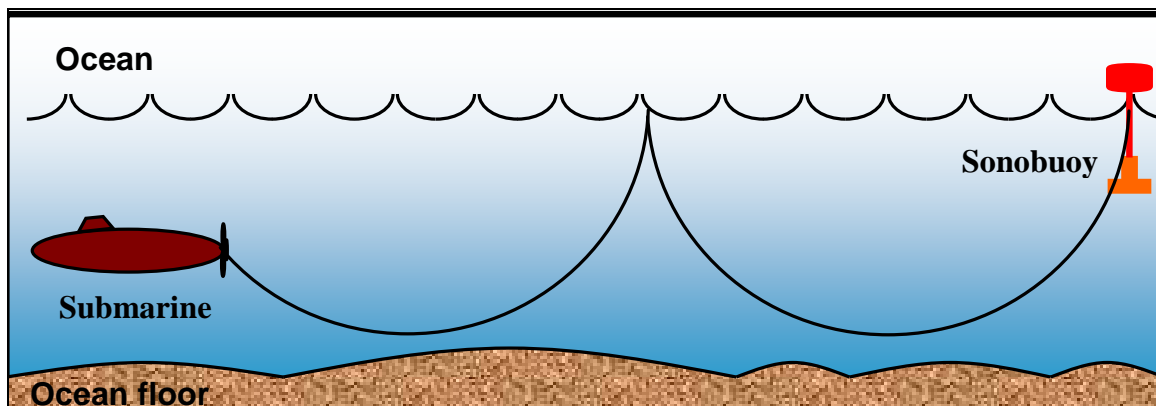


Figure 2.5 Sound Propagation in Half Channel

5) Bottom bounce

Bottom bounce [Urick96] is the reflection of a sound ray off the ocean floor (Figure 2.6). Major factors affecting bottom-bounce transmission include water depth, angle of incidence, signal frequency, bottom composition, and bottom topography. For ASW, bottom bounce enhances the ranges by which receivers can receive sound rays [Ultra06].

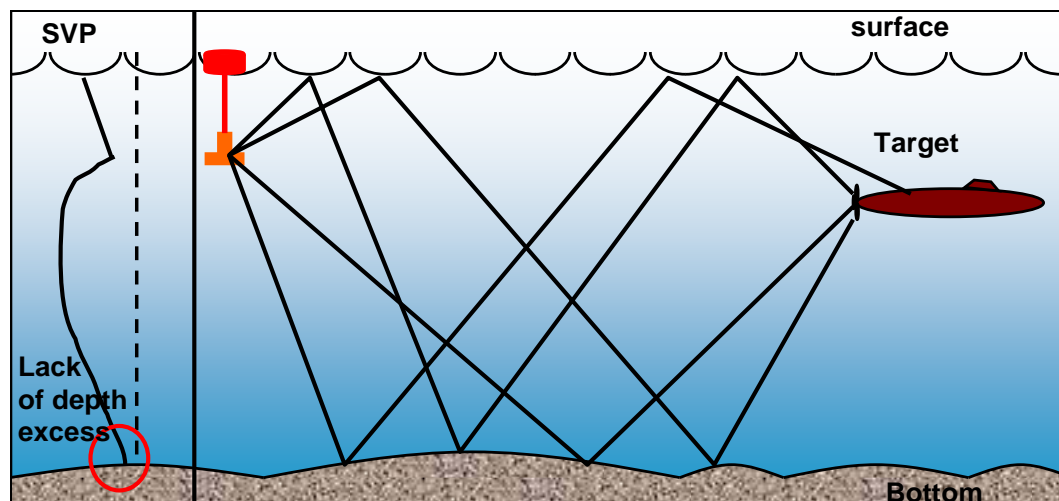


Figure 2.6 Bottom Bounce

6) Convergence zone (CZ)

Convergence zones [Urick96 and Burdick84] are regions at or near the ocean surface where sound rays are focused (converge), resulting in high sound levels. This convergence of sound rays forms intense sound fields that are useful in detecting distant submarines. Figure 2.7 illustrates the convergence zone effect on underwater sound propagation.

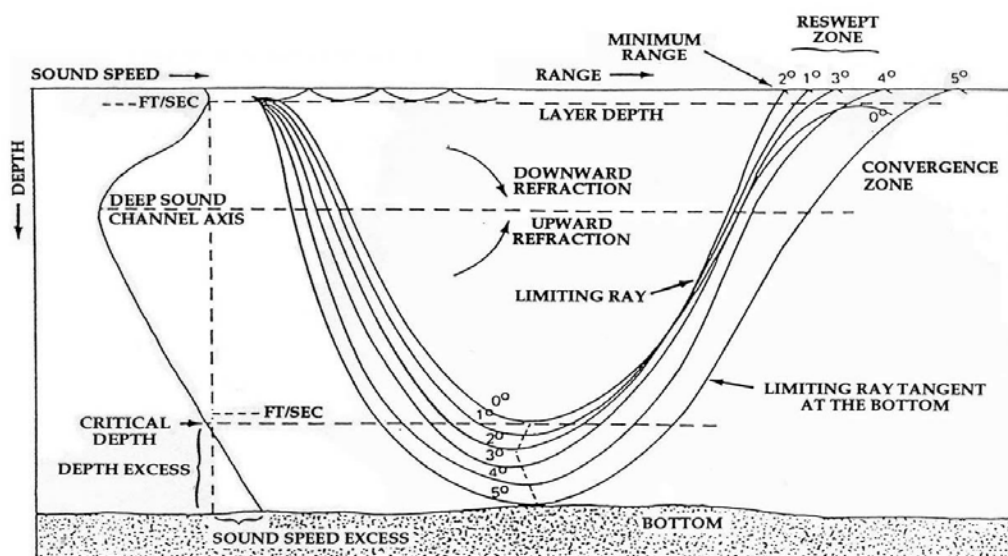


Figure 2.7: Convergence Zone [Ultra06]

7) Reliable acoustic path

These are paths [Urick96] that are not influenced by the near-surface effects and bottom bounce varying losses.

8) Shallow water.

This forms Less than 8% of the total ocean area. In shallow water, multiple reflected paths usually accomplish sound propagation [Urick96]. Figure 2.8 shows propagation paths in shallow water.

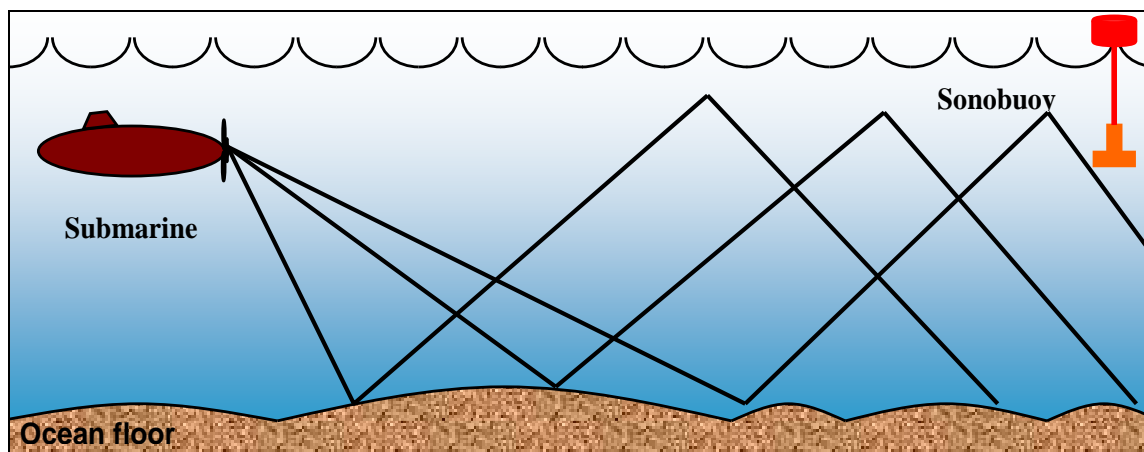


Figure 2.8 Sound Propagation in shallow Water

It is very common to study propagation loss using the “Propagation Loss Profiles” [Urick96]. Propagation loss profiles are curves that express propagation loss (in dB) for specific frequencies as a function of range from the source [Ultra06]. An example of a typical propagation loss profile is shown in Figure 2.9. The shape, slope, and loss levels shown in such profiles are dependent upon frequency of interest, depth of source and receiver, and oceanographic factors existing in the location of interest (e.g. water depth, bottom type, salinity, etc.). Propagation loss profiles are calculated using standard fleet acoustic performance models [Ultra06]. These models use a mix of both historic and current data (e.g. recently measured temperature profiles) for a given location of interest, along with target frequencies of interest, expected target depth, and hydrophone depth to calculate predicted propagation loss profiles for a given passive sensor.

Propagation loss profiles (Figure 2.9) are representations of the combined effects of direct path, bottom bounce, surface duct, convergence zone, and sound channel modes of sound propagation in the ocean. In Figure 2.9 it is clear that in general as range increases, dB loss also increases; that is, as the signal travels over greater and greater distances, more and more of the signal level is lost due to propagation effects. However, sometimes there are limited exceptions to this generality which are shown on Figure 2.9. The propagation loss curve in the range of 6-15 Km reveals a cessation of its downward trend, followed by a short rise, before the trace again continues its downward trend. This is caused by the existence of bottom bounce reflected energy as the height, width and location of the rise are dependent upon the specific physical and oceanographic circumstances existing at a given location for a given frequency of interest [Ultra06].

It can also be determined from Figure 2.9 that a rise occurs in the range of 29-37 km. This characteristic results when oceanographic conditions permit the existence of a CZ sound transmission mode. Here again the size, shape and location of the rise may vary or fail to exist, depending upon the specific circumstances occurring at that time and location [Ultra06]. Recently a Canadian Parabolic equation (PECan) was introduced [Brooke01]. This is a model that has been developed and enhanced in recent years to become a fully modern underwater acoustic propagation modeling tool capable of computing acoustic predictions in realistic oceanic environments.

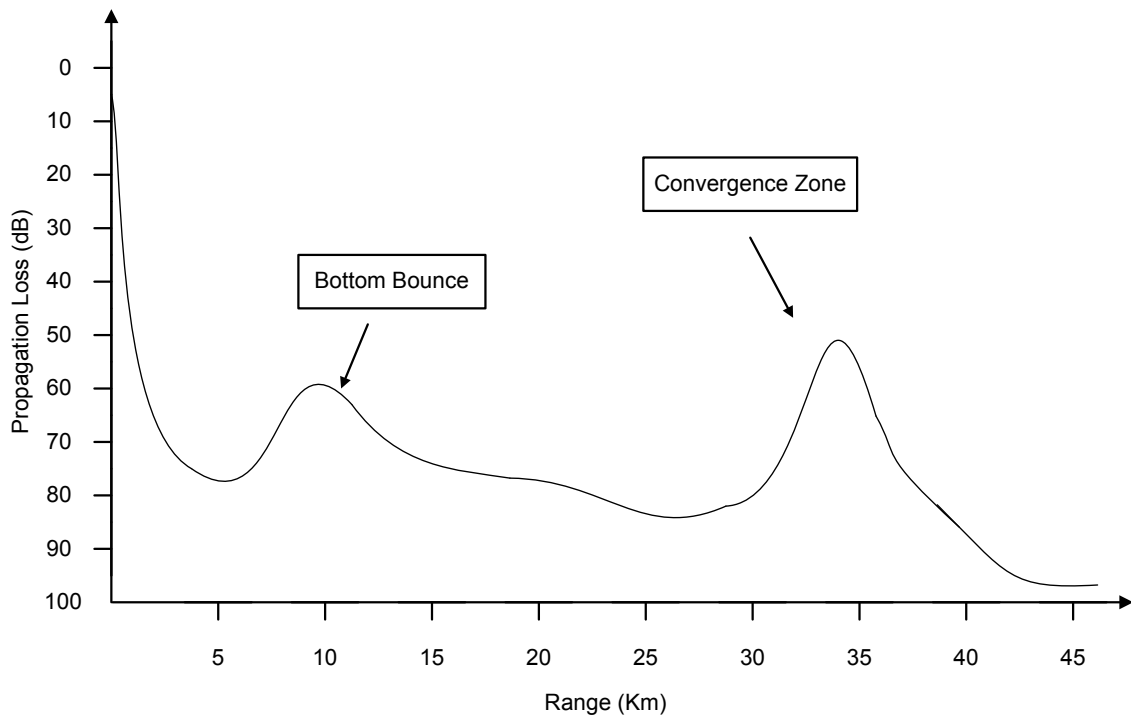


Figure 2.9 An Example of Propagation Loss Profile

2.2 Acoustic sources of ASW targets

The frequencies of interest radiated by a TOI are primarily composed of sounds generated as a vessel (either a surface ship or a submarine) propels itself through the ocean, and operates non-propulsion-related onboard systems. These sources are commonly grouped into 3 categories: the machinery sound, the propeller sound, and the hydrodynamic sound. The spectral shape of these components defines sources that can be exploited for identification and localization of a target [Des99].

The machinery sounds is resultant from pumps and motors used to keep onboard systems operating. Machinery sound tends to have a consistent frequency and lasts a

long-duration (continuous). The propeller sounds is resultant from the propulsion elements of a vessel, including the motor, the shaft, and the propeller. These sounds can vary from short to long duration, and are often very loud for a moderate to high speed target. Hydrodynamic noise results from the flow of material through pipes, as well as the flow of seawater over the hull and control surfaces of the vessel. These sources are highly dependent on speed, depth, and operating configuration of the vessel and can be readily exploited in traditional ASW [Boh05].

The acoustic sources which most easily identify a target are all narrowband in nature. Narrowband sources typically have a bandwidth of 0.3% to 0.03% of the source frequency (therefore typically less than 1 Hertz). On the contrary, broadband sources can have a bandwidth above 1% (therefore 1 Hz to several hundred or more Hertz). The amplitude of a narrowband source generally dominates above the broadband noise sources radiated by a target, making them easily identifiable [Des99]. It is these narrowband sources that are of interest to this research. Figure 2.10 is an illustration of sound levels of narrowband and broadband sources.

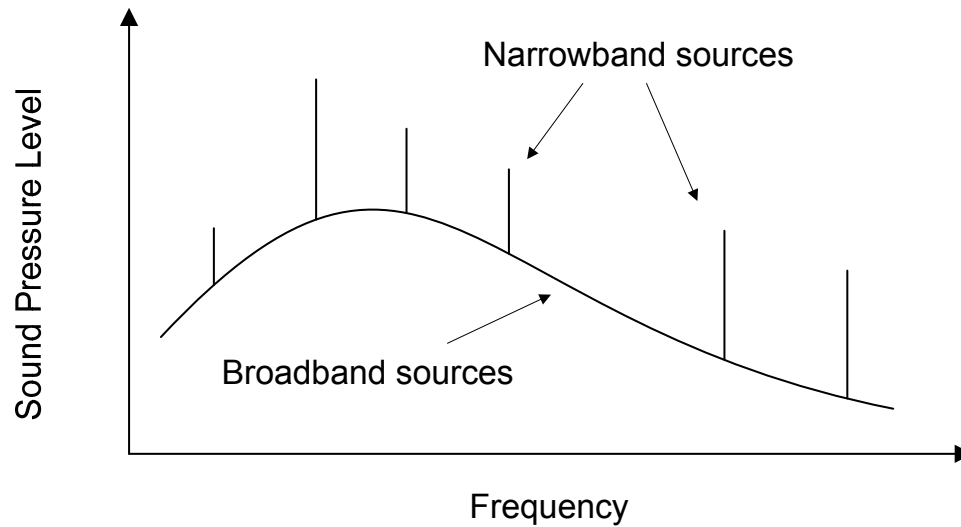


Figure 2.10 Sound Pressure Levels of Broadband and Narrowband Sources

The frequency region of interest of passive SONAR for the purpose of ASW lies between 10 and 1000 Hz [Boh05]. Below 10Hz, turbulent pressure fluctuates due to oceanic and seismic activities drown out most other sources of interest. Above 1 kHz, high attenuation results in very short propagation ranges, making detection of a source above 1 kHz unlikely given the expected source level of radiated noise. The basic sonobuoy performs low-frequency analysis and recording (LOFAR), and is therefore known as a LOFAR sonobuoy.

2.3 Sonobuoys Devices

A sonobuoy is a free floating and disposable sensor system [Whi04]. The sonobuoy uses acoustic sensors in the water column connected by wire to a float on the surface of the ocean to listen to submarine radiating noise or sonar echoes. An

electromagnetic transmitter in the float relays the acoustic signals back to an airplane or other receiving platform for further processing.

If the sonobuoy contains a magnetic compass and a beamformer to localize the acoustic signal in azimuth, then the submarine's bearing can be determined relative to the sonobuoy's location. Sonobuoys are grouped into three categories [Horsley89]:

- i) Passive Sonobuoys, which quietly listen to the acoustic signal from a target.
- ii) Active Sonobuoys, which emit a sound pulse (ping) to generate an echo from the target.
- iii) Special purpose buoys, which provide information about the environment such as water temperature, ambient noise level, etc.

A sonobuoy can be deployed from an airborne platform such as the CP-140 Aurora, a rotary-wing aircraft, or a surface vessel. Detected signals are processed for immediate tactical use and recorded for later analysis. More detailed analysis on this issue can be found in [Boh05 and Whi04].

2.4 Passive Sonobuoys

Target localization using passive sonars requires three successive steps to get the sources locations from the beamforming outputs [Solal91]: (1) Detecting the possible targets at regular time intervals by comparing the beamforming outputs to a threshold; (2) Data association and tracking which is based on associating events from the same target using a model of bearing time variation [Solal91]; (3) Target Motion Analysis (TMA)

which is the estimation of the source velocity and position from bearing measurements tracks. Generally, the measurements from the whole duration (batch method) are processed by the Maximum Likelihood estimator [Streit 2002]. TMA is mainly used in naval vessels to track vessels around ownship and use this information in deciding an appropriate course of action [Cunn05]. In the naval terms used in TMA, ownship refers to the current observation platform for the bearings. A bearing is the azimuth angle from an observation platform to the target [Nardone97]. Target refers to a source of bearings being tracked by ownship and the terms target and source may be used interchangeably [Cunn05]. The problem space is the set of possible scenarios of the location and movement of a target [Cunn05]. Solution is considered to be a single resolution to the location and movement of a target based in the problem space [Cunn05].

In general, passive sonar systems exploit an array of hydrophones to infer bearings corresponding to a tracked target by using beamforming. Beamforming is utilized by the array signal processor to estimate the azimuthal arrival angle of the target acoustical emissions [Streit02]. This process is known as bearings-only TMA (BO-TMA) [Aidala79, Bavencoff06, Bonneton07 and Streit02] or bearings-only tracking (BOT) [Bavencoff06]. Passive sonobuoys adopt this technique in target tracking [Urlick96, Boh05 and Des99].

2.5 DIFAR Sonobuoy

A DIFAR is an acronym for directional frequency analysis and recording. A DIFAR sonobuoy is an expendable unit for the reception of acoustic energy in the ocean which is transmitted via UHF link to another platform for analysis. It is composed of a 3-element hydrophone array co-located in a submerged unit, attached to a floating electronics package at the surface [Boh05].

A DIFAR sonobuoy is an improvement over a LOFAR sonobuoy in that its 3-element construction makes it possible to obtain the incident direction of an incoming acoustic signal. The basic technique allows processing of the DFT of each channel to generate a bearing estimate through a simple arctangent calculation. A display of bearing versus frequency, known as a B-scan display, allows targets to be localized and discerned based on the estimated bearing presented to an operator.

A sonobuoy of the AN/SSQ-53 series is a DIFAR sonobuoy constituted from a small array of 3 acoustic sensors located in a single unit to provide both Omni-directional amplitude and directional information. The acoustic sensors are suspended below a floating electronics assembly which contains processing and transmitter hardware.

2.5.1.1 System Operation

At the receiver unit, an Omni-directional element measures incident acoustic energy from any direction. A separate cruciform shaped assembly is composed of four ceramic discs, the orientation of which results in a beam pattern for each pair of discs

similar to a dipole. These beam patterns are referred to as the sine and cosine lobes, and are referenced to Magnetic North. Therefore, they are often called North-South and East-West lobes [Whi04].

Figure 2.1 illustrates the acoustic dipoles of a DIFAR sensor [Des99]. The direction-of-arrival (along the acoustic arrival axis) is referenced to the two orthogonal dipoles, which are aligned to Magnetic North, by the angle φ . Two orthogonal response axes are offset from Magnetic North by the local magnetic variation angle α . The total angle which provides a bearing to an acoustic source is θ between the arrival axis and the True North. The conversion between the Magnetic North and the True North is made at the processor prior to displaying to the operator. The vertical plane, corresponding to the depth direction, is not measured with a DIFAR sonobuoy. Therefore, it is not considered in this work. Acoustic pressure waves arrive at each sensor and induce a voltage by the piezo-electric properties of the ceramic material. The three separate channels of voltage information are referred to as the *Omni*, *sine*, and *cosine* channels, respectively. The time series of acoustic information are used to create a power spectral density (PSD) for the incoming acoustic signal. The PSDs are then used to calculate directional information.

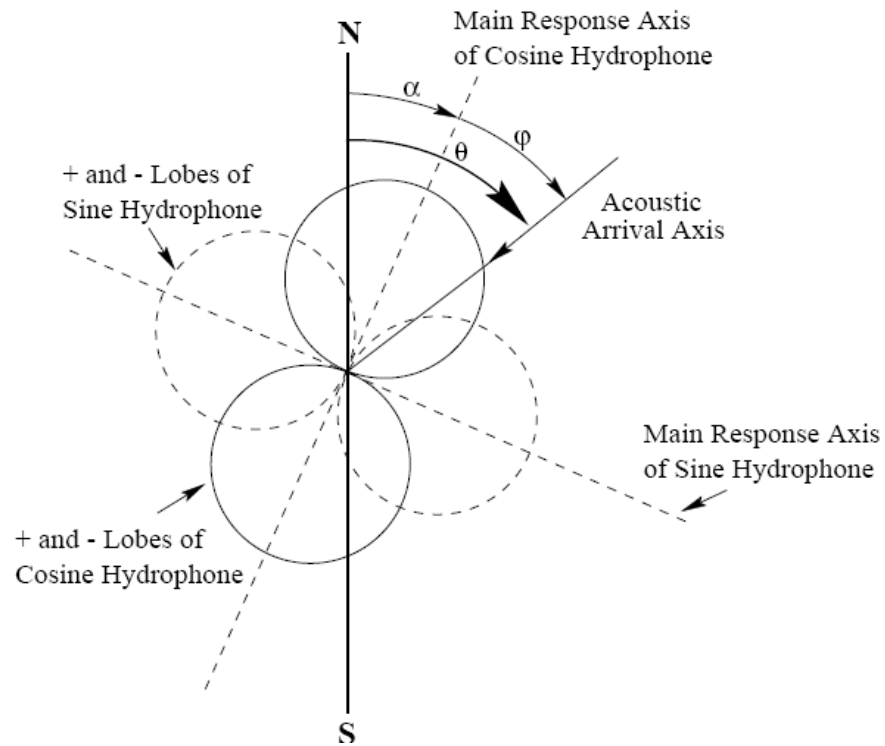


Figure 2.11 Illustration of Acoustic Dipole Response of DIFAR Sensor

2.5.1.2 Signal Processing Techniques and their Limitations

The output of the sonobuoy based on the incoming acoustic signal is a time series for each of the three channels. The data of the three channels are multiplexed at the upper electronics portion of the sonobuoy assembly [Boh05] and transmitted to a processor (located onboard of an aircraft or a ship) via a UHF radio link. The latest generation of DIFAR sonobuoys digitally transmits the time series in order to avoid the limited dynamic range of the UHF link, and to minimize outside interference. After receiving the acoustic signal, the processor demultiplexes the signal to create three concurrent time series [Boh05]. The Omni time series is expressed as x_{ok} , where o denotes Omni and the k

represents the index of the series, $k=2..N$. The three time series can be considered to be related by equation (2.1), such that:

$$\begin{aligned}
 x_{ok} & \quad \text{Omni-directional Channel} \\
 x_{sk} = x_{ok} \sin \mathcal{G} & \quad \text{Sine (East-West) Channel} \\
 x_{ck} = x_{ok} \cos \mathcal{G} & \quad \text{Cosine (North-South) Channel}
 \end{aligned} \tag{2.2}$$

Spectrum analysis

The basic processing of sonobuoy output is mainly based on the power spectral density (PSD) of the received time series which is calculated from the discrete Fourier transform (DFT) of the received time series, as shown below.

$$X(k) = \frac{1}{N} \sum_0^{N-1} x(n) e^{-2\pi jkn/N} \tag{2.3}$$

Where $x(n)$ is the time series at time n ; $X(k)$ is the DFT at frequency k ; N is the number of samples in the received time series. The general power spectral density (PSD) is obtained as:

$$\Phi(k) = X(k) \cdot X^*(k) = |X(k)|^2 \tag{2.4}$$

Where the asterisk (*) indicates the complex conjugate.

In DIFAR sonobuoys, the DFTs are created from band-limited sampled data to avoid aliasing, and are time averaged to create the PSD. Figures 2.12 and 2.13 show examples of spectral analysis performed on the Omni directional channel of DIFAR sonobuoy using simulated underwater tracking scenario. The simulated scenario consisted of four underwater sources with constant amplitude of $140 \text{ dB re } \mu\text{Pa}$ and arriving at the receiver with SNRs -10dB (Figure 2.12) and -30 dB (Figure 2.13). It can be observed that the low SNR of the case of Figure 2.13 has a negative impact on the overall target detection capabilities. The source at 200 Hz becomes totally buried in noise and as a result it may not be detected. One of the methods explored in this thesis is to improve target detection at low levels of SNR utilizing advanced spectral estimation.

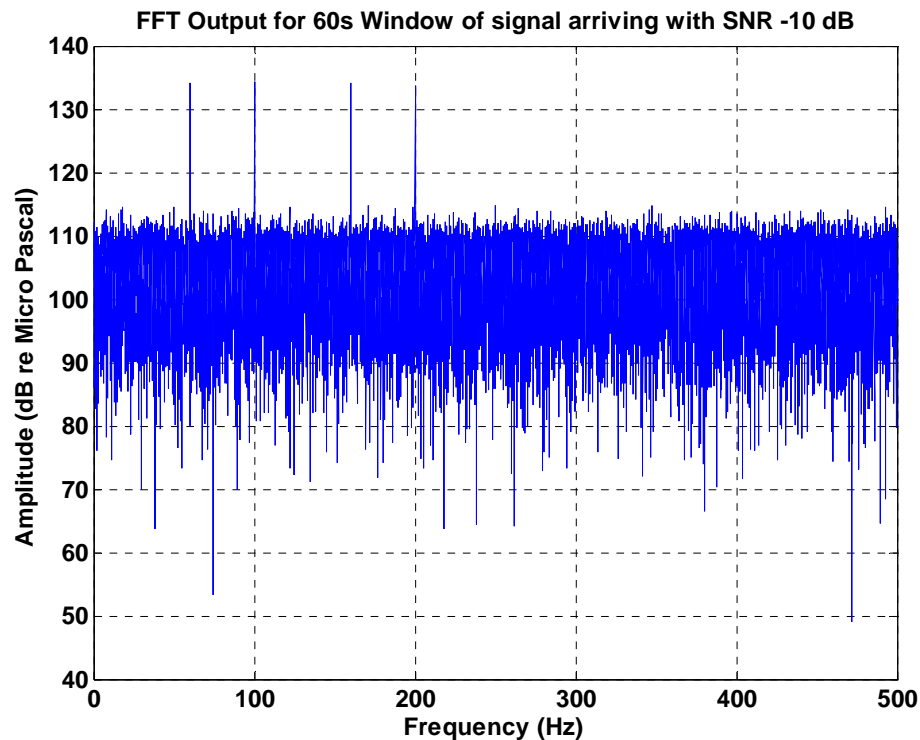


Figure 2.12 DFT for Signal Received from Four sources at SNR -10 dB

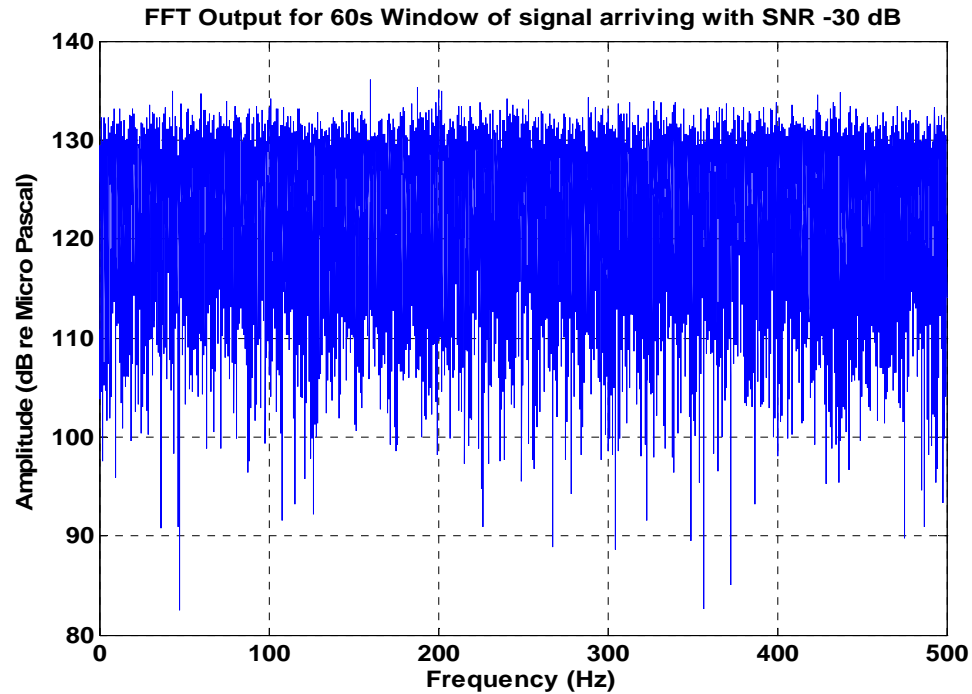


Figure 2.13 DFT for Signal Received from Four sources at SNR -30 dB

As can be depicted in Figures 2.12 and 2.13, the amplitude of each frequency component is given in decibel relative micro Pascal ($dB\ re\ \mu\ Pascal$) which is the common unit for measuring underwater sound pressure level. This process is the first step in target detection and localization where the frequencies detected provide information for the system operator about the target type and its bearing.

Limitations of spectrum analysis

The spectral estimate of the data in the frequency domain is generally obtained through the use of the DFT or a spectral modeling technique, such as linear prediction (LP) or auto-regressive moving average (ARMA). However, the frequency resolution introduced by these techniques is limited and hence resolving sources of frequency

components close to each other may become very difficult. In addition, the above spectrum analysis procedure may not work efficiently in case of low SNR. Figure 2.13 shows the same case as Figure 2.12 but at -30 dB SNR. It can be depicted that the component at 200 Hz (representing a submarine) is now totally buried in noise. Therefore, different spectral analysis methods are needed to deal with low SNR scenarios, which are mostly the case in underwater target tracking.

Bearing calculation

The cross spectra are used to calculate the direction of arrival of a sound at the receiver, also known as a bearing to a TOI. The quotient of the Omni-sine and Omnicosine PSD estimates yields a bearing from the simple trigonometric identity [Boh05]

$$\hat{\theta} = \arctan\left(\frac{\Phi_{os}}{\Phi_{oc}}\right) \quad 2.5$$

Where the caret (^) indicates an estimate, Φ_{os} and Φ_{oc} are the Omni-sine and Omnicosine cross-spectra, respectively.

The value of $\hat{\theta}$ provides a single direction estimate between 0 and 2π for each frequency bin using a four-quadrant arctangent calculation. $\hat{\theta}$ is relative to magnetic north and must be corrected for local magnetic variation prior to being displayed to the operator as a true bearing [Des99 and Boh05].

Current systems employ Bartlett Beamforming which is known as the conventional beamforming [Des99, Puska05]. Conventional Beamforming technique

relies on the Cross Spectral Matrix (CSM) estimate \widehat{Q} . The CSM is calculated from all the channels available and FFT can be used to build this matrix efficiently. Equations 2.6-2.9 detail the calculation of CSM. The subscripts o, s and c indicate the omni, sine and cosine channels.

$$\widehat{\Phi} = \begin{bmatrix} \widehat{\Phi}_o \\ \widehat{\Phi}_s \\ \widehat{\Phi}_c \end{bmatrix} \quad 2.6$$

$$\widehat{Q} = \widehat{\Phi} \widehat{\Phi}^* \quad 2.7$$

Where $\widehat{\Phi}^*$ is the conjugate transpose of $\widehat{\Phi}$.

$$\widehat{Q} = \begin{bmatrix} \widehat{\Phi}_{oo} & \widehat{\Phi}_{os} & \widehat{\Phi}_{oc} \\ \widehat{\Phi}_{so} & \widehat{\Phi}_{ss} & \widehat{\Phi}_{sc} \\ \widehat{\Phi}_{co} & \widehat{\Phi}_{cs} & \widehat{\Phi}_{cc} \end{bmatrix} \quad 2.8$$

The conventional beam power estimate at any arbitrary direction $\widehat{E}_{CB}(\theta)$ is given by

$$\widehat{E}_{CB}(\theta) = \beta^T \widehat{Q} \beta \quad 2.9$$

Where $\beta = [\mathbf{1} \quad \sin \theta \quad \cos \theta]$ and the subscript ‘‘CB’’ stands for conventional beamforming. The direction of arrival of a signal with certain frequency is the one that

has a maximum power estimate at that frequency bin. $\hat{E}_{CB}(\theta)$ is calculated for the whole spectrum estimated by FFT.

Limitations of bearing calculations

The data used to determine bearings are integrated over a relatively long period, and are subject to significant bearing errors. The following are the major error sources [Urick96, Des99, and Boh05]

A. Bearing lag

To provide a bearing estimate in a real-time system, only past information can be used. For a rapidly moving target, this will cause the bearing to lag behind the source.

B. Bearing pull (Bearing bias)

When two sources at the same frequency are received from different directions, the resultant bearing estimate will lie somewhere between the actual targets, usually closer to the stronger one. This effect is known as "bearing bias".

C. Interference sources

Ocean noise can also greatly influence the incoming target signals. When the noise originates from specific directions and is of relatively high amplitude, it may introduce significant bearing errors or mask the TOI entirely. The operator is then provided with directional information from the stronger signal, which may be the noise. A similar error may also occur in the presence of two broadband signals from different origins.

Bearing debiasing algorithms have been devised to reduce bearing bias effects. These algorithms remove non-signal components, determined from adjacent bins from the bearing calculation, under the assumption that the signal of interest is narrowband. This method only addresses the bias that is introduced by relatively broadband interference over discrete tonals. However, bearing errors are still likely to occur in case of two sources producing narrowband signals in the same frequency bin. Noise sources of high amplitude may also introduce errors despite of debiasing algorithms.

The PSD estimate for each segment of N data points in the time series can be displayed as a line on an image plot called [Des99 and Boh05], with amplitude scaled to brightness. The result of subsequent PSD slices being plotted is a 2-dimensional image with frequency on the x -axis, time on the y -axis, and the corresponding PSD amplitude is represented as display intensity.

There are two types of displays [Des99] *waterfall* image and *reverse waterfall* image. In the *waterfall* image each new PSD slice is placed at the bottom of the image and all other slices are displaced upwards. While in *reverse waterfall* image older slices are displaced downwards. The general term for a frequency versus time plot is a low-frequency analysis and recording spectrogram (abbreviated as LOFARgram), or simply a gram. A sample LOFARgram is shown in Figure 2.14 sources which are continuously present at a single frequency appear as a vertical line on the image. Noise, which contains signals at varying frequencies, amplitudes and phases, results in the overall salt-and-pepper appearance of the gram as a whole.

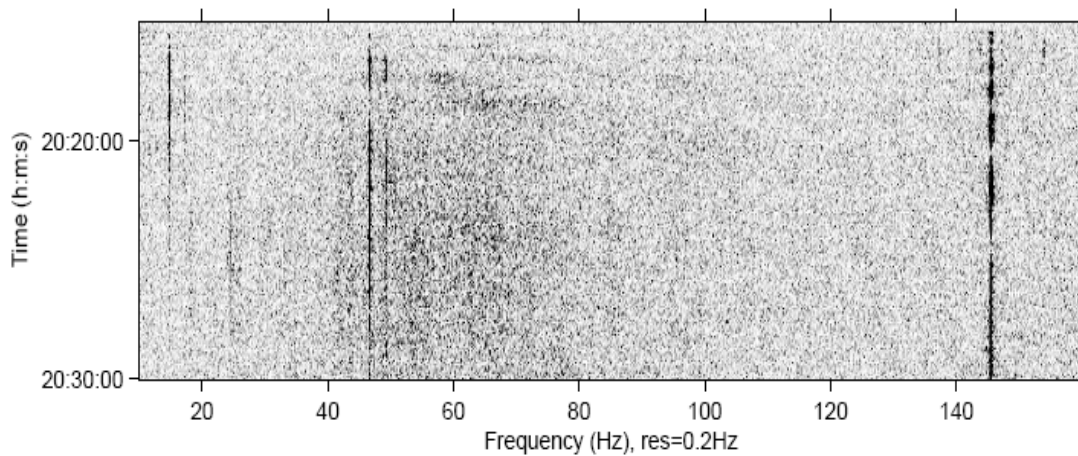


Figure 2.14 Sample LOFARgram 10-150 Hz [Boh05]

The output of the bearing calculation can be displayed similarly. For a given time slice, each frequency bin will have one bearing associated with it. With the frequency on the x -axis and the bearing on the y -axis, the plot indicates a bearing estimate for every frequency bin. This display format is referred to as a B-scan plot. A sample B-scan plot is shown in Figure 2.15.

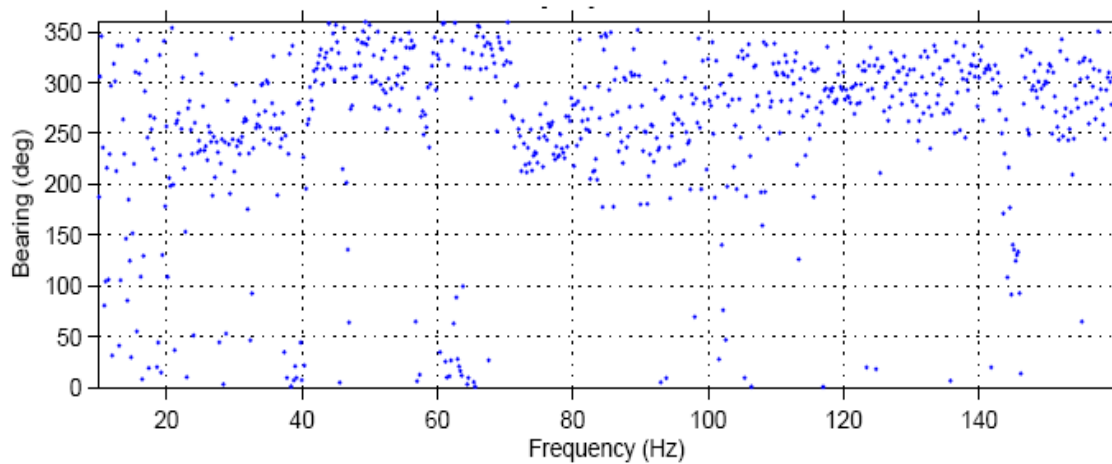


Figure 2.15 Sample B-scan plot corresponding to Figure 2.17 [Boh05]

The combination of a display of a LOFARgram and B-scan with matched x -axes provides sufficient information for a system operator to allow identification, localization, and tracking of acoustic targets. Because the frequency bins in the two displays correspond, sources identified based on their appearance in the gram can be localized by looking at the corresponding bearing in the B-scan display.

A user-selectable threshold can be applied to the B-scan display to show only bearings that have sufficient amplitude to be of interest. This threshold is generally set to remove all bearings from the B-scan display that are of no interest; this assumes that signals-of-interest are of significantly greater amplitude than undesirable narrowband or broadband acoustic noise. Directional information can be incorporated into the LOFARgram through the use of color mapping. Algorithms to automate the tracking of sources based on bearing changes also exist [Boh05].

2.6 Research progress and Current state of the art

Most of the research work adopted by DIFAR sonobuoys is inherent from research techniques and methods generally developed for passive sonar systems. Most of the research efforts towards the enhancement of TMA using passive sonar systems are mainly designed for BO-TMA. This area has attracted considerable attention since the passive sonar systems were introduced to the underwater tracking problem. The research work in the area of BO-TMA comprises a wide area of research since the process of BO-TMA involves different stages that are integrated to provide adequate TMA [Solal91]. The research efforts conducted for BO-TMA can be classified into three categories

corresponding to the passive sonar data processing stages [Solal91]. The first category involves the detection of acoustic signals. The second stage is the bearing estimation of the detected acoustic signals. The third stage integrates the obtained measurements from several passive sonar systems to provide TMA.

2.6.1 Target detection

This is the initial stage of the target localization process [Solal91]. The successive stages are mainly based on the accuracy of the spectral analysis method employed at this stage [Urick96 and Boh05]. Usually Fourier transform is used for spectral analysis [Maranda91, Boh05 and Urick96]. The research work associated with target detection is mainly concerned with employing different spectral estimation techniques [Boh05, Gabriel80, Jhonson91, Luby87, and Ping91]. Johnson [Jhonson91] proposes the application of maximum-linear-prediction estimation technique for spectral estimation and he showed improvement in the resolution of the spectral estimation when compared to windowed Fourier transform estimation procedure. Gabriel [Gabriel80] introduced super-resolution spectral estimator using maximum entropy spectral analysis (MESA) and the maximum-likelihood method (MLM). The super-resolution spectral estimator provided the ability to detect multiple targets with unequal-strength. However detecting multiple targets when they are relatively too close was unsuccessful using the super-resolution spectral estimator. Moreover the super-resolution of coherent spatial sources or radar targets required sufficient relative motion or “Doppler cycles” for proper detection. This puts the limitation on the frequency and number of snapshots required for target

detection. Camillet [Camillet98] introduced a suboptimal method to detect wideband signals embedded in the reverberation noise they have created. The method introduced in [Camillet98] assumed local stationarity of the reverberation. Using this assumption, the proposed method cuts the received signal into blocks and on each block the noise is modeled as an autoregressive (AR) process. The received signal is whitened by using the modeled noises. The whitened signal is then applied to a matched filter to extract the desired signal. Camillet [Camillet98] demonstrated improvement in SNR of the received signal with some limitations related to the stationarity of the source acoustic signal.

Bohac [Boh05] applied FOS for spectral estimation as a substitute for DFT. The significance of the work in [Boh05] is mainly the improvement of system capability in detecting narrowband targets when the difference between their frequencies is less than the DFT resolution. The results reported by Bohac illustrated the overall system improvement introduced by using FOS. However, the minimum SNR examined by Bohac was -10 dB and data record lengths employed were 10 seconds and 125 seconds. The data processed from each data record was formed by dividing the data record into 5 slices and averaging them. This study can be extended to examine FOS versus DFT at lower SNRs and for variable data record lengths.

2.6.2 Bearing Estimation

Bearing estimation research work focused mostly on exploring bearing estimation methods to enhance the accuracy of the target localization [Jhonson82, Des99, Ziomek89, Greshman95, Des99, Bonneton07,]. Johnson [Johnson82] studied the analogy

between the problem of determining the bearing of a radiating source with an array of sensors and the problem of estimating the spectrum of a signal. The author [Johnson82] examined the application of spectral estimation methods to the problem of bearing estimation. Results showed improvement in the bearing estimation resolution with some limitations on the level of SNR and the conditions required for the application of the proposed spectral estimation methods. Desroches [Des99] examined the application of some high-resolution beamforming techniques to the bearing estimation using single DIFAR sonobuoy. The results reported by Desroches examined the bearing estimation using a single DIFAR sonobuoy for SNRs ranging between 0.5 dB and 4 dB. It showed that high resolution bearing estimation techniques can enhance bearing estimation with some limitation on the level of SNR. Another approach for improving the resolution of bearing estimation was proposed in [Imai2000]. The proposed approach employed Wigner-Ville distribution method [Imai2000] for sonar beamforming to obtain sharper beam patterns than those of the beamforming method using conventional beamforming based on Fourier transform. The author in [Imai2000] demonstrated the enhancement in beamwidth over the conventional beamforming method; however the algorithm was not examined for noisy signal. The results presented were demonstrating the capability of the proposed algorithm in detecting the true bearing out of a set of echoes received from the target. Other approaches for improving bearing estimation resolution employed adaptive beamforming techniques to provide higher resolution beamforming [Greening02 and Kogon02]. Nevertheless, the arrays examined in [Greening02 and Kogon02] had an inter-element spacing less than half wavelength of the tracked sources which can be more suitable for towed arrays.

2.6.3 TMA

This area of research focuses on the manipulation of system recorded data to provide a complete solution of target trajectory and its moving velocity. The system recorded data includes target bearings, SNR, Doppler shift and other information from recording environmental conditions [Urick 96, Solal91, Nardone97 and Streit02]. A novel method of TMA is presented in [Maranda91]. In contrast to conventional TMA techniques, which use sequences of bearing and/or frequency estimates as their inputs, this new TMA method [Maranda91] estimates the target track directly from beam spectra. This method provided high accuracy of target tracking for acoustic signals of -20 dB SNR. Another area of research in TMA is the matched-field processing [Bucker76 and Wilmut98]. The matched field tracking (MFT) method introduced by Buker [Buker76] provides solution for target tracking by estimating the target trajectory parameters. The estimated parameters are obtained by matching a measured acoustic field with a set of fields generated for different source locations. In [Wilmut98], piecewise MFT algorithm was introduced for finding the portion of a track that maximizes the track SNR. These methods enhanced system accuracy at low SNR and provided direct estimation of TMA parameters. However these methods are based on the bearing estimates obtained from the sensors and hence can significantly benefit from further improvement of the accuracy of bearing estimates observed by the acoustic sensors.

2.7 Conclusion

The major weaknesses of the present processing techniques for DIFAR sonobuoys stem from their associated limitations. Those limitations can significantly degrade the system performance especially with the advances in submarine technologies. The system vulnerability is further increased by the environmental conditions. This suggests the modernization of current processing schemes in order to boost up the current systems and enhance their effectiveness against new technologies in submarine. Moreover, improving the current processing schemes of DIFAR sonobuoys enables robust operation in different oceanic environments. The main processing techniques introduced in this research fall in two main approaches. The first category involves enhancing the SNR of the received acoustic signal for DIFAR sonobuoys by introducing advanced spectral analysis technique, namely FOS. The second approach considers the processing of a group of DIFAR sonobuoys coherently in order to further enhance SNR of received signal and provide significant improvement of current system resolution. Finally the integration of the proposed approaches will provide significant improvement to the current system performance and extend the operational range of current DIFAR sonobuoys systems.

Chapter Three: Improved Target detection and Bearing Estimation Utilizing Fast Orthogonal Search for Real-Time Spectral Analysis

In Chapter 2, it was demonstrated that the target detection and bearing estimation using DIFAR sonobuoys are obtained through spectral analysis of received signals which is carried out using DFT or a spectral modeling technique, such as LP or ARMA. However, the frequency resolution introduced by these techniques is limited and hence resolving sources of frequency components close to each other may become very difficult. The above spectrum analysis procedures may not work efficiently in case of low SNR due to spectral leakage caused by their limited frequency resolution.

This chapter studies the implications of processing data received by GPS-equipped sonobuoys using FOS for improving target detection and bearing estimation accuracies at low SNRs. The proposed methodology is FOS which offers high resolution spectral estimation and therefore enhances target detection and bearing estimation.

Orthogonal search [Tseng93, Korenberg89A] is a technique developed for identifying difference equation and functional expansion models by orthogonalizing over the actual data record. It mainly utilizes Gram-Schmidt orthogonalization to create a series of orthogonal functions from a given set of arbitrary functions. This enables signal representation by a functional expansion of arbitrary functions and therefore provides a wider selection of candidate functions that can be used to represent the signal. FOS is a variant of the orthogonal search [Korenberg88] where the major difference is that FOS

achieves orthogonal identification without creating orthogonal functions at any stage of the process. As a result FOS is many times faster and less memory storage intensive than the earlier technique, while equally as accurate and robust [Armstrong06].

FOS has been applied before in several applications [Adeney94, Korenberg88, Korenberg89A, Korenberg89B, McGaughey03, Armstrong06, and Bohac05]. The research work in [Bohac05] proposes the application of FOS in order to detect multiple signals that are non-separable by Fast Fourier Transform (FFT). In this research FOS is proposed as a search algorithm that can detect and extract target sound from the received signal at very low SNR's.

For the scope of this research, we decided to use FOS for its general advantages and capabilities as reported in previous research and other applications. We also compared its performance over the conventional method (based on FFT) presently used in processing the GPS Sonobuoys data. In addition, we briefly examined the benefits of wavelet multi-resolution analysis, but we determined that FOS could provide better advantages including: (1) higher frequency resolution that can reach 1/10 the FFT resolution; (2) the minimization of spectral leakage by using non orthogonal set of candidate functions to represent the signal. However, FOS is computationally expensive if compared to FFT. Spectral leakage minimization procedures have not been examined for FFT. The comparison is carried between FFT and FOS with no additional pre-processing.

3.1 Fast Orthogonal Search (FOS)

FOS [Adeney94, Korenberg88, Korenberg89A, Korenberg89B, McGaughey03] is a general purpose modelling technique which can be applied to spectral estimation and time-frequency analysis. The algorithm uses an arbitrary set of non-orthogonal candidate functions $p_m(n)$ and finds a functional expansion of an input $y(n)$ in order to minimize the mean squared error (MSE) between the input and the functional expansion.

The functional expansion of the input $y(n)$ in terms of the arbitrary candidate functions $p_m(n)$ is given by:

$$y(n) = \sum_{m=0}^M a_m p_m(n) + \varepsilon(n) \quad 3.1$$

Where a_m is the set of weights of the functional expansion, and $\varepsilon(n)$ is the modelling error.

By choosing non-orthogonal candidate functions, there is no unique solution for Eq.3.1. However, FOS may model the input with fewer model terms than an orthogonal functional expansion [Korenberg89A]. For the FFT to model a frequency that does not have an integral number of periods in the record length, energy is spread into all the other frequencies, which is a phenomena known as spectral leakage [Ifeachor02]. By using candidate functions that are non-orthogonal, FOS may be able to model this frequency between two FFT bins with a single term resulting in a many fewer weighting terms in the model [Chon01].

FOS begins by creating a functional expansion using orthogonal basis functions

such that

$$y(n) = \sum_{m=0}^M g_m w_m(n) + e(n) \quad 3.2$$

Where $w_m(n)$ is a set of orthogonal functions derived from the candidate functions $p_m(n)$, g_m is the weight, and $e(n)$ is an error term. The orthogonal functions $w_m(n)$ are derived from the candidate functions $p_m(n)$ using the Gram-Schmidt (GS) orthogonalization algorithm. The orthogonal functions $w_m(n)$ are implicitly defined by the Gram-Schmidt coefficients α_{mr} and do not need to be computed point-by-point.

The Gram-Schmidt coefficients α_{mr} and the orthogonal weights g_m can be found recursively using the equations [Korenberg89A]

$$w_0(n) = p_0(n) \quad 3.3$$

$$D(m,0) = \overline{p_m(n)p_0(n)} \quad 3.4$$

$$D(m,r) = \overline{p_m(n)p_r(n)} - \sum_{i=0}^{r-1} \alpha_{ri} D(m,i) \quad 3.5$$

$$\alpha_{mr} = \frac{\overline{p_m(n)w_r(n)}}{w_r^2(n)} = \frac{D(m,r)}{D(r,r)} \quad 3.6$$

$$C(0) = \overline{y(n)p_0(n)} \quad 3.7$$

$$C(m) = \overline{y(n)p_m(n)} - \sum_{r=0}^{m-1} \alpha_{mr} C(r) \quad 3.8$$

and

$$g_m = \frac{C(m)}{D(m,m)}. \quad 3.9$$

In its last stage, FOS calculates the weights of the original functional expansion

a_m (Eq.3.1), from the weights of the orthogonal series expansion, g_m and Gram-Schmidt coefficients α_{mr} . The value of a_m can be found recursively using

$$a_m = \frac{\sum_{i=m}^M g_i v_i}{v_m}, \quad v_m = 1 \quad 3.10$$

where,

$$v_i = - \sum_{r=m}^{i-1} \alpha_{ir} v_r, \quad i = m+1, m+2, \dots, M. \quad 3.11$$

From 3.4, 3.5, 3.7 and 3.8 it can be noted that FOS requires the calculation of the correlation between the candidate functions and the calculation of the correlation between the input and the candidate functions. The correlation between the input and the candidate function $\overline{y(n)p_m(n)}$ are typically calculated point-by-point once at the start of the algorithm and then stored for later quick retrieval.

The MSE of the orthogonal function expansion has been shown to be [Chon01]:

$$\overline{\varepsilon^2(n)} = \overline{y^2(n)} - \sum_{m=0}^M g_m^2 \overline{w_m^2(n)} \quad 3.12$$

It then follows that the MSE reduction given by the m^{th} candidate function is given by:

$$Q_m = g_m^2 \overline{w_m^2(n)} = g_m^2 D(m, m) \quad 3.13$$

FOS can fit a model with a small number of model terms by fitting terms which reduce the MSE in order of their significance. The FOS search algorithm is stopped in one of three cases. The first is when certain maximum number of terms is fitted. The second case is when the ratio of MSE to the mean squared value of the input signal is below a pre-defined threshold. **The third case is when adding another term to the model reduces the mse no more than would be expected if it were fitting white noise**

[McGaughey03].

Spectral analysis with FOS is accomplished by selecting candidates $p_m(n)$ that are pairs of sine and cosine terms at each of the frequencies of interest. The candidate functions $p_m(n)$ are given by

$$\begin{aligned} p_{2m}(n) &= \cos(\omega_m n) \\ p_{2m+1}(n) &= \sin(\omega_m n) \end{aligned} \tag{3.14}$$

Where $m = 1, \dots, P$, ω_m is the digital frequency of the candidate pair normalized to Nyquist frequency and P is the number of candidate pairs. By fitting a sine and cosine pair at each candidate frequency, the magnitude and phase at the candidate frequency can be determined [Ali03, McGaughey03].

There are two significant differences between FOS and conventional Fourier transform techniques (i.e. DFT or FFT) [Ali03, Chon01, Korenberg89B, Korenberg98, McGaughey03]: (1) FOS yields a parsimonious sinusoidal series representation by selecting the most significant sinusoidal components first; and (2) the frequencies of the sinusoids selected need not be commensurate nor integral multiples of the fundamental frequency corresponding to the record length [Korenberg89A]. This translates to better frequency resolution in the spectral model.

FOS is appreciably better at rejecting coloured and white noise than the commonly used FFT techniques (example in [Chon01]), which is significant since these types of errors are typically present in underwater received sound.

It was reported [Adeney94] that when the time samples are equally spaced, closed form expressions may usually be used to obtain required cross correlations $\overline{p_m(n)p_k(n)}$ between the non-orthogonal basis functions. In this case, FOS requires on the order of $CN + CM_t^2$ floating-point operations, where C is the number of candidates, N is the number of samples and M_t is the number of terms in the final model. If only cross correlations between data and candidate basis functions are stored, but the closed-form expressions mentioned are used, then $CN + CM_t^3$ operations are required. If the closed-form expressions to obtain the required cross correlations are not used, but, once computed, these cross correlations are saved, then $CMN + CM_t^3$ operations are required. Thus, in all cases, the required number of floating-point operations used in FOS is roughly proportional to C . The number of operations required by FFT [Helms 67] is in the order of $N \log_2 N$. Thus FOS is more computationally expensive than FFT.

3.2 Application of FOS to the problem of underwater target detection and localization

Apparently, FOS provides spectral analysis with a resolution better than FFT, hence providing better separation between different targets detected at closely spaced frequencies and better overall bearing estimation. This research also explores how the FOS algorithm can be tuned to provide reliable target detection and accurate bearing estimation in the case of extremely low SNR, which is presently a major challenge in ASW. The proposed model for FOS application is shown in Figure 3.1. The FOS

accuracy enhancement technique initially segments a noisy input time series into smaller analysis windows that are treated as stationary data. The input time series represents the signal received by one of the DIFAR sonobuoy three channels (omni, sine and cosine).

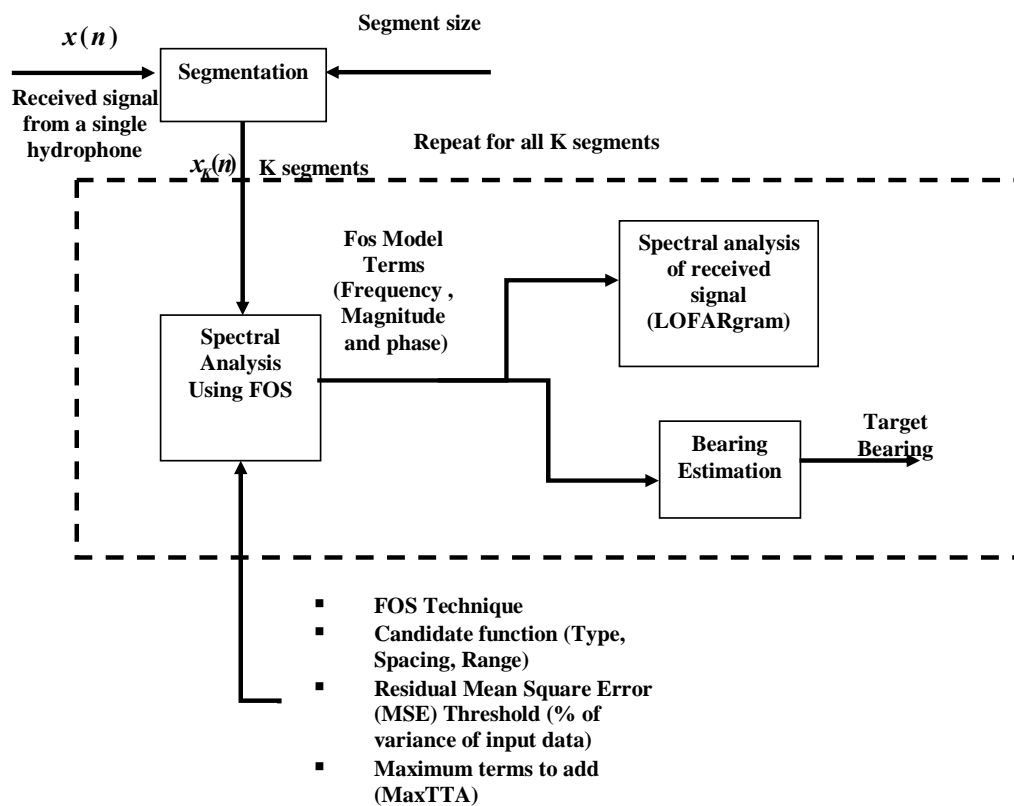


Figure3.1. Application of FOS to the problem of underwater target detection and localization

Each segment is modelled using FOS to extract the frequency components of the received signal. The output of this stage is the FOS model terms, which provides information on frequency, magnitude and phase for that segment of data. This process

repeats for all segments. The FOS model terms can be used to draw LOFARgram and also can be processed to provide bearing estimation of the received signal components.

FOS accuracy enhancement parameters

As FOS is generally known to be a data dependent algorithm [Adeney94, Korenberg88, Korenberg89A, Korenberg89B, McGaughey03]; the accuracy of the model produced by FOS depends on the data record being modelled, the candidate functions used to compute correlations, and the stopping conditions (thresholds) in the algorithm. Sinusoidal candidate functions were selected in this research because they had been successfully applied to de-noising [Korenberg89B] and in non-stationary signal analysis [Davis93]. Furthermore, the closed-form expressions for computing the cross-correlations between sinusoids [Dwight60] make the execution time of FOS with sinusoidal basis functions considerably faster than it would be with most other types of basis functions [Korenberg89A].

The FOS candidate frequencies are chosen to have a higher resolution than FFT to achieve better de-noising. The frequency resolution of FFT is given by:

$$\text{FFT Resolution} = f_s / N, \quad 3.15$$

where f_s is the sampling frequency and N is the number of points in the record. Subject to the SNR, it has been shown that FOS can achieve frequency resolutions up to 5 [Korenberg98], 8 [Korenberg91], or 10 [McGaughey03] times the frequency resolution of the FFT.

From Eq. 3.15 it can be seen that a long record length gives good spectral resolution, which is needed to accurately model a time-series. However, in case of moving targets, a short record length is desired for accurate bearing estimation at different time instants. For this research, the candidate function spacing was typically set in the order of 1/10 the FFT resolution for each segment.

Candidate frequencies can be selected so that the candidate functions focus on a particular frequency range of interest. For example, the candidates can be spaced with a high resolution on a range of interest and outside the range of interest; the candidates can be spaced by FFT resolution intervals.

It is desirable to have the minimum number of candidate frequencies in the spectral estimate. These should represent the most significant components of received signal. However, too few terms results in a model that does not accurately represent the received signal and too many terms will add noise terms into the received signal spectral estimate as well as increase the computation time. In this research, maximum terms to add (MaxTTA) is typically set between 5 and 15, not including a DC model term.

FOS stops the modeling procedure when the MSE reaches certain threshold. This threshold is chosen so that it is equivalent to the variance of the white Gaussian noise (WGN). It is known that underwater sound received by the hydrophones includes WGN and coloured noise, which may not be rejected by this threshold. Thus, a candidate acceptance threshold, requiring a frequency pair to fit a minimum percentage of the overall energy in the signal, is set. These thresholds allow FOS to model the underwater received sound and reject frequency terms that model the noise.

3.3 Simulation WORK

In this research the developed simulation is based on a module for normal mode generation which is a part of a simulation program developed at Curtin University of Technology [Centre for Marine Science and Technology (Actup version2.2)]. The selection of normal modes takes into consideration different environmental conditions including sound propagation path, speed profile, diffraction and reflection coefficients of different levels of the ocean and other factors affecting the propagation loss profile of sound [Hawker79, Porter85, Lim94A, and Lim94B].

To study the effect of applying FOS technique, two scenarios are presented in this research. The first scenario examines single target detection. The second scenario examines target detection in presence of two additional interfering sources. For both scenarios target tone was simulated at 100 HZ and moving at a speed of 4 m/s at a constant depth of 100 m. The ocean depth of simulated environment is 900 m. The hydrophone part of the GPS-equipped sonobuoy was assumed to be at 100m depth. Simulation duration is 1 minute and sampling frequency used was 1 kHz. The additional sources in the second scenario were simulated with tone frequencies of 60 Hz and 160 Hz moving with speeds of 20 ms and 30 m/s respectively. Interfering sources are assumed to be at depth of 100 m and their power was simulated such that the minimum value of their SNR's at the receiver is -10 dB. The SNR is considered to be the ratio between the signal power received by each sensor and the white noise power. It should be also noticed that target movement introduces Doppler shift in the received frequency. Doppler shift is a change in frequency of emitted waves produced by motion of an emitting source relative

to an observer. The Doppler shift introduced by the source movement is not significant since the 100 Hz source is moving at relatively low speed (4 m/s). The Doppler shift introduced by the sources can be calculated by:

$$\Delta f = \frac{v_{sr}}{v_o} f_o \quad 3.16$$

Where v_{sr} is the relative velocity between source and receiver, v_o is the underwater sound propagation velocity and, f_o is the source frequency. Given that the average underwater sound propagation velocity is 1500 m/s, the maximum Doppler shifts expected by the target is 0.27 Hz.

Different levels of received SNR for the target tone were tested assuming different source level of the target signal in each case. The simulated noise was assumed to be white Gaussian although it is not guaranteed to be white Gaussian but white Gaussian noise assumption can be considered convenient for the comparison of FOS performance against FFT performance at same SNR values.

Figure 3.2 shows the simulated sources trajectories. In the first scenario only the target of interest is present. FOS performance is compared to FFT at different levels of white noise and different length of the data set window. In the second scenario, two sources trajectories were simulated near the sonobuoy in order to investigate the performance of FOS in presence of other sources. The selected window sizes for the two scenarios are 5s , 10s, 20s, 30s, 40s and 60s. The transmission loss for the signals were calculated through the simulation program based on the ocean parameters, depth of sources ,depth of receiver hydrophone and frequency of acoustic source. Figure 3.3 shows the transmission loss at different depths of the ocean. This figure shows that signal

level can significantly degrade with the depth even at close ranges. This transmission loss profile is very close to real environmental conditions which show it is very likely to receive signals at very low signal to noise ratios. Transmission loss profiles at depth of 100m are shown in Figures 3.3-3.6.

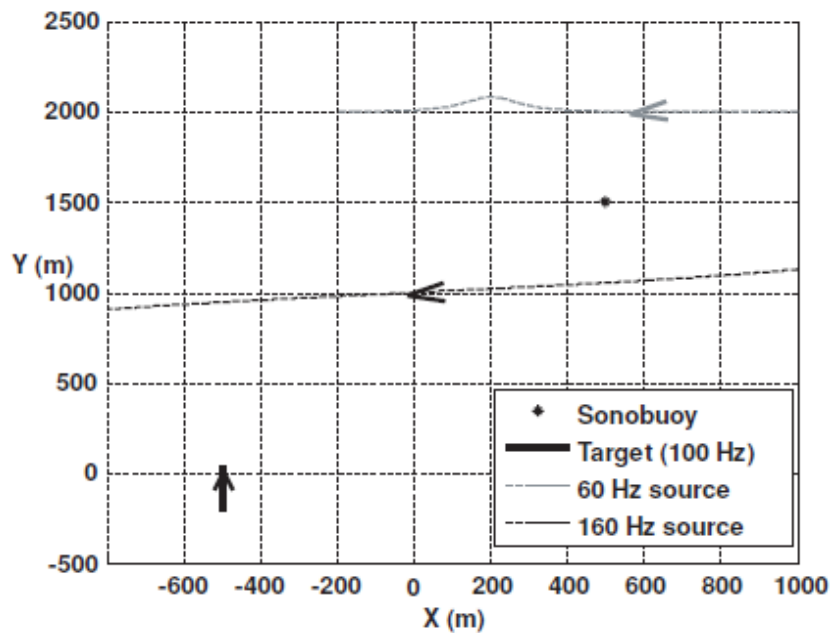


Figure 3.2 Trajectory of simulated sources relative to sonobuoy location

Transmission loss vs depth and range for 100Hz source located at 100m depth

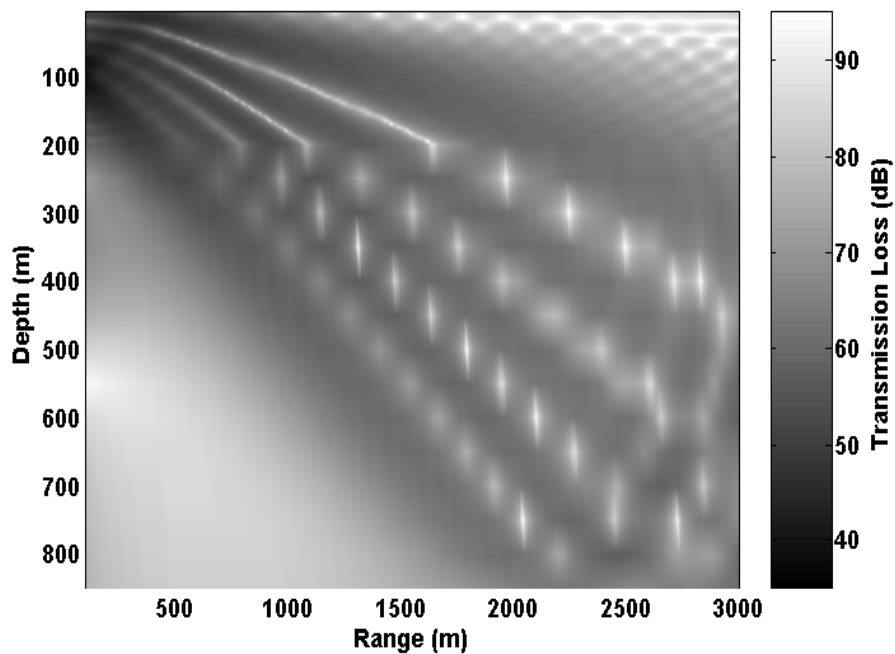


Figure 3.3 Transmission Loss vs. depth and range for 100Hz source lying at a depth of 100 m

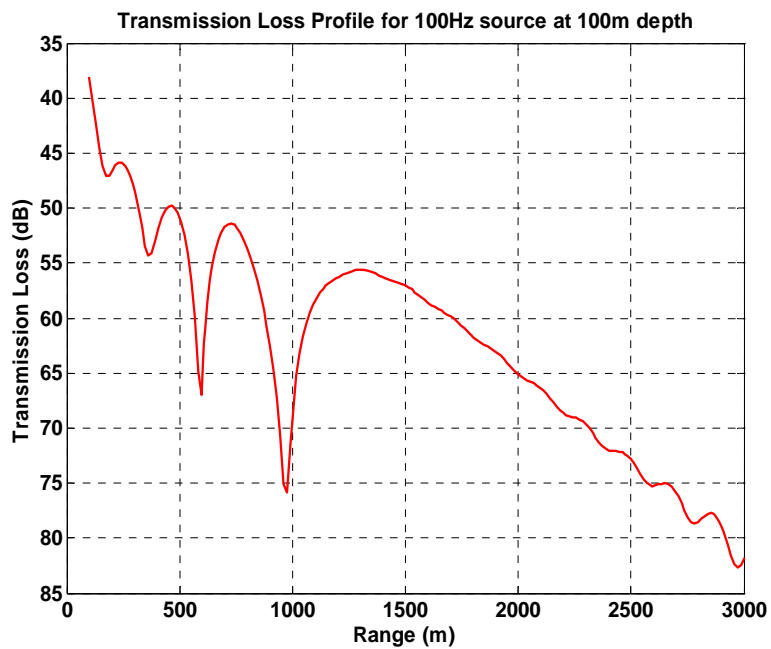


Figure 3.4 Transmission Loss vs. range for 100Hz source; source and receiver at a depth of 100 m

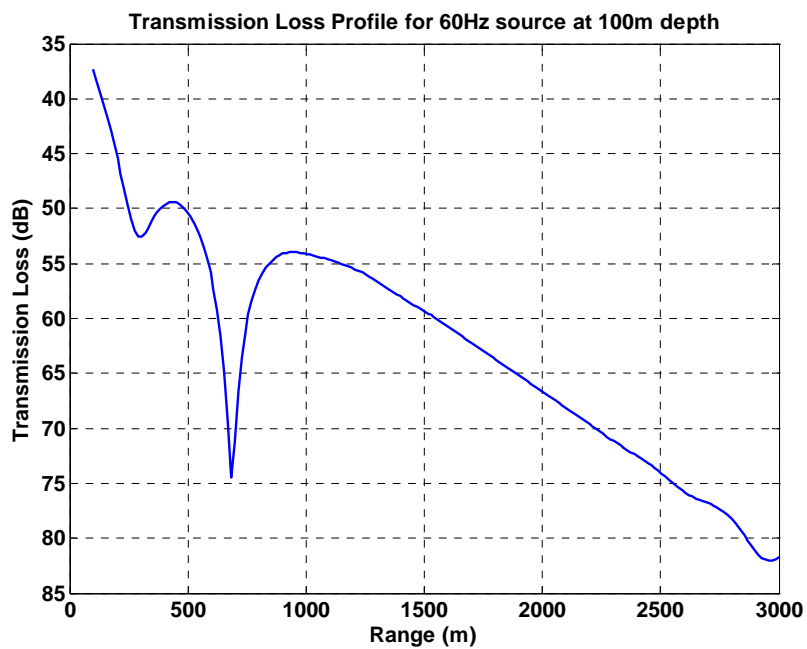


Figure 3.5 Transmission Loss vs range for 60Hz source; source and receiver at a depth of 100 m

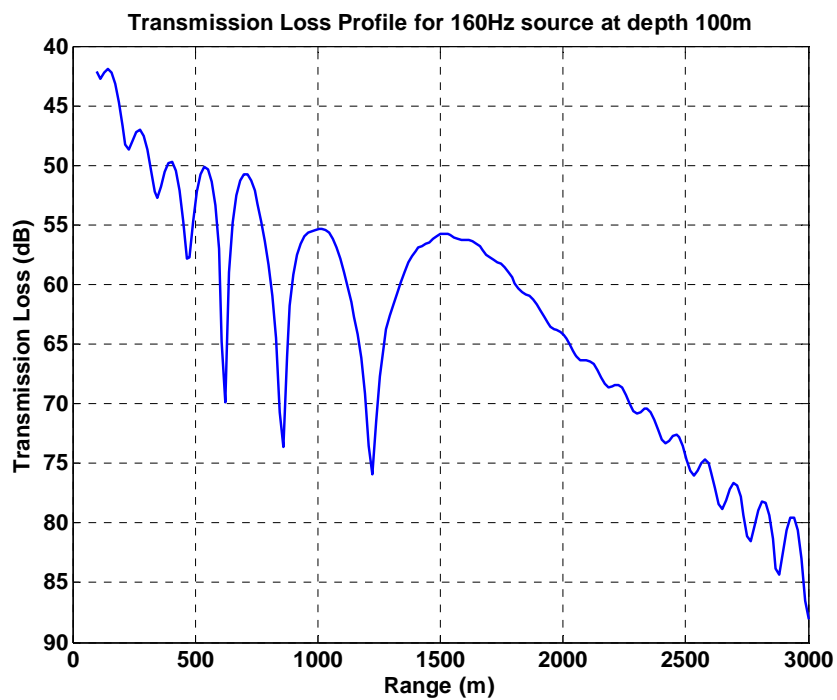


Figure 3.6 Transmission Loss vs range for 160Hz source; source and receiver at a depth of 100 m

The bearing error is calculated by comparing the estimated bearing to the average bearing during the time window of the tested data. FOS may select candidate frequencies that do not lie exactly at the same bin for each of the three channels, even though they are the result of the same real frequency in the time series (i.e., the bins don't line up). The problem becomes that for a given frequency, an error of only one FOS frequency bin in any of the three channels will result in no available bearing information.

Two previously suggested techniques to overcome this problem are mentioned in [Bohac 05]. One of these options is to average the spectral estimate for each channel in order to ensure the frequencies chosen by FOS are more likely to correspond for each channel. Another option is to reduce the frequency resolution of FOS to force the choice of frequency bins that correspond across the channels. Both of these techniques, however, dilute the significant resolution advantage of FOS over FFT. The approach suggested by Filip Bohac in [Bohac 05] is based on forcing FOS algorithm to use certain candidates in the model, regardless of their MSE reduction. Therefore it creates a model with the force-fit candidates without performing a search, and then searches through all remaining candidates to complete the model until a stopping condition is reached.

For this implementation, the corresponding values of frequency components computed for the three channels are chosen by selecting the nearest components to reference frequency bins. Reference frequency bins are extracted from the spectral analysis of the received signal component of the omni-directional sensor. In this manner FOS keeps its significant features which are high resolution and high accuracy spectral estimation without forcing certain candidate frequencies. This is essential for this research work as it targets the study of relatively very low SNR's cases and therefore

spectral power assigned to each component has a crucial effect on accuracy of bearing estimation.

3.4 Results and Discussion

In this section, FOS is compared to FFT from two aspects: 1) Accuracy of detection and bearing estimation for different window sizes; 2) Accuracy of detection and bearing estimation at SNR's -10,-15,-20,-25,-30 and -35 dB for each window size. For each of the window sizes and each SNR, we calculate the percentage of failure in bearing estimation for both FOS and FFT. Cases with failure percentages over 60% are not considered in the comparison. We noticed that FOS minimized the spectral leakage inherent in FFT, thus improved the bearing estimation accuracy.

3.4.1 First Scenario (Single source)

A. Target Detection

Target detection is based on detecting the presence of target frequency in the spectrum of the received signal. Figures 3.7 and 3.8 show the spectral estimate calculated using FOS versus the one calculated using FFT for SNR's of -25 dB using window sizes of 5s and 60s respectively.

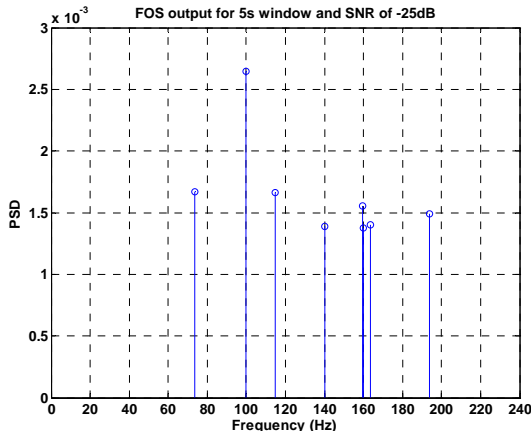


Figure 3.7a. PSD using FOS for SNR=-25 dB using 5s data window

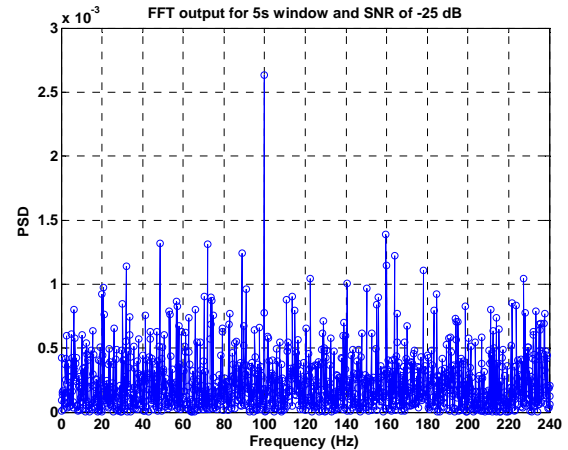


Figure 3.7b. PSD using FFT for SNR=-25 dB using 5s data window

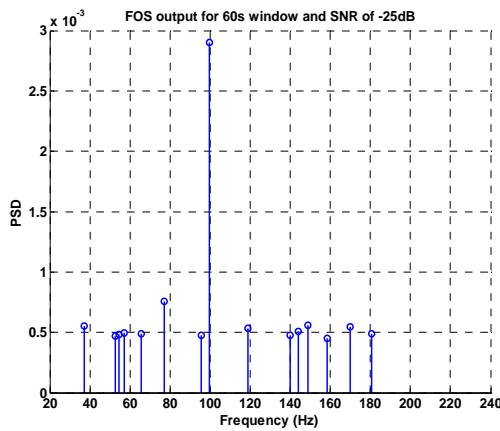


Figure 3.8a. PSD using FOS for SNR=-25 dB using 60s data window

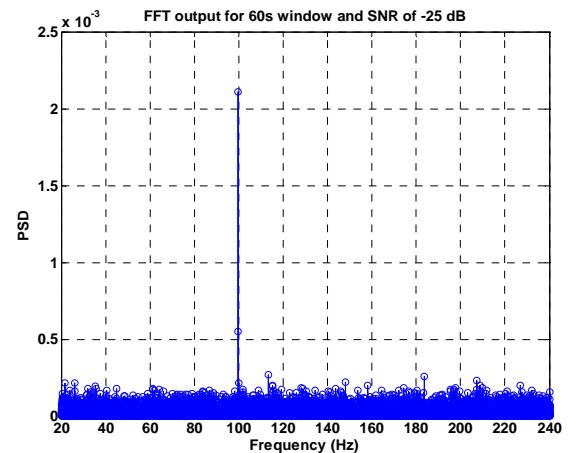


Figure 3.8b. PSD using FFT for SNR=-25 dB using 60s data window

The outputs of FOS and FFT at SNR of -25dB in figures 8 and 9 shows that most of the signal power is assigned to the target frequency. However the value of power assigned to target using FFT varies as the window size varies. For 5s window the value of target signal power was around 0.0025 Watt. For FFT this value changed at 60s window where the value of power assigned to the target was around 0.002 Watt. On the other hand the target signal power value is almost constant for the PSD generated using FOS

for both window sizes. The power allocated to target frequency using FOS depends on the search algorithm that minimizes MSE and hence power is accurately allocated. In FFT spectral leakage causes some of the signal power to be distributed over the spectrum. This can effectively enhance target detection, especially when we are dealing with relatively very low SNRs.

Figures 3.9 and 3.10 show the PSD calculated using FOS and FFT. The observed performance at -30 dB was almost similar to that at -25 dB except that signal power detected at 5s window was influenced by the high noise level. This caused allocation of some noise power to the target frequency component PSD. For the 5 sec window, both FOS and FFT produced noise based frequency components with higher amplitude than the 100 Hz. However, since FOS produced fewer spectral components, it is easier for an operator looking for the 100Hz to identify it in FOS output than in the FFT output.

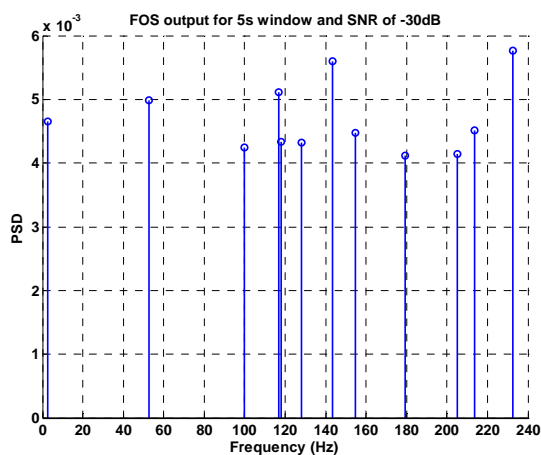


Figure 3.9a. PSD using FOS for SNR=-30 dB using 5s data window

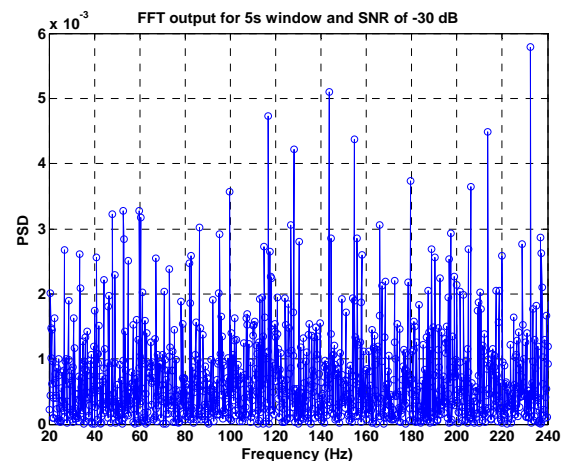


Figure 3.9b. PSD using FFT for SNR=-30 dB using 5s data window

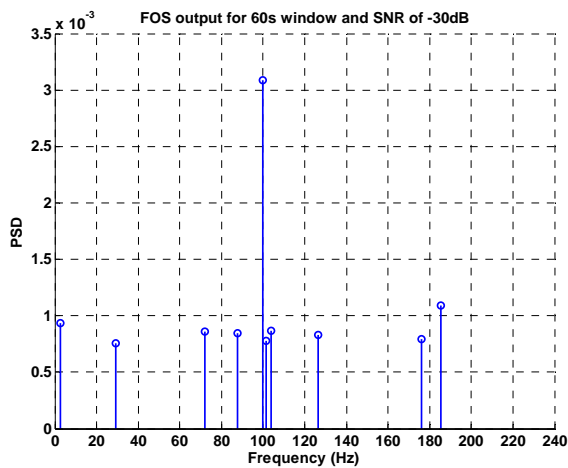


Figure 3.10a. PSD using FOS for SNR=-30 dB using 60s data window

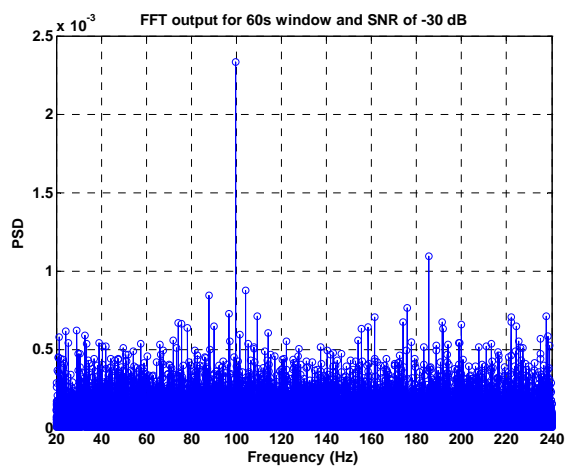


Figure 3.10b. PSD using FFT for SNR=-30 dB using 60s data window

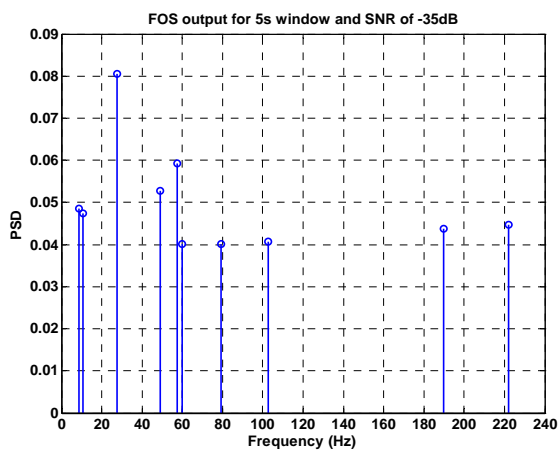


Figure 3.11a. PSD using FOS for SNR=-35 dB using 5s data window

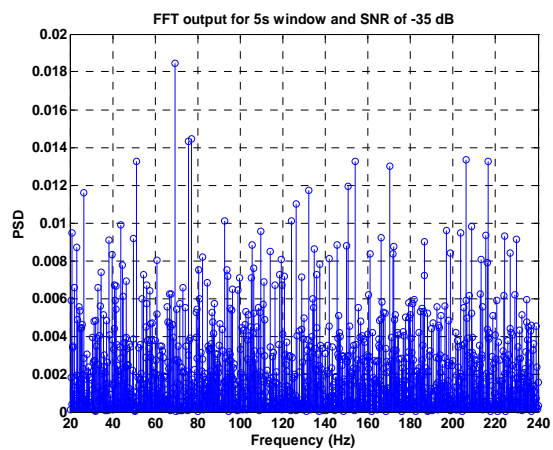


Figure 3.11b. PSD using FFT for SNR=-35 dB using 5s data window

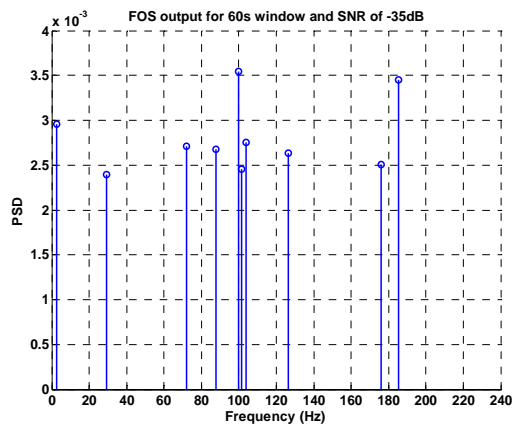


Figure 3.12a. PSD using FOS for SNR=-35 dB using 60s data window

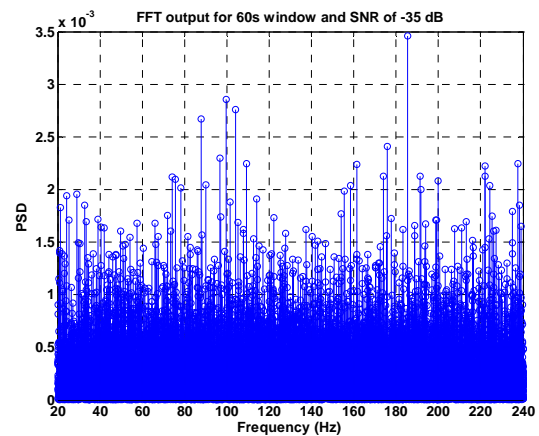


Figure 3.12b. PSD using FFT for SNR=-35 dB using 60s data window

Figures 3.11 and 3.12 show the results from FOS versus FFT at -35 dB. The shown figures represent power spectral density calculated at 5s and 60s windows. Looking at the two figures it can be observed that the target signal is totally buried in noise at such low SNR. The noise levels appear with high amplitudes which makes source signal detection and extraction more difficult. On the other side FOS detected the 100 Hz source with high accuracy. It can be noticed that there is an increase in power due to assigning some noise power to the source at 100 Hz. This did not influence the detection but, as discussed later, affected the bearing estimation since the same process was applied to the other two sensors (sine and Cosine).

B. Bearing Estimation

Bartlett Beamforming was used to compute bearing estimation as discussed in Chapter 2. In order to study performance of system using FOS in spectral estimation against system using FFT, 30 runs were simulated for all cases. Each case represents a

definite window size and SNR of received signal. The error is the absolute difference between estimated bearing and the mean bearing of the target. The output estimate is considered to be correct if the error in bearing estimation is less than 10° . This value is related to the fact that ± 10 degrees are the operationally accepted accuracy of a DIFAR sonobuoy [Bohac05]. Therefore the estimated bearing within 10 degrees of the input signal bearing is considered successful bearing estimation.

Table 3.1 shows the results for different cases examined. The percentage of failure in bearing estimation is tabulated for both methods FOS and FFT. The results show that the accuracy of bearing estimation increases as the window size increase. This can be noticed from the results for SNR cases of -25 dB, -30 dB and -35 dB. This is because increasing window size increases the total power of signal of interest relative to the noise which is a random signal.

Comparing the bearing estimation percentage of failure between FOS and FFT we can observe the following:

- i) FOS outperforms FFT in all cases of SNR's lower than -20 dB. This is related to the spectral estimation method used by FFT and FOS. FOS fitting of candidate functions achieves higher accuracy estimation of spectral power density as mentioned in the detection part. This influences the values of sine and cosine output PSD and hence provides more accurate bearing estimation.
- ii) In some cases (5s window and 10s window at SNR's -30 dB and -35 dB), we noticed that both FOS and FFT methods have similar and relatively

large failure rates. These cases were ignored since both methods led to totally unreliable target detection.

- iii) Two factors determine the lowest SNR at which the target can still be detected. These are the window size and the desired acceptable accuracy. This depends on the system requirement. Small windows provide more accurate localization of the target and large windows provide less accurate localization. For SNR's lower than -20 dB, the window size affects the percentage of failure. In less noisy environment, small windows of data can be applied. Relatively large windows will provide more accurate detection in highly noisy environments. However it will estimate an average bearing over the larger windows.
- iv) It is clear that FOS outperforms FFT in case of SNR -30 dB in all window sizes with different percentages. Moreover -30 dB SNR could be detected by system employing FOS with 0% failure versus 14% of failure for system employing FFT.
- v) FFT is faster than FOS. This difference in processing speed increase as the window size increase. This remains a disadvantage for FOS

Table 3.1. Bearing estimation results for first scenario

Window Size	SNR	Percentage of Failure using FOS	Percentage of Failure using FFT	Percentage of Improvement
5	-10	0%	0%	0%
	-15	0%	0%	0%
	-20	0%	0%	0%
	-25	28%	56%	28%
	-30	80%	87%	7%
	-35	94%	100%	6%
10	-10	0%	0%	0%
	-15	0%	0%	0%
	-20	0%	0%	0%
	-25	10%	10%	0%
	-30	65%	75%	10%
	-35	85%	95%	10%
20	-10	0%	0%	0%
	-15	0%	0%	0%
	-20	0%	0%	0%
	-25	5%	5%	0%
	-30	43%	71%	28%
	-35	70%	95%	25%
30	-10	0%	0%	0%
	-15	0%	0%	0%
	-20	0%	0%	0%
	-25	0%	0%	0%
	-30	30%	30%	0%
	-35	90%	95%	5%
40	-10	0%	0%	0%
	-15	0%	0%	0%
	-20	0%	0%	0%
	-25	0%	0%	0%
	-30	10%	10%	0%
	-35	50%	58%	8%
60	-10	0%	0%	0%
	-15	0%	0%	0%
	-20	0%	0%	0%
	-25	0%	0%	0%
	-30	0%	14%	14%
	-35	20%	30%	10%

3.4.2 Second Scenario (Target and two interference sources)

A. Target Detection

In this experiment we studied how target detection and bearing estimation are affected by strong interference sources at different levels of white background noise. Different window sizes were tested against different SNR's in the same way as in the single source experiment. Figures 3.14-3.16 shows the spectral estimate from FOS versus FFT for SNR's of -25 dB using window sizes of 5s and 60s.

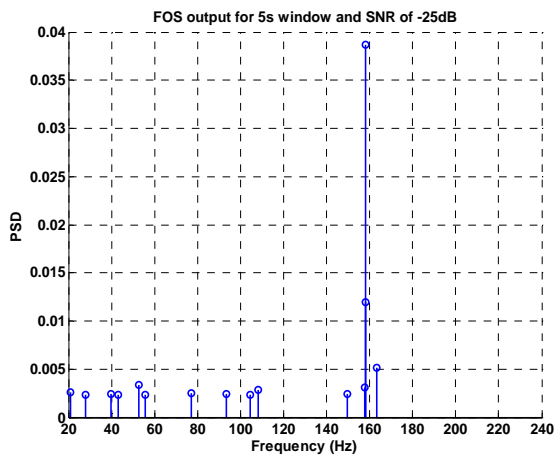


Figure 3.13a. PSD using FOS for SNR=-25 dB using 5s data window

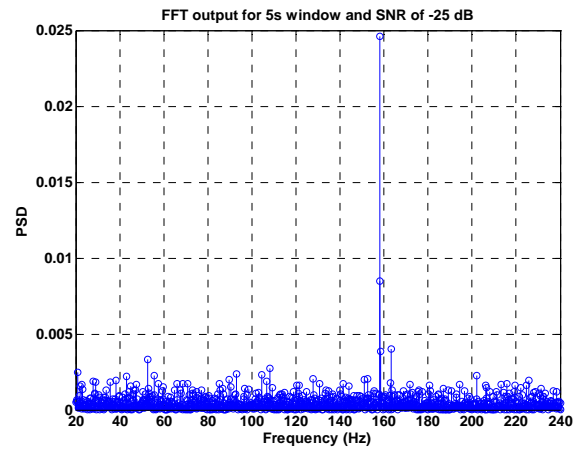


Figure 3.13b. PSD using FFT for SNR=-25 dB using 5s data window

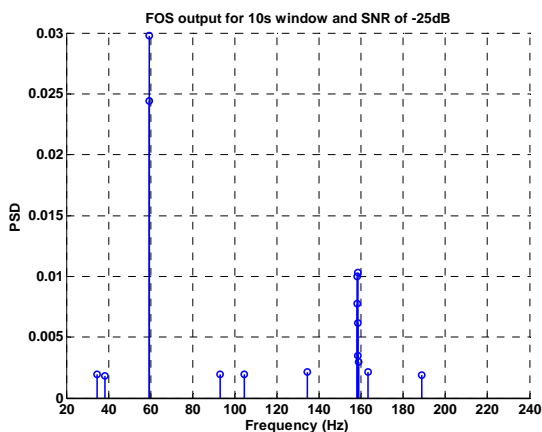


Figure 3.14a. PSD using FOS for SNR=-25 dB using 10s data window

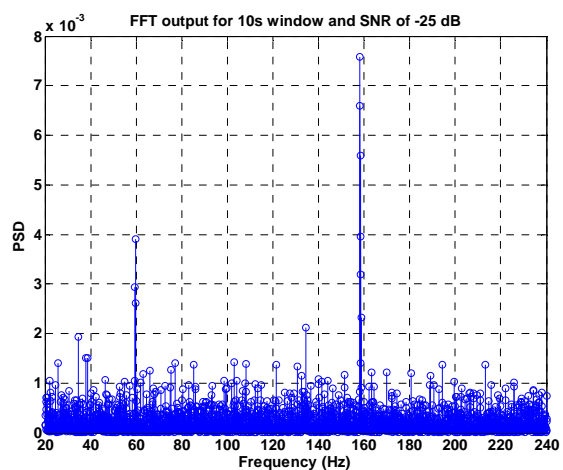


Figure 3.14b. PSD using FFT for SNR=-25 dB using 10s data window

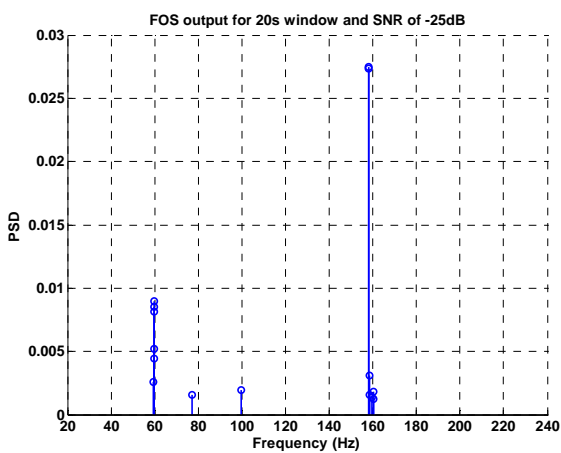


Figure 3.15a. PSD using FOS for SNR=-25 dB using 20s data window

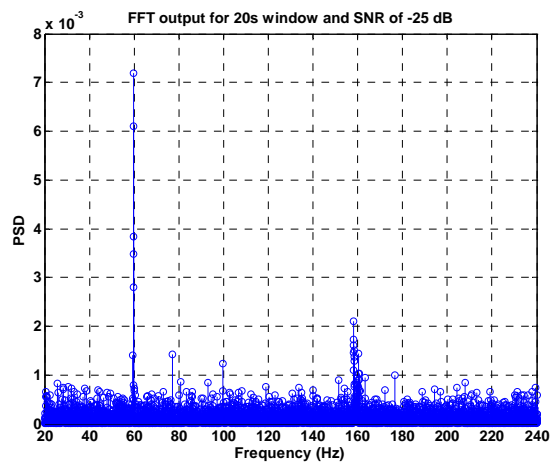


Figure 3.15b. PSD using FFT for SNR=-25 dB using 20s data window

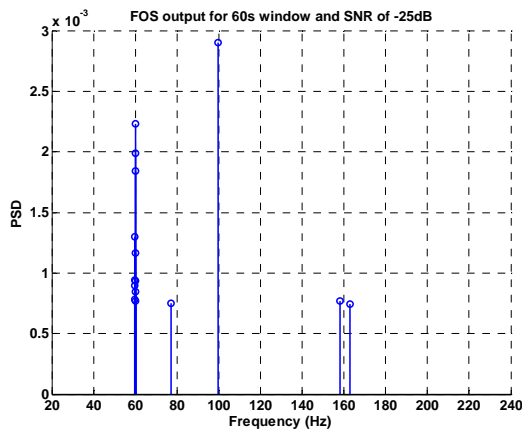


Figure 3.16a. PSD using FOS for SNR=-25 dB using 60s data window

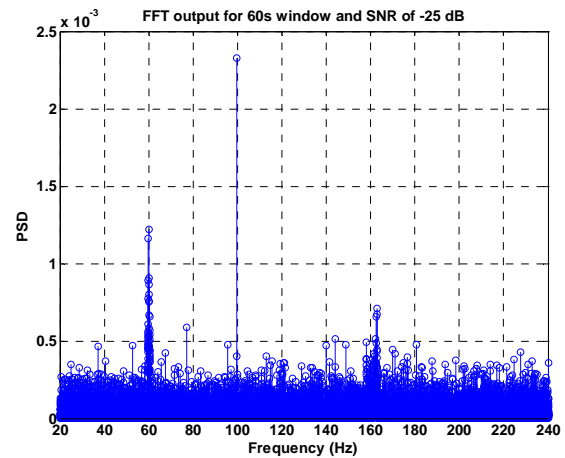


Figure 3.16b. PSD using FFT for SNR=-25 dB using 60s data window

For windows of 5s and 10s the value of target signal power is not clear since two signal components are detected around 100 Hz which may be considered as a failure in target detection or if the closest frequency component to 100 Hz is considered a source then there exist a decrease in the power assigned to that source. Note that considering the closest frequency component as the target is a primary decision which can be enforced by examining successive windows. If nearly the same frequency keeps appearing in successive windows this component will be considered a target although it hasn't been accurately detected. The output of FFT at SNR's of -25dB for 20s window shows some degradation in performance which affects the value of the signal power assigned to the target frequency (100 Hz) that is around 0.0015 watt. The PSD at 100 Hz is more accurately detected using FOS (around 0.0025 watt). The values of PSD for the two interference sources varies as the window size varies since the other two sources are moving with relatively higher speed than the target and hence their power level exhibit significant variance over small intervals of time.

Similar degradation in performance was found at SNR's of -30 dB and -35 dB. However FOS showed better performance in allocating signal power to target. The effect of interference, system degradation and robustness of FOS against interference sources can be clearly shown in bearing estimation of target.

B. Bearing Estimation

Bearing estimation technique and error detection criterion were applied similar to single source case. Table II shows the results for different cases considered. In Each case the percentage of failure in bearing estimation is tabulated for system output calculated using FOS against the one calculated using FFT. The results show that the accuracy of bearing estimation degraded as a result of interference sources added in this scenario. However FOS preserves its superiority over FFT especially when results are considered reliable (i.e at low levels of percentage of failure).

From Table II we can observe that FOS outperforms FFT in all cases of SNR's lower than -20 dB. In some cases of very low SNR's FFT showed better performance but the percentages of failure in these cases are over 60%. These percentage shows error in bearing estimation for frequency components detected close to the target frequency which may be noise component at the selected window.

The Table shows that system capabilities are significantly affected by interference sources. The main effect is shown in the system failure to accurately detect and estimate bearing for target at -35 dB using different window sizes. However FOS robustness against interference sources is fairly more than that of FFT. This is clear in cases of 10s window at SNR of -20 dB; Also in case of SNR -25 at 20s and 30s windows. Moreover

when looking at the case of -30 dB SNR and 60s window FOS shows significant improvement in detecting signals of low SNR. The failure percentage of system employing FOS (10 %) is half that of the system employing FFT and at the same time it is relatively low percentage.

Table 3.2 Bearing estimation results for second scenario

Window Size	SNR	Percentage of Failure using FOS	Percentage of Failure using FFT	Percentage of Improvement
5	-10	0%	0%	0%
	-15	0%	0%	0%
	-20	35%	40%	5%
	-25	85%	65%	-20%
	-30	90%	90%	0%
	-35	75%	95%	20%
10	-10	0%	0%	0%
	-15	0%	0%	0%
	-20	5%	15%	10%
	-25	60%	60%	0%
	-30	80%	85%	5%
	-35	85%	85%	0%
20	-10	0%	0%	0%
	-15	0%	0%	0%
	-20	0%	0%	0%
	-25	10%	20%	10%
	-30	30%	25%	-5%
	-35	90%	95%	5%
30	-10	0%	0%	0%
	-15	0%	0%	0%
	-20	0%	0%	0%
	-25	0%	5%	5%
	-30	55%	60%	5%
	-35	90%	95%	5%
40	-10	0%	0%	0%
	-15	0%	0%	0%
	-20	0%	0%	0%
	-25	0%	0%	0%
	-30	45%	35%	-10%
	-35	80%	80%	0%
60	-10	0%	0%	0%
	-15	0%	0%	0%
	-20	0%	0%	0%
	-25	0%	0%	0%
	-30	10%	20%	10%
	-35	90%	80%	-10%

3.5 Conclusions

The results showed that performance crucially depends on SNR and window size of analyzed data set. However, FOS showed better performance than FFT for most cases in which failure percentages were below 60%. For cases of small window size and low SNR, both FFT and FOS methods failed to accurately detect the target. FOS also provided clearer spectral estimation since it allocated power only for selected number of candidates. FOS nature of operation helps in providing a clear view of spectrum without using an amplitude threshold which might cause the loss of Target signal. This can provide a clear LOFARgram which facilitates target detection. Moreover, the use of FOS enhances the accuracy of bearing estimation especially at relatively low SNR which was observed at SNR's lower than -25 dB. Although in some cases similar performance in bearing estimation was noticed but FOS showed to be more robust than FFT at SNR's below -25 dB for. For short data records FOS showed better performance than FFT in both target detection and bearing estimation. This research shows that using FOS enhances the performance of underwater target tracking using DIFAR sonobuoys. Further work on interference cancellation can improve the overall system performance and enable robust target detection and bearing estimation at very low SNR's.

Chapter Four: Direction of Arrival Estimation using an Array of GPS Sonobuoys

Currently the bearing estimation of underwater targets using DIFAR sonobuoys field is based on combining the bearings obtained through individual element processing. This preserves the advantage of having a widely spread field of sonobuoys to detect underwater targets. Chapter 2 detailed the direction of arrival (DOA) estimation using Bartellet beamforming from the signals monitored by the three sensors of each DIFAR sonobuoy [Bohac05, Desroches99 and Maranda03]. In Chapter 2 it was shown that the detection range and bearing estimation accuracy of DIFAR sonobuoys are mainly influenced by the SNR of the received acoustic signals. It has been reported that array processing can provide an enhanced SNR compared to a single sensor system [Johnson93 and Chen03]. Accordingly, processing a group of DIFAR sonobuoys field can introduce significant improvement to the bearing estimation accuracy, especially at low SNR environments which are presently common in ASW. Nevertheless, the DIFAR sonobuoys operation environment imposes some limitations on array processing. These limitations are mainly imposed by the deployment methods and the variation of inter-element spacing over time. In ASW, DIFAR sonobuoys are deployed from a helicopter or surface ship [Joh97, Boh05 and Des99]. Based on deployment method, the distance between the deployed DIFAR sonobuoys may range from few meters to hundreds of meters [Ultra06]. In addition the ocean tides cause relatively huge drifts in the locations of sonobuoys [Urick96]. Consequently array processing of DIFAR sonobuoys becomes challenging process throughout ASW operations.

In this chapter, a new approach for array processing of DIFAR sonobuoys is introduced and analyzed showing its significant contribution in improving the overall system performance. In addition, this chapter discusses the limitations associated with array processing of a group of DIFAR sonobuoys.

The proposed technique was tested using simulated data developed for two different scenarios with different underwater environmental conditions. Comparisons between the proposed method and the technique presently utilized for DIFAR sonobuoys are demonstrated in this chapter. The results show that processing of an array of DIFAR sonobuoys is capable of enhancing the accuracy of target bearing estimation especially in cases of very low SNR. Moreover, array processing provides critical enhancement for the resolution of bearing estimation. Merits and limitations of the proposed technique are discussed and analyzed in this study.

4.1 Underwater Tracking Using Single DIFAR Sonobuoy

As discussed in Chapter 2, the basic processing of single DIFAR sonobuoy is mainly based on applying Bartellet beamforming to the three sensor array of the DIFAR sonobuoys. Figure 4.1 illustrates the acoustic dipoles of DIFAR sensors [Bohac05, Des99, Maranda03 and Osma09]. The DOA along the acoustic arrival axis is referenced to the two orthogonal dipoles, which are aligned to magnetic North, by the angle φ . Two orthogonal response axes are offset from magnetic North by the local magnetic variation angle α . The total angle θ which provides a bearing to an acoustic source is between the

arrival axis and the true North. The conversion between the magnetic North and the true North is made at the processor prior to displaying to the operator.

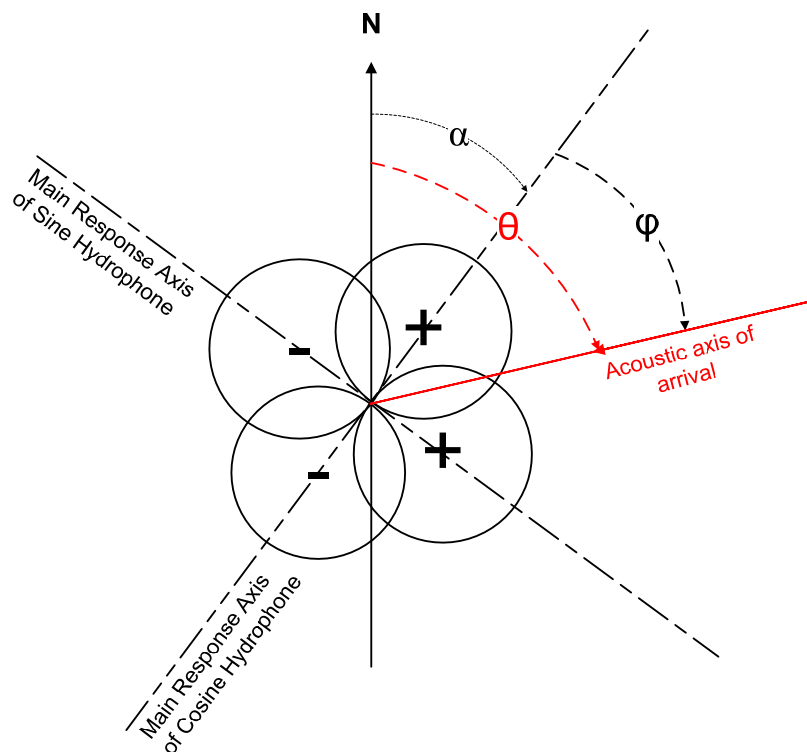


Figure 4.1 Acoustic dipole response of DIFAR sonobuoy

The output of the sonobuoy based on the incoming acoustic signal is a time series of N samples for each of the three channels. The data of these channels are converted into frequency domain by applying the DFT of the received time series. The general PSD is then obtained. The cross spectral matrix is then obtained which is used to calculate the DOA at the receiver, also known as the bearing to a target of interest (TOI). The quotient of the omni-sine and omni-cosine PSD estimates yields a bearing estimate using Bartellet Beamforming [Bohac05, Desroches99, Maranda04 and Osman09].

4.2 Underwater Tracking Using Uniform Linear Array (ULA) of DIFAR Sonobuoys

A Linear array processing of DIFAR sonobuoys can be established by using omni sensors only or by using omni, sine and cosine sensors of all sonobuoys in the array. Evaluation of these two modes of performance can be achieved by examining their radiation patterns.

4.2.1 Radiation Pattern for a Linear Array of Omni-directional sensors

The radiation pattern for ULA of DIFAR sonobuoys using omni-directional sensors is typical to that of omni-directional antenna array. The later was previously reported in literature [Johnson93 and Skolnik80]. Therefore the magnitude of the radiation pattern of ULA of N omni-directional sensors spaced a distance d is given by [Skolnik80]:

$$|E(\theta, \theta_0)| = \left| \frac{\sin(N\pi d(\sin \theta - \sin \theta_0)/\lambda)}{\sin(\pi d(\sin \theta - \sin \theta_0)/\lambda)} \right| \quad 4.1$$

Where θ_0 is the DOA of the received signal, λ is the received signal wavelength and θ is the domain of the scanned DOAs.

This pattern has nulls (zeros) when the numerator is zero which occurs when $N\pi ds(\sin \theta - \sin \theta_0)/\lambda = 0, \pm\pi, \pm2\pi, \dots, \pm n\pi$

The denominator becomes zero when $\pi d(\sin \theta - \sin \theta_0) / \lambda = 0, \pm\pi, \pm2\pi, \dots, \pm n\pi$ which causes the numerator to be zero. Thus L'Hoptial rule can be used to evaluate the field intensity pattern. It can be determined that the maximum field intensity for an array of N omni-directional sensors is equal to N and occurs when $\pi d(\sin \theta_0) / \lambda = 0, \pm\pi, \pm2\pi, \dots, \pm n\pi$. The maximum at $\pi d(\sin \theta - \sin \theta_0) / \lambda = 0$ is the center of the main beam and takes place at $\theta = \theta_0$. The grating lobes appear at $\pi d(\sin \theta - \sin \theta_0) / \lambda = \pm\pi, \pm2\pi, \dots, \pm n\pi$. Thus, the first grating lobe occurs at $\pi d(\sin \theta - \sin \theta_0) / \lambda = \pm\pi$. This corresponds to $(\sin \theta - \sin \theta_0) = \pm\lambda / d$.

Since the maximum value of $|(\sin \theta - \sin \theta_0)|$ is 2, the grating lobes are avoided by ensuring that $\lambda / d > 2$ or $d < \lambda / 2$. Consequently DOA ambiguity arises if the spacing between the DIFAR sonobuoys exceeds half the minimum wavelength of tracked target spectrum. This represents a challenge to the application of array processing of DIFAR sonobuoys since the spacing between the sonobuoys is most likely to exceed this value.

4.2.2 Radiation Pattern for a Linear Array of DIFAR sonobuoys

In this research, the radiation pattern for a Linear array of DIFAR sonobuoys was developed by defining a steering vector for the linear array of DIFAR sonobuoys and multiplying it by the normalized Fourier Transform of the received signal.

4.2.2.1 Modified Steering vector

The steering vector of the individual DIFAR array was modified to accommodate all receivers of the ULA of the DIFAR sonobuoys. The introduced modification assumed that the DOA of the acoustic signal is identical at all DIFAR sonobuoys comprising the array. This assumption is based on two conditions: (1) The DIFAR sonobuoys are aligned to the same reference which is the magnetic North; (2) The radiation source is relatively far from the DIFAR sonobuoys. The first condition can be achieved through calibration [D'Spain92] while the second condition is most likely to be associated with low SNR which represents the main motivation for applying array processing of DIFAR sonobuoys. Therefore, the new array steering vector $a(\theta)$ for a source arriving at angle θ is given by:

$$a(\theta) = \begin{bmatrix} 1, \sin \theta, \cos \theta, e^{-j\omega_0\Delta t_1}, \sin \theta e^{-j\omega_0\Delta t_1}, \cos \theta e^{-j\omega_0\Delta t_1}, \dots \\ \dots, e^{-j\omega_0\Delta t_n}, \sin \theta e^{-j\omega_0\Delta t_n}, \cos \theta e^{-j\omega_0\Delta t_n} \end{bmatrix}^T \quad 4.2$$

Where ω_0 is the source frequency and Δt_n is the relative delay of the omni sensor associated with the n^{th} DIFAR sonobuoy and is measured relative to the reference DIFAR sonobuoy.

4.2.2.2 Obtaining Radiation Pattern for a Linear Array of DIFAR sonobuoys

In order to obtain the radiation pattern of ULA of DIFAR sonobuoys, let us first consider the radiation pattern of single DIFAR sonobuoy. The normalized Fourier Transform of input sinusoidal signal arriving from direction θ_0 and received by the DIFAR sonobuoy three-sensors (Omni, sine and cosine) is given by [Des99]:

$$\Phi_{Single\ DIFAR} = [1 \quad \sin \theta_0 \quad \cos \theta_0] \quad 4.3$$

As Illustrated in Chapter 2, the bearing estimation using Bartlett beamforming is obtained as the bearing value corresponding to the maximum beam power estimate ($\hat{E}_{CB}(\theta)$) which is given by

$$\hat{E}_{CB}(\theta) = a(\theta)^T \hat{Q} a(\theta) \quad 4.4$$

Where $a(\theta)$ is the steering vector of the DIFAR sonobuoy and $a_{Single\ DIFAR}(\theta) = [1 \quad \sin \theta \quad \cos \theta]$.

Therefore for a linear array made up of N DIFAR sonobuoys equally spaced by a distance d . the normalized Fourier Transform of the received signal can be calculated as the vector given by:

$$\Phi = [1 \quad \sin \theta_0 \quad \cos \theta_0 \quad \exp(j2\pi d \sin \theta_0 / \lambda) \quad \exp(j2\pi d \sin \theta_0 / \lambda) \sin \theta_0 \quad \exp(j2\pi d \sin \theta_0 / \lambda) \cos \theta_0 \quad \dots \dots \exp(j2N\pi d \sin \theta_0 / \lambda) \quad \exp(j2N\pi d \sin \theta_0 / \lambda) \sin \theta_0 \quad \exp(j2N\pi d \sin \theta_0 / \lambda) \cos \theta_0]^T \quad 4.5$$

Similarly the steering vector of a linear array made up of N DIFAR sonobuoys can be driven from the steering vector of single DIFAR sonobuoy and is given by:

$$a(\theta) = \begin{bmatrix} 1 & \sin \theta & \cos \theta & \exp(j2\pi d \sin \theta / \lambda) & \exp(j2\pi d \sin \theta / \lambda) \sin \theta & \exp(j2\pi d \sin \theta / \lambda) \cos \theta \\ \dots\dots & \exp(j2N\pi d \sin \theta / \lambda) & \exp(j2N\pi d \sin \theta / \lambda) \sin \theta & \exp(j2N\pi d \sin \theta / \lambda) \cos \theta \end{bmatrix}^T \quad 4.6$$

Consequently, the magnitude of the radiation pattern can be obtained as:

$$E(\theta, \theta_0) = a(\theta)^H \Phi \quad 4.7$$

Where $E(\theta, \theta_0)$ is the magnitude of the radiation pattern for a sinusoidal signal arriving at θ_0 . The result is the sum of multiplying the corresponding terms of the steering vector and the normalized Fourier transform of the received signal which can be manipulated using the law of the sum of arithmetical series [Bromwich26] to give:

$$E(\theta, \theta_0) = (1 + \sin \theta \sin \theta_0 + \cos \theta \cos \theta_0) \sum_{n=0}^N \exp(-j2\pi n d (\sin \theta - \sin \theta_0) / \lambda) \quad 4.8$$

The first term can be simplified using the trigonometric relation $\cos(\theta - \theta_0) = \sin \theta \sin \theta_0 + \cos \theta \cos \theta_0$ and the sum term can be simplified by using the theory of sum of series [Bromwich26]. Accordingly, the final radiation pattern can be given as:

$$E(\theta, \theta_0) = (1 + \cos(\theta - \theta_0)) \frac{\sin(N\pi d (\sin \theta - \sin \theta_0) / \lambda)}{\sin(\pi d (\sin \theta - \sin \theta_0) / \lambda)} \quad 4.9$$

The term $(1 + \cos(\theta - \theta_0))$ represents the radiation pattern of the DIFAR sonobuoy [Desroches99] while the term $\frac{\sin(N\pi d(\sin \theta - \sin \theta_0)/\lambda)}{\sin(\pi d(\sin \theta - \sin \theta_0)/\lambda)}$ is the radiation pattern of N omni-directional sensors [Skolnik80]. Similar to the above analysis the value of the second term at zeros of the denominator can be evaluated by using L'Hopital rule. It can be determined that the maximum value of the second term in equation 4.9 is equal to N and occurs when $\pi d(\sin \theta - \sin \theta_0)/\lambda = 0, \pm\pi, \pm2\pi, \dots, \pm n\pi$. The maximum at $\pi d(\sin \theta - \sin \theta_0)/\lambda = 0$ is the center of the main beam and takes place at $\theta = \theta_0$. Similar values of the second term of equation 4.9 appear at $\pi d(\sin \theta - \sin \theta_0)/\lambda = \pm\pi, \pm2\pi, \dots, \pm n\pi$. For an array of omni-directional sensors the first grating lobe occurs at $\pi d(\sin \theta - \sin \theta_0)/\lambda = \pm\pi$. This corresponds to $(\sin \theta - \sin \theta_0) = \pm\lambda/d$. The grating lobes are avoided by ensuring that $\lambda/d > 2$ or $d < \lambda/2$. This limitation is extended when employing a group of linearly aligned DIFAR sonobuoys. This is because the value of the first term in equation 4.9 $((1 + \cos(\theta - \theta_0)))$ is maximum only at $\theta = \theta_0$. The grating lobes therefore does not exist in this case since the product of the DIFAR beam pattern and linear sensor beam pattern suppresses the grating lobes associated with the linear sensor array. This is considered an advantage since it permits array processing for spacing values exceeding half the minimum wavelength of the observed spectrum. However, there is a limitation on the spacing value since the increase in the spacing values causes the grating lobes associated with the omni-directional pattern take values close to the main beam value when multiplied by the radiation pattern of the single DIFAR array. Therefore, for reliable performance the first

grating lobe should be spaced away from the main beam. The value set for separation between the main beam and the first grating lobe defines the maximum allowable value of d .

To simplify the calculation consider the case of $\theta_0 = 0$. In this case the condition for the maximum allowable distance between the DIFAR sonobuoys is given by:

$$d < \lambda / (\sin(\theta_1) - \sin \theta_0) \quad 4.10$$

Since $-1 < -\sin \theta_0 < 1$, therefore the equation defining the limit of the distance between DIFAR sonobuoys can be given by:

$$d < (\lambda / (\sin \theta_1 + 1)) \quad 4.11$$

In order to suppress side lobes, the distance between the DIFAR sonobuoys can be set so that the first grating lobe occurs at $|\theta_1 - \theta_0| > 65.5^\circ$ which is the value at which the intensity of the radiation pattern of single DIFAR sonobuoy is equal to half the power of the main beam. This will guarantee that the value of highest side lobe is relatively small when compared to that of the main beam. Therefore:

$$d_{\max}^{DIFAR} = (\lambda_{\min} / (\sin 65.5 + 1)) = \lambda_{\min} / 1.91 \quad 4.12$$

This value is close to the condition required for a ULA of omni-directional sensors. The condition can be extended by allowing the first grating lobe of the ULA to exist at closer range to the main lobe. This value has to be carefully selected to ensure stability of system performance at low SNRs. Figure 4.2 shows the radiation pattern of DIFAR sonobuoy. Figure 4.3 demonstrates performance comparison between four omni-directional sonobuoys and four DIFAR directional sonobuoys using the radiation pattern for different values of spacing between the sonobuoys (10, 50 and 300m). These figures were obtained using equation 4.8 where the target is assumed to have a wavelength of 15m and bearing of 60° . As can be depicted from these two figures, the radiation pattern for a group of DIFAR sonobuoys possesses some important features which provides significant enhancement for the overall system performance. The DIFAR sonobuoy array formed by omni, sine and cosine sensors provides a low resolution radiation pattern since the inter-element spacing are very close together and the number of sensors is relatively small.

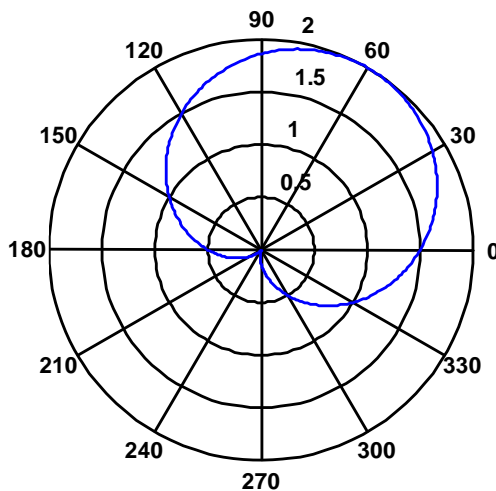


Figure 4.2. Radiation Pattern for DIFAR Sonobuoy (DOA=160°)

If Figures 4.3a, 4.3c and 4.3e (the case of omni-directional sonobuoys) are carefully examined, it can be determined that when the inter-element spacing values exceed $\lambda/2$, grating lobes appear and bearing estimation of signal source becomes ambiguous. On the other hand, when Figures 4.3b, 4.3d and 4.3f (the case of DIFAR sonobuoys) are examined, enhanced radiation pattern can be observed. The amplitude of the grating lobes were significantly reduced. One can also notice the enhancement introduced to the received SNR. This can be observed by comparing the amplitude values of the single sonobuoy pattern and the pattern of an array of sonobuoys. Moreover, the beamwidth of the main beam is significantly reduced in case of array processing. Consequently, the processing of a group of DIFAR sonobuoys results in significant enhancement of bearing estimation accuracy, especially at low SNRs.

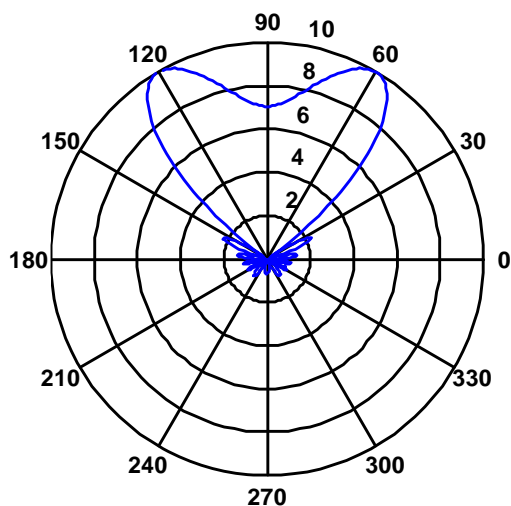


Figure 4.3a. Radiation Pattern for Linear array of 4 Omni-directional sensors (DOA=160° d=10 m)

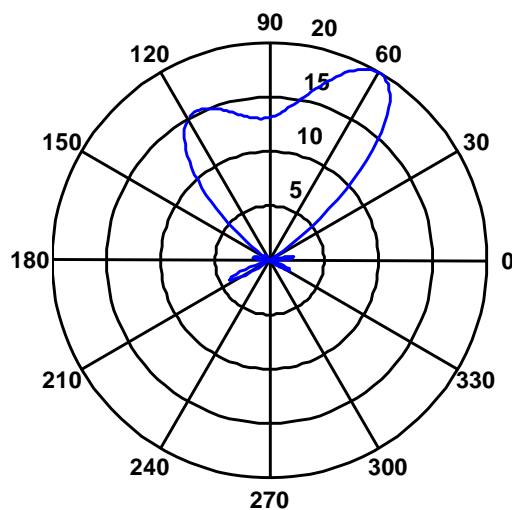


Figure 4.3b. Radiation Pattern for Linear array of 4 DIFAR sonobuoys (DOA=160° d=10 m)

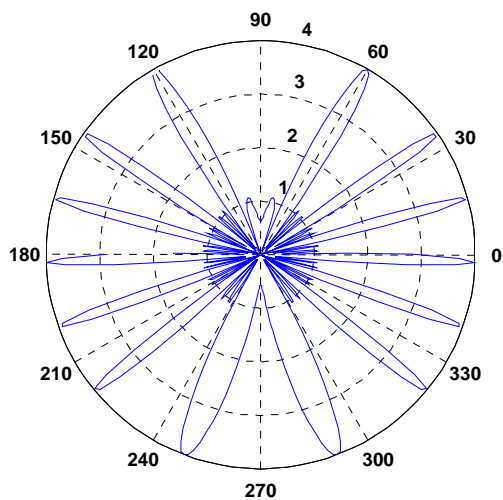


Figure 4.3c. Radiation Pattern for Linear array of 4 Omni-directional sensors (DOA=160° d=50 m)

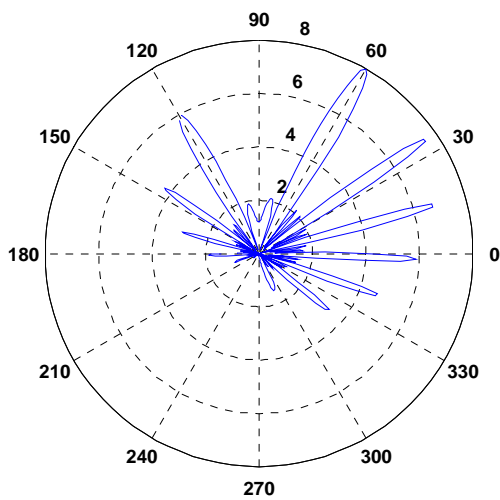


Figure 4.3d. Radiation Pattern for Linear array of 4 DIFAR sonobuoys (DOA=160° d=50 m)

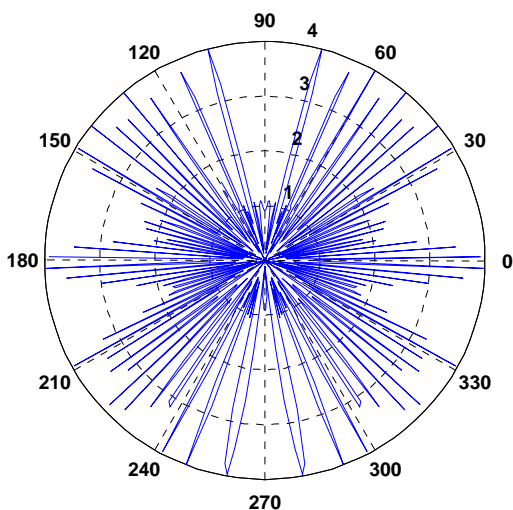


Figure 4.3e. Radiation Pattern for Linear array of 4 Omni-directional sensors (DOA=160° d=300 m)

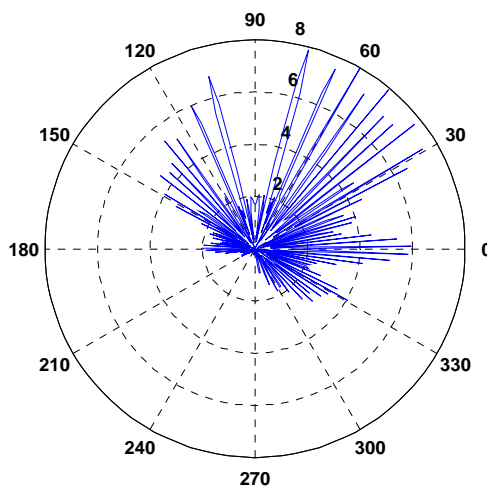


Figure 4.3f. Radiation Pattern for Linear array of 4 DIFAR sonobuoys (DOA=160° d=300 m)

From Eq. 4.9, it is clear that the array processing of DIFAR sonobuoys should always provide a unique solution of direction of arrival independent of the inter-element

distance. This is caused by the DIFAR beam pattern which provides a unique maximum value at the centre of the main lobe. However, the low resolution of Bartlett beamforming causes the solution to be numerically unstable [Stoer02] in cases where the side lobes are too close to the main lobe. Observing Eq. 4.10, it is clear that increasing the spacing between DIFAR sonobuoys brings the side lobes closer to the main lobe especially for relatively large values of d . Moreover, the numerical instability further increases in cases of very low SNRs. The two conditions of large spacing and low SNR are typical features of underwater target tracking. An additional limitation is introduced by the fact that target tracking is based on detecting the spectral signature of the target [Bohac05, Desroches99, Maranda03 and Urick96]. The spacing between main lobe and side lobes is proportional to the minimum wavelength of the spectrum of interest. Consequently the performance of system processing for an array of DIFAR sonobuoys can degrade significantly during operation especially in presence of strong tides that could extensively shift the original locations of DIFAR sonobuoys. Figures 4.3b, 4.3d and 4.3f show an illustration of the effect of inter-element spacing between DIFAR sonobuoys on overall system performance. From these figures it can be depicted that as the value of d increases side lobes amplitude becomes closer to the main lobe amplitude. In Figure 4.3d and 4.3f the amplitude of side lobe at 20 degrees is almost the same as the amplitude of the main lobe at 60 degrees.

4.2.3 Simulation work:

Acoustic level simulation was conducted to examine the performance of array processing of a linear array of four DIFAR Sonobuoys using Bartlett beamforming. The

noise added to the acoustic signal is white Gaussian noise and 100 Monte Carlo runs were used to calculate the percentage of error and examine the range of errors associated with different SNRs. In calculating the percentage of error, the estimated bearing was considered erroneous when absolute difference between the estimated bearing and the target DOA exceeds 10° . The received acoustic signal was assumed to be far field uniform plane wave. For the first scenario the sonobuoys are simulated with inter-element spacing of 10m, 50m and 300m. The simulated acoustic source had a single tone frequency of 100 Hz and amplitude of 140 dB re μPa . Acoustic sources were simulated with bearings at 50° , 120° , 160° and 220° .

The system performance was examined for SNRs of -25dB, -35 dB and -40 dB. Results compared the output from the processing of single source versus an array of DIFAR sonobuoys. These comparisons were carried for processing windows of 10 seconds. Figure 4.4 shows a general schematic of the simulations. The signal angle of arrival with respect to the north is similar at all array elements based on the far field assumption.

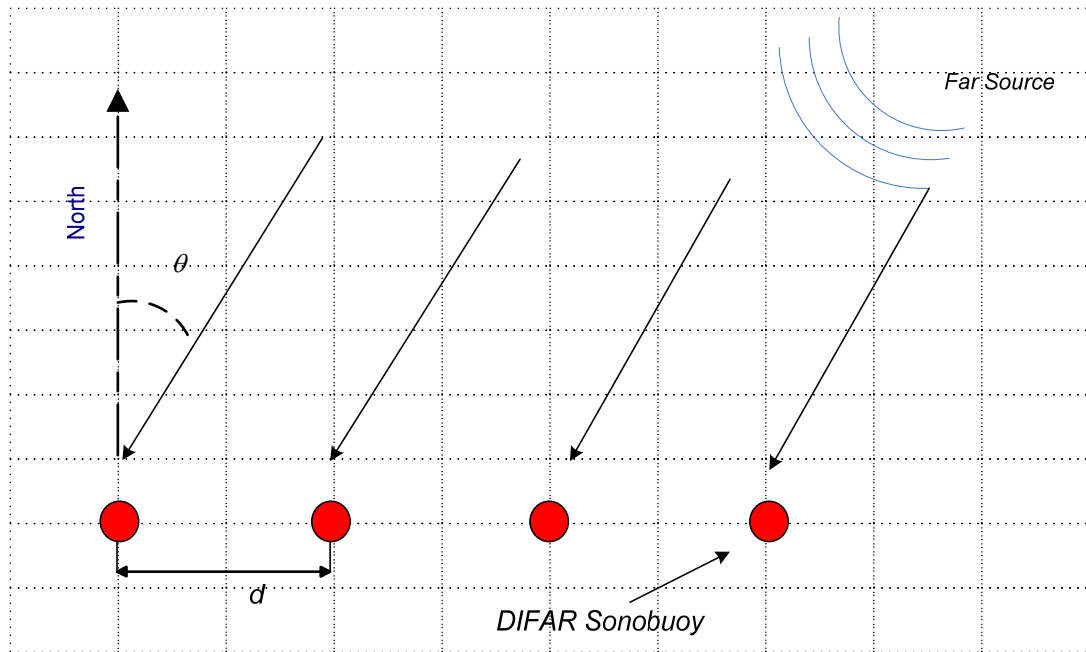


Figure 4.4 Linear Array of DIFAR Sonobuoys

4.2.4 Results and Discussion

The figures shown below illustrate the results obtained in testing the performance of an array of DIFAR sonobuoys versus single DIFAR sonobuoy processing. Results are shown for the case of target with bearing of 160° . The other cases of 50° , 120° and 220° showed similar performance for the different spacing values and different levels of SNR.

4.2.4.1 ULA of DIFAR Sonobuoys spaced 10 m apart

The spacing of 10 m violates the condition of stability defined by equation 4.11. However, the radiation pattern for this arrangement (Figure 4.3b) indicates that the first side lobe is reasonably spaced away from the main lobe. Hence the system can be considered stable. The results recorded for this case are shown in Figures 4.5, 4.6 and 4.7.

Figure 4.5 represents the case of -25 dB SNR. Up to this SNR, the performance of single sonobuoys processing is comparable to array processing. However array processing shows better performance since it possesses a 0% error corresponding to 2% error for the single sonobuoy processing. Figure 4.5a illustrates the improvement in the beamwidth which is around 40° in case of array of sonobuoys and around 130° in case of single sonobuoy. Figure 4.6 illustrates the dramatic degradation in the performance of single sonobuoy processing when the level of SNR decreases to -35 dB. The percentage of error increases to 48% which represents a significant system failure. On the other hand, the performance of array processing remains robust with 0% error. These results are consistent with the radiation pattern shown in Figure 4.3d which illustrates the amplitude gain achieved by employing an array of DIFAR sonobuoys. When the SNR is further decreased to -40 dB the performance of array processing of DIFAR sonobuoys shows some degradation in performance as the error rate jumps up to 22%. However the percentage of error for the single sonobuoy processing show severe degradation as it goes down to 78%. These results demonstrate the superior performance that can be obtained when utilizing array of GPS DIFAR sonobuoys.

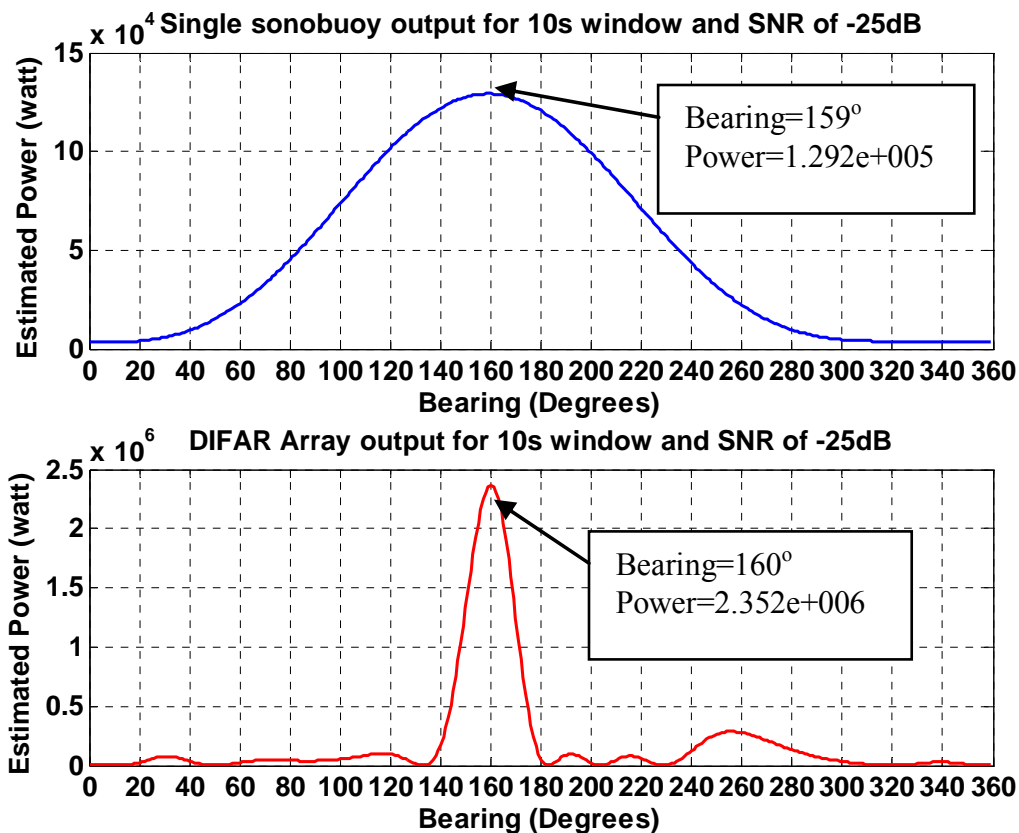


Figure 4.5a. A sample of Bartlett Beamforming output ((DOA=160°, d=10m, SNR=-25dB) for single DIFAR sonobuoy (top panel) and ULA of DIFAR sonobuoys (bottom panel)

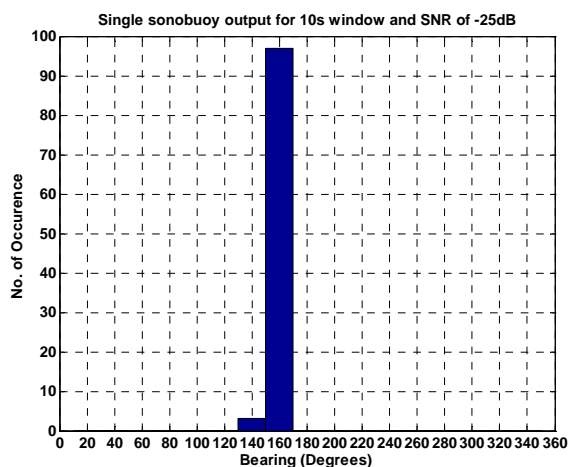


Figure 4.5b. Output of Monte Carlo simulations for single DIFAR sonobuoy ((DOA=160°, SNR=-25dB)

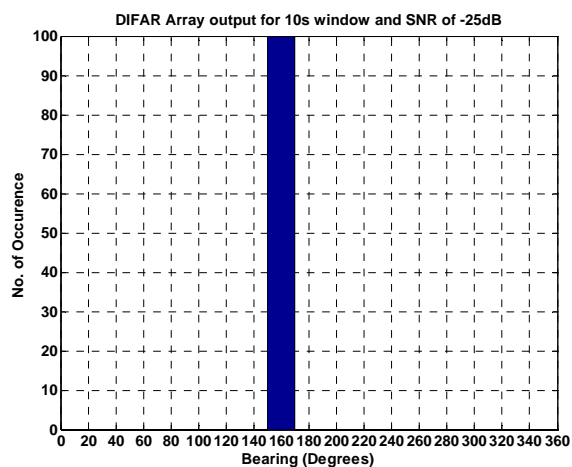


Figure 4.5c. Output of Monte Carlo simulations for ULA of DIFAR sonobuoys ((DOA=160°, d=10m, SNR=-25dB)

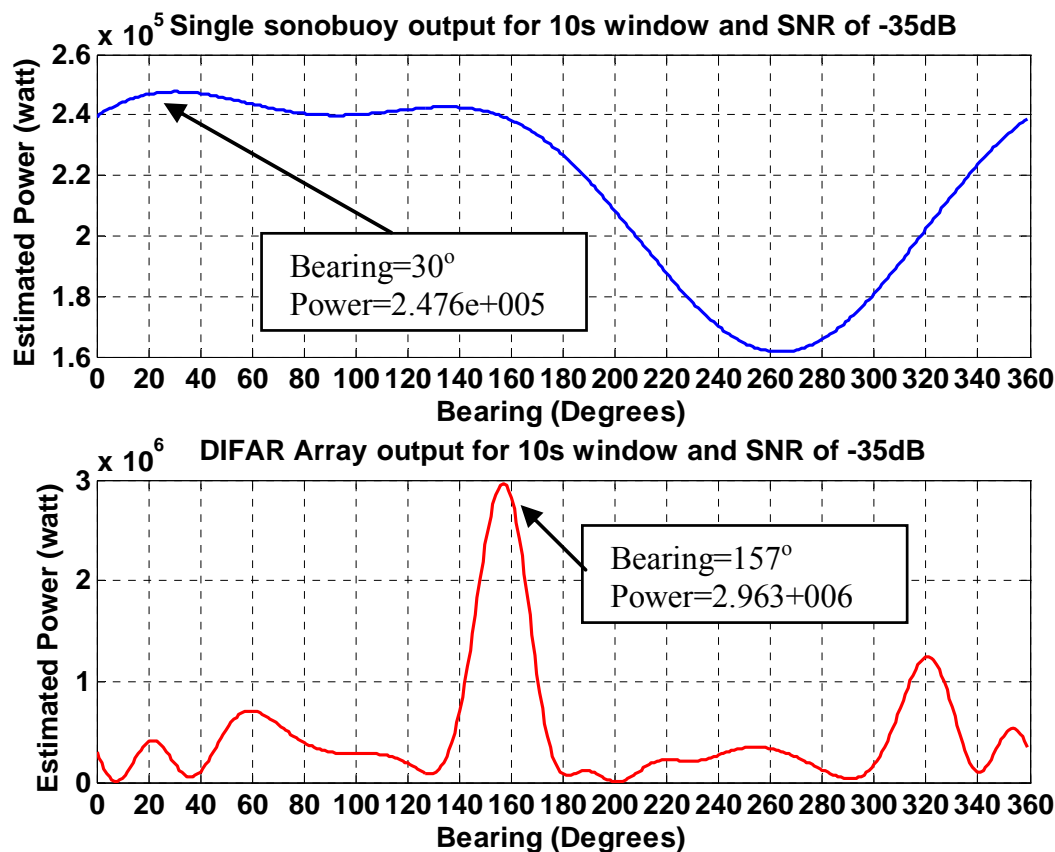


Figure 4.6a. A sample of Bartlett Beamforming output ((DOA=160°, d=10m, SNR=-35dB) for single DIFAR sonobuoy (top panel) and ULA of DIFAR sonobuoys (bottom panel)

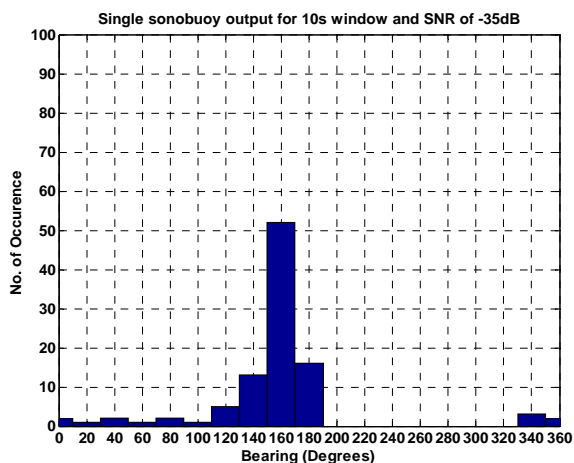


Figure 4.6b. Output of Monte Carlo simulations for single DIFAR sonobuoy ((DOA=160°, SNR=-35dB)

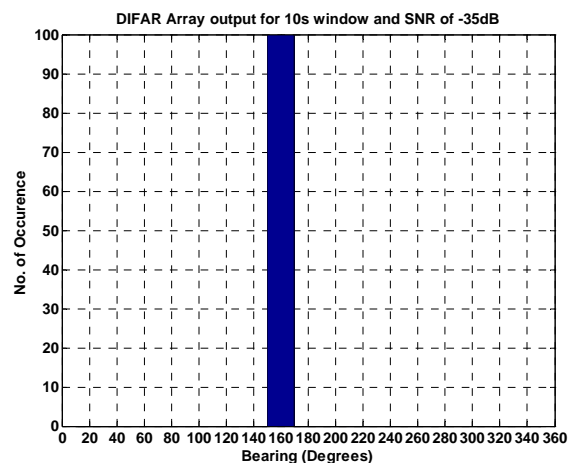


Figure 4.6c. Output of Monte Carlo simulations for ULA of DIFAR sonobuoys ((DOA=160°, d=10m, SNR=-35dB)

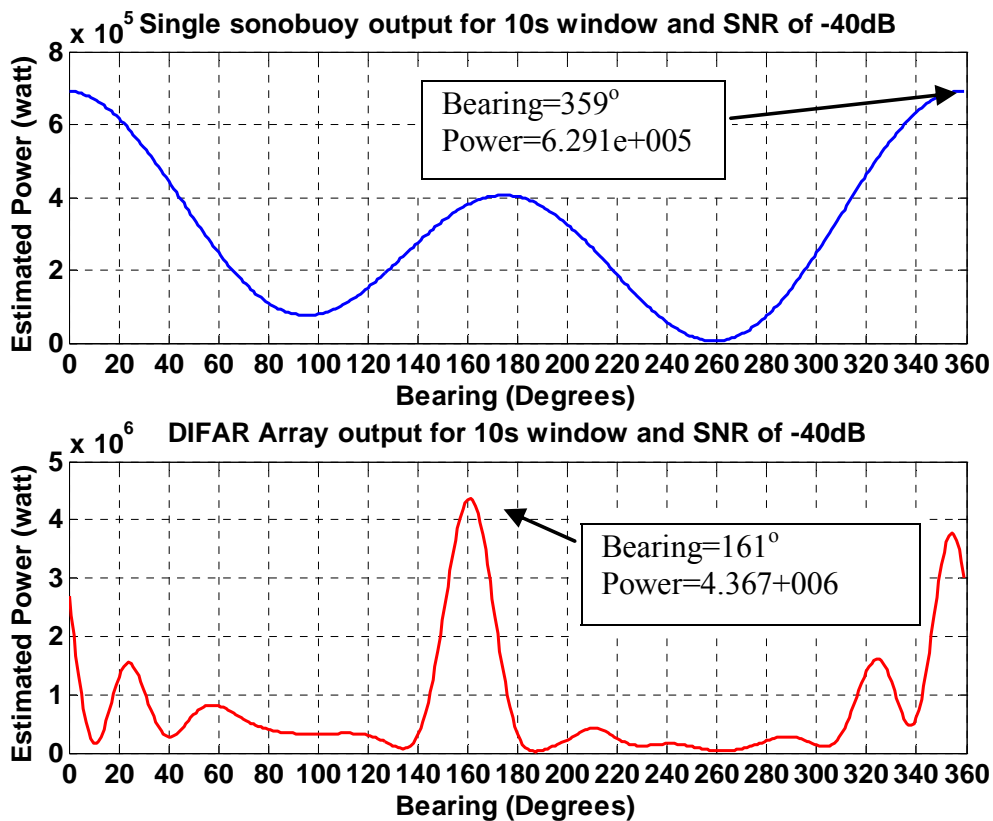


Figure 4.7a. A sample of Bartlett Beamforming output ((DOA=160°, d=10m, SNR=-40dB) for single DIFAR sonobuoy (top panel) and ULA of DIFAR sonobuoys (bottom panel)

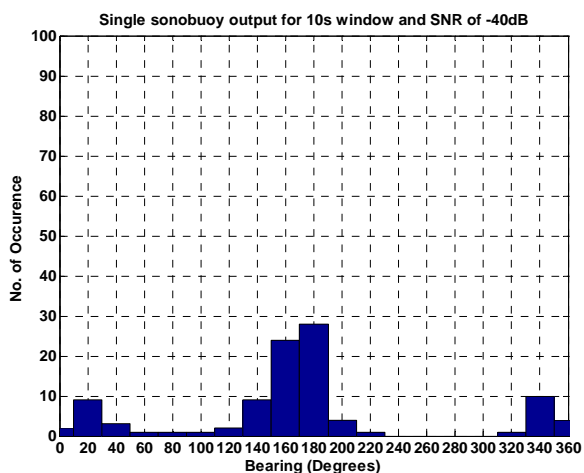


Figure 4.7b. Output of Monte Carlo simulations for single DIFAR sonobuoy ((DOA=160°, SNR=-40dB)

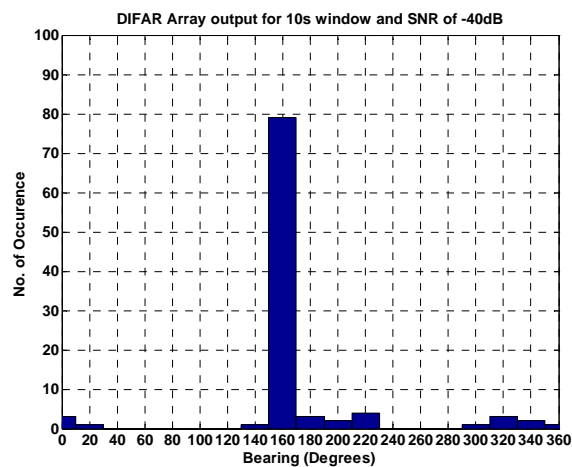


Figure 4.7c. Output of Monte Carlo simulations for ULA of DIFAR sonobuoys ((DOA=160°, d=10m, SNR=-40dB)

4.2.4.2 ULA of DIFAR Sonobuoys spaced 50 meters apart

The stability of system operation with such arrangement for DIFAR sonobuoys becomes questionable. Basically the distance between the main lobe and the first side lobe decreases significantly as shown in Figure 4.3d. This makes the system more susceptible to errors. Figures 4.8, 4.9 and 4.10 show a sample of the results obtained for processing ULA of DIFAR sonobuoys versus single processing. It is clear from these figures that the level of side lobes is notably amplified although the resolution of bearing estimation is improved. This effect is not noticeable at SNR of -25 dB as the percentage of bearing estimation error is 0%. At SNR's -35dB and -40dB performance degradation appears as the percentage of error rises to 32% and 50% respectively. This value represents a relatively significant degradation in performance when compared to the error percentages of 0% and 21% obtained for the same level of SNR when DIFAR sonobuoys were spaced by 10 meters.

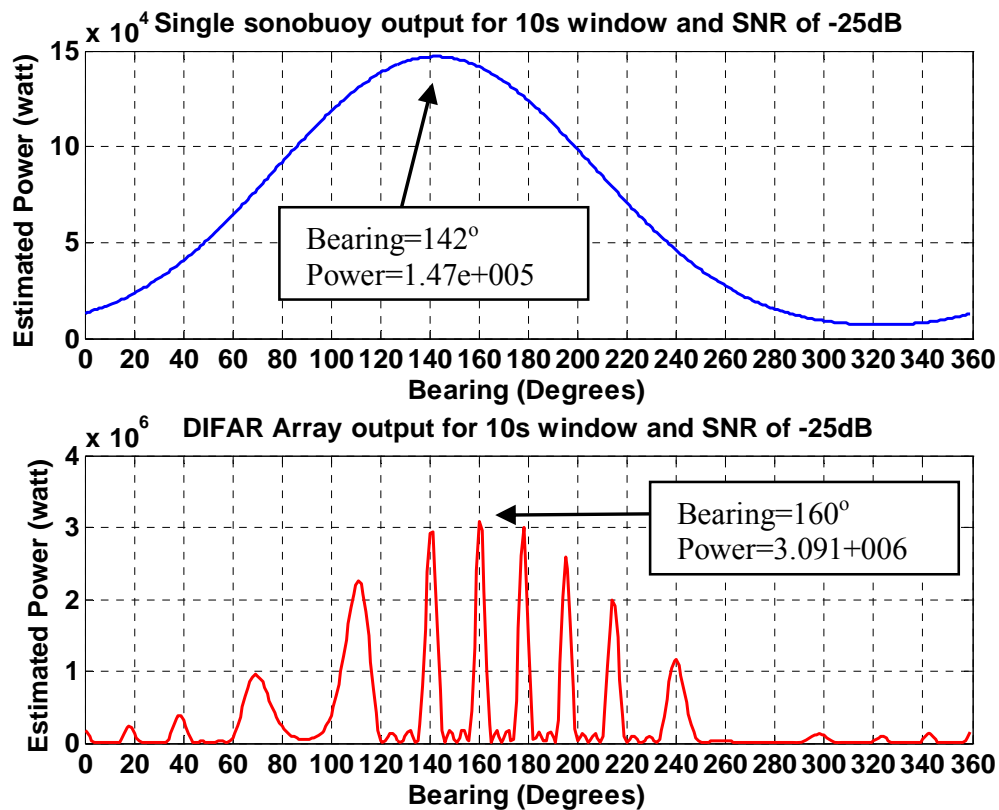


Figure 4.8a. A sample of Bartlett Beamforming output ((DOA=160°, d=50m, SNR=-35dB) for single DIFAR sonobuoy (top panel) and ULA of DIFAR sonobuoys (bottom panel)

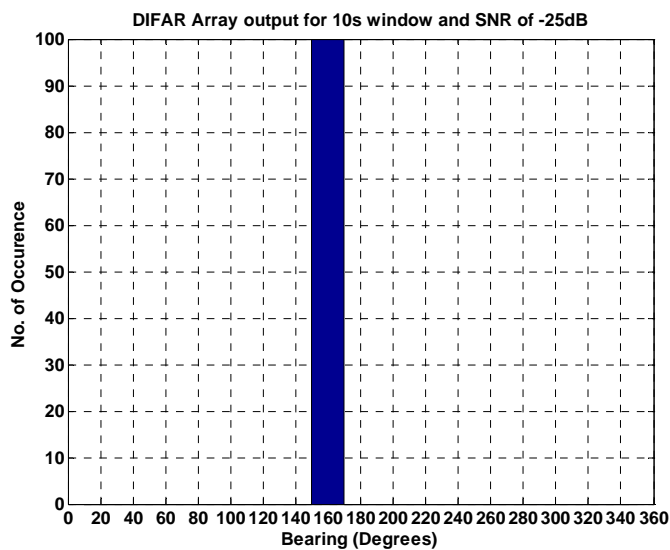


Figure 4.8b. Output of Monte Carlo simulations for ULA of DIFAR sonobuoys ((DOA=160°, d=50m, SNR=-25dB)

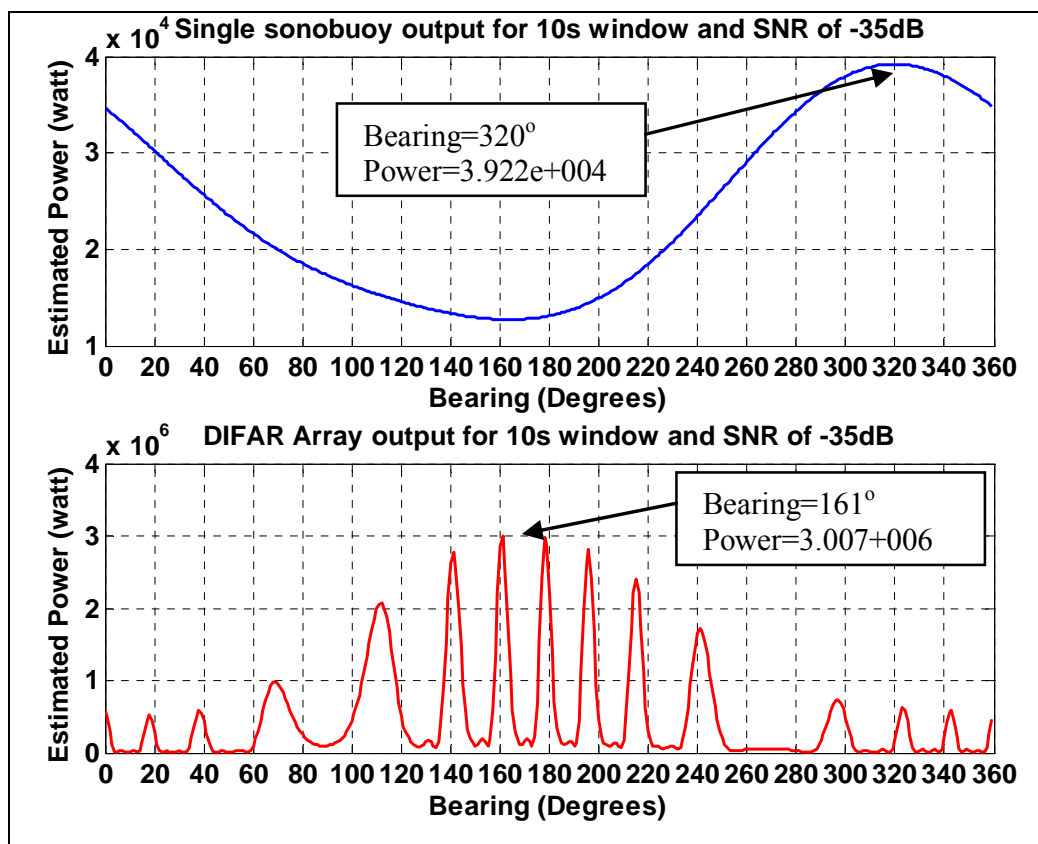


Figure 4.9a. A sample of Bartlett Beamforming output ((DOA=160°, d=50m, SNR=-35dB) for single DIFAR sonobuoy (top panel) and ULA of DIFAR sonobuoys (bottom panel)

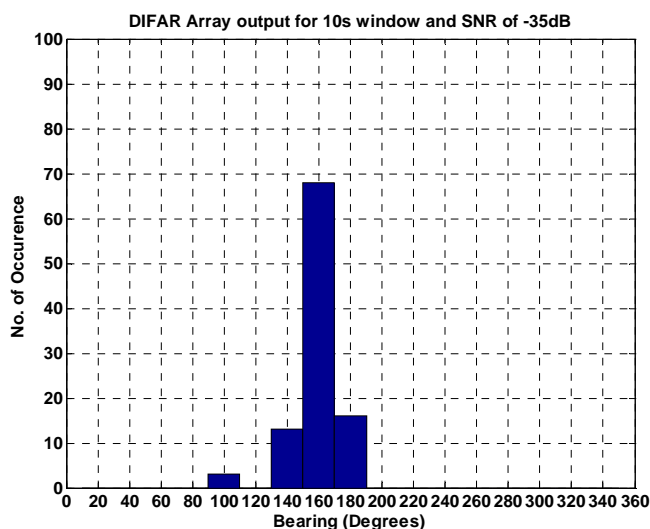


Figure 4.9b. Output of Monte Carlo simulations for ULA of DIFAR sonobuoys (DOA=160°, d=50m, SNR=-35dB)

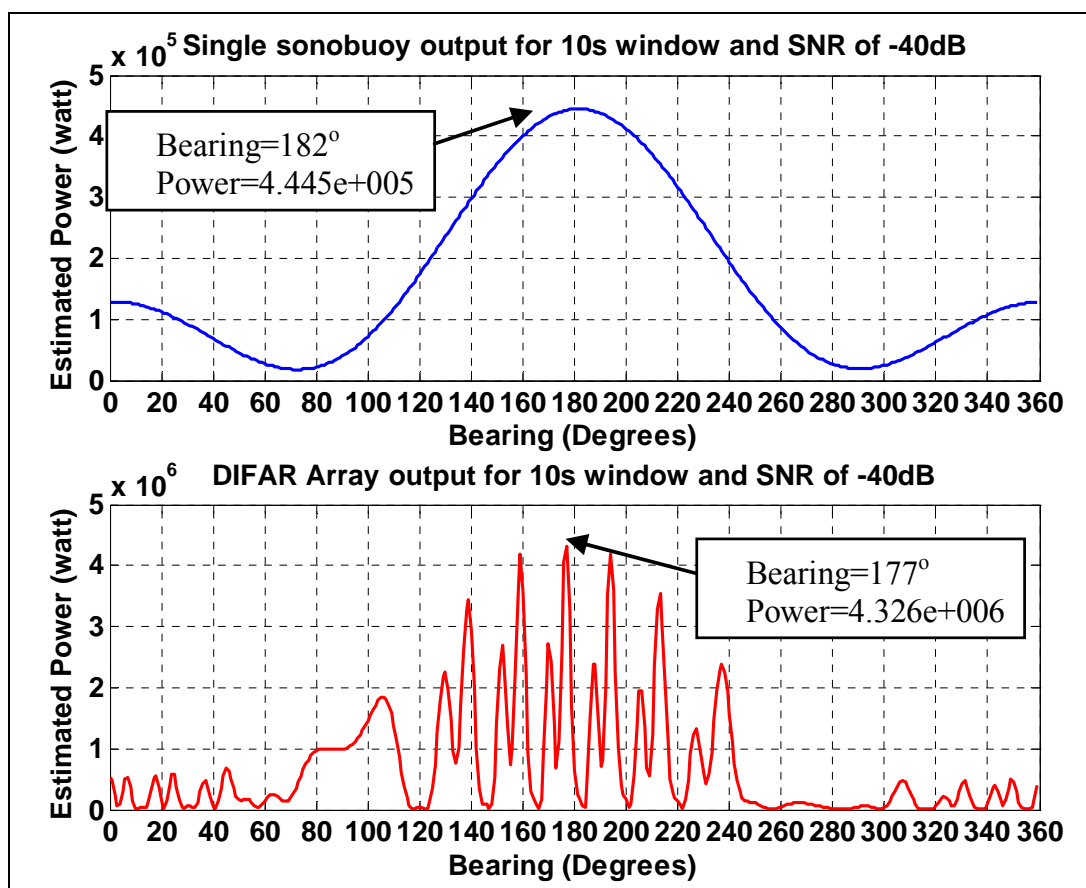


Figure 4.10a. A sample of Bartlett Beamforming output (d=50m, SNR=-40dB) for single DIFAR sonobuoy (top panel) and ULA of DIFAR sonobuoys (bottom panel)

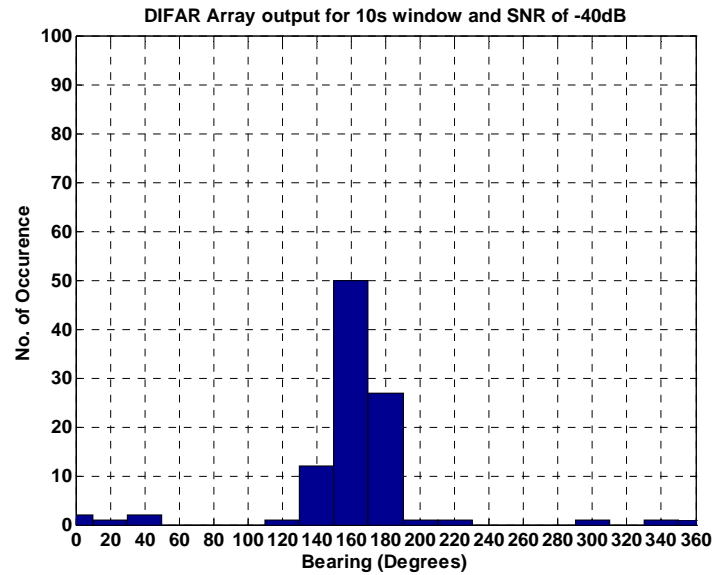


Figure 4.10b. Output of Monte Carlo simulations for ULA of DIFAR sonobuoys ((DOA=160°, d=50m, SNR=-40dB)

4.2.4.3 ULA of DIFAR Sonobuoys spaced 300m Apart

The results recorded for this part showed huge degradation in system performance. Mainly at such wide spacing the performance of single sonobuoy processing outperformed the array processing of sonobuoys group. Figures 4.11a shows an example where the performance of the single sonobuoy processing outperforms the array processing of sonobuoys group at SNR of -25dB. Moreover, the percentage of error recorded (10%) at this SNR is lower than the error percentage recorded for single sonobuoy processing (2%) at the same level of SNR. The system vulnerability increases at lower SNRs. This can be observed in Figures 4.12 and 4.13 where the system shows higher values of errors. In addition the range of errors in case of -40 dB SNR extends to cover the whole DOA possible values.

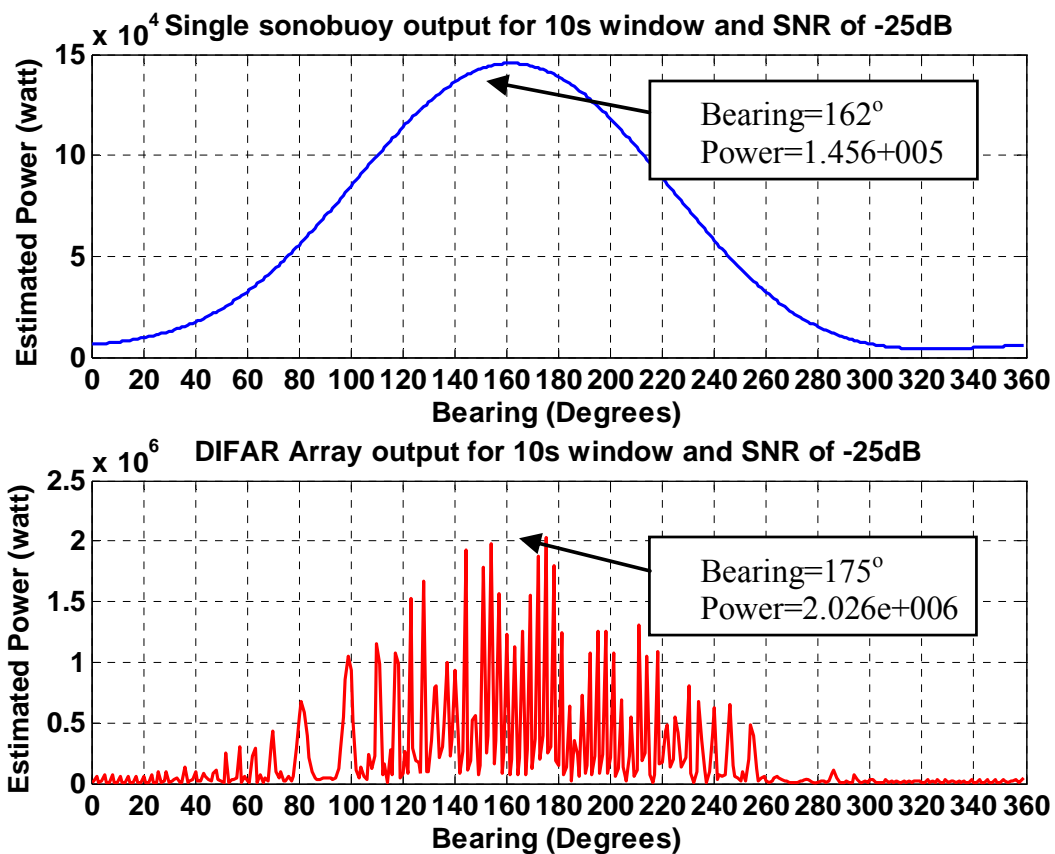


Figure 4.11a. A sample of Bartlett Beamforming output ((DOA=160°, d=300m, SNR=-25dB) for single DIFAR sonobuoy (top panel) and ULA of DIFAR sonobuoys (bottom panel)

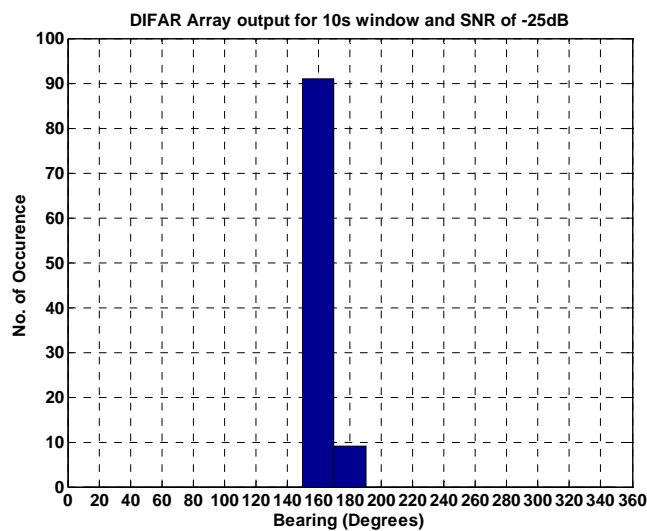


Figure 4.11b. Output of Monte Carlo simulations for ULA of DIFAR sonobuoys ((DOA=160°, d=300m, SNR=-25dB)

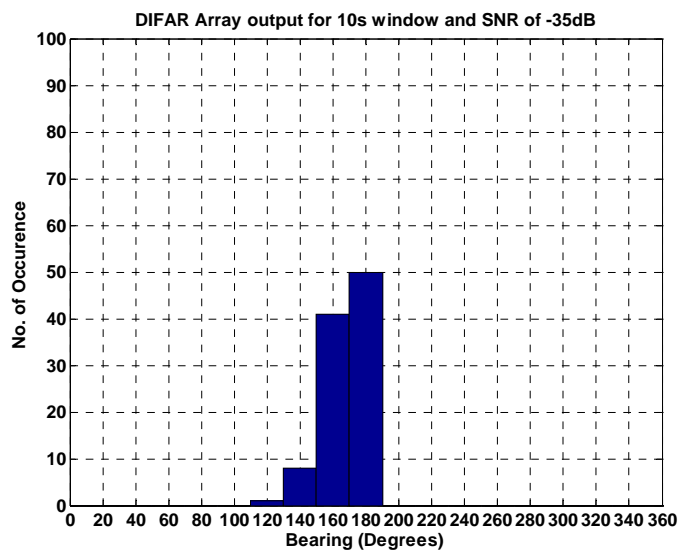


Figure 4.12. Output of Monte Carlo simulations for ULA of DIFAR sonobuoys ((DOA=160°, d=300m, SNR=-35dB)

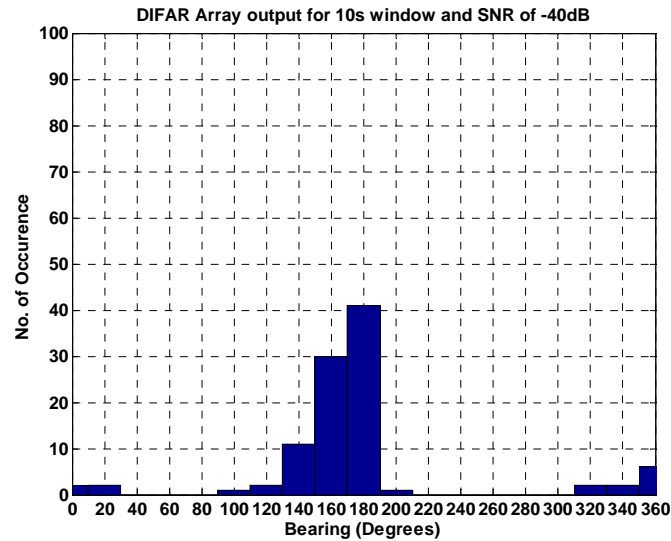


Figure 4.13. Output of Monte Carlo simulations for ULA of DIFAR sonobuoys ((DOA=160°, d=300m, SNR=-40dB)

4.3 Processing arbitrary array of DIFAR sonobuoys:

The environmental conditions of oceans are very likely to continuously cause irregular changes in the locations of the GPS sonobuoys. This results in a non-uniform array of sonobuoys. In this research the radiation pattern for the non-uniform array of DIFAR sonobuoys was obtained in similar fashion to the linear array of DIFAR sonobuoys (i.e the radiation pattern resulting from the product of the steering vector of the non-uniform array and the normalized Fourier Transform of the received signal arriving from the direction θ_0). The radiation pattern equation for the non-uniform array of DIFAR sonobuoys did not have a simplified form as equation 4.8 as it comprises all the irregularities which can be produced at any location.

For the case study of array constellation shown in Figure 4.14a, the normalized Fourier Transform of the received signal arriving from direction θ_0 is give by:

$$\Phi = [1 \quad \sin \theta_0 \quad \cos \theta_0 \quad \exp\{j2\pi(d_1 \sin \theta_0 + d_2 \cos \theta_0)/\lambda\} \quad \exp\{j2\pi(d_1 \sin \theta_0 + d_2 \cos \theta_0)/\lambda\} \sin \theta_0 \\ \exp\{j2\pi(d_1 \sin \theta_0 + d_2 \cos \theta_0)/\lambda\} \cos \theta_0 \quad \exp\{j2\pi(2d_1 \sin \theta_0 + d_3 \cos \theta_0)/\lambda\} \\ \exp\{j2\pi(2d_1 \sin \theta_0 + d_3 \cos \theta_0)/\lambda\} \sin \theta_0 \quad \exp\{j2\pi(2d_1 \sin \theta_0 + d_3 \cos \theta_0)/\lambda\} \cos \theta_0 \\ \exp\{j2\pi(3d_1 \sin \theta_0 + d_4 \cos \theta_0)/\lambda\} \quad \exp\{j2\pi(3d_1 \sin \theta_0 + d_4 \cos \theta_0)/\lambda\} \sin \theta_0 \\ \exp\{j2\pi(3d_1 \sin \theta_0 + d_4 \cos \theta_0)/\lambda\} \cos \theta_0]^T$$

4.13

The steering vector is given by

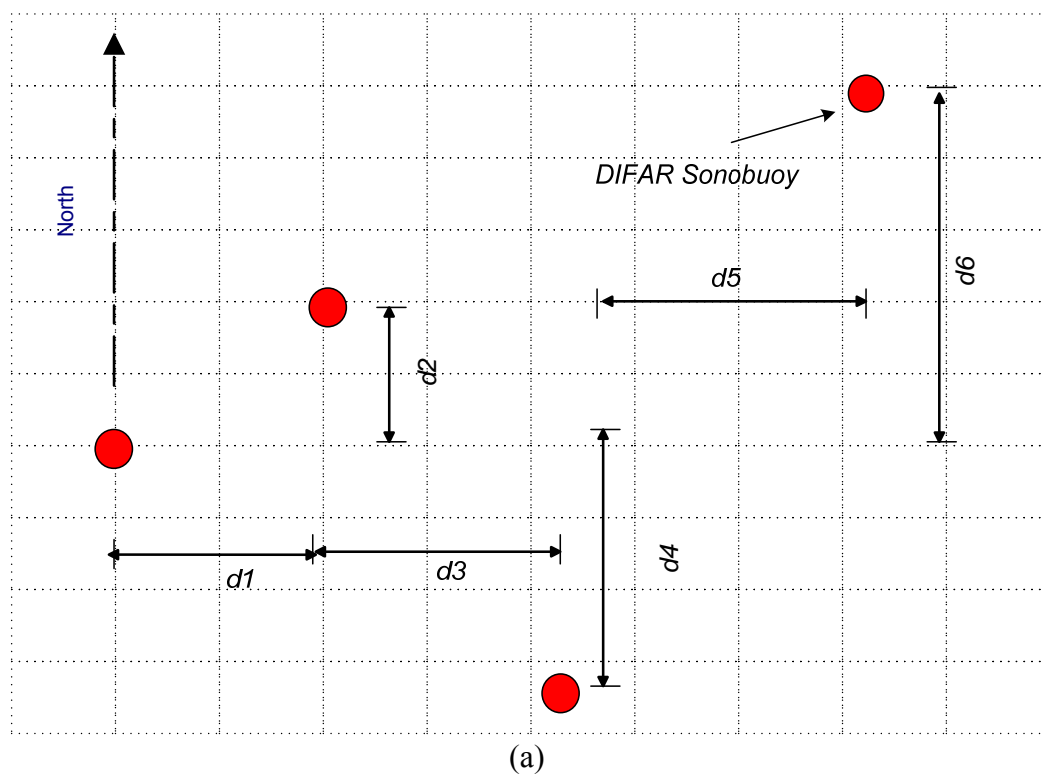
$$B = [1 \quad \sin \theta \quad \cos \theta \quad \exp\{j2\pi(d_1 \sin \theta + d_2 \cos \theta)/\lambda\} \quad \exp\{j2\pi(d_1 \sin \theta + d_2 \cos \theta)/\lambda\} \sin \theta \\ \exp\{j2\pi(d_1 \sin \theta + d_2 \cos \theta)/\lambda\} \cos \theta \quad \exp\{j2\pi(2d_1 \sin \theta + d_3 \cos \theta)/\lambda\} \\ \exp\{j2\pi(2d_1 \sin \theta + d_3 \cos \theta)/\lambda\} \sin \theta \quad \exp\{j2\pi(2d_1 \sin \theta + d_3 \cos \theta)/\lambda\} \cos \theta \\ \exp\{j2\pi(3d_1 \sin \theta + d_4 \cos \theta)/\lambda\} \quad \exp\{j2\pi(3d_1 \sin \theta + d_4 \cos \theta)/\lambda\} \sin \theta \\ \exp\{j2\pi(3d_1 \sin \theta + d_4 \cos \theta)/\lambda\} \cos \theta]^T$$

4.14

4.3.1 Simulation work

In this part, an arbitrary array of 4 DIFAR sonobuoys is simulated. The inter-element spacing values on the horizontal axis (east-west direction) are set to random selected values. Also the elements were shifted on the vertical axis (north-south direction) with random values. The acoustic source is similar to the one simulated in the test of linear array of DIFAR sonobuoys with the same features including a 10 second window size. The performance of arbitrary array processing is compared to single sonobuoy processing for SNR of -35 dB. The noise simulated is simulated in similar fashion to the noise simulated in the simulation of Linear DIFAR array tests. Figure 4.14 and 4.15 show an illustration of the two simulated arbitrary arrays of DIFAR sonobuoys. For the first arbitrary array, the inter-element spacing of the horizontal axes are $d1=50m$,

$d_3=62m$ and $d_5=70m$. The values of $d_2=40m$, $d_4=70$ and $d_6=100m$. The second arbitrary array is similar to the first one except that $d_2=70m$ and $d_4=40m$. The radiation pattern can be obtained by using equations 4.12 and 4.13 Figures 4.14b and 4.15b illustrates the radiation patterns obtained for the two set values of d_1 , d_2 , d_3 , d_4 , d_5 and d_6 .



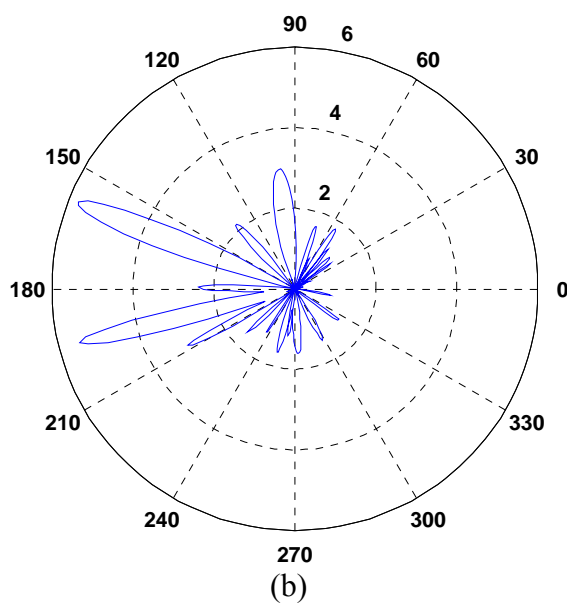
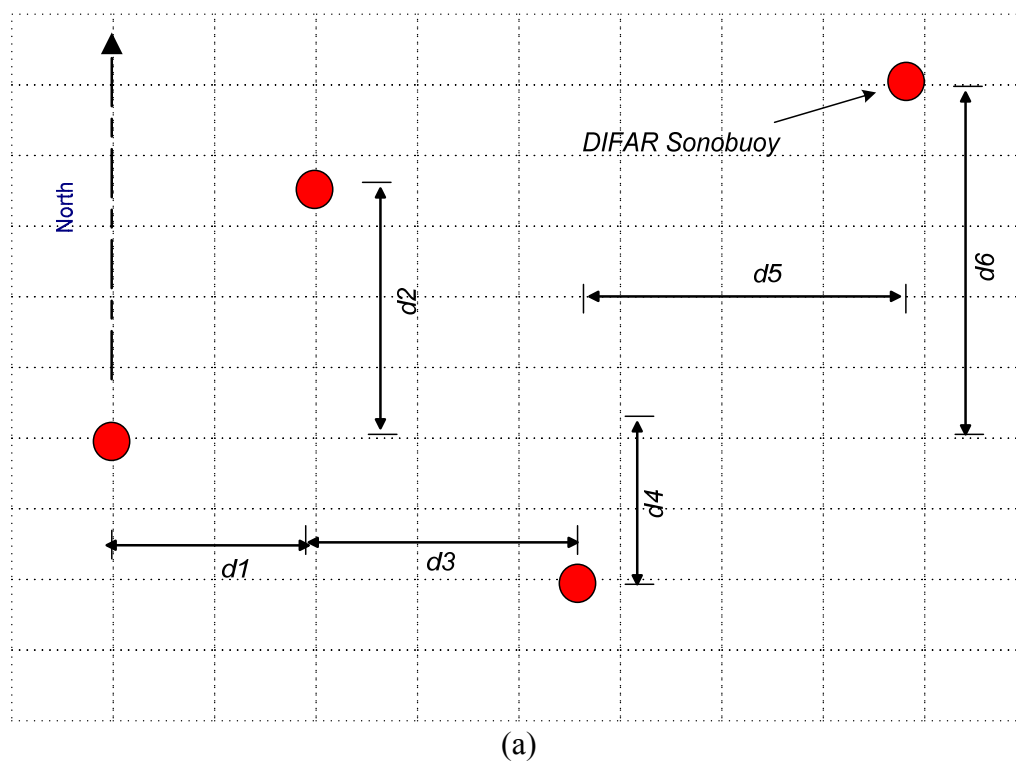


Figure 4.14 (a) Irregular array of DIFAR sonobuoys, (b) Radiation pattern for a source with a bearing of 160 degrees impinging an irregular array of 4 DIFAR sonobuoys with $d_1=50$ m, $d_2=40$ m, $d_3=55$ m, $d_4=70$, $d_5=58$ and $d_6=100$ m.



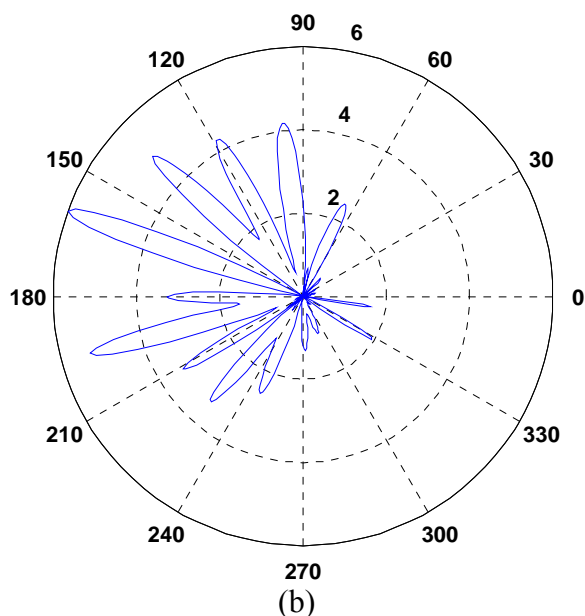


Figure 4.15 (a) Irregular array of DIFAR sonobuoys , (b) Radiation pattern for a source with a bearing of 160o impinging an irregular array of 4 DIFAR sonobuoys with $d_1=50$ m, $d_2=70$ m, $d_3=55$ m, $d_4=40$, $d_5=58$ and $d_6= 100$ m.

4.3.2 Results and discussion

The radiation pattern of the arbitrary arrangement of sonobuoys shown in Figures 4.14b and 4.15b demonstrate that the irregularity in the arrangement of sonobuoys can considerably change the array radiation pattern. Although the radiation pattern for the second arbitrary array exhibits more side lobes, the difference between the highest level of side lobe and the main lobe for the second arbitrary array is slightly lower than that of the first arbitrary array. The results recorded for the response of irregular array to different levels of SNR confirmed the observation depicted from its radiation pattern. Figures 4.16 ad 4.17 show the results obtained for SNR of -35db. Figure 4.16b shows the percentage of error obtained at SNR -35db (26%) which is still below that of single sonobuoy processing (50%) shown before at Figure 4.6b. The error percentage for the

arbitrary array of sonobuoys is close to the error percentage shown in Figure 4.9b (32%) for ULA of sonobuoys spaced at 50 meters apart for the same level of SNR. This suggests that arbitrary arrays of DIFAR sonobuoys can still provide superior results to the single sonobuoy processing. Moreover, the performance of arbitrary array is further enhanced by a small change in the arrangement of the array elements. In this case the arbitrary array shows a superior performance with 10% error as shown in Figure 4.17b. This means that arbitrary array can provide better performance than ULA. However the radiation pattern of the arbitrary array is very sensitive to the locations of the array elements and can provide unpredictable high side lobes which in turn can jeopardize the bearing estimation process.

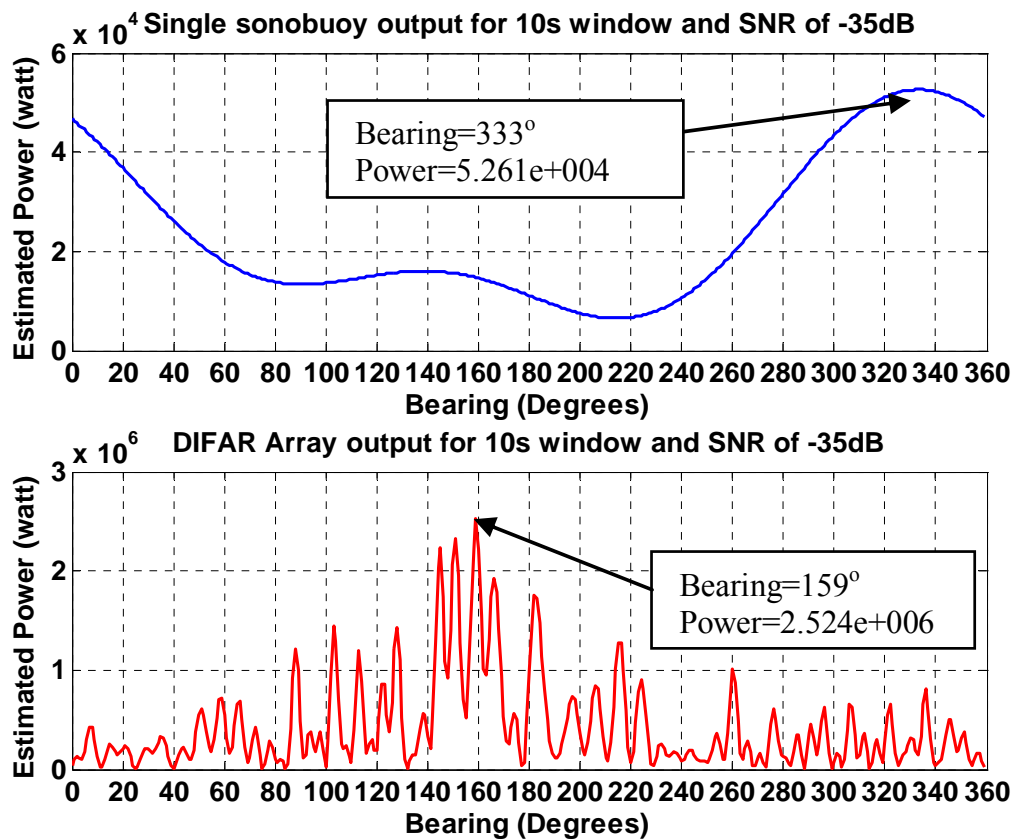


Figure 4.16a. A sample of Bartlett Beamforming output (DOA=160° SNR=-35dB) for single DIFAR sonobuoy (top panel) and Arbitrary of DIFAR sonobuoys shown in Figure 4.14 (bottom panel)

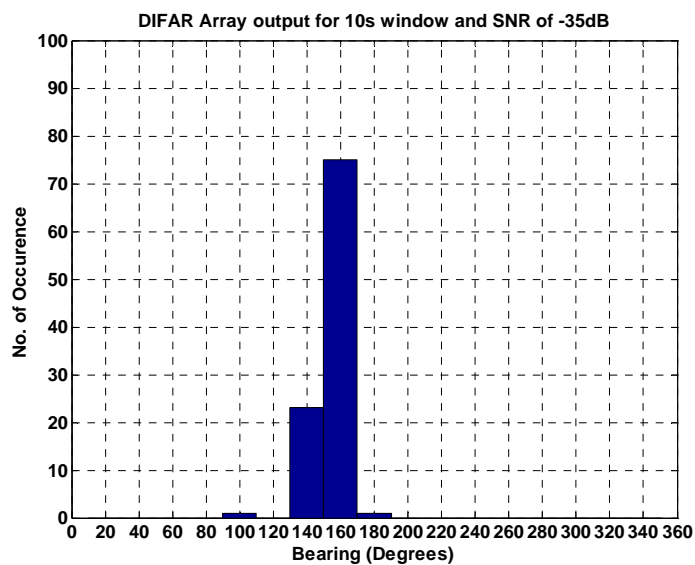


Figure 4.16b. Output of Monte Carlo simulations for the Arbitrary array of DIFAR sonobuoys shown in Figure 4.14 (DOA=160° SNR=-35 dB)

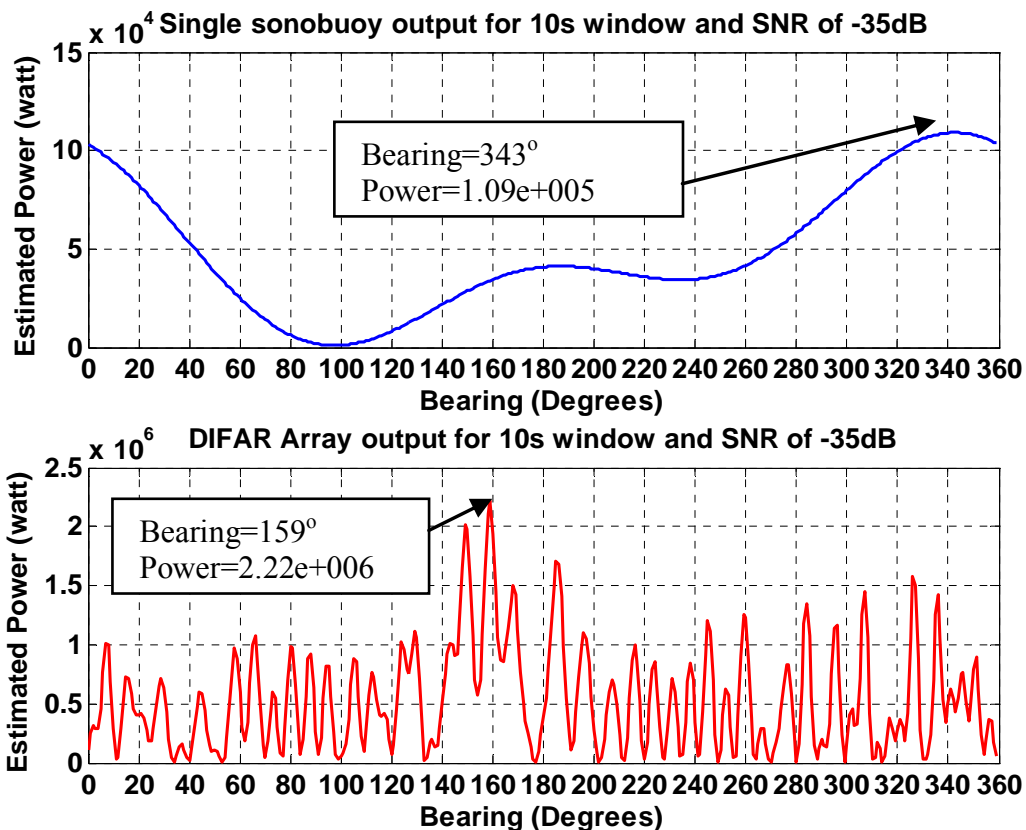


Figure 4.17a. A sample of Bartlett Beamforming output (DOA=160° SNR=-35dB) for single DIFAR sonobuoy (top panel) and Arbitrary of DIFAR sonobuoys shown in Figure 4.15 (bottom panel)

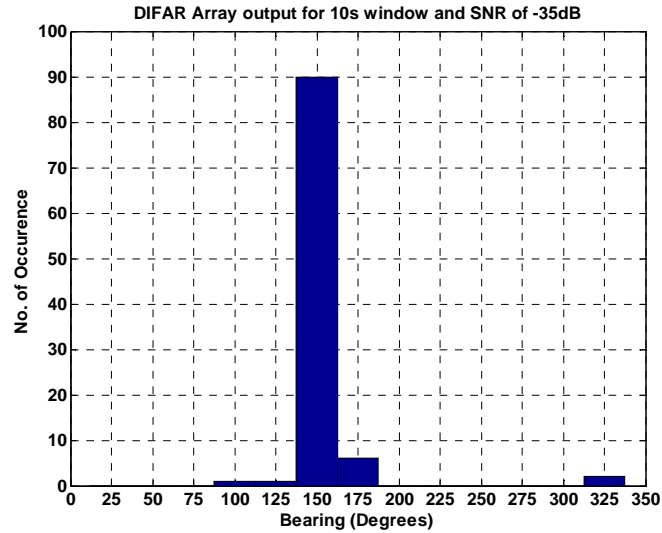


Figure 4.17b. Output of Monte Carlo simulations for the Arbitrary array of DIFAR sonobuoys shown in Figure 4.15 (DOA=160° SNR=-35 dB)

4.4 Conclusion

This chapter discussed the merits and limitation of a method suggested for array processing for a group of DIFAR sonobuoys. The steering vector for the array of DIFAR sonobuoys was derived as well as the radiation pattern of the array of sonobuoys. This was used to suggest a criterion for selecting the maximum spacing value between the DIFAR sonobuoys which showed that for guaranteed system stability the criterion obtained is close to the omni-directional array criterion. Nevertheless, a system with acceptable stability can be obtained with inter-element spacing exceeding the critical value of spacing with few meters. The array processing showed significant enhancement of system performance especially at SNR -35db and -40db which are considered

relatively very low SNR levels. The system of 10 meter spacing was able to provide a completely robust operation with 0% percentage error. Superior performance was also obtained at a SNR of -40 dB with of error percentage of 21%. System performance degraded with the increase in spacing values. This can be considered the main limitation on applying array processing to a group of free floating sonobuoys. Moreover the irregularity in the sonobuoys array arrangement provided some performance enhancement with 10% error at -35 dB DNR. This can be considered a limited improvement since the obtained performance is very sensitive to the changes in the locations of array elements.

In general, it can be concluded that the array processing for a group of DIFAR sonobuoys provides noticeable enhancement to system accuracy and robustness. For ULA, the only limitation is imposed by the spacing between the DIFAR sonobuoys which can range from few meters to hundreds of meters that in turn provides unreliable performance for bearing estimation. Arbitrary array processing has an additional limitation which is the sensitivity of system performance to any changes in array arrangement. This research has further investigated these problems and explored several methods to mitigate the above limitation. Some new methods and approaches have been developed in this thesis and are presented in the next two chapters.

Chapter Five: A New DOA Estimation Approach for widely spaced arrays using Frequency Beamforming and ANN

Beamforming using an array of sensors is one of the key methods of DOA estimation. Most of the DOA estimation methods employing beamforming impose limitations on the inter-element spacing between the array sensors. The maximum permissible distance is half the wavelength of the minimum frequency of the spectrum of interest. It was proved that exceeding the maximum distance generates grating lobes which lead to defective DOA estimation. In some cases it is not possible to comply with the array inter-element distance condition especially in cases of high frequency narrowband sources. In this case the array is spatially aliased. This research introduces a new method for processing spatially aliased arrays. The proposed approach employs a frequency beamforming technique aided with ANN. ANN is employed to resolve DOA ambiguity caused by spatial aliasing. The proposed method was tested using acoustic level simulated data and results show that the proposed method enables the processing of aliased arrays with different accuracies based on SNR and the inter-element distances of the aliased array.

Spatial aliasing in uniformly spaced arrays is analogous to the time aliasing problem [Hinich78]. In spectral analysis the sampling interval must be less than half the smallest time period to avoid aliasing [Oppenheim98]. Similarly, spatial aliasing in uniformly spaced arrays can be avoided by ensuring that the spacing between array

elements is less than half the minimum wavelength of the received spectrum [Skolnik80]. This half wavelength spacing between array elements is mandatory to avoid ambiguities in DOA estimation.

It has been reported that the half wavelength condition might not be always feasible [Zoltowski94]. For example in case of high upper end frequencies of observed spectrum, the elements become closely spaced [Zoltowski94]. This causes mutual coupling between array elements and provides poor resolution for DOA. The resolution capability and estimator accuracy of any arrival angle estimation algorithm is proportional to the aperture length measured in units of wavelengths. Moreover in some applications it is not possible to arrange the array sensors so that their inter-element spacing is less than half the minimum wavelength of the spectrum of interest. The spatial aliasing makes the system inappropriate for DOA estimation using conventional bearing estimation techniques.

ANN have proven their ability as an efficient engineering tool for mapping complex nonlinear behavior, especially when there is significant scatter in the modeling data [Tsoukalas97]. ANN has been applied for the problem of DOA estimation (see El-Zooghby97, Du02 and Gotsis09). The examined array structures in [El-Zooghby97 and Gotsis09] were designed with inter-element spacing less than half the wavelength of the upper bound frequency of interest. Applying the approaches proposed in [El-Zooghby97 and Gotsis09] to the problem of DOA for spatially aliased arrays might provide a non robust solution due to the DOA ambiguity. This ambiguity might cause steering to the wrong direction which is masking the correct one.

Simplifying the parameters introduced to the artificial neural network provides a more robust DOA estimation. This can be achieved by applying an adequate DOA estimation algorithm combined with ANN to detect the DOA.

To overcome the drawbacks of traditional beamformers, non conventional approach to adaptive beamforming are adopted in this research for underwater target detection and localization. The frequency based adaptive beamforming algorithm [Ziomek89] was chosen since it suits the problem of DOA estimation. This method doesn't require directional information and at the same time provides iterative adaptive bearing estimation for all frequency components of the received signal

The selected method is a modified complex least-mean-square (LMS) adaptive bearing estimation which is based on spectrum analysis of the received signal. It mainly processes the output frequency domain data from all elements in a planar array and provides estimates of the bearing of the incident plane wave fields [Ziomek89]. This was augmented by ANN to generate a non linear relation between DOA estimation parameters obtained from aliased array processing and the correct parameters.

This research aims at: 1) Exploring the application of FB method for DOA estimation using spatially aliased arrays; 2) Identifying the effect of spatial aliasing on the FB method; 3) Identifying the parameters required to resolve the aliasing effect; 4) Deriving the relations governing those parameters together with their possible range of values; 5) Designing ANN to estimate the values of the spatial aliasing resolution parameters; 6) Integrating FB and ANN to introduce a module that incorporates the benefits of FB and ANN to estimate DOA using aliased array of sensors and 7) Examining the proposed module by using acoustic level data simulation.

5.1 Frequency domain adaptive beamforming for planar arrays

The algorithm employed in this research is based on Frequency domain adaptive beamforming method for planar arrays [Ziomek89]. The algorithm is a modified complex LMS adaptive algorithm that processes the output complex frequency domain data from $M \times N$ elements arranged in a planar array in order to provide estimate of the bearing of incident plane wave fields. Least mean square solution is achieved through the minimization of an error factor. The error factor is defined as the difference between the signal received by the element at the array center and the estimated signal. The algorithm $M \times N$ structure requires an odd number of sensors in both X and Y directions in order to perform properly [Ziomek89]. Also it assumes that the array is composed of equally spaced point source elements lying in the XY plane, where M and N are the total odd number of elements in the X and Y directions respectively.

The received signal values utilized in error calculation are obtained from the DFT of received signal with respect to the time index. The complex frequency domain samples at array elements are given by:

$$R(q, m, n) = Y(q, m, n) + Z(q, m, n) \quad 5.1$$

$$q = -L', \dots, 0, \dots, L',$$

$$m = -M', \dots, 0, \dots, M',$$

$$n = -N', \dots, 0, \dots, N',$$

$Y(q, m, n)$ and $Z(q, m, n)$ are the frequency spectrum of the deterministic signal and random receiver noise, respectively.

$$L' = (L-1)/2, \quad M' = (M-1)/2, \quad N' = (N-1)/2, \quad \text{And} \quad L \geq 2K + 1 \quad 5.2$$

L is the total number of time samples.

The acoustic field incident upon the planar array is assumed to be a general plane-wave. Therefore the frequency spectrum of the deterministic signal $Y(q, m, n)$ is represented by [Ziomek89]:

$$Y(q, m, n) = Y(q, 0, 0) \exp(\mp j 2\pi q f_o u_o m d_x / c) \times \exp(\mp j 2\pi q f_o v_o n d_y / c) \quad 5.3$$

Where

d_x and d_y are the interelement spacing in meters in the X and Y directions, respectively and c is the speed of sound in meters per second.

u_o and v_o Are the dimensionless direction cosines with respect to the X and Y axes, respectively.

$$u_o = \sin \theta_o \cos \psi_o$$

$$v_o = \sin \theta_o \sin \psi_o \quad 5.4$$

θ_o and ψ_o are the depression and bearing angles respectively.

The algorithm uses a planar array to estimate both angles θ_o and ψ_o for each harmonic q present in the multiple incident plane-wave fields via frequency domain adaptive beamforming. This research focuses on 2D direction of arrival estimation. Thus the proposed algorithm is only used to estimate the bearing ψ_o .

The signal direction of arrival estimation in 2D is based on processing the output complex frequency domain data $R(q, m, n)$ from all $M \times N$ elements in the planar array.

The algorithm defines the complex estimation error as [Ziomek89]:

$$e(q) \triangleq s(q) - \hat{s}(q) \quad 5.5$$

Where $s(q)$ is defined as the reference signal and $\hat{s}(q)$ is the estimated signal

The estimated signal is defined by [Ziomek89]:

$$\hat{s}(q) = w^T(q)Z(q)w(q)/(LMN) \quad 5.6$$

Where $w(q)$ is the weight vector

$$w(q) \triangleq \begin{bmatrix} c(q) \\ d(q) \end{bmatrix} \quad 5.7$$

$$\text{And } Z(q) = A^T R(q) B \quad 5.8$$

$$\text{Where } A = \begin{bmatrix} I & 0 \\ M \times M & M \times N \end{bmatrix} \text{ and } B = \begin{bmatrix} I & 0 \\ M \times M & M \times N \end{bmatrix} \quad 5.9$$

$c(q)$ and $d(q)$ are the $M \times 1$ and the $N \times 1$ complex weigh vectors in the X and Y directions respectively given by [Ziomek89]:

$$c(q) = [c(q, -M') \quad \dots \quad c(q, 0') \quad \dots \quad c(q, M')]^T$$

$$d(q) = [d(q, -N') \quad \dots \quad d(q, 0') \quad \dots \quad d(q, N')]^T$$

$R(q)$ is M X N complex data matrix.

$$R(q) = \begin{bmatrix} R(q, -M', -N') & \dots & R(q, -M', 0) & \dots & R(q, -M', N') \\ \vdots & & \vdots & & \vdots \\ R(q, 0, -N') & \dots & R(q, 0, 0) & \dots & R(q, 0, N') \\ \vdots & & \vdots & & \vdots \\ R(q, M', -N') & \dots & R(q, M', 0) & \dots & R(q, M', N') \end{bmatrix} \quad 5.10$$

The complex weight vector that minimizes the mean-square error $E\{|e(q)|^2\}$ is given by [Ziomek89]:

$$w_{i+1}(q) = w_i(q) + 2\mu e_i(q) [Z(q) + Z^T(q)]^* w_i^*(q) \quad 5.11$$

Where

$e_i(q) = s(q) - \hat{s}_i(q)$ is the estimation error after the i th iteration, $\hat{s}_i(q) = w_i^T(q)Z(q)w_i(q)/(LMN)$ is the estimate of $s(q)$ after the i th iteration and μ is step size.

The obtained steady state complex vectors are processed [Ziomek89] to obtain estimates of the direction cosines $\hat{u}_o^{LS}(q)$ and $\hat{v}_o^{LS}(q)$. This starts by obtaining the real wrapped phase weights from the steady state complex weight vectors using the following relation

$$\begin{aligned} c_{ss}(q, m) &= \exp[+j\theta_{ss}(q, m)] \\ d_{ss}(q, n) &= \exp[+j\phi_{ss}(q, n)] \end{aligned} \quad 5.12$$

$\theta_{ss}^w(q, n)$ and $\phi_{ss}^w(q, n)$ are the real, "wrapped" phase weights.

The relation between the estimates of the direction cosines and the real wrapped phase weights is given by:

$$\begin{aligned} \theta_{ss}^w(q, m) &= 2\pi q f_0 u_0(q) m d_x / c \\ \phi_{ss}^w(q, n) &= 2\pi q f_0 u_0(q) n d_y / c \end{aligned} \quad 5.13$$

After unwrapping the phase weights, a least square estimate of the direction cosines ($\hat{u}_o^{LS}(q)$ and $\hat{v}_o^{LS}(q)$) is obtained. $\hat{u}_o^{LS}(q)$ and $\hat{v}_o^{LS}(q)$ are used to calculate the angle of arrival (AoA) $\psi_o(q)$ at each harmonic q using inverse tangent as shown in equation 11.

$$\hat{\psi}_o(q) = \tan^{-1} \left[\hat{v}_o^{LS}(q) / \hat{u}_o^{LS}(q) \right] \quad , \quad q \neq 0 \quad 5.14$$

5.2 Methodology

5.2.1 FB for spatially aliased arrays

The mathematical features of the FB method make it suitable to be oriented for the processing of spatially aliased uniform planar arrays. By analyzing the procedures of the FB algorithm it is clear that the effect of spatial aliasing appears mainly in equations 11 to 14. The ambiguity in the DOA estimation is mainly caused by the calculation of the unwrapped steady state phase weights in equations 11 and 12. The phases of the complex exponents in these two equations are confined to the values between $-\pi$ and π .

To study the effect of aliasing on the phase weights, consider a single harmonic source of frequency f_{source} . The output index q_{source} of the FFT is given by:

$$q_{source} = \frac{f_{source}}{f_0} \quad 5.15$$

At $m=n=1$, the maximum absolute values of $\theta_{ss}^w(q, n)$ and $\phi_{ss}^w(q, n)$ correspond to

$u_o = v_o = 1$. Also the minimum values of $\theta_{ss}^w(q, n)$ and $\phi_{ss}^w(q, n)$ correspond to

$u_o = v_o = -1$. To obtain a unique solution for the estimated AoA, the phase values must lie between $-\pi$ and π .

$$\left| \phi_{ss}^w(q, m) \right|_{\max} = 2 \pi f_{source} d_y / c \quad 5.16$$

This implies that

$$2 \pi f_{source} d_x / c \leq \pi \quad 5.17$$

$$\text{Since } \lambda_{source} = \frac{c}{f_{source}} \quad 5.18$$

Therefore

$$d_x \leq \frac{\lambda_{source}}{2} \quad 5.19$$

Similarly it can shown that

$$d_y \leq \frac{\lambda_{source}}{2} \quad 5.20$$

Equations 23 and 24 are the condition required to prevent phase ambiguity. This is typically the condition to prevent spatial aliasing for the uniform planar array. Spatial aliasing takes place if any of d_x and d_y are larger than $(\lambda_{source} / 2)$. The effect of spatial aliasing on the estimation of the direction cosines (u_o and v_o) is caused by the wrapped phase ambiguity. This ambiguity can be resolved by proper estimation of unwrapping parameters. These parameters and their ranges were defined using equations 17 and 19 as follows:

Considering the case of $m = n = 1$, $u_0(q_{source})$ is thus given by:

$$u_0(q_{source}) = \theta_{ss}^w(q_{source}, m) * \frac{c}{2 \pi f_{source} d_x} \quad 5.21$$

$$u_0(q_{source})|_{unwrapped} = (2 * r_x * \pi + \theta_{ss}^w(q_{source}, m)) * \frac{c}{2 \pi f_{source} d_x}, \quad 5.22$$

Where r_x is an integer value.

This can be written as

$$u_0(q_{source})|_{unwrapped} = \left(\frac{r_x \lambda_{source}}{d_x} + u_0(q_{source}) \right) \quad 5.23$$

Since $-1 \leq u_0(q_{source})|_{correct} \leq 1$

Therefore it implies that $-1 \leq \left(\frac{r_x \lambda_{source}}{d_x} + u_0(q_{source}) \right) \leq 1$ 5.24

Therefore we can obtain a range of possible values of i by using the above boundary condition. First we define the minimum and maximum possible values of I ($r_{x\max}$ and $r_{x\min}$) as follows:

$$r_{x\max} = \text{integer} \left[\frac{d_x (1 - u_0(q_{source}))}{\lambda_{source}} \right] \text{ and } r_{x\min} = -\text{integer} \left[\frac{d_x (1 + u_0(q_{source}))}{\lambda_{source}} \right] \quad 5.25$$

This implies that the range of possible values of r_x is given by:

$$r_x \in \left[\text{integer} \left(\frac{2d_x}{\lambda_{source}} \right), -\text{integer} \left(\frac{d_x}{\lambda_{source}} \right) \right] \quad 5.26$$

By following the same procedure for v_0 we get that

$$v_0(q_{source})|_{unwrapped} = \left(\frac{r_y \lambda_{source}}{d_y} + v_0(q_{source}) \right) \quad 5.27$$

Where r_y is an integer value.

The range of r_y can be derived in similar fashion as r_x shown above. Therefore

$$r_y \in \left[\text{integer} \left(\frac{2d_y}{\lambda_{source}} \right), -\text{integer} \left(\frac{d_y}{\lambda_{source}} \right) \right] \quad 5.28$$

The selection of r_x and r_y values resolves the phase ambiguities caused by the spatial aliasing. As the inter-element spacing increases the range of r_x and r_y value increases. In this research work ANN is used to select the appropriate r_x and r_y values.

5.2.2 Design of an ANN module for phase ambiguity resolution

The ANN is adopted to construct a non-linear relation that between the unwrapped direction cosines and the phase ambiguity resolution parameters. ANN is a massively parallel distributed processor that allows modeling highly complex and nonlinear problems with high level of stochastic that cannot be solved using conventional algorithmic approaches [Haykin99, Ham01]. It is composed of simple elements operating in parallel. Being inspired by the biological nervous system these elements are called “Neurons” [Ham01]. ANN functionality is determined by the connections between the neurons. It can be trained to perform a particular function by tuning the values of the weights (connections) between the neurons. The ANN resembles the brain in two aspects. First, the network acquires knowledge through a learning process. Second, the interneuron connection weights are used to store the knowledge. The input to the network includes the wrapped direction cosines while the network output is the corresponding unwrapping parameters (r_x and r_y). The developed ANN corresponds to a fixed array design and a single harmonic value. Data set is formed by simulating a single harmonic acoustic source with different SNR’s. The frequency of the simulated signal is the targeted source frequency. This takes place for all possible directions of arrival between $-\pi$ and π .

As shown in Figure 5.1, during the training procedure of the network the wrapped direction cosines are fed to the network and the outputs are the unwrapping parameters corresponding to the simulated source DOA. The network outputs are compared to the desired unwrapping parameters. The error in between is fed to the learning criterion, which adjusts the network parameters in a way to minimize the mean square value of the error. Figure 5.2 shows the operation of the ANN module in the operation mode. It provides an estimate of unwrapping parameters based on the direction cosines at the input. The unwrapping parameters are used to calculate the unwrapped direction cosines and hence provide an estimate of signal DOA.

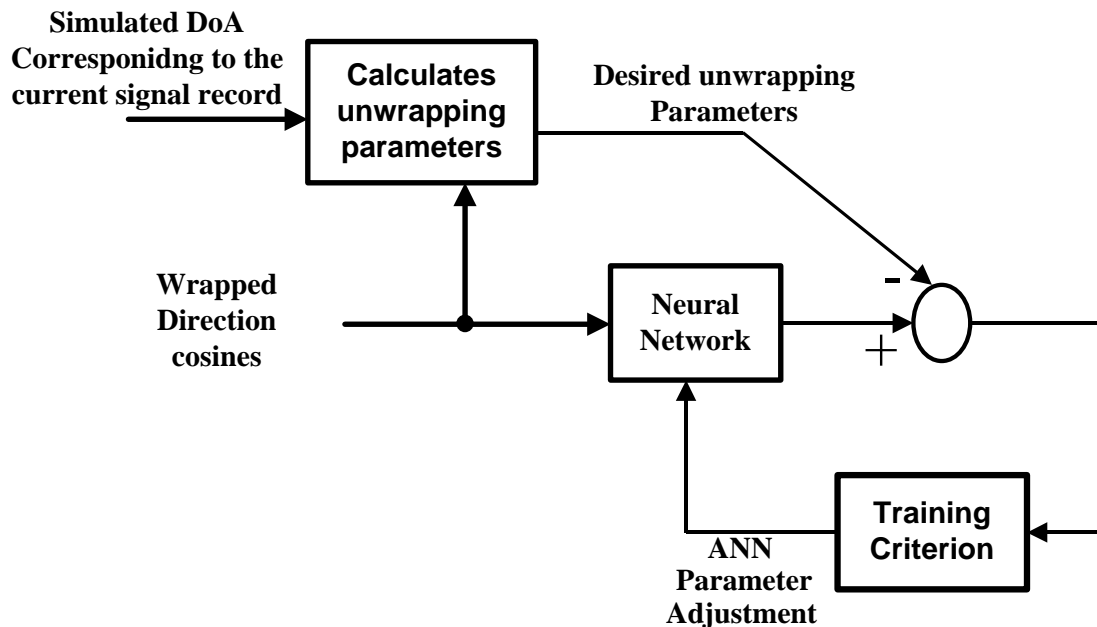


Figure 5.1. Training procedure of ANN module.

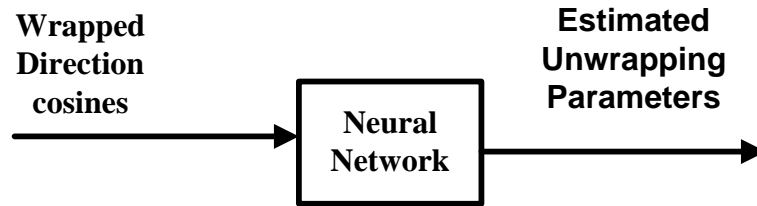


Figure 5. 2. ANN operation for estimating the unwrapping parameters (r_x and r_y)

In this study, a multi-layer perceptron (MLP) network with the architecture shown in Figure 5.3 is considered. The input layer of the network has two input neurons for the direction cosines. The output layer has two output neurons for the corresponding unwrapping parameters. We have also considered only one hidden layer. Different numbers of neurons were examined for the speed of convergence and minimum error value achieved. The optimum number found was 256 neurons. More complex network structures of more hidden layers and more neurons in each layer can be adopted. However, we have determined that the network architecture shown on Figure 5.3 is appropriate enough for the considered application.

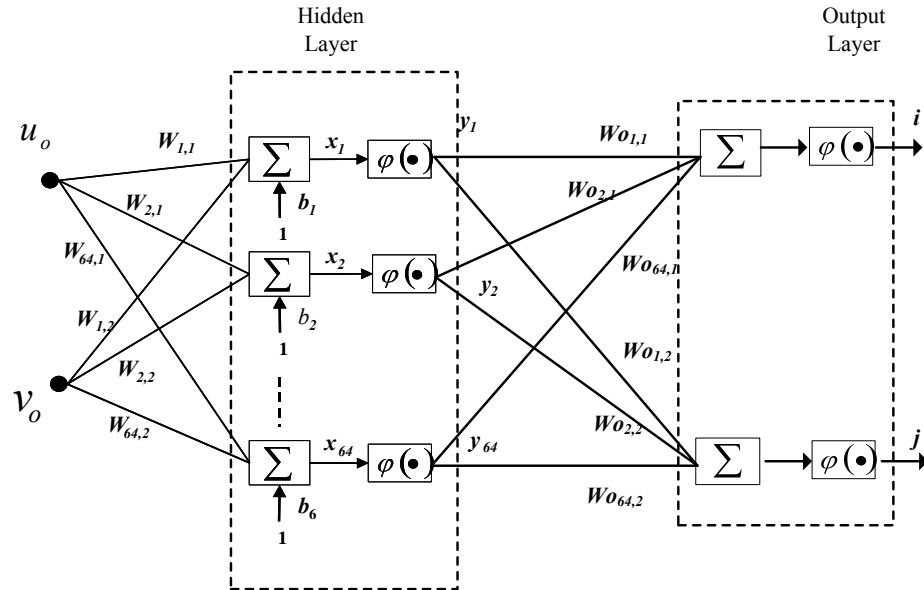


Figure 5. 3. Architecture of one hidden layer MLP network for phase ambiguity resolution

The weights W and the biases b are the ANN parameters that are computed during the training procedure and they determine the input/output functionality of the network. The weights are multiplied by the inputs to each neuron while the biases are considered at each neuron to limit or lower down the input to the activation function φ [Ham01]. A Hyperbolic tangent function (*tansigmoid*) is employed inside the hidden neurons to model the non-linearity in the input/output relationship. A linear activation function is considered at the neuron of the output layer to perform as a linear superposition of the outputs of the hidden neurons. It should be highlighted that individual ANN module of the form shown on Figure 5.3 is designed for each array design and desired source frequency. These types of networks are known as feed forward back propagation (FFBP) neural networks. The forward path of the computation involves feeding the inputs to the network starting from the input layer [Ham01]. The output is obtained and compared to

the target (desired performance) to determine the estimation error. This error is propagated through the network in the backward direction (opposite to the flow of the input data) starting from the output layer and is utilized to update the computation of the network parameters. The forward and backward computations are repeated until achieving the optimal values of the weights, which correspond to certain objective mean square estimation error. The network weights are updated according to certain learning rule to minimize the mean square value of the estimation error. In this study, we have utilized the Levenberg-Marquardt learning rule, which provides the fastest training algorithm among other learning rules [Ham01].

5.2.3 FB-NN DOA estimation module

The module adopted in this research is demonstrated in Figure 5.4. First the received signal is processed using FB module which computes the unwrapped direction cosines. The desired frequency and direction cosines are fed into the unwrapping module. This module consists of various neural networks corresponding to the frequency bins of the spectrum of interest. The desired frequency is used to select the corresponding trained NN. The direction cosines are then fed into the selected NN to generate an estimate of unwrapping parameters. Using the unwrapping parameters, the final module unwraps the direction cosines and obtains an estimate of DOA for the intended source.

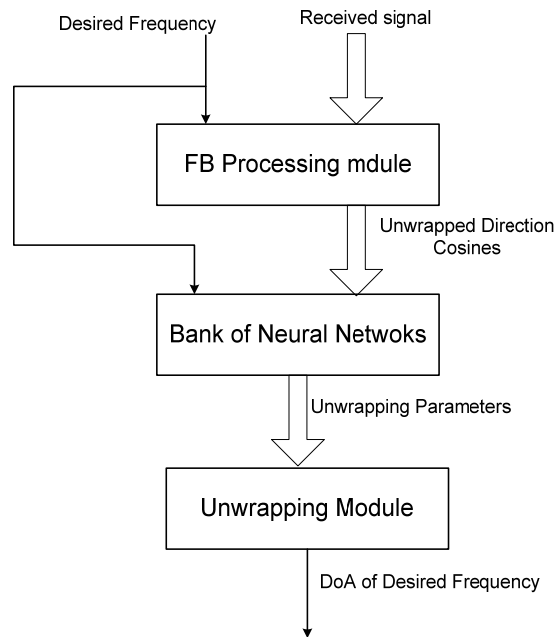


Figure 5.4. FB-NN DOA estimation module

5.3 Results and Discussion

5.3.1 Simulation Scenario

The simulation results presented in this section are based on processing the output electrical signals from a 3 X 3 planar array of hydrophones. The simulated data was generated using acoustic level simulation previously introduced in chapter 3. The simulated source is a non-moving acoustic source emitting single harmonic plan wave. In all tested cases the received signal frequency was chosen to be $f=100\text{Hz}$ with an amplitude of 10 volts sampled at a rate of 1000 Hz. The data record used in each test is 5 seconds which generate 5000 samples per record. The propagation velocity of the simulated signal is 1500 m/s which represent the average sound velocity underwater. This implies that the received signal wavelength is 7.5 m. Test cases represent different inter-

element spacing values which exceeds 7.5 m (the maximum allowable inter-element spacing). The presented cases here correspond to inter-element spacing of 10 m, 19 m and 101m. These values were chosen to represent the effect of increased inter-element spacing on the proposed processing method. For each test case results were obtained for different levels of SNR. The SNR's examined in each test are 0 dB, -10 dB, -15 dB and -20 dB. Different noise levels were simulated using additive, wide-sense stationary, zero mean, white, Gaussian noise samples to corrupt the time samples of the signals. Figure 5.3 shows a general representation of the simulated cases.

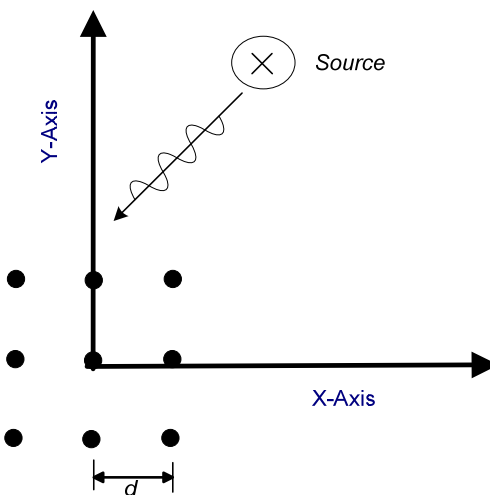


Figure 5. 3 X 3 planar array with d inter-element spacing and non moving source

5.3.2 Results

Bearing angle estimation errors were obtained by running the simulation once and allowing the modified complex LMS algorithm 1000 iterations. The result bearing angle estimation parameters are then passed to the neural network to obtain the unwrapping parameters. Results are shown for all expected bearings between $-\pi$ and π .

The number of iterations and step size used in the FB method had a significant effect on solution accuracy. Selection of step size and number of iterations was based on examination of different combinations of these two parameters. The best parameters were 6.6×10^{-8} for step size and 2000 the number of iterations.

Feed forward back propagation (FFBP) network was then trained using a set of simulated data with SNR's ranging between 0 dB and -20 dB. Each record of the data set represents DOA parameters corresponding to single harmonic signal. Data records were generated for bearings between $-\pi$ and π with a resolution of 1 degree. This was repeated for different SNR's (0 dB, -10 dB, -15 dB and -20 dB) resulting in a data set of 1800 records. After building the ANN bank, test cases were run using additive, wide-sense stationary, zero mean, white, Gaussian noise samples to corrupt the time samples of the signal. Each test record is a single harmonic source signal. The test record included test signals for sources arriving from all directions between $-\pi$ and π . Test data sets were generated for SNRs 0 dB, -10 dB, -15 dB and -20 dB.

The ANN training set was applied in a random order to generate a robust mapping that resolves ambiguity of aliased DOA parameters. The selection of the number of hidden layer nodes was based on several trials to achieve the optimum number of nodes corresponding to minimal error for NN solution. Figures 5.6, 5.7 and 5.8 demonstrate the significance of the number of hidden neurons. The error percentage represents the average error obtained for DOA estimation. The average error shown in Figures 5.6, 5.7 and 5.8 is calculated by applying the no noise data set to the ANN and comparing the estimated DOA's to the simulation data DOA's. The total number of errors corresponds to the instances when the difference between the estimated DOA and simulation data

DOA exceeds 5 degrees. This is divided by the total number of records to get the average error percentage. For the proposed design the selected optimum value for the NN hidden nodes was 256. This value provided the minimum error for the considered cases and hence it was employed for the evaluation of system performance in different cases and different SNR's.

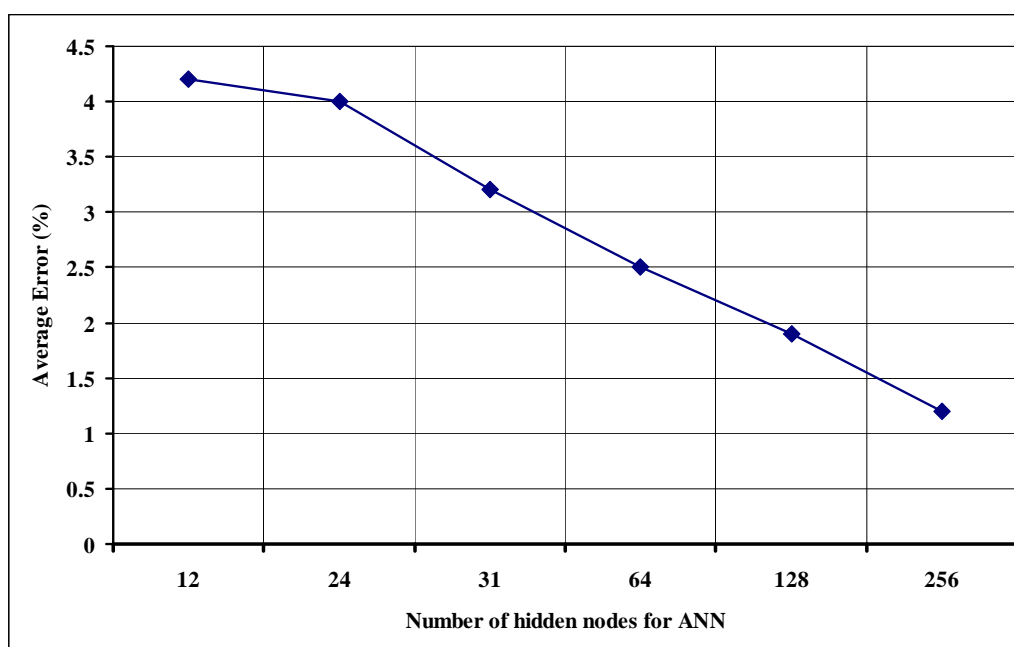


Figure 5.6. Error variation with the number of hidden nodes for Case I (10m dinter-element spacing)

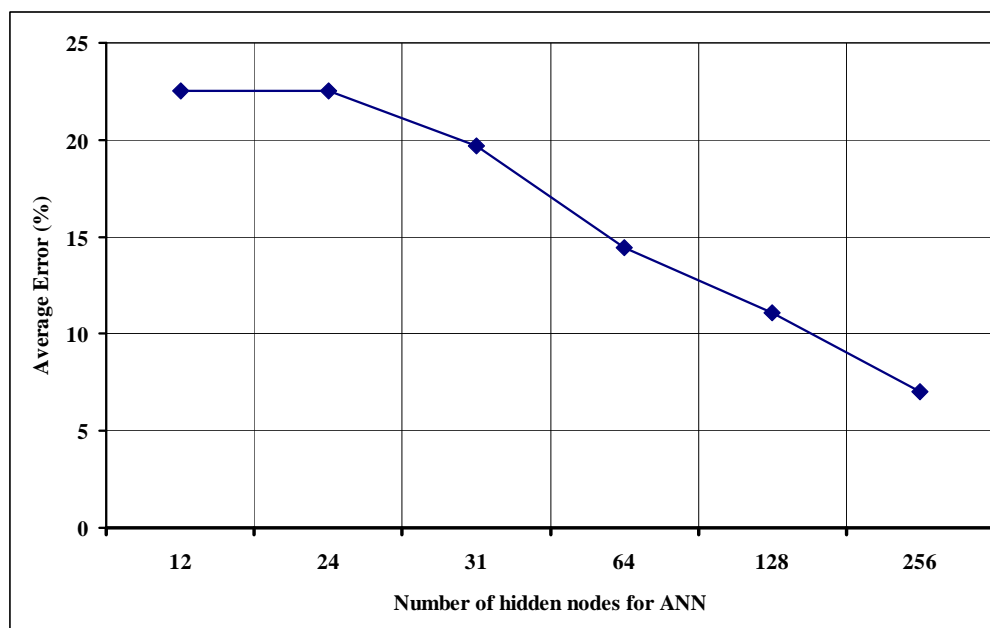


Figure 5.7. Error variation with the number of hidden nodes for Case II (19m inter-element spacing)

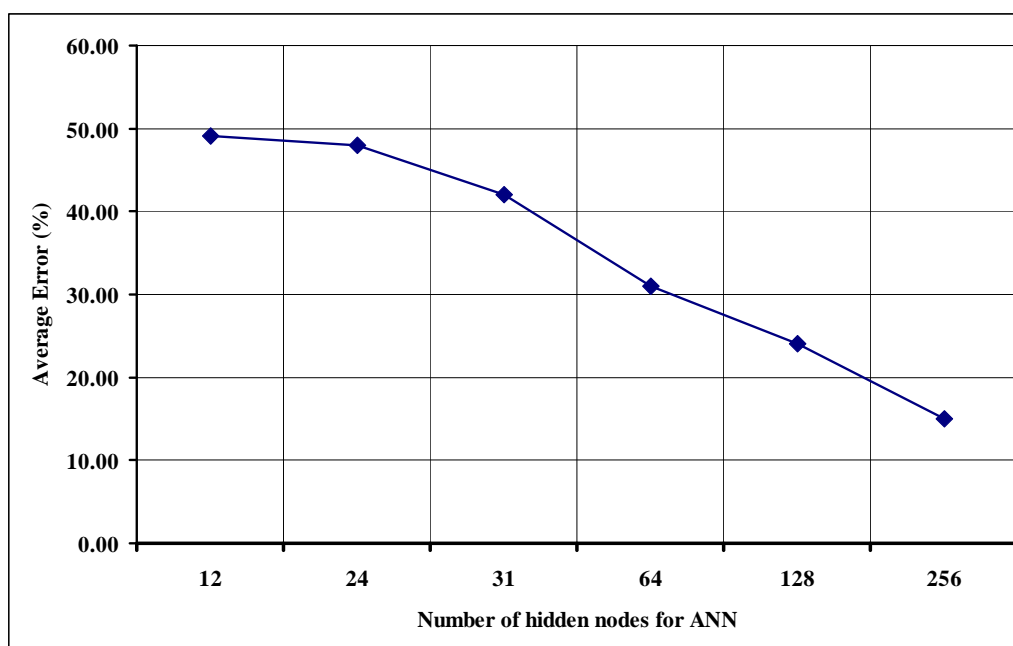


Figure 5.8. Error variation with the number of hidden nodes for Case III (101m)

It can be observed that increasing the inter-element distance deteriorates the performance of the spatially aliased array. The increase in the inter-element spacing results in an increase of the unwrapping parameters range which broadens the solution space. Accordingly the system becomes more susceptible to errors. Figures 5.9 and 5.10 illustrate the behavior of the unwrapped direction cosines versus the source bearing for the tested cases. The reference values represent the direction cosines associated with the simulated source. Direction cosines for each case correspond to different array inter-element spacing (10m, 19m and 101m). This verifies the degradation in performance accompanying the increase in the inter-element spacing of the spatially aliased array. However it can be depicted from Figures 5.6, 5.7 and 5.8 that the variations in the average error percentages values achieved are significantly minimized as the number of hidden nodes of the ANN increase. The minimum average error percentages for the test cases vary between 1.2% and 11.1%. This shows a significant reduction compared to the initial range of average error percentages which vary between 4.1% and 49.7%.

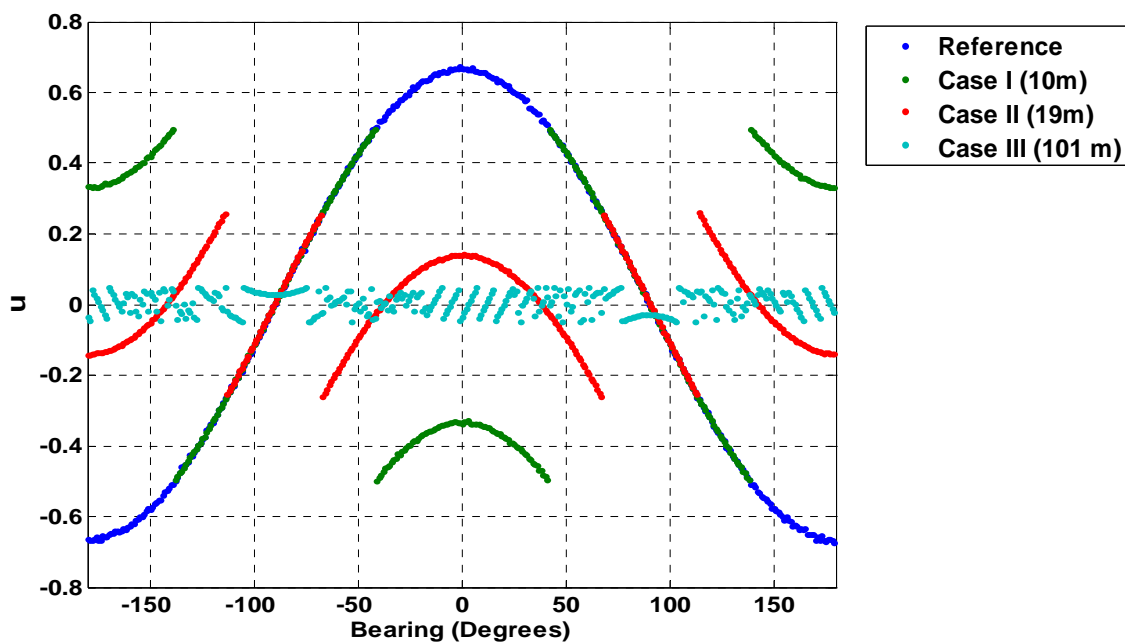


Figure 5.9. Variation of estimated unit vector in x axis against different source bearings

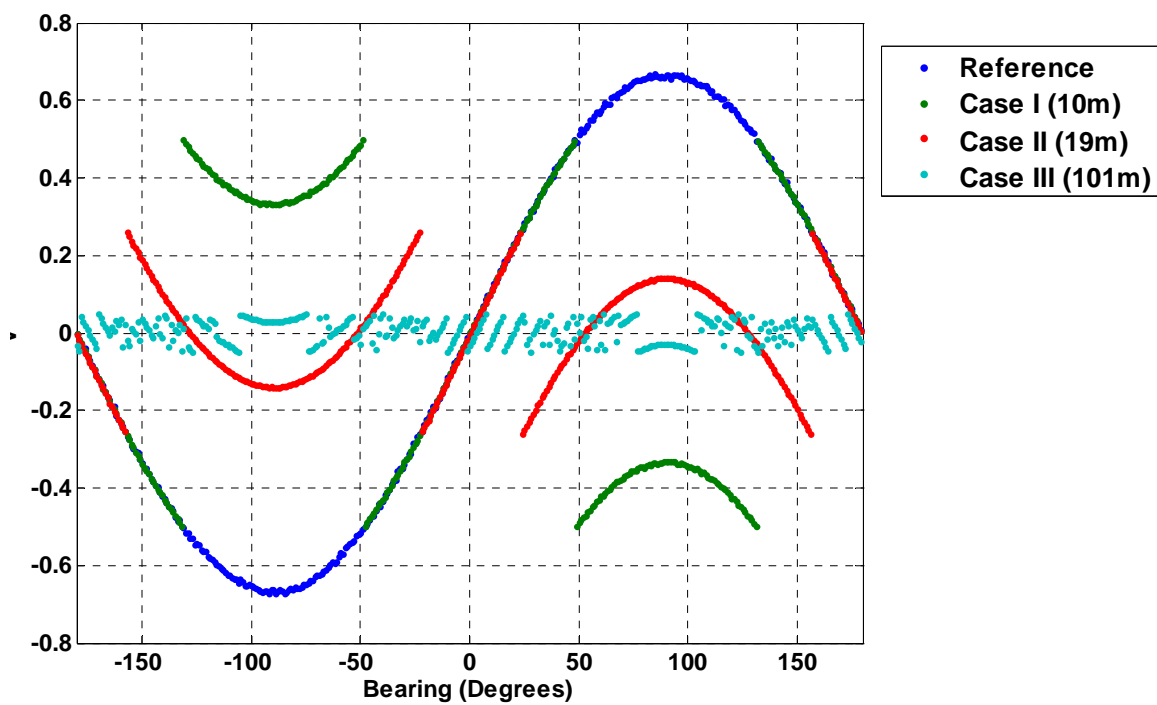


Figure 5.10. Variation of estimated unit vector in y axis against different source bearings

The second testing phase for the developed module was to examine its performance against different levels of SNR. Figure 5.11 illustrates the average error percentage for different cases versus SNR. These values were calculated using the module corresponding to ANN of 256 hidden nodes. For no noise case the variations in the average error percentage for different cases was considerably minimized by proper selection of the number of hidden nodes for the ANN. The system behavior degrades as the level of SNR decreases. The system degradation becomes more significant as the inter-element spacing increases. This fact can be considered a limitation over the increase of inter-element spacing for spatially aliased arrays. However using some denoising technique can boost the performance of the spatially aliased arrays and provide a wider range of proper inter-element spacing.

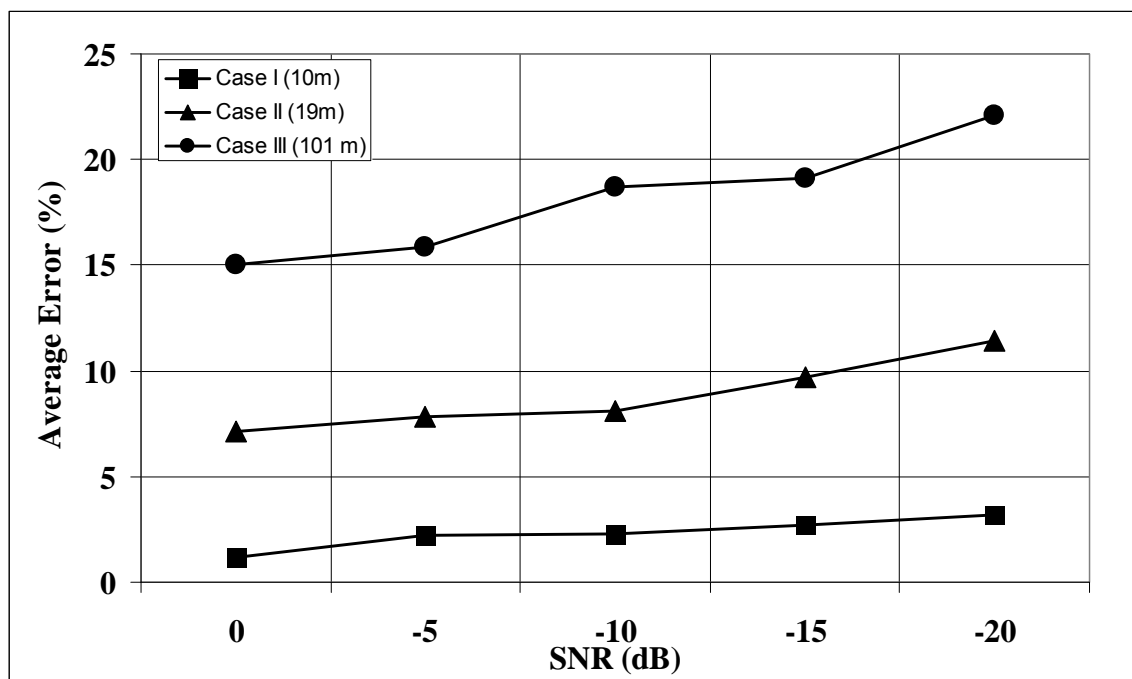


Figure 5. 11. Error variation with SNR for 256 hidden layers

5.4 Conclusion

This chapter introduced a spatially aliased array processing method based on non conventional FB technique augmented by ANN that enabled DOA ambiguity resolution when the inter-element distance between array elements exceeded the maximum allowable distance. The performance of the proposed method is influenced by the noise level and the distance between the array elements. We determined that at low SNR environments, this method cannot provide adequate performance for relatively large inter-element spacing. Another major limitation on the proposed FB-based method is the requirement of two dimensional array constellations with equal inter-element spacing and odd number of sensors in each dimension. In some applications, this array constellation can be realized, thus the proposed method can be applied efficiently. However, the

limitations of this method preclude the use of this method when sonobuoys are deployed into water where their locations can vary over time so that equal inter-element spacing cannot be maintained and the required array arrangement cannot be realized. Therefore, this research has been extended further to explore innovative methods that enable processing an array of GPS sonobuoys with minimal limitations on the inter-element spacing and with no special requirements on the array constellation. This method shall be able to coherently process a sparse array of GPS sonobuoys and will benefit from the data recorded by the three sensors of DIFAR type of sonobuoys.

Chapter Six: Direction of Arrival Estimation using Virtual Array Search (VAS)

In this chapter a new method for DOA estimation is introduced. This method employs advanced array interpolation technique for effective DOA estimation using an array of DIFAR sonobuoys. In chapter 4, it was shown that array processing of DIFAR sonobuoys field introduced significant improvement for the bearing estimation accuracy at relatively low SNR environments. The radiation pattern for a group of DIFAR sonobuoys should always provide a unique DOA solution independent of the inter-element distance. This corresponds to the tip of the DIFAR sonobuoy beam pattern at the centre of the main lobe. However, the low resolution of Bartlett beamforming may cause the solution to be numerically unstable [Nicholas96] in cases where the side lobes are too close to the main lobe. In this case the level of side lobes is very close to the main lobe and hence the system becomes unstable. Furthermore, the environmental conditions and deployment strategies cause the inter-element distance between sonobuoys to exceed the minimum distance required for stable array processing. These conditions can prohibit adequate processing of an array of DIFAR sonobuoys.

In order to avoid the above limitations, virtual array (VA) processing using array interpolation is proposed as a technique for mapping an array of DIFAR sonobuoys to desirable constellations that enables reliable system processing. Array interpolation (mapping) was introduced around 1990 [Hyperg04]. It was usually applied for two main reasons [Hyperg04]: (1) to interpolate between available calibration points; (2) to

transform the sonobuoys received data to a corresponding one of particular array geometry. This enables the use of available fast DOA estimators that requires definite arrangements for the array elements [Hyperg04] (e.g. Multiple signal classification (MUSIC) [Schmidt86]). In this research array interpolation is applied to generate a virtual array.

Virtual array search (VAS) is proposed in this research to mitigate the system deficiency caused by wide spacing between DIFAR sonobuoys. The proposed VAS algorithm is mainly based on advanced array interpolation technique which is suitable for one dimensional and two dimensional arrays. Thus it enables processing the sonobuoy recorded data for different array deployment strategies. In addition, this method increases system efficiency by enabling coherent array processing for an array of widely spaced elements. The array mapping process is mainly based on the design of transformation matrix that maps the signals received at the original array to the virtual array. This transformation matrix can significantly affect the operation of the virtual array depending on its mapping accuracy. Systematic mapping errors may dominate over noise effects and cause significant bias in the DOA estimates. To prevent mapping errors from improperly affecting the DOA estimates, the technique proposed in [Hyperg04] uses a geometrical interpretation of a Taylor series expansion of the DOA estimator criterion function to derive an alternative design of the mapping matrix. The key feature of the proposed design is that it takes into account the orthogonality between the manifold mapping errors and certain gradients of the estimator criterion function. With the new design, mapping of narrowband signals between dissimilar array geometries over wide sectors and large frequency ranges becomes feasible. The interpolation technique introduced in [Hyperg04]

suggests the processing of wide sectors and design one common mapping matrix for each sector (and each frequency band). Each of these mapping matrices has to be a compromise over its sector which represents a fundamental difficulty that leaves unavoidable mapping errors. As the width of these sectors increases, the interpolation errors increase. Although these errors cannot be brought to zero, they are to some extent controllable through the proper choice of the interpolation matrix. Usually, the mapping matrix is designed to provide the best least squares fit between the transformed response vectors of the real array and the response vectors of the virtual array for a set of DOAs comprising a sector. Such a best array manifold match does not in general guarantee the smallest DOA estimate bias [Hyperg04] and hence introduces large mapping errors. The employed interpolation technique minimizes the influence of mapping errors on the DOA estimates by rotating the mapping errors into orthogonality with the gradient of the estimator criterion function.

The proposed method was tested using simulated data. A comparative analysis is presented with respect to Bartellet beamforming on GPS sonobuoys field. The results show that the proposed method is capable of enhancing the accuracy of target bearing estimation especially in cases of very low SNR. Merits and limitations of the proposed method are discussed and analyzed in this chapter.

6.1 Virtual Array Search (VAS)

In this research, the virtual array processing is introduced in a new approach different from those discussed above. The virtual array search is commonly used to

transfer an array arrangement to a designated one that suits the DOA estimation technique. In this research, the bearing estimation using Bartlett beamforming and is aided by the VAS approach. The received signals at the original array elements are mapped to the virtual array elements using all possible transformation matrices that are designed for all sectors covering all possible DOAs. Bartlett beamforming is then applied to all mapped arrays. The maximum power corresponding to each transformation matrix is recorded. The bearing corresponding to the maximum of the recorded maxima is selected to be the DOA. The procedure of using virtual array represents an additional condition to examine the DOA. VAS searches the original array radiation pattern for the true bearing based on the fact that the best fit for the DOA is the transformation matrix designed for its sector. Therefore, the VAS approach rejects other sectors and increases the accuracy level of the array processing system. Moreover, proper selection of sector width provides higher resolution for the system and efficient suppression of side lobes. Figure 6.1 shows an explanatory block diagram for the newly proposed VAS approach.

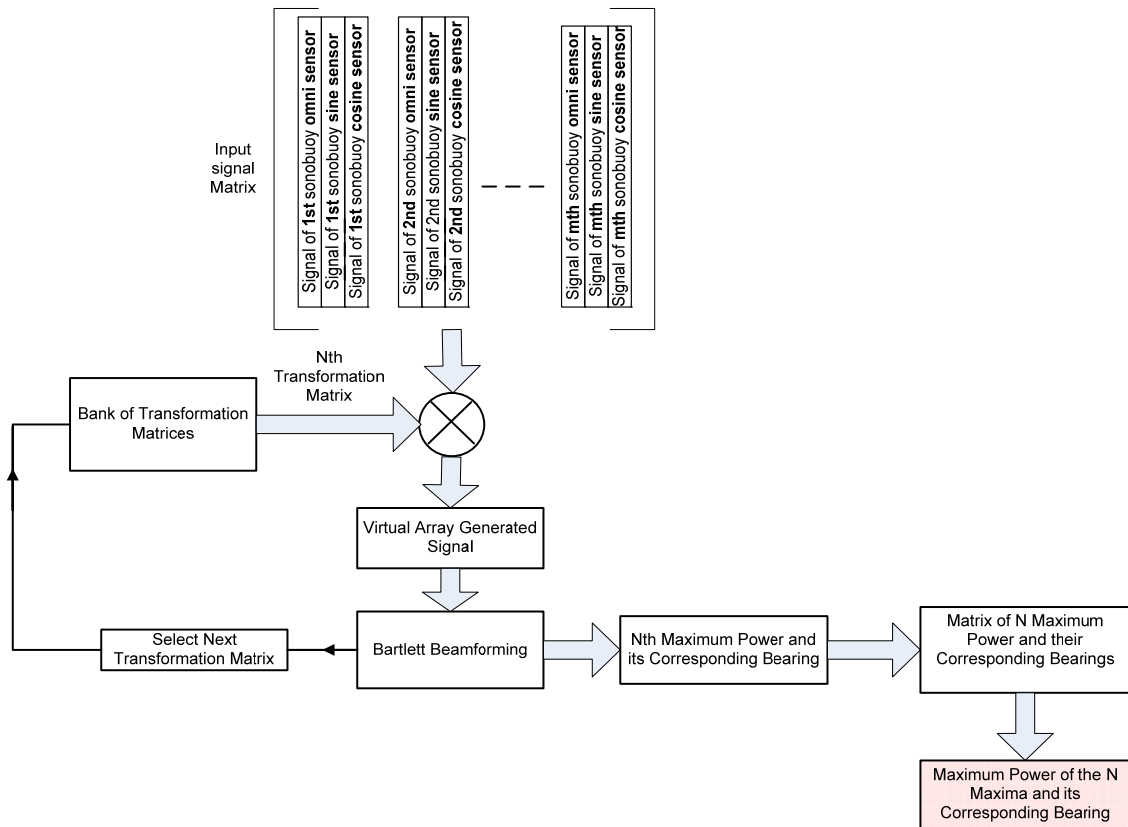


Figure 6.1. VAS approach

6.2 Array Mapping

The signal model used in this research has some assumptions including: (1) The received signal is a narrowband far-field; (2) The emitter is confined to the horizontal plane. The second assumption was used to simplify design since the tracking nature of DIFAR sonobuoys considers calculating the DOA only in the horizontal plane, thus no need for 2-D extension of the array elements [Hyperg04]. The complex baseband model for the received signal is given by:

$$x(t) = a(\theta)s(t) + n(t)$$

Where $x(t)$ is $m \times 1$ array output vector at discrete time instant t ;

θ is the azimuth angle.

$a(\theta)$ is $m \times 1$ complex array response to a source in direction θ with unity power;

$s(t)$ is received signal at a reference point at time t ;

$n(t)$ is $n \times 1$ noise vector at time t ;

Figures 6.2 and 6.3 demonstrate the steering vectors associated with the elements of the original array and the virtual array, respectively. For the particular original and virtual arrays shown in these two figures, the steering vectors $a(\theta)$ and $a_v(\theta)$ are given as follows:

$$\begin{aligned}
 a(\theta) &= [1 \quad \sin \theta \quad \cos \theta \quad \exp(j2\pi d \sin \theta / \lambda) \quad \exp(j2\pi d \sin \theta / \lambda) \sin \theta \quad \exp(j2\pi d \sin \theta / \lambda) \cos \theta_0]^T \\
 a_v(\theta) &= [1 \quad \sin \theta \quad \cos \theta \quad \exp(j2\pi d_v \sin \theta / \lambda) \quad \exp(j2\pi d_v \sin \theta / \lambda) \sin \theta \quad \exp(j2\pi d_v \sin \theta / \lambda) \cos \theta \\
 &\quad \exp(j4\pi d_v \sin \theta / \lambda) \quad \exp(j4\pi d_v \sin \theta / \lambda) \sin \theta \quad \exp(j4\pi d_v \sin \theta / \lambda) \cos \theta \\
 &\quad \exp(j6\pi d_v \sin \theta / \lambda) \quad \exp(j6\pi d_v \sin \theta / \lambda) \sin \theta \quad \exp(j6\pi d_v \sin \theta / \lambda) \cos \theta]^T
 \end{aligned}
 \tag{6.2}$$

Where $a_v(\theta)$ is the steering vector of virtual array of DIFAR sonobuoys, d and d_v are the inte-element distances for the Original array and virtual array respectively and λ is the wavelength of the received signal.

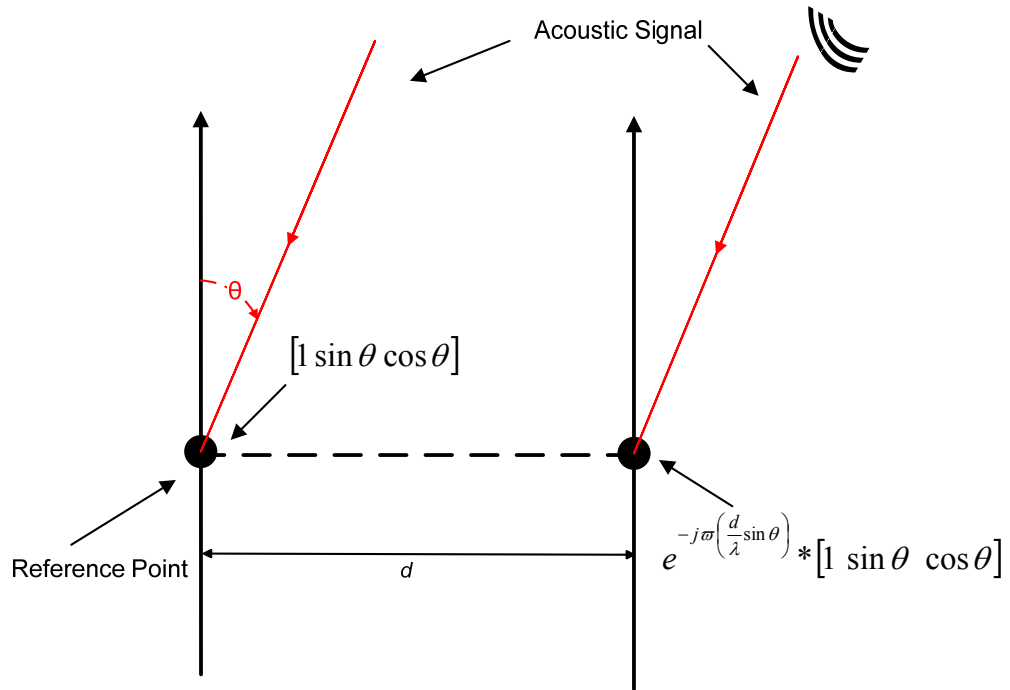


Figure 6.2 ULA of 2 DIFAR Sonobuoys

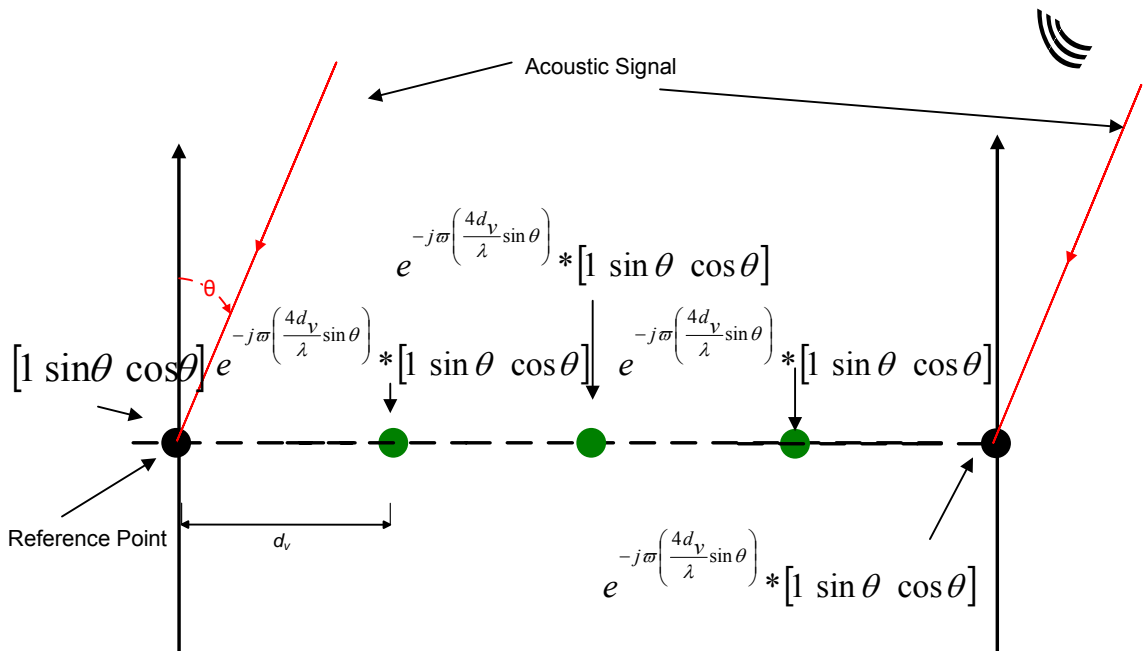


Figure 6.3 Virtual Array of DIFAR sonobuoys

The matrices comprising the steering vectors obtained at N_{cal} calibration directions for the original and virtual arrays shown respectively in Figures 6.2 and 6.3 can be given as follows:

$$\begin{aligned} A(\theta^{(c)}) &= [a(\theta^{(1)}) a(\theta^{(2)}) \dots a(\theta^{(N_{cal})})] \\ A_v(\theta^{(c)}) &= [a_v(\theta^{(1)}) a_v(\theta^{(2)}) \dots a_v(\theta^{(N_{cal})})] \end{aligned} \quad 6.3$$

Where $\theta^{(c)}$ is the collection of adjacent N_{cal} calibration directions, $A(\theta^{(c)})$ and $A_v(\theta^{(c)})$ are the transformation matrices comprising steering vectors for original and virtual arrays respectively.

The transformation matrix that maps the original array to the virtual array can be simply obtained by obtaining least squares fit between the transformed array response and the response of the virtual array over a sector of interest, that is [Hyperg04]:

$$T_{LS} = \arg \min_T \|T^H A(\theta^{(c)}) - A_v(\theta^{(c)})\|_F^2 \quad 6.4$$

Where $\|\cdot\|_F$ denotes the Frobenius norm

With $3m$ elements in the original array and $3m_v$ elements in the virtual array, the matrix of virtual response vectors has $3m_v \times N_{cal}$ size. This implies that T has size $3m \times 3m_v$. If is not known analytically, the columns of $A(\theta^{(c)})$ are chosen as the array responses obtained from a calibration experiment. Assuming more calibration points than antenna elements in the real array ($N_{cal} \geq m$) and that $A(\theta^{(c)})$ is full rank, the least squares solution to (6.4) is [Hyperg04]

$$T_{LS} = \left(A(\theta^{(c)}) A^H(\theta^{(c)}) \right)^{-1} A(\theta^{(c)}) A_v^H(\theta^{(c)}) \quad 6.5$$

The Bias effect of mapping the matrix obtained by least square fitting can be obtained by subtracting virtual array response vector from the product of array response vector of the real array and the Hermiston of transformation matrix. [Hyperg04]

$$\Delta A(\theta^{(c)}) \underline{\underline{\Delta T^H A(\theta^{(c)}) - A_v(\theta^{(c)})}} \quad 6.6$$

The ultimate objective is to reach zero mapping error, however, for mapping between dissimilar and/or wide spaced arrays over large sectors, a perfect match will seldom be the case, and biased estimates may result. The interpolation technique introduced in [Hyperg04] incorporates additional properties to the T_{LS} calculation procedures to minimize DOA bias in situations where $\Delta A(\theta^{(c)}) \neq 0$.

The DOA bias mitigation procedure employed in [Hyperg04] was developed for DOA using MUSIC and weighted subspace fitting (WSF) [Viberg91]. In this research work, the transformation matrix introduced in [Hyperg04] is applied to DOA using Bartlett beamforming. Since the transformation matrix obtained for MUSIC and WSF provides the optimum mapping parameters for these methods, the obtained solution for the transformation matrix can be considered an optimum mapping method for Bartlett beamforming. This assumption is based on the fact that the optimum transformation provides highly accurate interpolation of the array received signal.

In case of MUSIC approach, the transformation matrix bias reduction is based on minimization of deterministic signal subspace eigenvector errors due to array transformations. Subspace-based DOA estimators are considered, and therefore, an estimate of the signal subspace eigenvector of the virtual array is needed. In this research,

VAS uses the same approach but with using the normalized steering vector instead of the eigenvalue vector employed by MUSIC. The design of the transformation matrix using the eigenvalue approach is explained in Appendix A and is shown in Eq. 6.7:

$$T_{LS} = \arg \min_T \sum_{i=1}^{N_{cal}} (1-k) \left\| T^H \bar{a}(\theta^{(i)}) - \bar{a}_v(\theta^{(i)}) \right\|^2 + k \left| 2 \operatorname{Re} \left\{ g_v^{(i)H} \Delta e_v^{(i)} \right\} \right|^2 \quad 6.7$$

Where g_v is the complex gradient of $V(\theta_0, e_v)$ with respect to with respect to the signal eigenvector of the virtual array (e_v) and $V(\theta, \hat{e}_v)$ is the criterion function associated with the MUSIC algorithm The derivation of formula of g_v is detailed in Appendix A. $\Delta e_v^{(i)}$ is the virtual signal eigenvector mapping error in the i th calibration direction, $\Delta e_v^{(i)} = T^H e_s^{(i)} - e_v^{(i)}$ ($e_s^{(i)}$ is the signal eigenvector of the real array from a single emitter in the i th calibration direction and $e_v^{(i)}$ is the signal eigenvector of the virtual array from a single emitter in the i th calibration direction).

The algorithm presented in [Hyperg04] uses the property that the range of the signal subspace e_s equals the range of $a(\theta)$ and that e_s is only determined up to a phase factor. Therefore a unique signal eigenvectors can be obtained by choosing the phase factor so that e_s equals the corresponding normalized array response vector $\bar{a}(\theta)$, that is:

$$e_s = \bar{a}(\theta) = a(\theta) \left(a^H(\theta) a(\theta) \right)^{-1/2} \quad 6.8$$

This property enables the application of the above array mapping algorithm to the problem of DOA estimation using Bartlett beamforming. The transformation matrix minimization problem can therefore be expressed as:

$$T_{LS} = \arg \min_T \sum_{i=1}^{N_{cal}} (1-k) \left\| T^H \bar{a}(\theta^{(i)}) - \bar{a}_v(\theta^{(i)}) \right\|^2 + k \left| 2 \operatorname{Re} \left\{ g_v^{(i)H} \left(T^H \bar{a}(\theta) - \bar{a}_v(\theta) \right) \right\} \right|^2 \quad 6.9$$

The minimization problem (Equation 6.9) is solved by [Hyperg04] applying the *vec* operator to both terms inside each norm and solve for a vectorized \mathbf{t} version of \mathbf{T} . First step is to reverse order between factors by taking the Hermitian transpose of Eq. 6.9. The transformation matrix criteria can then be written as [Hyperg04]:

$$T_{opt} = \arg \min_T \left\{ (1-k) \left\| \bar{A}^H(\theta^{(c)})T - \bar{A}_v^H(\theta^{(c)}) \right\|_F^2 + k \cdot \sum_{i=1}^{N_{cal}} \left| \text{Re} \left\{ \bar{a}^H(\theta^{(i)})T \mathbf{g}_v^{(i)} - \bar{a}_v^H(\theta^{(i)}) \mathbf{g}_v^{(i)} \right\} \right|^2 \right\} \quad 6.10$$

Where \bar{A} and \bar{A}_v are matrices of normalized response vectors, and $\theta^{(c)}$ is a $1 \times N_{cal}$ vector of calibration azimuths. Consequently, the *vec* operator (that transforms a matrix into a vector) is applied to get:

$$T_{opt} = \arg \min_T \left\{ (1-k) \left\| (\mathbf{I} \otimes \bar{A}^H(\theta^{(c)})) \text{vec}(T) - \text{vec}(\bar{A}_v^H(\theta^{(c)})) \right\|_F^2 + k \cdot \sum_{i=1}^{N_{cal}} \left| \text{Re} \left\{ (\mathbf{g}_v^{(i)T} \otimes \bar{a}^H(\theta^{(i)})) \text{vec}(T) - \bar{a}_v^H(\theta^{(i)}) \mathbf{g}_v^{(i)} \right\} \right|^2 \right\} \quad 6.11$$

Where \otimes is the Kronecker product [Steeb97]. The terms of Equation 6.11 are then represented by the following notations [Hyperg04]:

$$M_1 = \sqrt{1-k} (\mathbf{I} \otimes \bar{A}^H(\theta^{(c)})) \quad 6.12$$

$$m_2 = \sqrt{1-k} \text{vec}(\bar{A}_v^H(\theta^{(c)})) \quad 6.13$$

$$M_3^{(i)} = \sqrt{k} (\mathbf{g}_v^{(i)T} \otimes \bar{a}^H(\theta^{(i)})) \quad 6.14$$

$$m_4^{(i)} = \sqrt{k} (\bar{a}_v^H(\theta^{(i)}) \mathbf{g}_v^{(i)}) \quad 6.15$$

The sizes of M_1 , m_2 and $M_3^{(i)}$ are $m_v N_{cal} \times m_v m$, $m_v N_{cal} \times 1$ and $1 \times m_v m$ respectively.

The term $m_4^{(i)}$ is a scalar. By using these terms equation 6.11 can be written in the following form [Hyperg04]:

$$T_{opt} = \arg \min_T \left\| \begin{bmatrix} \operatorname{Re}\{M_1\} & -\operatorname{Im}\{M_1\} \\ \operatorname{Im}\{M_1\} & \operatorname{Re}\{M_1\} \\ \operatorname{Re}\{M_3^{(1)}\} & -\operatorname{Im}\{M_3^{(1)}\} \\ \vdots & \vdots \\ \operatorname{Re}\{M_3^{(N_{cal})}\} & -\operatorname{Im}\{M_3^{(N_{cal})}\} \end{bmatrix} \cdot \begin{bmatrix} \operatorname{vec}(\operatorname{Re}\{T\}) \\ \operatorname{vec}(\operatorname{Im}\{T\}) \end{bmatrix} - \begin{bmatrix} \operatorname{Re}\{m_2\} \\ \operatorname{Im}\{m_2\} \\ m_4^{(1)} \\ \vdots \\ m_4^{(N_{cal})} \end{bmatrix} \right\|^2 \quad 6.16$$

The short hand notation for equation 6.16 can be given as follows [Hyperg04]:

$$T_{opt} = \arg \min_T \|Mt - m\|^2 \quad 6.17$$

The vectorized version of optimal transformation matrix is then obtained from the least square solution of Eq 6.17 ad given by [Hyperg04]:

$$t_{opt} = \begin{bmatrix} \operatorname{vec}(\operatorname{Re}\{T\}) \\ \operatorname{vec}(\operatorname{Im}\{T\}) \end{bmatrix} = M^+ m \quad 6.18$$

Where M^+ is the Moore-Penrose Pseudoinverse [Stoer02] of M .

6.2.1 Virtual array design parameters

Since the virtual array design procedure can be carried offline, different design strategies can be tested to determine the one that is best suited for the application of interest. The virtual array design is mainly determined by three parameters: (1) the value of k ; (2) the number of virtual elements; (3) The width of sectors for which optimum transformation matrices are developed.

The parameters of the optimum design were selected to achieve minimum DOA bias over all possible directions (i.e. $[0 \ 2\pi]$). This bias was calculated by examining the estimated bearing for simulated single tone signals. Each simulated signal corresponded to one of the possible DOAs.

6.3 Simulation work

The performance of VAS was evaluated using an array of 3 DIFAR sonobuoys with different inter-element spacing. VAS was tested using two scenarios for DIFAR sonobuoys arrangement. In the first scenario DIFAR sonobuoys are arranged as a ULA with inter-element spacing of 60m. In the second scenario DIFAR sonobuoys are arranged as an arbitrary array. Figure 6.4a and 6.5a illustrates the simulated ULA array and the arbitrary array respectively. The large circles represent the real DIFAR sonobuoys and the small circles represent the virtual array elements generated using array interpolation method. The signal angle of arrival with respect to the North is similar at all array elements based on the far field assumption. To hold the far field condition, the simulated acoustic source is set at a distance of 5000 m from the central element of the original DIFAR array. This value is much greater than 60 m and hence the far field condition holds for the simulated scenarios. The radiation pattern associated with the array arrangements are shown in Figure 6.4b and 6.5b. The high side lobes in the radiation pattern of the ULA (Figure 6.4b) increase the system vulnerability to bearing estimation errors especially at relatively low SNRs. The radiation pattern of the arbitrary array shown in Figure 6.5b demonstrates the increase in the level of side lobes with the

introduction of irregularities in the positions of the DIFAR sonobuoys. This significantly degrades the bearing estimation accuracy and hence it jeopardizes the overall TMA process. VAS is applied for these two scenarios to enhance the bearing estimation accuracy at low SNRs. The first step in applying VAS is to generate the transformation matrices for all sectors of angular space. The design of the transformation matrices includes selecting the appropriate value for the parameter k (Eq 6.11); 2), selecting the sector width and selecting the inter-element spacing between the virtual array elements. The minimum bias criterion is used to select the appropriate set of transformation matrices. VAS is then applied to the received signal to obtain an estimate of the target bearing. Three sonobuoys are simulated with inter-element spacing of 60 m. Simulations were carried for single tone source with bearings at 160° and 30° . The performance of VAS in bearing estimation for the two values of target bearing is examined to study the variation of VAS at different bearings. In both cases the source acoustic signal has a single tone frequency of 100 Hz and amplitude of 140 dB re μPa . The system performance was examined for SNRs of -30dB and -40 dB. Results compare the output from the processing of real array and virtual array of DIFAR sonobuoys.

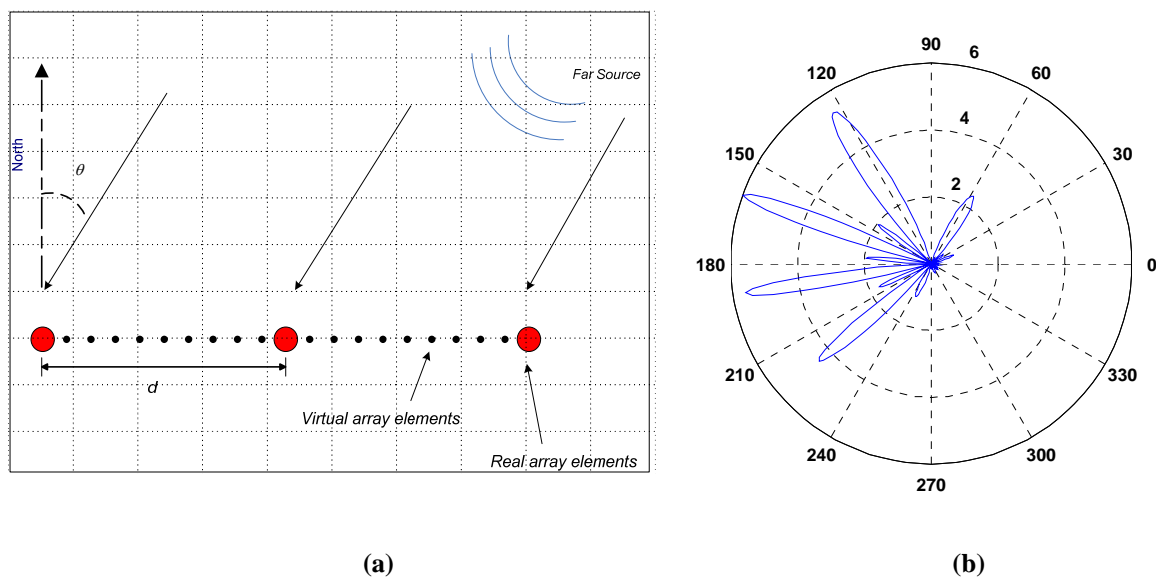


Figure 6.4 (a) ULA of 3 DIFAR sonobuoys , (b) Radiation pattern for a source with a bearing of 160° impinging ULA of 3 DIFAR sonobuoys with $d=60$ m

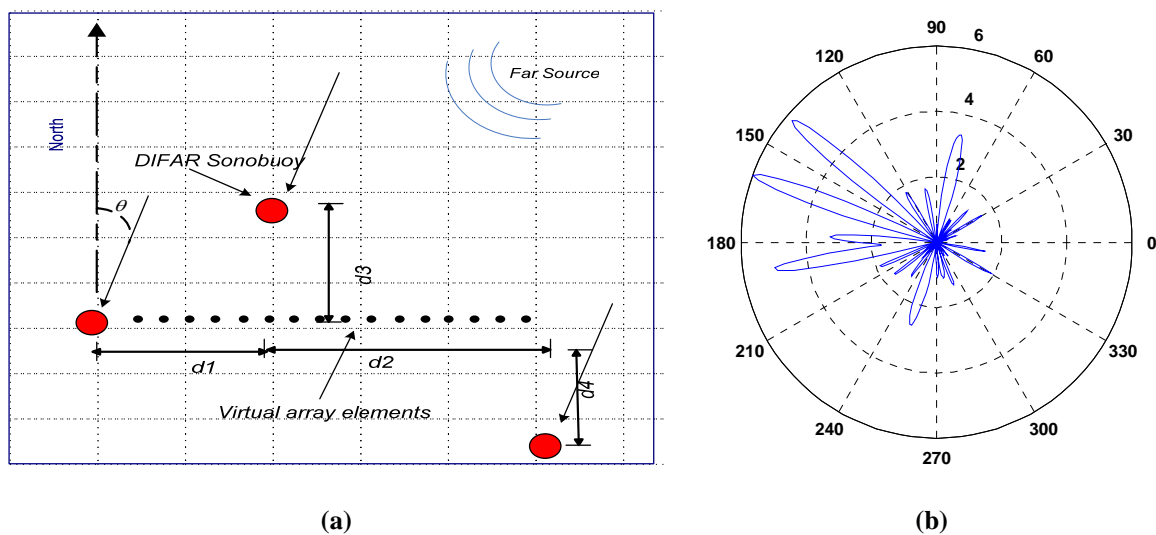


Figure 6.5 (a) Arbitrary array of DIFAR sonobuoys , (b) Radiation pattern for a source with a bearing of 160° impinging an arbitrary array of 3 DIFAR sonobuoys with $d_1=60$ m, $d_2=80$ m, $d_3=70$ and $d_4= 40$ m

6.3.1 Transformation Matrix design

The transformation matrix sector width and the parameter \mathbf{k} were selected using basic simulation of single tone signal without noise. Figure 6.6 shows the bias in degree introduced by the virtual array transformation matrix for the case of 3 DIFAR sonobuoys with inter-element spacing of 60 m. The number of virtual elements is constant for all shown plots and equal to 10 elements. This corresponds to virtual inter-element spacing is 10m. The shown biases correspond to different values of sector width. Observing the bias values, it can be depicted that decreasing the sector width mitigates the bias effect. The effect of virtual array inter-element spacing was examined as well using the simulated 3 DIFAR sonobuoys array. The results obtained for fixed sector widths of 2 degrees and 1 degree are shown in Figures 6.7 and 6.8 respectively. These figures clearly demonstrate the effect of decreasing the virtual array inter-element spacing on mitigation of the bias effect. The results obtained in Figures 6.6, 6.7 and 6.8 were used for the selection of sector width and virtual array inter-element spacing in the evaluation of VAS performance. It is clear from Figure 6.8a that using a sector width of 1 degree minimizes the bearing estimate bias for different inter-element spacing. The bias has a maximum value of 2 degrees for the case of 16 m inter-element spacing for the virtual array. The minimum bias is obtained for the case of 6 m inter-element spacing between virtual array elements. Based on these observations, the selected set of transformation matrices corresponded to the one shown in Figure 6.8b. The parameters of this set of transformation matrices are $k=0.99$, sector width= 1° and virtual array inter-element

spacing= 6m. It can be noted that the spacing of 6m holds the condition of stability for an array of DIFAR sonobuoys which is defined in chapter 4 (equation 4.13).

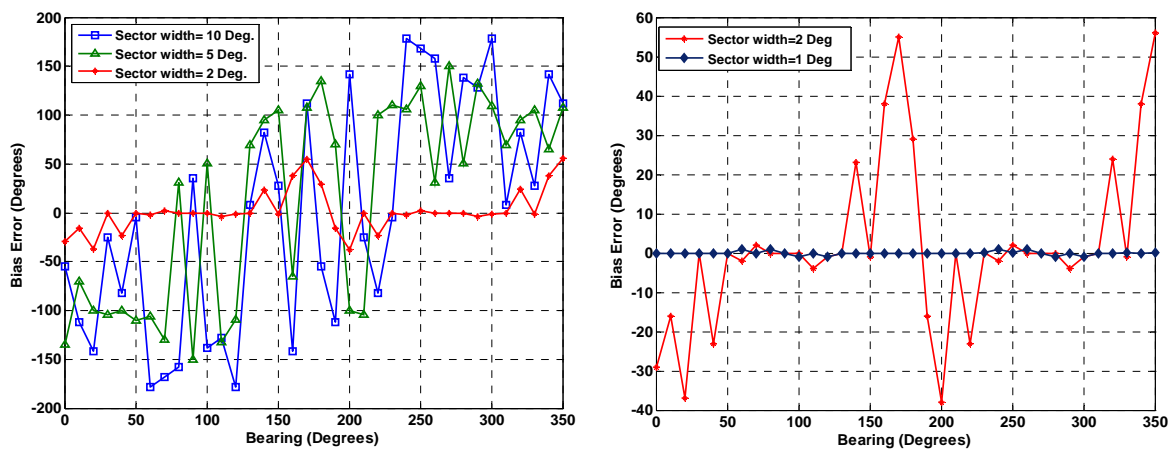


Figure 6.6 Bias error in bearing estimation for different sector width and fixed virtual inter-element spacing of $dv=10m$

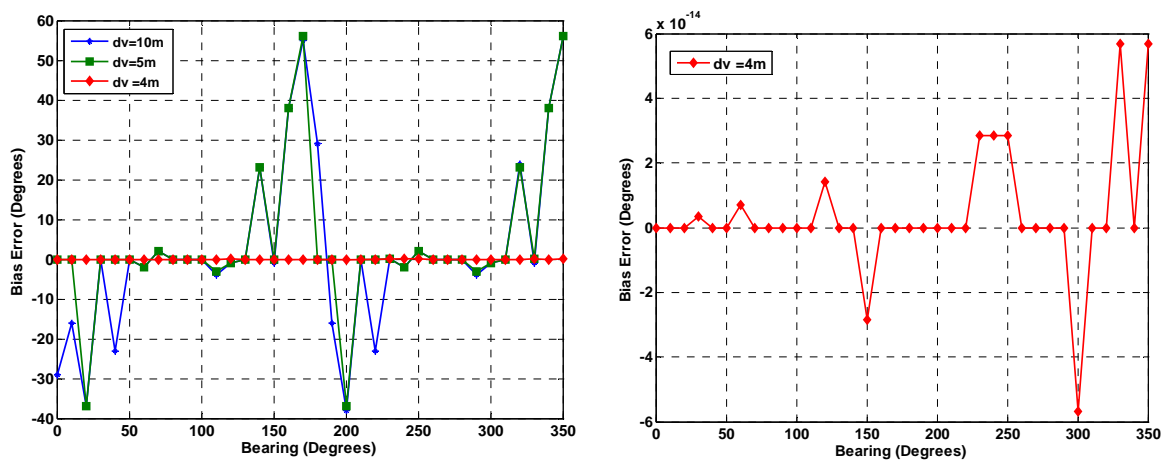


Figure 6.7. Bias error in bearing estimation for different virtual inter-element spacing (dv) and fixed sector width of 2 degree

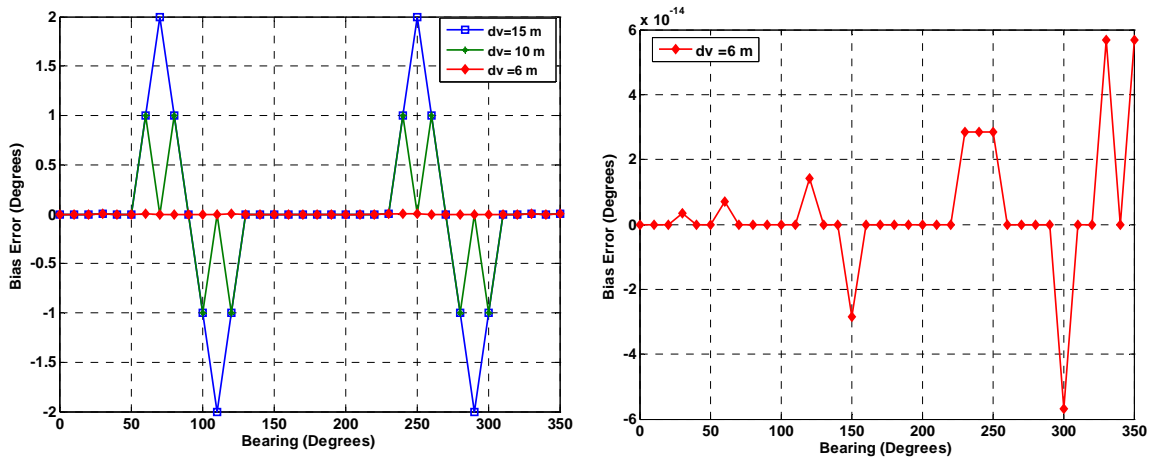


Figure 6.8. Bias error in bearing estimation for different virtual inter-element spacing (dv) and fixed sector width of 1 degree

6.3.2 Bearing estimation using VAS

VAS performance was evaluated based on transformation of an array of sparse DIFAR sonobuoys to a uniform linear array (ULA) with inter-element spacing less than d_{\max}^{DIFAR} . The real and virtual arrays are confined to the same plane. Bartlett beamforming was used for DOA estimation. The noise added to the acoustic signal is white Gaussian noise and 100 Monte Carlo runs were used to calculate the bearing error ranges. The various mapping matrices were calculated with the sector width set at 1 degree and inter-element spacing of 6m. The weighting constant (k) was set to 0.99. A set of calibrated directions uniformly spread across the azimuthal sector are used by VAS to estimate the true bearing of the target. The performance of VAS is evaluated by comparing its output to the output of the real array processing at different SNRs.

6.4 Results and Discussion

The figures shown below illustrate the results obtained in testing the performance of an array of DIFAR sonobuoys versus single DIFAR sonobuoy processing. Results are shown for the case of target with bearings of 160° and 50° .

6.4.1 DIFAR ULA array and Virtual array with 60m and 6m Inter-element spacing respectively

The results recorded for this scenario are shown in Figures 6.9-6.16. Figure 6.9 and 6.10 represents the case of -30 dB SNR. At this level of SNR, VAS showed slightly better performance over the real array processing with 10 % bearing error instead of 20%. The main contribution introduced by VAS is illustrated in Figures 6.9, 6.11, 6.13 and 6.15 as it shows that VAS resultant radiation pattern was able to select the main lobe. The maximum value of this lobe takes place at the closest bearing to the true bearing of the target. Figure 6.12 and 6.16 illustrates the dramatic degradation in the performance of real array processing when the level of SNR decreases to -40 dB. The bearing error jumps to 58% which represents a severe system failure in bearing estimation. On the other hand, the performance of VAS remains close to the performance at -30 dB with only 15% error. The degradation in real array processing performance is caused by the high side lobes in the radiation pattern shown in Figure 6.4b. Moreover the errors resultant at -40 dB covers a wider range with some cases having bearing estimation error of 200° . The VAS on the other hand, exhibits a much smaller range of errors with a maxim error value of 30° . These results demonstrate the superior performance obtained by VAS which provided an

additional constrain for bearing estimation process. The results obtained for the case of simulated target with bearing of 30° (Figures 6.13-6.16) are very close to the results of simulated target with bearing of 160° . A slight variation can be observed in the performance of real and virtual array. However the real array processing results exhibited severe system failure at -40 dB with wider range of errors and the VAS processing preserved the system accuracy with bearing error of 20%.

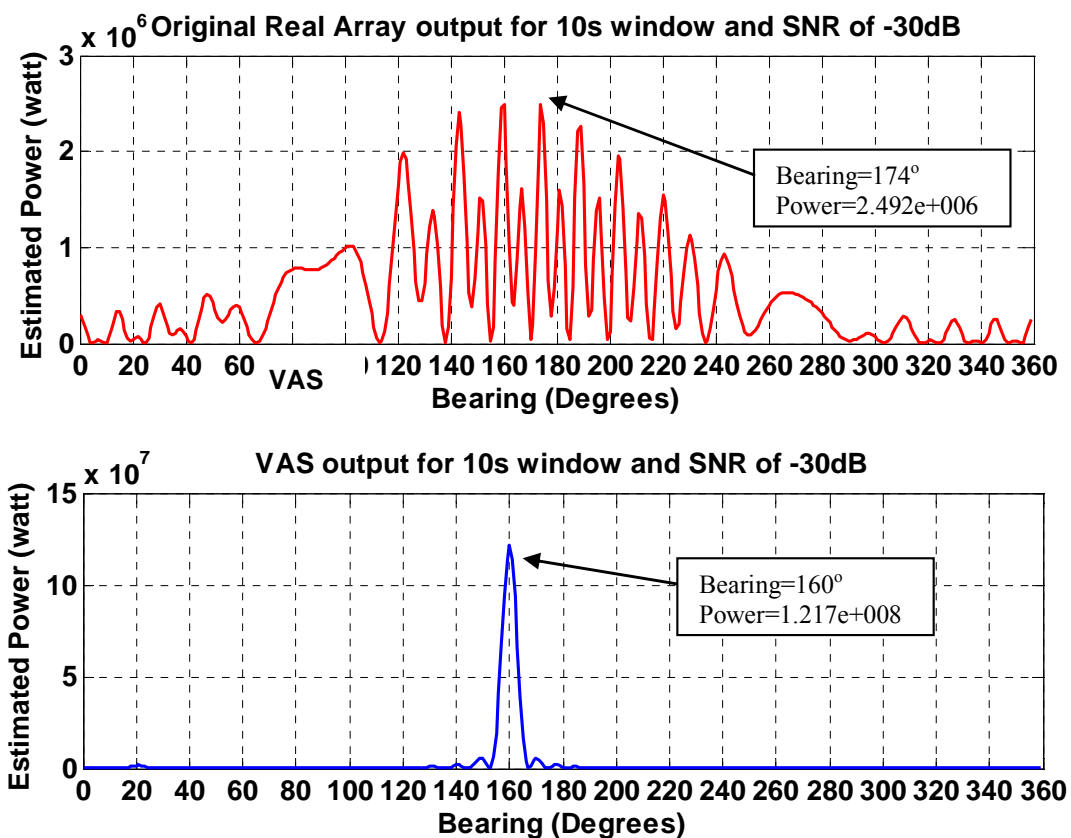


Figure 6.9 A sample of Bartlett Beamforming output ($d=60\text{m}$, $\text{SNR}=-30\text{dB}$) for ULA of 3 DIFAR sonobuoy (top panel) and virtual array of 23 DIFAR sonobuoys (bottom panel)

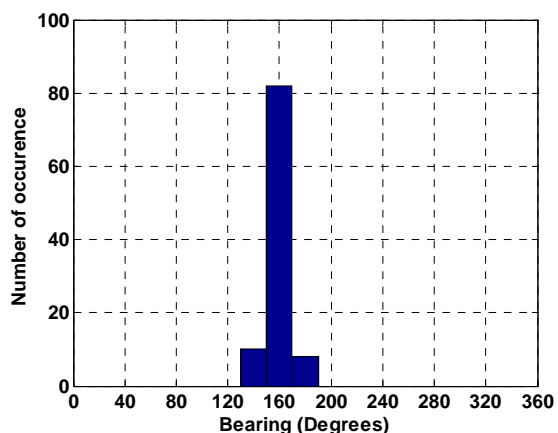


Figure 6.10a Output of Monte Carlo simulations for ULA of 3 DIFAR sonobuoys ($d=60\text{m}$, $\text{SNR}=-30\text{dB}$)

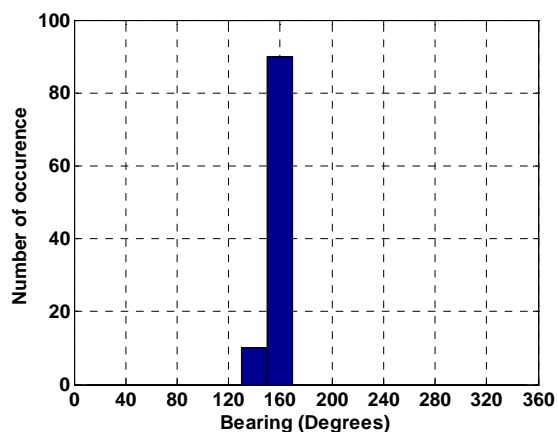


Figure 6.10b Output of Monte Carlo simulations for VA of 23 DIFAR sonobuoys ($d=6\text{m}$, $\text{SNR}=-30\text{dB}$)

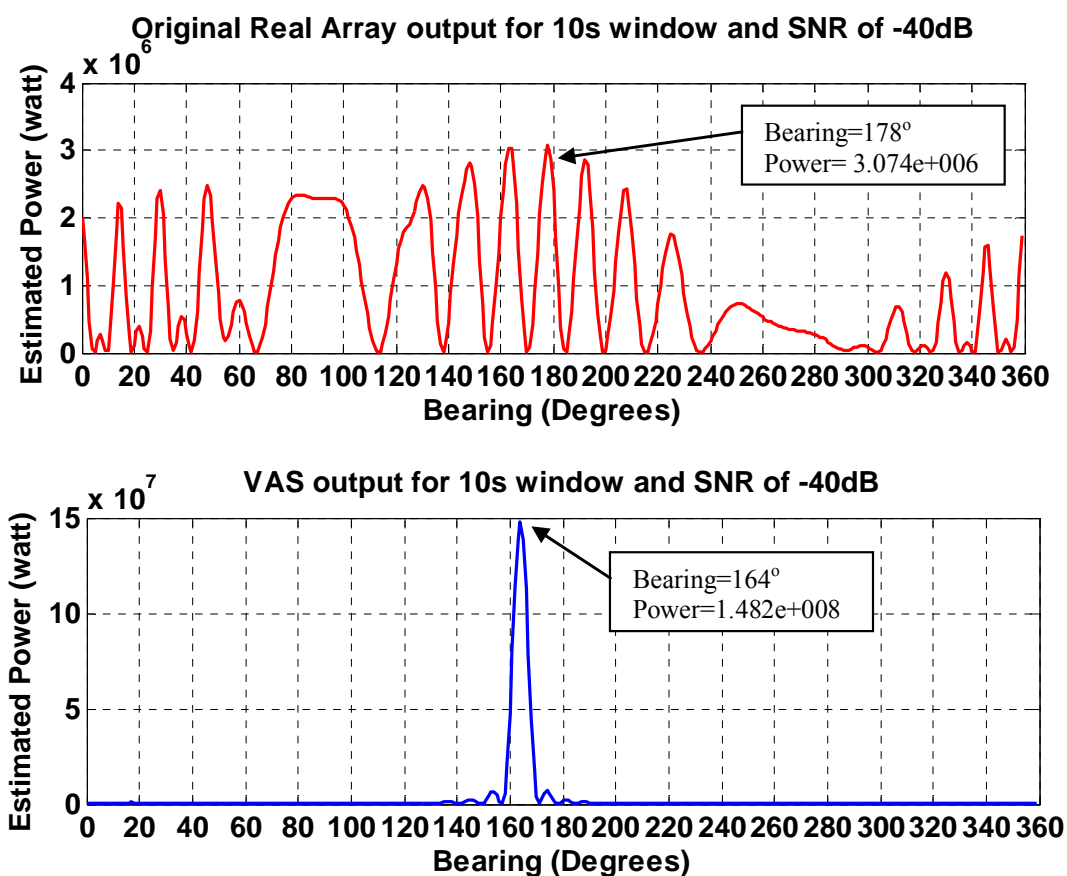


Figure 6.11 A sample of Bartlett Beamforming output ($d=60\text{m}$, $\text{SNR}=-40\text{dB}$) for ULA of 3 DIFAR sonobuoy (top panel) and virtual array of 23 DIFAR sonobuoys (bottom panel)

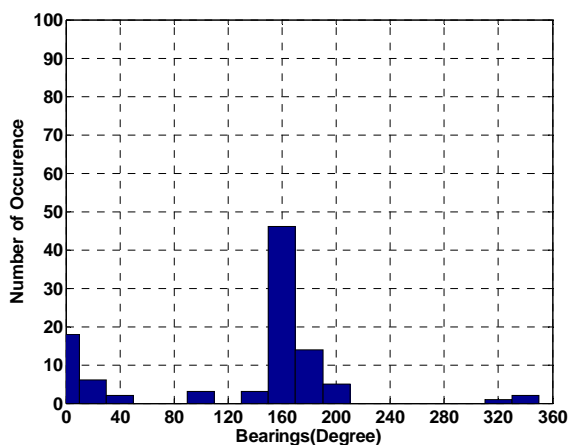


Figure 6.12a Output of Monte Carlo simulations for ULA of 3 DIFAR sonobuoys ($d=60\text{m}$, $\text{SNR}=-40\text{dB}$)

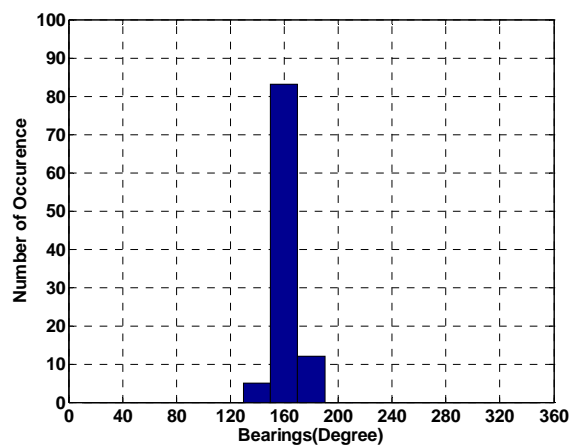


Figure 6.12b Output of Monte Carlo simulations for VA of 23 DIFAR sonobuoys ($d=6\text{m}$, $\text{SNR}=-40\text{dB}$)

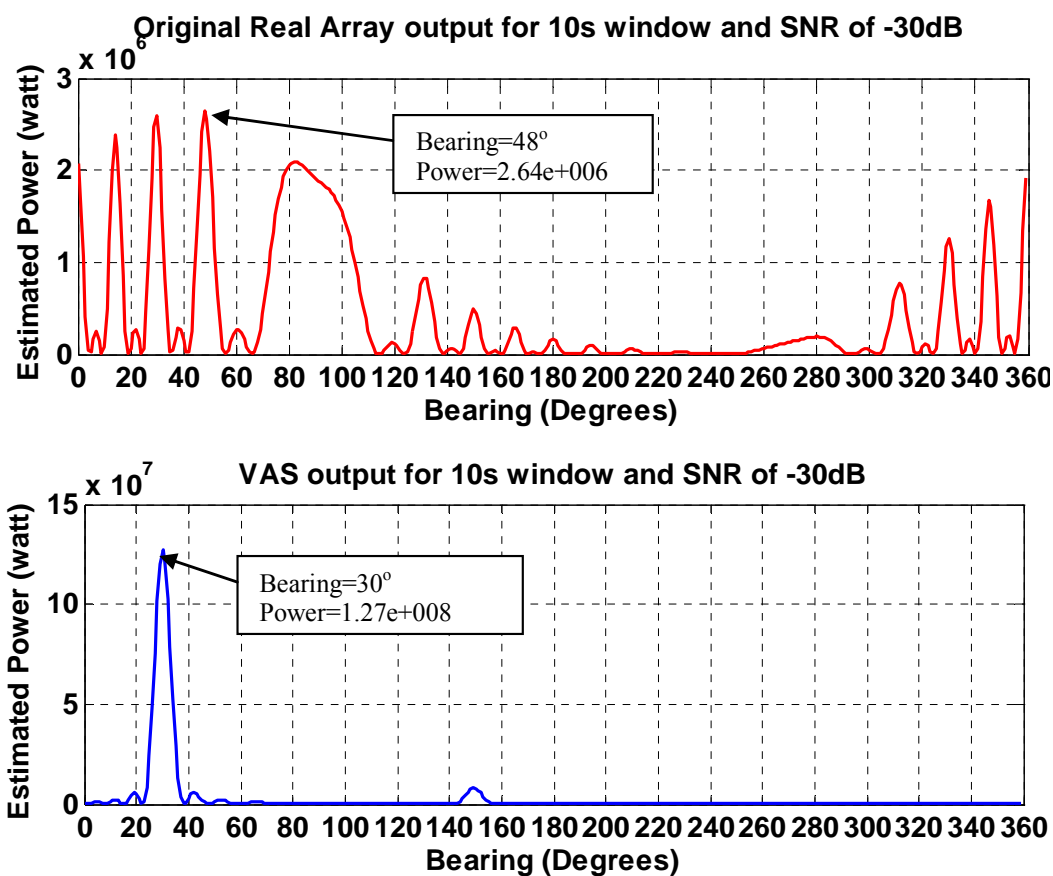


Figure 6.13 A sample of Bartlett Beamforming output ($d=60\text{m}$, $\text{SNR}=-30\text{dB}$) for ULA of 3 DIFAR sonobuoy (top panel) and virtual array of 23 DIFAR sonobuoys (bottom panel)

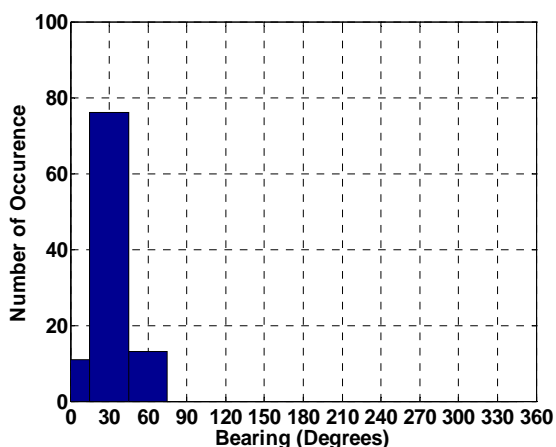


Figure 6.14a Output of Monte Carlo simulations for ULA of 3 DIFAR sonobuoys ($d=60\text{m}$, $\text{SNR}=-30\text{dB}$)

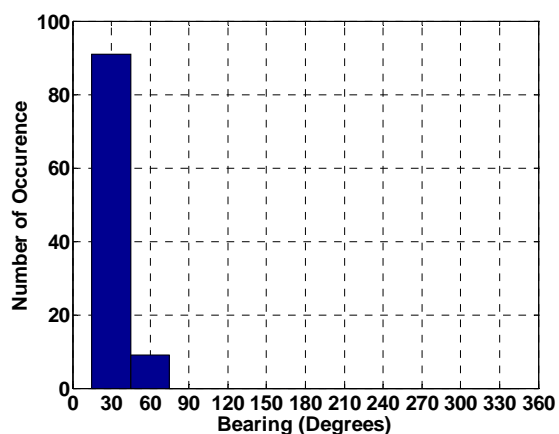


Figure 6.14b Output of Monte Carlo simulations for VA of 23 DIFAR sonobuoys ($d=6\text{m}$, $\text{SNR}=-30\text{dB}$)

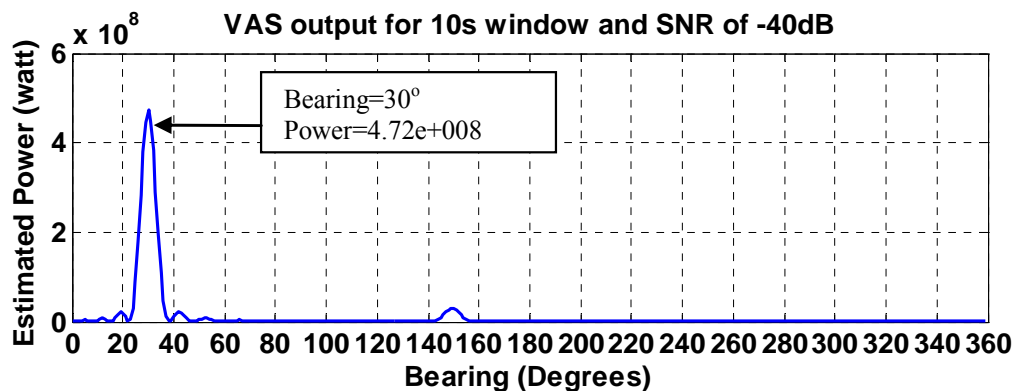
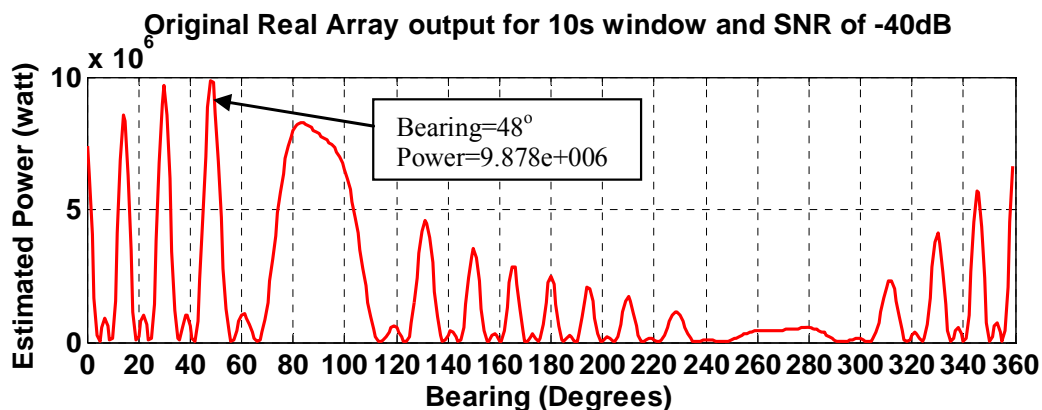


Figure 6.15 A sample of Bartlett Beamforming output ($d=60\text{m}$, $\text{SNR}=-40\text{dB}$) for ULA of 3 DIFAR sonobuoy (top panel) and virtual array of 23 DIFAR sonobuoys (bottom panel)

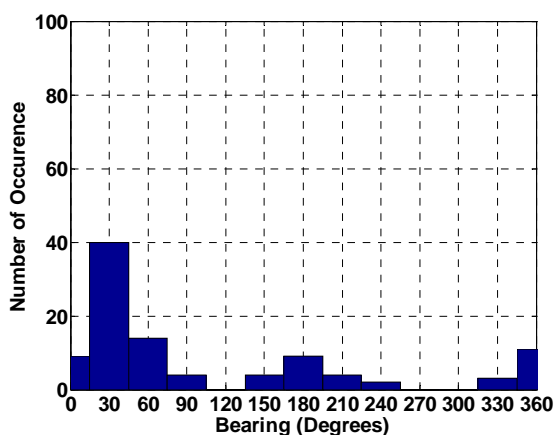


Figure 6.16a Output of Monte Carlo simulations for ULA of 3 DIFAR sonobuoys ($d=60\text{m}$, $\text{SNR}=-40\text{dB}$)

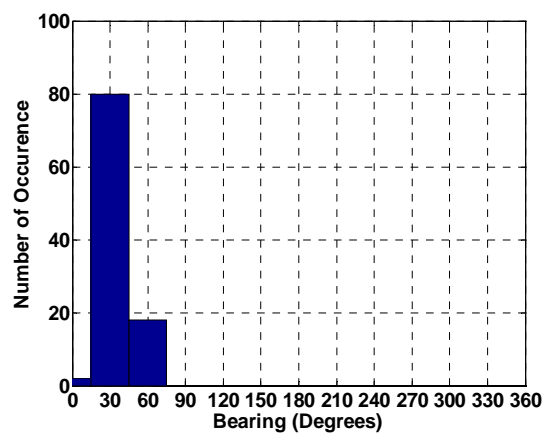


Figure 6.16b Output of Monte Carlo simulations for VA of 23 DIFAR sonobuoys ($d=6\text{m}$, $\text{SNR}=-40\text{dB}$)

6.4.2 Arbitrary array of DIFAR sonobuoys

The results recorded for this scenario are shown in Figures 6.17-6.24. It can be noticed that the performance of the arbitrary array of DIFAR sonobuoys is comparable to the performance of ULA of DIFAR sonobuoys. However, there is a slight increase in the error range for the arbitrary array of DIFAR sonobuoys at -30 dB SNR. The reason for this wider range of errors can be depicted from Figures 6.17, 6.19, 6.21 and 6.23. Obviously the arbitrary array of DIFAR sonobuoys exhibits a wider range of grating lobes and higher levels of side lobes. This results in degradation of performance in terms of error range. The performance of VAS remains consistent at -30 dB SNR with almost the same range of errors. This originates from the way VAS operates as it selects the true bearing out of the grating lobes. Figures 6.20 and 6.24 illustrate a huge degradation in the performance of arbitrary array processing when the level of SNR decreases to -40 dB .

This degradation is very close to that of the ULA of DIFAR sonobuoys as the bearing error is around 60% which represents a severe system failure in bearing estimation. On the other hand, the performance of VAS remains close to the performance at -30 dB SNR with only 15 % bearing error. The results obtained for the case of simulated target with bearing of 30° (Figures 6.21-6.24) are very close to the results of simulated target with bearing of 160° . This indicates the consistent operation of VAS as it provides similar performance at different bearings. In addition VAS provides robust means for processing arbitrary arrays as ULA which can be considered as an advantage for bearing estimation methods designed for ULA processing.

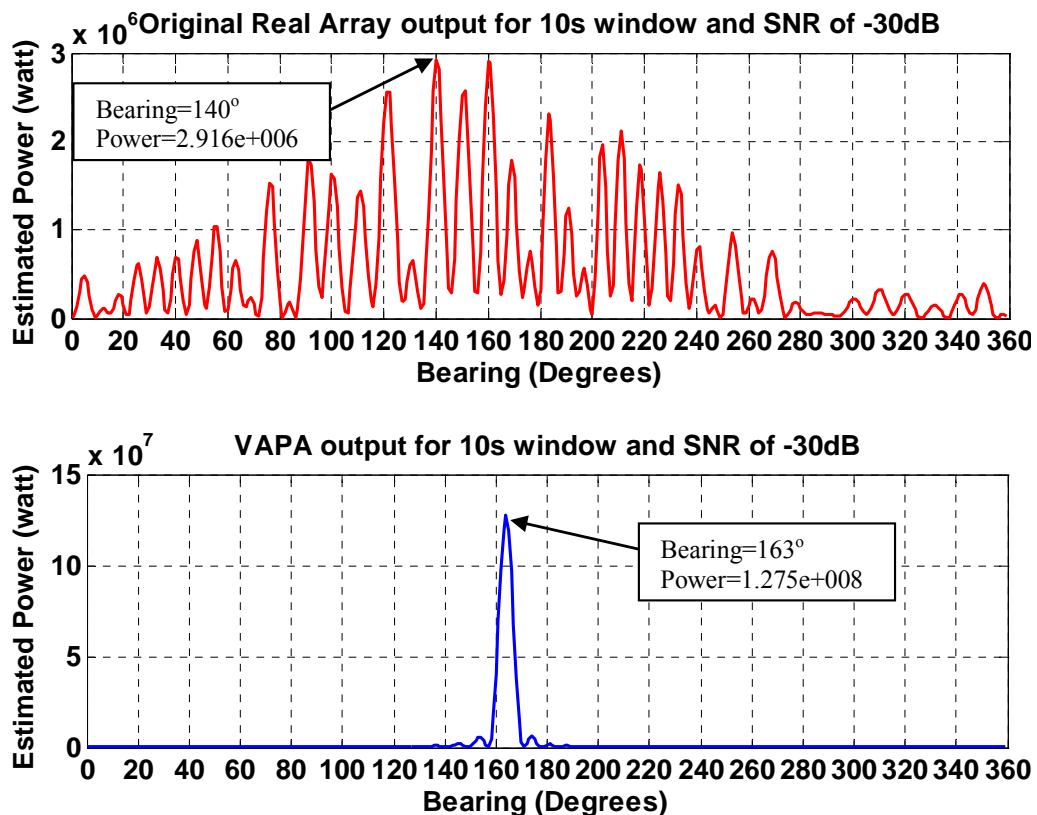


Figure 6.17 A sample of Bartlett Beamforming output for arbitrary array shown in Figure 6.5 (top panel) and virtual array of 26 DIFAR sonobuoys (bottom panel) with SNR -30 dB

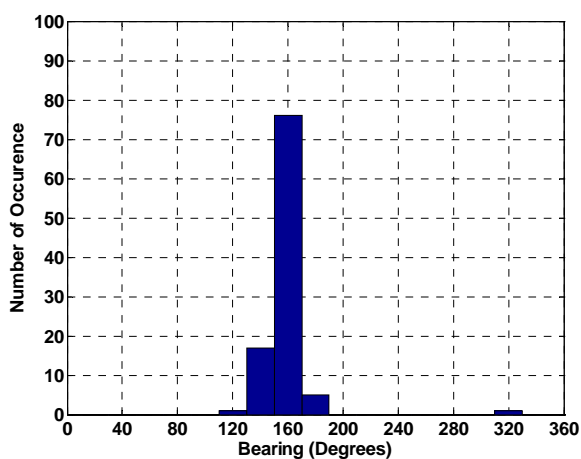


Figure 6.18a The output of Monte Carlo simulations for ULA of 3 DIFAR sonobuoy with $d=60\text{m}$ and $\text{SNR}=-30\text{ dB}$

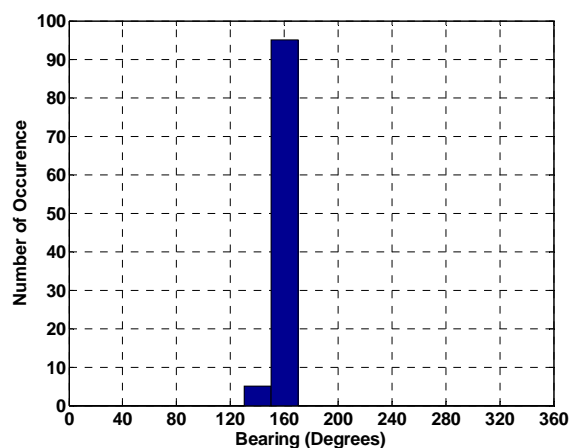


Figure 6.18b The output of Monte Carlo simulations for Virtual ULA of DIFAR sonobuoys with $d=6\text{m}$ and $\text{SNR}=-30\text{ dB}$

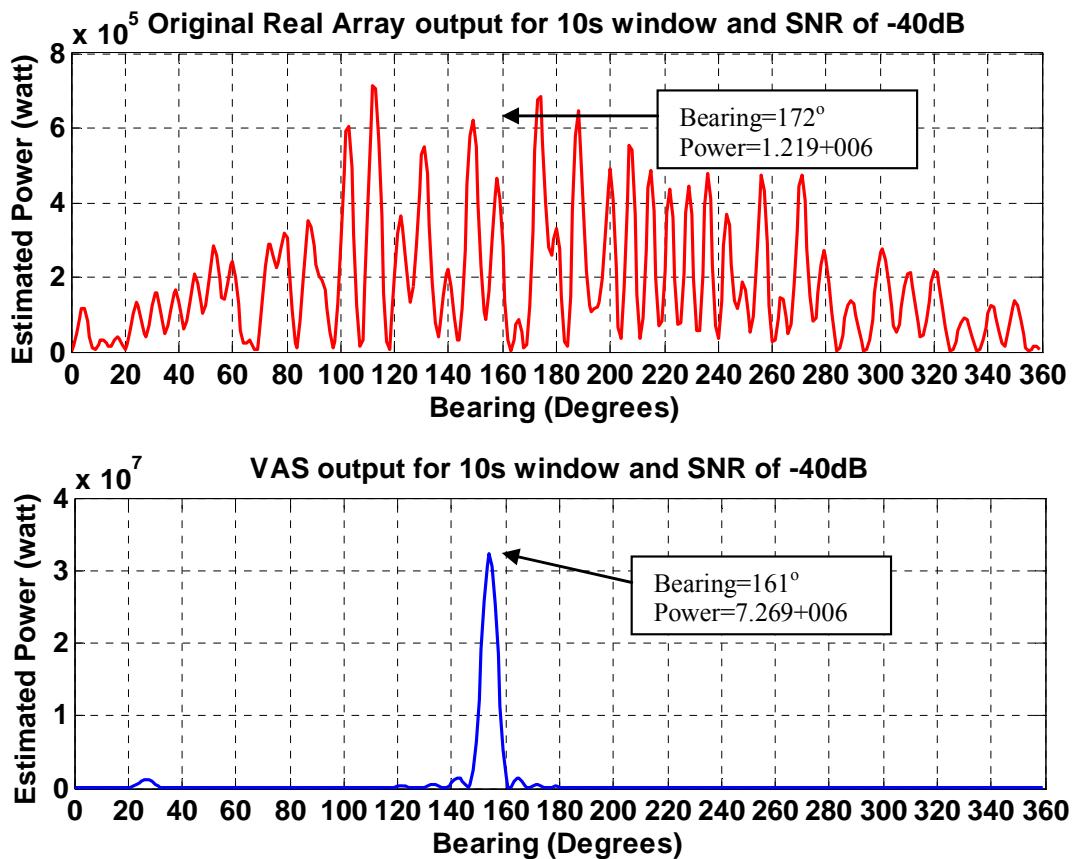


Figure 6.19 A sample of Bartlett Beamforming output for arbitrary array shown in Figure 6.2 (top panel) and virtual array of 26 DIFAR sonobuoys (bottom panel) with SNR -40 dB

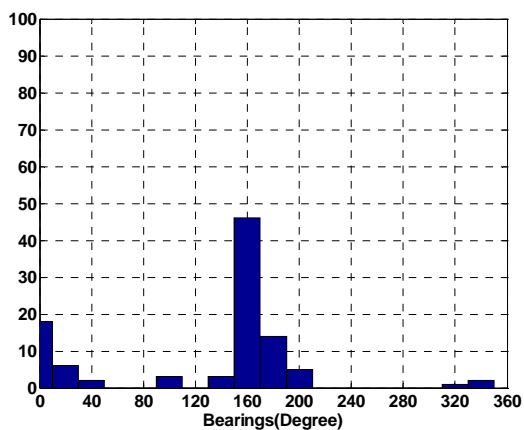


Figure 6.20a The output of Monte Carlo simulations for ULA of 3 DIFAR sonobuoy with $d=60m$ and $SNR=-40$ dB

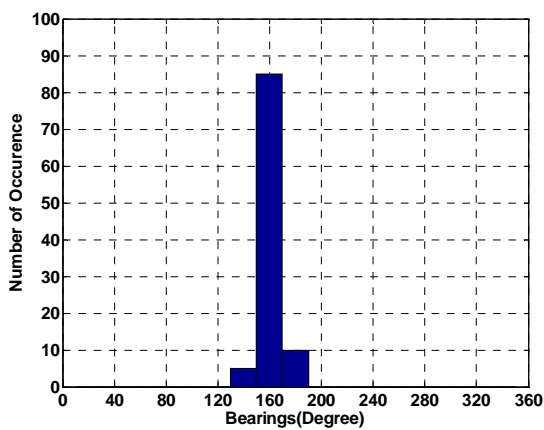


Figure 6.20b The output of Monte Carlo simulations for Virtual ULA of DIFAR sonobuoys with $d=6m$ and $SNR=-40$ dB

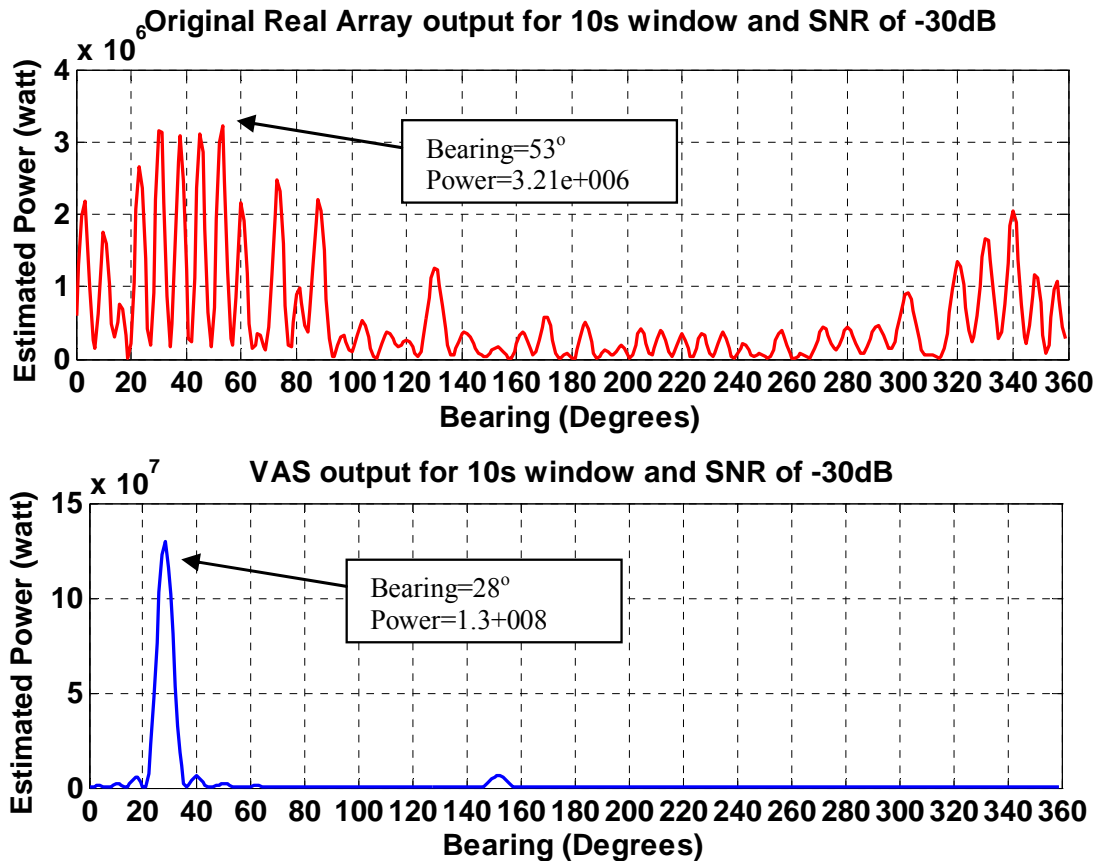


Figure 6.21 A sample of Bartlett Beamforming output for arbitrary array shown in Figure 6.2 (top panel) and virtual array of 26 DIFAR sonobuoys (bottom panel) with SNR -30 dB

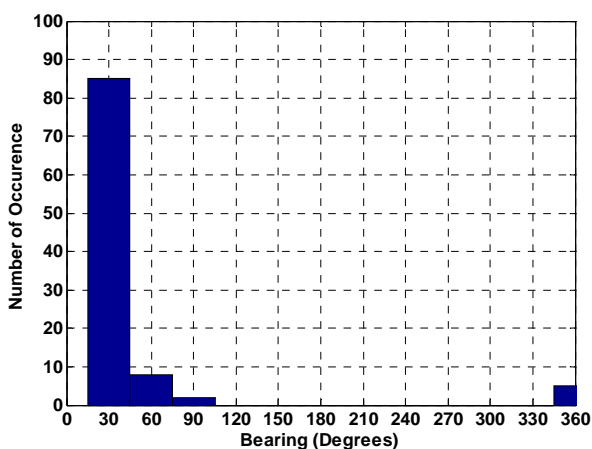


Figure 6.22a The output of Monte Carlo simulations for ULA of 3 DIFAR sonobuoy with $d=60m$ and $SNR=-30$ dB

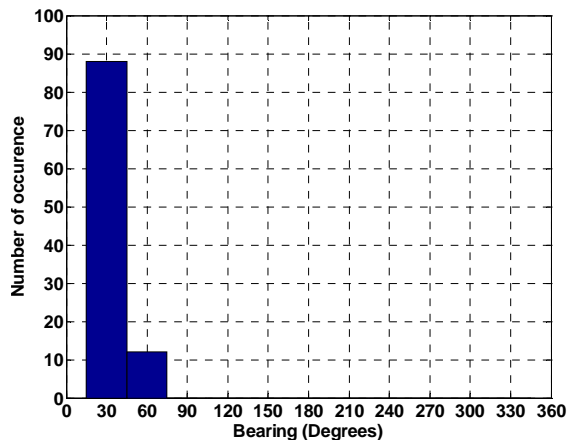


Figure 6.22b The output of Monte Carlo simulations for Virtual ULA of DIFAR sonobuoys with $d=6m$ and $SNR=-30$ dB

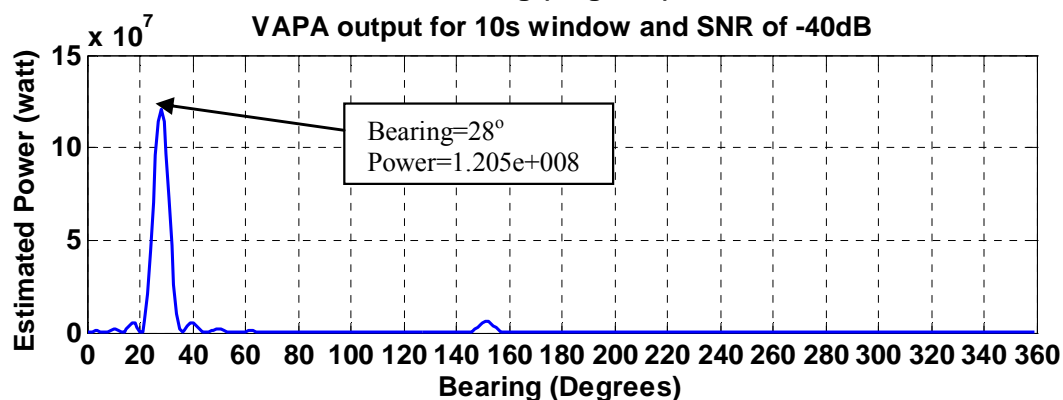
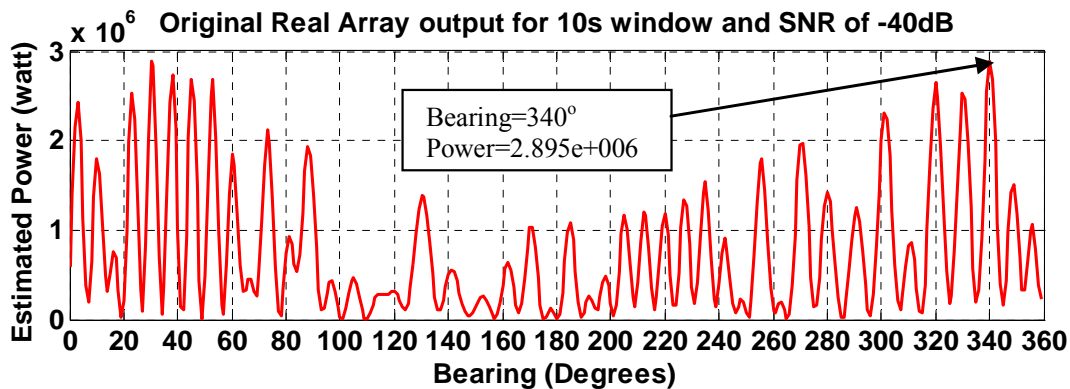


Figure 6.23 A sample of Bartlett Beamforming output for arbitrary array shown in Figure 6.2 (top panel) and virtual array of 26 DIFAR sonobuoys (bottom panel) with SNR -40 dB

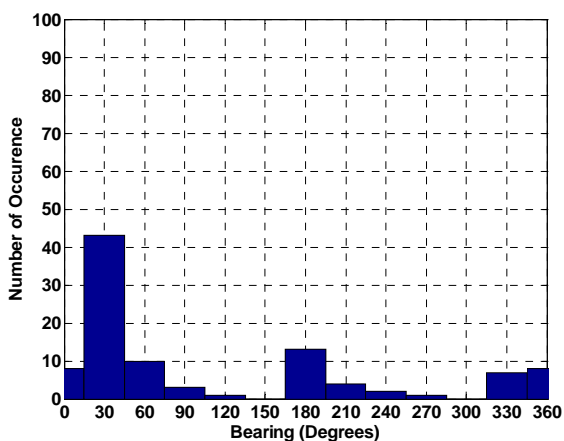


Figure 6.24a The output of Monte Carlo simulations for ULA of 3 DIFAR sonobuoy with $d=60\text{m}$ and $\text{SNR}=-40\text{ dB}$

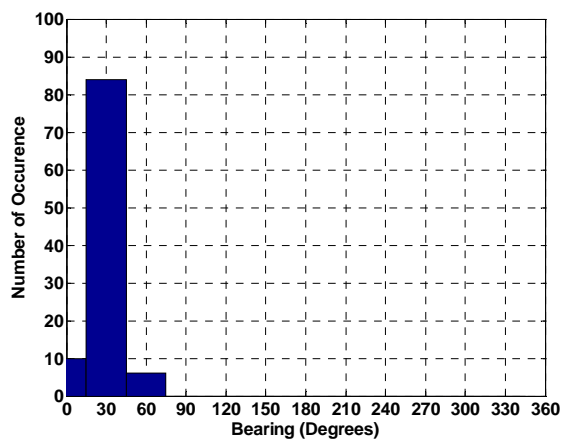


Figure 6.24b The output of Monte Carlo simulations for Virtual ULA of DIFAR sonobuoys with $d=6\text{m}$ and $\text{SNR}=-40\text{ dB}$

6.5 Performance analysis and limitations of VAS

In this section the limitations of VAS are discussed based on the processing of ULA of DIFAR sonobuoys. The examination of VAS is based on the comparison of its performance at different inter-element spacing values of ULA of DIFAR sonobuoys. The inter-element spacing of virtual array elements were fixed to 6m to preserve the minimum bias in the transformation matrix as this value showed minimum bias for the transformation of the examined ULA spacing values. The ULA of DIFAR sonobuoys had inter-element spacing values of 60m, 150m and 300m. Arbitrary arrays of DIFAR sonobuoys do not have specified forms that can be compared to one other, therefore they were not considered in this section. Figures 6.25 and 6.26 demonstrate the results obtained using the same simulated signal utilized in the previous sections.

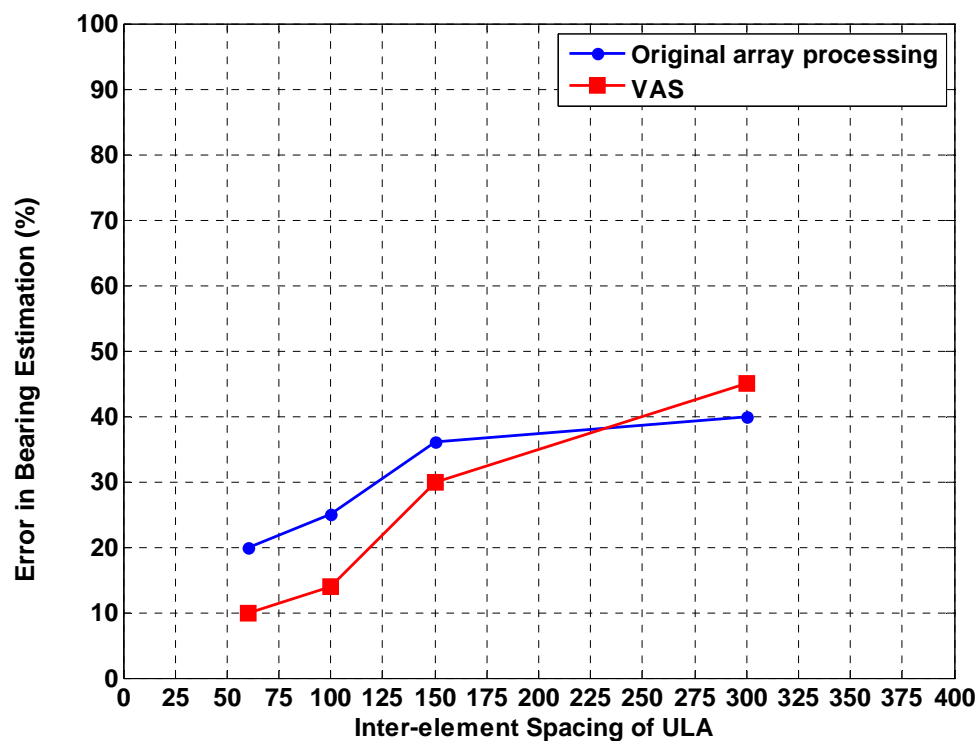


Figure 6.25 Performance of VAS versus Basic Processing of ULA at different inter-element distances for SNR -30 dB

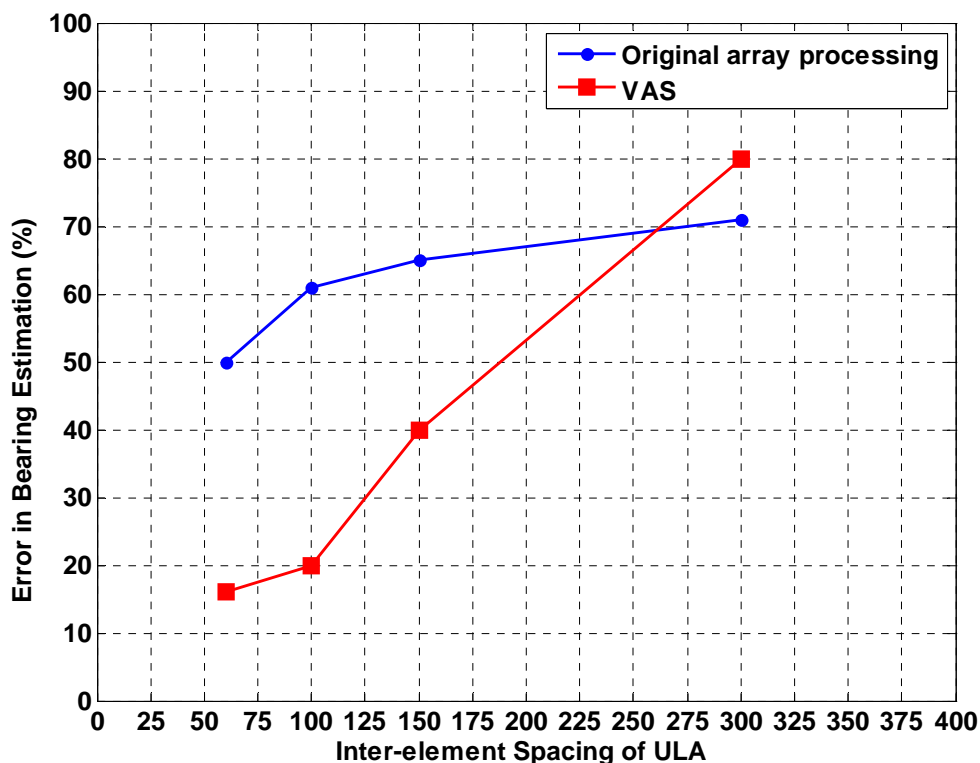


Figure 6.26 Performance of VAS versus Basic Processing of ULA at different inter-element distances for SNR -40 dB

The above Figures illustrate the significant contribution introduced by VAS. The maximum error reduction introduced by VAS is 10% for the case of SNR -30 dB (Figure 6.25). This corresponded to ULA inter-element spacing of 50m. However the bearing error of VAS increases as the inter-element spacing between DIFAR sonobuoys increases. The improvement introduced by VAS is further illustrated in Figure 6.26 for -40 dB SNR where the error reduction established by VAS ranges between 25% and 40%. The VAS method in this case provides robust system performance at very low SNR. This is more significant for the case of ULA of 100 m inter-element spacing. At this point VAS reduced the bearing error from 60% to 20% and hence it converted unstable system performance to a reliable one with a relatively acceptable accuracy. It

can be observed that at inter-element spacing of 300m the performance of original array processing is better than that of VAS. This can be considered as a limitation on the VAS method. However the system performance for this inter-element spacing possesses relatively high bearing errors for original array processing and VAS. In Chapter 4 it was shown in section 4.2.3.4 that single sonobuoy processing provides better results than ULA array processing when inter-element spacing is 300m. This suggests that bearing errors exhibited by original array processing and VAS can be considered as a general limitation on array processing for ULA of DIFAR sonobuoys.

6.6 Conclusion

This chapter discussed the merits and limitation of a new method for array processing for a group of DIFAR sonobuoys. The new method (VAS) is based on searching a set of transformation matrices corresponding to different sectors of possible target bearing. The transformation matrices parameters or the VAS were selected based on minimizing the bearing bias. A set of transformation matrices was generated for different inter-element spacing values. These were used to examine the performance of VAS against conventional methods for processing an array of DIFAR sonobuoys. VAS showed significant enhancement of system performance especially at SNR of -40db which is considered relatively very low SNR level. The system of 50 m spacing was able to provide a robust operation using VAS with 10% bearing error. Superior performance was also obtained at a SNR of -40 dB with 16% bearing error. System performance degraded with the increase in inter-element spacing. This can be considered as the main

limitation on VAS or array processing to a group of free floating sonobuoys. Moreover, the VAS approach performed equally for both ULA and irregular arrays of DFAR sonobuoys.

In general, it can be concluded that applying VAS for a group of DFAR sonobuoys provides noticeable enhancement to system accuracy and robustness. The only limitation is imposed by the spacing between the DFAR sonobuoys which can range from few meters to hundreds of meters. Further investigation of alternative techniques for transformation matrix design could extend system capabilities for larger values of array inter-element spacing.

Chapter Seven: CONCLUSION AND RECOMMENDATIONS FOR FUTURE RESEARCH

7.1 Summary

This thesis aimed at introducing a new signal processing scheme for bearing estimation using array of GPS sonobuoys. The objective of this research was to apply advanced high resolution spectral estimation method and develop a robust coherent array processing module of GPS sonobuoys field in order to enhance the target detection and bearing estimation accuracy.

This research started with a qualitative study of the feasibility of utilizing FOS for spectral analysis of the acoustic signals for target detection phase in TMA process, which showed the low susceptibility of the FOS to various levels of noise.

A new approach for array processing using a group of DIFAR sonobuoys was examined as well, showing its significant enhancements to the bearing estimation accuracy at very low SNRs. The new approach examined the radiation pattern of both ULA and arbitrary array of DIFAR sonobuoys. The DIFAR array radiation pattern was developed for two operational modes of DIFAR sonobuosity which are: (1) omnidirectional operational mode, where DIFAR sonobuoys employ only omnidirectional sensor data in bearing estimation process; (2) full operational mode, where the DIFAR sonobuoys used data recorded from the three sensors of each sonobuoy in the array. The equations for the radiation pattern of group of DIFAR sonobuoys were derived for the full operational mode. This approach showed a significant enhancement to bearing

estimation accuracy over the one provided by single sonobuoy processing at relatively low SNRs. The performance of array processing showed huge degradation at wide inter-element spacing. This research proposed two bearing estimation techniques in order to account for the wide inter-element spacing between the elements of the DIFAR sonobuoys array. The first technique was based on bearing estimation using complex least mean square algorithm augmented by ANN to resolve the DOA ambiguity resulting from the wide inter-element spacing for a uniform 2-D array of omni-directional hydrophones. This technique provided enhanced bearing estimation accuracy at very low SNRs and relatively wide inter-element spacing. The second technique was based on bearing estimation using the conventional Bartlett beamforming augmented by the VAS approach. The VAS is mainly based on generating transformation matrices that are unique for different sectors. This provided additional criterion that enhanced bearing estimation accuracy for a group of widely spaced ULA of DIFAR sonobuoys and arbitrary array of DIFAR sonobuoys. Moreover this method provided an extension to the maximum inter-element spacing with relatively high bearing estimation accuracy.

7.2 Conclusions

The following conclusions can be drawn from the results of the simulations performed in the course of this study:

7.2.1 Qualitative study for the applicability of FOS in underwater Target Detection and Bearing Estimation

The results showed that FOS provided better performance than FFT for most cases of low SNR. FOS also offered clearer spectral estimation since it allocated power only for selected number of candidates without using an amplitude threshold which might cause the loss of the target signal. Moreover, the use of FOS enhanced the accuracy of bearing estimation especially at relatively low SNR which was observed at SNRs lower than -25 dB. For short data records FOS outperformed FFT in both target detection and bearing estimation. The simulation results demonstrated in Chapter 3 showed that FOS could significantly enhance the bearing estimation process by providing highly accurate spectral estimates.

7.2.2 DOA Estimation using an Array of GPS Sonobuoys

The steering vector for the array of DIFAR sonobuoys was derived as well as the radiation pattern of the array of sonobuoys. These were used to define the maximum spacing value between the DIFAR sonobuoys which showed that for guaranteed system stability, the maximum allowable inter-element spacing was close to the omni-directional array case. Nevertheless, it was shown that a system with acceptable stability can be obtained with inter-element spacing exceeding the critical value of spacing with few meters. The array processing for a group of DIFAR sonobuoys showed significant enhancement of system performance especially at SNR as low as -40dB. A completely robust operation with almost 0% error was obtained at relatively close inter-element

spacing of DIFAR sonobuoys array. Superior performance was also obtained at a SNR of -40 dB with an error of 21% which is compared to 75% error obtained for the case of single sonobuoy processing. Of course system performance degraded with the increase in inter-element spacing values. This can be considered the main limitation on applying array processing to a group of free floating sonobuoys. Arbitrary arrays of DIFAR sonobuoys were also examined and showed different performances based on the arrangement of the DIFAR sonobuoys. The irregularity in the sonobuoys array arrangement provided some performance enhancement with errors ranging between 10% and 26% at -35 dB SNR. Apparently, the error varied with the change in the arrangement pattern. Therefore, this can be considered a limited improvement since the obtained performance was very sensitive to the changes in the locations of array elements. In general the array processing for a group of DIFAR sonobuoys provides noticeable enhancement to system accuracy and robustness.

7.2.3 DOA Estimation using Frequency Beamforming and ANN

This approach was adopted to address the processing of spatially aliased array of Omni-directional hydrophones. The proposed method was based on non conventional FB technique augmented by ANN. Results showed that the proposed approach provided a robust module for processing spatially aliased arrays. For no noise cases the proposed module was capable of providing bearing estimation with average error of 11.1% which corresponds to 101m inter-element spacing. It was shown that the system performance is crucially affected by SNR of the received signal and the proper design of ANN. The

system performance degradation at relatively low levels of SNR imposed a limitation on inter-element spacing. The proposed approach had further limitations on the arrangement of array elements that required arranging the elements in 2-D constellation with odd number of sensors in each direction.

7.2.4 Direction of Arrival Estimation using VAS

The application of VAS to the problem of array processing for a widely spaced array of DIFAR sonobuoys showed considerable enhancement to the overall system performance. The new method (VAS) was based on searching a set of transformation matrices corresponding to different sectors of possible target bearings. The transformation matrices parameters of the VAS were selected based on bearing bias minimization. VAS showed improvement to system performance especially at relatively very low SNR environments. The system of 50 meter spacing was able to provide a robust operation using VAS with 10% error in bearing estimation at -30 dB SNR. Superior performance was also obtained at a SNR of -40 dB with an error of only 16%. System performance degraded with the increase in spacing values which was considered as the main limitation on VAS for array processing to a group of free floating sonobuoys. However, VAS was still able to perform adequately up to distances larger than those of other methods proposed in this thesis. Moreover the irregularity in the sonobuoys array arrangement did not affect the operation of VAS as it showed almost similar performance to those obtained when VAS was applied to a ULA of DIFAR sonobuoys.

7.3 Thesis contributions

In this thesis, a new spectral analysis methodology (FOS) based on orthogonal search was introduced as a replacement of the widely used DFT. This method provides higher resolution spectral estimation which mitigates spectral leakage caused by the relatively low resolution of DFT. This method enhanced the detection accuracy of the DIFAR sonobuoys and provided a clear spectral estimate if compared to the conventional method. Moreover, this method enhanced the DIFAR sonobuoys bearing estimation accuracy at relatively low SNRs and outperformed DFT at relatively short data records.

This thesis also introduced a new approach for coherent processing a group of DIFAR sonobuoys rather than combining the bearing estimates of a group of DIFAR sonobuoys processed individually. The new approach adopted the coherent processing of a group of DIFAR sonobuoys in ULA arrangement as well as arbitrary array arrangement. This approach showed significant improvement in bearing estimation accuracy at relatively very low SNRs with some limitations on inter-element spacing and arbitrary arrangements of the array elements.

In this thesis, a new method augmenting FB with ANN for processing omnidirectional array of GPS sonobuoys was proposed. The ANN module was efficiently utilized to resolve the DOA ambiguity resulting from the relatively large inter-element spacing. This research has also introduced the VAS approach used in processing a group of DIFAR sonobuoys using their omni, sine and cosine sensors.

7.4 Recommendations for future research

The bearing estimation techniques developed in this thesis are new approaches to enable coherent array processing of a group of DIFAR sonobuoys. The research work presented in this thesis provided merits and limitations associated with this approach. Therefore, the following recommendations are made for future studies on coherent array processing of a group of DIFAR sonobuoys:

7.4.1 Improving the parameters of TMA

The proposed methods in this thesis can be integrated with other system recorded data to provide a complete solution of target trajectory and its moving velocity. The system recorded data includes target bearings, SNR, Doppler shift and other information from recording environmental conditions. Investigating the enhancement of the accuracy of Doppler shift recorded data and environmental information can benefit the target tracking process and provide more accurate solution for TMA. Moreover TMA analysis techniques previously developed for bearing estimates from different sonobuoys can be modified to make use of the coherent array processing algorithm. The modification would be to divide the DIFAR sonobuoys into multiple arrays that provide bearing estimation with higher accuracy than individual DIFAR sonobuoy processing. Bearing estimates from multiple arrays can then be used by the TMA methods instead of using bearing estimates from data recorded by each DIFAR sonobuoy.

7.4.2 Exploring the application of VAS with other bearing estimation methods

In order to avoid the shortcomings of the conventional bearing estimation algorithm provided by Bartlett beamforming, other techniques can provide more enrichment to the system performance and their suitability for bearing estimation might be investigated. The bearing estimation methods employing adaptive beamforming techniques to provide higher resolution beamforming [Greening02 and Kogon02] had an inter-element spacing less than half wavelength of the tracked sources which can be more suitable for towed arrays. These methods can be investigated for their application to DIFAR sonobuoys. Also VAS can be used as a tool that provides robust bearing estimation when inter-element spacing values are relatively large or array elements are arbitrary arranged.

7.4.3 Exploring the Benefits of FOS for ambiguity resolution of direction cosines in the frequency beamforming method

In this thesis ANN was utilized to provide mapping between the ambiguous direction cosines and the correct ones. ANN requires long training time and provides empirical mapping function. It is therefore recommended to investigate the use of FOS to provide a nonlinear model for this ambiguity resolution. Establishment of the model could be faster than that of ANN while providing similar performance.

References

- [Adeney94] Adeney, K.M. and Korenberg, M. J., “*Fast orthogonal search for array processing and spectrum estimation*”, IEE Proceedings-Vision, Image and Signal Processing, v 141, n 1, Feb. 1994, p 13-18.
- [Aidala79] Aidala, V.J., “*Kalman Filter Behavior in Bearings-Only Tracking Applications*”, Aerospace and Electronic Systems, IEEE Transactions on, v 15, n1, Jan. 1979, p 29 – 39.
- [Ali03] Ali, E.F.A., “*Application of the Fast Orthogonal Search in Automatic Target Detection*”, Ph.D. Thesis, Department of Electrical and Computer Engineering, Royal Military College of Canada, Kingston, Ontario, 2003.
- [Armstrong06] Armstrong, J., “*Application of fast orthogonal search to accuracy enhancement of Inertial sensors for land vehicle navigation*”, M.Sc.Thesis, Department of Electrical and Computer Engineering, Royal Military College of Canada, 2006.

- [Atkins94] Atkins, P., "*Tutorial introduction and historical overview of the need for heading sensors in sonar applications*", IEE Colloquium on Heading Sensors for Sonar and Marine Applications, 1994, p 1-6.
- [Bavencoff06] Bavencoff, F.; Vanpeperstraete, J.M. and Le Cadre, J.P., "*Constrained bearings-only target motion analysis via Markov chain Monte Carlo methods*", Aerospace and Electronic Systems, IEEE Transactions on, v 42, n 4, Oct. 2006, p 1240 – 1263.
- [Beisner74] Beisner, H.M, "*Numerical calculation of normal modes for underwater sound propagation*", IBM Journal of Research and Development, v 18, n 1, Jan. 1974, p 53-58.
- [Bienvenu91] Bienvenu, G. and Owsley, N. L., "*High resolution passive array processing. An overview of principles*", Lecture Notes in Control and Information Sciences, v 155, 1991, p 9-28.
- [Bonneton07] Bonneton, F and Jauffret, C., "*Bearing Line Tracking and Bearing-Only Target Motion Analysis*", IEEE Aerospace Conference 2007, 3-10 March 2007, p 1 – 9.

- [Brooke01] Brooke, G.H.; Thomson D.J. and Ebbeson G.R., "*PECan: a Canadian parabolic equation model for underwater sound propagation*", Journal of Computational Acoustics, v 9, n 1, March 2001, p 69-100.
- [Bromwich26] Bromwich, T.J., "*An Introduction to the Theory of Infinite Series*" MacMillan & Co. 1926.
- [Brown96] Brown, P. and Kirby, S., "*Operational field trials of GPS equipped Sonobuoys*", Proceedings of ION GPS 1996, v 2, Sept. 1996, p 1553-1561.
- [Boh05] Bohac, F., "*DIFAR Sonobuoy Bearing Estimation Using the Fast Orthogonal Search Algorithm*", M.Sc.Thesis, Department of Electrical and Computer Engineering, Royal Military College of Canada, 2005.
- [Bucker76] Bucker, H.P., "*Use of calculated sound fields and matched-field detection to locate sound sources in shallow water*", Journal of the Acoustical Society of America, v 59, n 2, Feb. 1976, p 368-73.
- [Chan95] Chan, Y.T.; Niezgoda, G.H. and Morton, S.P., "*Passive sonar detection and localization by matched velocity filtering*", Oceanic Engineering, IEEE Journal of, v 20, n 3, July 1995, p 179 – 189.

- [Chen03] Chen, J.C.; Yip, L.; Elson, J.; Hanbiao Wang; Maniezzo, D.; Hudson, R.E.; Kung, Yao and Estrin, D., “*Coherent acoustic array processing and localization on wireless sensor networks*”, Proceedings of the IEEE, v 91, n 8, Aug. 2003, p 1154 – 1162.
- [Chon01] Chon, K.H., “*Source Accurate identification of periodic oscillations buried in white or colored noise using fast orthogonal search*”, IEEE Transactions on Biomedical Engineering, v 48, n 6, June 2001, p 622-629.
- [Cunn05] Cunningham, A.and Thomas, B., “*Target motion analysis visualization*”, Asia Pacific Symposium on Information Visualisation (APVIS 2005), v 45, Sydney, Australia, 2005, p 81 – 90.
- [D’Spain92] D’Spain, G.L.; Hodgkiss, W.S; Edmonds, G.L.; Nickles J.C.; Fisher, F.H.and Harriss, R.A, “*Initial Analysis Of The Data From The Vertical DIFAR Array*”, OCEANS '92 Proceedings,v1, October 26-29, 1992 p 346 – 351.
- [Davis93] Davis, T.E., “*A Comparison of Fast Orthogonal Search, Fourier Transform and Wavelet Transform Approaches in Nonstationary Signal Analysis*”, M.Sc. Thesis, Department of Electrical Engineering, Queen’s University, 1993.

- [Des99] Desrochers, D., "*High resolution Beamforming Techniques Applied to a DIFAR Sonobuoy*", M.Sc.Thesis, Department of Electrical and Computer Engineering, Royal Military College of Canada, 1999.
- [Du02] Du, K.-L.; Lai, A.K.Y.; Cheng, K.K.M. and Swamy, M.N.S., "*Neural methods for antenna array signal processing:A review*", *Signal Processing*, v 82, 2002, p547–561.
- [Dwight60] Dwight, H. B., "*Tables of integrals and other mathematical data*", MacMillan, New York, 1960.
- [El-Zooghby97] El-Zooghby, A.H.; Christodoulou, C.G. and Georgiopoulos, M., "*A neural network-based smart antenna for multiple source tracking*", *IEEE Transactions on Antennas and Propagation*, v 48, n 5, May 2000, p 768 - 776
- [Gabriel80] Gabriel, W. F., "*Spectral Analysis and Adaptive Array Superresolution Techniques*", in *Proceedings of the IEEE*, v 68, n 6, June 1980, p 654-666.
- [Gotsis09] Gotsis, K.A.; Siakavara, K. and Sahalos, J.N., "*On the Direction of Arrival (DoA) Estimation for a Switched-Beam Antenna System Using*

- Neural Networks*”, IEEE Transactions on Antennas and Propagation, v 57, n 5, May 2009, p 1399-1411.
- [Graves76] Graves R.D., Nagl A., Uberall H., Zarur G.L., “*Normal mode theory of underwater sound propagation in a range dependent environment*”, IEEE International Conference on Acoustics Speech and Signal Processing, April 1976, p 668-670.
- [Gershman95] Gershman, A. B.; Turchin, V. I. and Zverev, V. A., “*Experimental results of localization of moving underwater signal by adaptive beamforming*”, IEEE Transactions on Signal Processing, v 43, n 10, Oct. 1995, p 2249-2257.
- [Greening02] Greening, M.V. and Perkins, J.E., “*Adaptive beamforming for nonstationary arrays*”, Journal of the Acoustical Society of America, v 112, n 6, Dec. 2002, p 2872-2881.
- [Gregory01] Gregory, J. B. and Bonin, Y.R.M., “*GPS Equipped sonobuoy*”, Defense Research Establishment, Ultra Electronics -Hermes Electronics, 2002.
- [Ham01] Ham, F.M. and Kostanic, I., “*Principles of Neurocomputing for Science and Engineering*”, McGraw-Hill, 2001.

- [Hawker79] Hawker, K.E., “*A normal mode theory of acoustic Doppler effects in the oceanic waveguide*”, Journal of the Acoustical Society of America, v 65, n3, March 1979, p 675-681.
- [Haykin99] Haykin, S.,” *Neural Networks. A Comprehensive Foundation, 2nd ed*”, Englewood Cliffs, NJ: Prentice-Hall, 1999.
- [Haykin04] Haykin, S., “*Adaptive Filter Theory*”, Prentice Hall, 4th edition, Sept.14 2001.
- [Hinich78] Hinich, M. J., “*Processing spatially aliased arrays*”, Journal of the Acoustical Society of America, v 64, n 3, Sept. 1978, p 792-794.
- [Holler06] Holler, R., Horbach, A. and McEachern, J., “ *Not ready for retirement: The sonobuoy approaches age 65*”, Sea Technology, v 47, n 11, Nov. 2006, p 10-14
- [Horsley89] Horsley, L.E., ”*Modification and deployment techniques for hand-deployed Arctic long-life sonobuoys*”, IEEE Journal of Oceanic Engineering, v 14, n 2, April 1989, p 211 – 220.

- [Hyberg04] Hyberg, P., Jansson, M. and Ottersten, B., "*Array interpolation and bias reduction*", IEEE Transactions on Signal Processing, v 52, n 10, Oct. 2004, p 2711-2720.
- [Ifeachor02] Ifeachor, E. C. and Jervis, B. W., "*Digital Signal Processing*", Prentice Hall, 4th edition, Sept. 14, 2001.
- [Imai2000] Imai, R.; Hashimoto, Y.; Kikuchi, K. and Fujii, S, "*High-resolution beamforming by the Wigner-Ville distribution method*", IEEE Journal of Oceanic Engineering, v 25, n 1, Jan. 2000, p 105 – 110
- [Johansson97] Johansson, K. and Svensson, P., "*Submarine Tracking by Means of Passive Sonobuoys*", Methodology report, Division of Command and Control Warfare Technology SE-581, Sweden, June 1997.
- [Johnson82] Johnson, D.H., "*The application of spectral estimation methods to bearing estimation problems*", Proceedings of the IEEE, v 70, n 9, Sept. 1982 p 1018 – 1028
- [Johnson93] Johnson D. H. and Dudgeon D. E., "Array Signal Processing", Prentice Hall, 1993.

- [Kat95] Katsikas, S. K., Leros, A.K. and Lainiotis, D.G, "*Underwater Tracking of a Maneuvering Target Using Time Delay Measurements*", *Signal Processing*, v 41, January 1995, p 17-29.
- [Keonwook03] Keonwook, Kim and George, A.D., "*Parallel subspace projection beamforming for autonomous, passive sonar signal processing*", *Journal of Computational Acoustics*, v 11, n 1, March 2003, p 55-74.
- [Kogon02] Kogon, S.M., "*Robust adaptive beamforming for passive sonar using eigenvector/beam association and excision*", *IEEE Sensor Array and Multichannel Signal Processing Workshop Proceedings*, 2002, p 33-7.
- [Korenberg88] Korenberg, M.J., "*Identifying nonlinear difference equation and functional expansion representations: the fast orthogonal algorithm*", *Annals of Biomedical Engineering*, v 16, n 1, January 1988, p 123-142.
- [Korenberg89A] Korenberg, M. J., "*A Robust Orthogonal Algorithm for System Identification and Time-Series Analysis*", *Biological Cybernetics*, v 60, February 1989, p 267-276.
- [Korenberg89B] Korenberg, M.J. and Paarmann, L.D., "*Applications of fast orthogonal search: time-series analysis and resolution of signals in noise*", *Annals of Biomedical Engineering*, v 17, n 3, May 1989, p 219-31.

- [Korenberg98] Korenberg, M.J. and Adeney, K.M., “*Iterative Fast Orthogonal Search for Modeling by a Sum of Exponentials or Sinusoids*”, *Annals of Biomedical Engineering*, v 26, March 1998, p 315-327.
- [Kung98] Kung, Y., Hudson, R.E., Reed, C.W., Daching, C. and Lorenzelli, F., “*Blind beamforming on a randomly distributed sensor array system*”, *IEEE Journal on Selected Areas in Communications*, v 16, n 8, Oct. 1998, p 1555-1567.
- [Lee05A] Lee, J.-H. and Wang, C.-C., “*Adaptive array beamforming with robust capabilities under random sensor position errors*”, *Radar, Sonar and Navigation, IEE Proceedings*, v 152, n 6, 9 Dec. 2005, p 383 – 390.
- [Lim94A] Lim, P.H. and Ozard, J.M., “*On the underwater acoustic field of a moving point source. I. Range-independent environment*”, *Journal of Acoustical Society of America*, v 95, n 1, January 1994, p 131-137.
- [Lim94B] Lim, P.H. and Ozard, J.M., “*On the underwater acoustic field of a moving point source. II. Range-dependent environment*”, *Journal of Acoustical Society of America*, v 95, n 1, January 1994, p 138-51.

- [Camillet98] Carmillet, V. and Jourdain, G., "*Low-speed targets sonar detection using autoregressive models inreverberation; experimental performances for wideband signals*", OCEANS'98 Proceedings, v 3, Oct. 1998, p 1285 – 1289.
- [Maranda91] Maranda, B.H. and Fawcett, J.A., "*Detection and localization of weak targets by space-time integration*", IEEE Journal of Oceanic Engineering, v 16, n 2, Apr. 1991, p 189 – 194.
- [Maranda03] Maranda, B.H., "The statistical accuracy of an arctangent bearing estimator", Oceans'03 Proceedings, v 4, Sept. 2003, p 2127-2132.
- [Marsden87] Marsden, R. F. and Juszko, B.A., "*An Eigenvector Method for the Calculation of Directional Spectra From Heave, Pitch and Roll Buoy Data*", Journal of Physical Oceanography, v 17, n 12, Dec. 1987, p 2157-2167.
- [McGaughey03] McGaughey, D.R.; Korenberg, M.J.; Adeney, K.M.; Collins, S.D. and Aitken, G.J.M., "*Using the Fast Orthogonal Search with First Term Reselection to Find Subharmonic Terms in Spectral Analysis*", Annals of Biomedical Engineering, June 2003, v 31, p 741-75.

- [McDonald04] McDonald, M.A., "*FAR hydrophone usage in whale research*", Canadian Acoustics, v 32, n2, June 2004, p 155-60.
- [McIntyre99] McIntyre, C. M., Wang, J., and Kelly, L., "*The effect of position uncertainty in multistatic acoustic localization*", in Proceedings of International Conference of Information, Decision, and Control, Adelaide, Australia, 1999.
- [Mirsky90] Mirsky, L., "*An Introduction to Linear Algebra*", Courier Dover Publications, 1990.
- [Nardone97] Nardone, S.C. and Graham, M.L., "*A closed-form solution to bearings-only target motion analysis*", IEEE Journal of Oceanic Engineering, v22,n 1, Jan 1997 p 168 – 178.
- [Osman08] Osman, A., Noureldin, A., El-Sheimy, N., Mellema, G., Jim Theriault and Scott Campbell, "*Synthetic Virtual Array Processing of GPS Sonobuoys for Underwater Target Tracking*", IEEE/MTS Oceans 2008, Quebec city, September 15 – 18, 2008
- [Oppenheim98] Oppenheim, Alan V.; Schafer, R. W. and Buck, J. R., "*Discrete-time signal processing*", N.J.: Prentice Hall 1998, Page146.

- [Ping91] Ping Cao; Cuschieri, J.M.; Sudhakar, R., “*A High Resolution 3-d Sonar Imaging System For Autonomous Underwater Vehicles*”, OCEANS '91 Proceedings, v 2, Oct. 1991, p 1019 – 1026
- [Porter85] Porter M.B. and Reiss E.L., “*A numerical method for bottom interacting ocean acoustic normal modes*”, Journal of the Acoustical Society of America, v 77, n5, May 1985, p 1760-1767.
- [Schmidt86] Schmidt, R.O., “*Multiple Emitter Location and Signal Parameter Estimation*”, IEEE Trans. Antennas Propagation, v 34, March 1986, p 276-280.
- [Skolnik80] Skolnik, M. I., “*Introduction to Radar Systems*”, 2nd ed., McGraw-Hill, NY ,1980.
- [Solal91] Solal, M.,Pillon D., Brasseur, S.,”*Simultaneous detection and target motion analysis from conventional passive beamforming outputs*”, International Conference on Acoustics, Speech, and Signal Processing, 1991. ICASSP-91., p 1321 – 1324.
- [Steeb97] Steeb, Willi-Hans, “*Matrix Calculus and Kronecker Product with Applications and C++ Programs*”, World Scientific Publishing, 1997.

- [Stoer02] Stoer, J.; Bulirsch, R., *“Introduction to Numerical Analysis”*, 3rd ed., Berlin, New York: Springer-Verlag, 2002.
- [Streit02] Streit, R.L. and Walsh, M.J., *“Bearings-only target motion analysis with acoustic propagation models of uncertain fidelity”*, Aerospace and Electronic Systems, IEEE Transactions on, v38, n 4, Oct. 2002, p 1122 – 1137.
- [Thorn80] Thorn, J.V.; Booth, N.O. and Lockwood, J.C., *“Random and partially random acoustic arrays”*, Journal of the Acoustical Society of America, v 67, n 4, April 1980, p 1277-1286.
- [Tiel 97] Tiel, R., *“The passive sonar equation - effects of additive interference”*, IEEE International Conference on Acoustics, Speech and Signal Processing, v 1, Apr 1976, p 675 – 678.
- [Tsoukalas97] Tsoukalas, L.H. and Uhrig, R.E.. *“Fuzzy and neural approaches in engineering”*, New York: John Wiley & Sons, Inc.,1997.
- [Tseng93] Tseng, C.and Powers, E.J., *“Application of orthogonal-search method to Volterra modeling of nonlinear systems”*, IEEE International Conference on Acoustics, Speech, and Signal Processing, 1993, v 4, p 512-515.

- [Ultra06] Ultra Electronics Maritime Systems, Informal Communication, October 10 2006.
- [Urick96] Urick, R. J., "*Principles of underwater sound*", Revised ed. xiii, New York: McGraw-Hill, 1996.
- [Viberg91] Viberg, M. and Ottersten, B., "*Sensor array processing based on subspace fitting*", IEEE Transactions on Signal Processing, v 39, May1991, p 1110–1121.
- [Wenz72] Wenz, G.M., "*Review of underwater acoustics research: noise*", Journal of the Acoustical Society of America, v 51, n 3, pt.2, March 1972, p 1010-1024.
- [White04] Whitehouse, H. J., Alsup J. M., Leese de Escobar A. and Sullivan S. F., "*A GPS sonobuoy localization system*", Position Location and Navigation Symposium, April 2004, p 414-417.
- [Wilcox7] Wilcox, R.E., "*Underwater Doppler tracking using optimization techniques*", Journal of the Acoustical Society of America, v 63, n3, March 1978, p 870-875.

- [Wilmut98] Wilmut, M.J.; Ozard, J.M.; O'Keefe, K. and Musil, M., "A piecewise matched-field tracking algorithm", *IEEE Journal of Oceanic Engineering*, v 23, n 3, July 1998, p 167-173.
- [Yoshinaga99] Yoshinaga, H.; Taromaru, M. and Akaiwa, Y., "*Performance of adaptive array antenna with widely spaced antenna elements*", *Gateway to 21st Century Communications Village. IEEE VTS 50th Vehicular Technology Conference*, v 1, pt. 1, 1999, p 72-76.
- [Ziomek89] Ziomek, L.J. and Behrie, C.D., "*Localization of multiple broadband targets via frequency domain adaptive beamforming for planar arrays*", *Journal of the Acoustical Society of America*, v 85, n 3, March 1989, p 1236-1244.
- [Zhong05] Zhong, W.; Li, S. and Tai, H.M., "*Signal subspace approach for narrowband noise reduction in speech*", *Vision, Image and Signal Processing, IEE Proceedings*, v 152, n 6, 9 Dec. 2005, p 800 – 805.
- [Zoltowski94] Zoltowski, M.D., Mathews, C.P., "*Real-time frequency and 2-D angle estimation with sub-Nyquist spatio-temporal sampling*", *IEEE Transactions on Signal Processing*, v 42, n 10, 1994, p2781-2794.

APPENDIX A: VIRTUAL ARRAY TRANSFORMATION MATRIX DESIGN

The transformation matrix bias reduction is based on minimization of deterministic signal subspace eigenvector errors due to array transformations. Subspace-based DOA estimators are considered, and therefore, an estimate of the signal subspace eigenvector of the virtual array is needed.

The DOA estimate is taken at the extreme point of a sufficiently smooth criterion function $V(\theta, \hat{e}_v)$ associated with the MUSIC algorithm. The symbol \hat{e}_v denotes a general approximation of e_v which represents the orthonormal eigenvectors corresponding to the eigenvalues of the signal subspace. The Taylor series expansion is given as [Hyberg04]:

$$\dot{V}(\hat{\theta}, \hat{e}_v) = \dot{V}(\theta_0, e_v) + \ddot{V}(\theta_0, e_v)\Delta\theta + 2\text{Re}\{g_v^H \Delta e_v^{(i)}\} + r \quad \text{A.1}$$

Where g_v is the complex gradient of $\dot{V}(\theta_0, e_v)$ with respect to e_v

$\Delta\theta$ is the deterministic DOA perturbation

r is the remainder term (can be neglected in a first-order analysis since it is at least quadratic in Δe_v and/or $\Delta\theta$).

Assuming invariability of the second derivative, the resulting perturbation $\Delta\theta$ in θ_0 can be expressed as (up to a first-order approximation)

$$\Delta\theta = [\ddot{V}(\theta_0, e_v)]^{-1} 2 \operatorname{Re}\{g_v^H \Delta e_v^{(i)}\} \quad \text{A.2}$$

This expression shows the effect of a small perturbation in Δe_v of the signal subspace e_v on the DOA estimate.

The transformation matrix is designed to achieve minimum bias for all possible DOAs in the sector of interest. The bias mitigation is achieved by satisfying two conditions: (1) Small error for the first order approximation (Equation A.2) to hold, and (2) Approximately preserving the orthogonality between the gradient of the criterion function and the mapping error. Thus, a bias minimization may be designed as [Hyperg04]:

$$T_{LS} = \arg \min_T \sum_{i=1}^{N_{cal}} (1 - \mu) \|\Delta e_v^{(i)}\|^2 + \mu \left| \frac{2 \operatorname{Re}\{g_v^{(i)H} \Delta e_v^{(i)}\}}{\ddot{V}(\theta^{(i)}, e_v^{(i)})} \right| \quad \text{A.3}$$

The first and second terms advocate the requirements 1 and 2 respectively. The symbol $\|\cdot\|$ is the vector 2-norm and μ a weighting factor $0 < \mu < 1$ that allows a balancing between the two properties i) and ii). Note that $\Delta e_v^{(i)}$ are affine functions of T , $\Delta e_v^{(i)} = T^H e_s^{(i)} - e_v^{(i)}$. Therefore the above criterion (Hyperg04), is a quadratic function of the elements of T .

A.1. Transformation matrix parameters

The least square solution for equation A.3 is obtained by using the design criterion associated with MUSIC and WSF [Hyperg04]. The MUSIC estimate for one-emitter scenarios is obtained by minimizing the criterion function [Hyperg04]:

$$V_{MUSIC}(\theta, \hat{e}_v) = a_v^H(\theta) \Pi_{\hat{e}_v}^\perp a_v(\theta) \quad A.4$$

Where \hat{e}_v an estimate of the signal subspace is, $\Pi_{\hat{e}_v}^\perp$ is the orthogonal projector onto the estimated noise subspace [Hyperg04 and Zhong05]. $\Pi_{\hat{e}_v}^\perp$ is given by [Hyperg04]:

$$\Pi_{\hat{e}_v}^\perp = I - \hat{e}_v (\hat{e}_v^H \hat{e}_v)^{-1} \hat{e}_v^H \quad A.5$$

The WSF estimate for one-emitter scenarios is obtained by minimizing the criterion function [Hyperg04]:

$$V_{WSF}(\theta, \hat{e}_v) = Tr\{\Pi_{a_v(\theta)}^\perp \hat{e}_v w \hat{e}_v^H\} \quad A.6$$

Where $Tr\{\cdot\}$ is the trace operator, w is the weighting matrix which reduces to scalar in case of single emitter. $\Pi_{a_v(\theta)}^\perp$ is the orthogonal projector onto the array manifold complement [Hyperg04 and Viberg91]. $\Pi_{a_v(\theta)}^\perp$ is given by [Hyperg04]:

$$\Pi_{a_v(\theta)}^\perp = \mathbf{I} - a_v(a_v^H a_v)^{-1} a_v^H \quad \text{A.7}$$

For the single source case, the two criterion functions lead to identical DOA estimates [Hyperg04]. By assuming that $a_v^H(\theta)a_v(\theta)$ is constant, the WSF and MUSIC DOA estimate is obtained as the minimizing argument of:

$$V(\theta, \hat{e}_v) = -\bar{a}_v^H(\theta) \hat{e}_v \hat{e}_v^H \bar{a}_v(\theta) \quad \text{A.8}$$

Where $\bar{a}_v(\theta)$ is the normalized array response vector for the virtual array and is given by [Hyperg04]:

$$\bar{a}_v(\theta) = a_v(\theta) (a_v^H(\theta) a_v(\theta))^{-1/2} \quad \text{A.9}$$

Using the criterion function (Eq. A.8), the complex gradient g_v is given by [Hyperg04]:

$$g_v = -\Pi_{a_v(\theta)}^\perp \bar{d}_v(\theta) \quad \text{A.10}$$

Where \bar{d}_v is the derivative of the normalized response vector $\bar{a}_v(\theta)$ of the virtual array with respect to θ , $\bar{d}_v = \partial(\bar{a}_v(\theta))/\partial\theta$.

A.2. Least mean square solution for Transformation matrix minimization criterion

The algorithm presented in [Hyperg04] solves for the optimal transformation matrix by first simplifying the criterion function (Equation A.3). This function can be simplified by assuming the second derivative of the DOA estimation criterion ($\ddot{V}(\theta_0, e_v)$) is constant over the design sector [Hyperg04]. Using this assumption, the weighting factor μ can be modified to include the second derivative. The simplified form [Hyperg04] of transformation matrix criterion function can then be obtained by substituting the parameters obtained in section A.1. The simplified form is given by [Hyperg04]:

$$T_{LS} = \arg \min_T \sum_{i=1}^{N_{cal}} (1-k) \left\| T^H \bar{a}(\theta^{(i)}) - \bar{a}_v(\theta^{(i)}) \right\|^2 + k \left| 2 \operatorname{Re} \left\{ \mathbf{g}_v^{(i)H} \Delta e_v^{(i)} \right\} \right|^2 \quad \text{A.11}$$

Where $0 < k < 1$ is the new weighting factor.